THE UNIVERSITY
of EDINBURGH

A study of the vortex flows of downwind sails

Abel Arredondo Galeana

THE UNIVERSITY
of EDINBURGH

Doctor of Philosophy

THE UNIVERSITY OF EDINBURGH

2019

To my wonderful and loving wife Anna, who was always by my side,

and to my parents, who provided me with strength and balance.

Lay Summary

Spinnakers are special sails used to sail downwind. It has been shown with computational studies, that such sails can promote a leading edge vortex (LEV). The LEV grows in diameter from the bottom to the top of the sail. According to recent computational studies, this vortex can remain attached to the surface of the sail near the leading edge. When this happens, the vortex increases the thrust force generated by the spinnaker.

An attached vortex occurs in gliding wings with sharp leading edges, for example at the wings of swifts. Its application in sailing opens up new design and control possibilities to enhance the performance of yacht sails, and unlocks new avenues of research where vortex flow is a dominant feature.

This thesis presents experimental observations of flow around a scale model spinnaker, in the absence of a hull, and 3D printed in rigid material. Using flow visualisation in water, the existence of an LEV is confirmed. The LEV can remain attached to the sail for finite periods.

A mathematical model is introduced to compute the contribution of the LEV to the force generation. It is found that the LEV contributes between 10% to 20% to the total lift force, in sections where it occurs. The LEV is not always attached; it can also convect downstream of the sail. The thesis provides measurements of forces and flow fields in the vicinity of three rigid spinnaker prototypes with different twist. It is found that the twist of a sail can alter the trajectory of leading-edge vortices and therefore alter the forces. High twist generates less lift and less drag, by keeping the clockwise-rotating LEVs more distant from the surface of the sail and allowing counter-clockwise-rotating flow to emerge on top of the surface of the sail.

This investigation expands our knowledge of downwind sail aerodynamics by revealing flow physics that has not been previously captured experimentally. Additionally, these exciting findings offer the possibility of incorporating the LEV effect to new technology where sail-like geometries are encountered. Examples include wind and tidal energy converters and micro-aerial vehicles.

Abstract

A leading-edge vortex (LEV) can be a robust lift generation mechanism on both the wings of natural fliers and delta wings. A spinnaker-type of sail is a thin wing that promotes the formation of LEVs due to a sharp leading edge. Recent numerical simulations (Viola et al., 2014) have demonstrated that this type of sail can prevent LEV shedding and instead, keeps it trapped near the leading edge. In such cases, the LEV could enhance lift generation (Saffman and Sheffield, 1977; Huang and Chow, 1982), and so there is a need to investigate the existence of the LEV and its role for sails.

To study the LEV in the context of sails, a rigid model scale spinnaker was tested in water at low Reynolds numbers and uniform flow. It was found that the flow separates at the leading edge, followed by turbulent reattachment, forming an LEV. For finite periods the LEV breaks down into weaker LEVs that are shed downstream; otherwise, the LEV remains coherent at the leading edge. On the lower half of the sail, the LEV has negligible diameter, and trailing edge separation occurs after the first quarter of the chord.

To understand whether there is a benefit from having the LEV trapped near the leading edge, as opposed to being shed downstream into smaller LEVs, the local circulation was measured and its value utilised in a complex potential model. The model maps a circular arc into a rotating cylinder and assumes the Kutta condition, to provide a bound circulation value that is a function of the position and circulation of each LEV (Pitt Ford and Babinsky, 2013; Nabawy and Crowther, 2017). It is found that when the LEV is trapped near the leading edge, the LEV provides a marginally higher lift than when it breaks down and sheds. Surprisingly, with the conservative assumption of the Kutta condition, the LEV contributes between 10% to 20% to the sail's sectional lift.

In actual sailing conditions, the spinnaker experiences a twisted onset flow, that could not be replicated in the water flume, such that the angle of attack varies along the span of the sail. To explore this effect three spinnaker models were made, where the original sail was twisted from top to bottom by different angles. PIV and force measurements were compared. It was observed that a low twist sail allows the LEVs to remain close to the body of the sail, whereas a high twist sail causes them to drift away and generates counter vorticity on the surface of the sail. This viscous effect results in a marginal reduction in lift, but significant reduction of induced drag.

The results presented in this PhD thesis aim to provide an improved understanding of the aerodynamics of downwind sails, where vortex flow is a dominant feature. The existence of trapped and shedding LEVs is demonstrated and an attempt is made to model LEVs through a complex potential model in order to assess their contribution to the sectional lift of the sail. Finally, the effect of twist is evaluated with regard to the aerodynamics of sails.

Acknowledgements

I'd like to thank my supervisor Dr. Ignazio Maria Viola for his invaluable help, hard work and endless support during the four years of my PhD. To my second supervisor Prof. Alistair Borthwick for his important feedback and encouragement in my annual reviews and at the end of this work. To Jean Baptiste Richon for his training with PIV and the equipment of the Sanderson lab. To my senior PhD colleagues Susan, Tamas, Rowan, Gabriel, Cathal, Mark, Manuel, Jaffar, Nicola, Tom and to the new generation Shuji, Daniele, JB, Weidong, Gabriele and all of the A.1234/1 office, for their insightful discussions and cheerful moments. To the academics who helped me revise this thesis before submission, Colin Anderson, Jean-Baptiste Souppez, Cathal Cummins, Brian Petersen, Alistair Borthwick and Ignazio Maria Viola. Finally, I'd like to thank CONACYT, for sponsoring the length of my PhD studies.

Declaration

I declare that this thesis was composed by myself, that the work contained herein is my own except where explicitly stated otherwise in the text, and that this work has not been submitted for any other degree or professional qualification except as specified.

Abel Arredondo Galeana

Contents

Figures and Tables

Figures

Tables

Nomenclature

LATIN SYMBOLS

a Lift curve slope in lift coefficient correction equation

A Area

A_m Cross sectional area of model

A_t Cross sectional area of test section

AR Aspect ratio

c_{av} Average chord length

c_0 Chord at 3/4 of the test section from bottom to top

C_L Lift coefficient corrected for solid and wake blockage and streamline curvature

$C_{L,u}$ Lift coefficient uncorrected

C_{L_b} Lift coefficient due to bound circulation

$C_{L_{LEV}}$ Lift coefficient due to external vortex circulation

$C_{L,\max}$ Maximum lift coefficient

$C_{L/D}$ Lift to drag ratio

$C_{L/D,\max}$ Maximum lift to drag ratio

$C_{L,p}$ Lift coefficient from potential-flow theory

$C_{L,v}$ Lift coefficient from vortex lift

C_l Sectional lift coefficient

$C_{l,\max}$ Maximum sectional lift coefficient

C_D Drag coefficient corrected for solid and wake blockage and streamline curvature

$C_{D,u}$ Drag coefficient uncorrected

$C_{D,i}$ Theoretical induced-drag coefficient

C_{DF} Drive force coefficient

$C_{DF,\max}$ Maximum drive coefficient

C_{SF} Lateral force coefficient

C_S Suction force coefficient

C_T Trust force coefficient

d Distance between uniformly distributed grid points

d_f Fringe spacing

d_τ Particle image diameter

D Drag force

D_{S_1} Drag calibration for geometry S_1

D_{S_2} Drag calibration for geometry S_2
D_{S_3} Drag calibration for geometry S_3
E Young Modulus
f Shedding frequency
f_o Frequency of source
f_{sc} Scattered frequency
f_D Doppler frequency
F Force applied on a body
F_{DF} Driving force
F_{SF} Side force
g Gravity of Earth
gm Gram
i Imaginary number equal to the squared root of negative one
I Turbulence intensity
I_o Intensity of light at origin
I_{sc} Intensity of light at source
K_1 Factor to calculate wing wake pressure drag
K_p Constant of proportionality for potential lift
l Half of the length of region S_w
l_0 Radius of the vortex where the tangential velocity (u_θ) is maximum
l/l_0 Ratio of half length of detection window to vortex core radius
L Lift force
L_{S_1} Lift calibration for geometry S_1
L_{S_2} Lift calibration for geometry S_2
L_{S_3} Lift calibration for geometry S_3
L/D Lift to drag ratio
m Mass
n Number of discrete samples
N_{ppp} Particle image density
ppp Particle images per pixel
Q Local vortex detection criterion
r Width to height ratio
Re Reynolds number
R_{fit} Statistic showing the goodness of the fit
S Span
St Strouhal number

S_0 High twist spinnaker, first design
S_1 High twist spinnaker, second design
S_2 Intermediate twist spinnaker
S_3 Low twist spinnaker
S_{ij} Strain tensor
S_w Window size for γ detection method
t Time
t_h Thickness
t_h/c_{av} Thickness to average chord ratio
u_i' Velocity fluctuations with respect to the mean value
u_{rms}' Root mean squared of the velocity fluctuations
u_i Velocity in the x, y and z direction (streamwise, normal, spanwise)
$u_{y,tilt}$ Tangential measured velocity oriented projected in the y-axis
$\overline{u}$ Mean value of velocity
u_p Particle velocity
u_{PIV} Particle velocity
u_θ Tangential velocity
U_∞ Freestream velocity
U_c Velocity around an object due to blockage and wake effect
U_{droplet} Droplet velocity
U_{wake} Velocity in the wake
V_t True wind
V_b Wind due to boat velocity
V_a Apparent wind
V_{a1} Apparent wind before twist adjustment
V_{a2} Apparent wind after twist adjustment
V_w Volume of the wing
v_o Output voltage of load cell
x_p Particle position
x Horizontal coordinate in the z-plane
y Vertical coordinate in the z-plane
$\hat{x}$ Horizontal coordinate in the $\hat{z}$-plane
$\hat{y}$ Vertical coordinate in the $\hat{z}$-plane
X Horizontal coordinate in the ζ-plane
Y Vertical coordinate in the ζ-plane
z Complex plane of circular arc after to rotation

$\hat{z}$ Complex plane of circular arc prior to rotation
$\overrightarrow{z}$ Normal plane

GREEK SYMBOLS

α Angle of attack
$\alpha_{\mathrm{X_i}}$ Angle between the chord line of the X-th cross-section of the i-th sail geometry and the flume flow direction, where X takes the values of $X = \mathrm{A,B,C,D,E}$ and i takes the values of $i = 1,2,3$ and refers to geometries $\mathrm{S_1}$, $\mathrm{S_2}$ and $\mathrm{S_3}$
β_{a} Apparent wind angle
$\beta_{\mathrm{a_{OPT}}}$ Optimum apparent wind angle
β_{a1} Apparent wind angle before twist adjustment
β_{a2} Apparent wind angle after twist adjustment
β Angle generated due to circle displacement in potential flow model
δ Uncertainty
δ_{b} Boundary correction factor
δt Time step or change in time
δL Lift uncertainty
δD Drag uncertainty
$\delta\rho_{\mathrm{d}}$ Density uncertainty
δu_{PIV} PIV velocity uncertainty
δU_{∞} Velocity uncertainty
$\delta_{\mathrm{E_iA_i}}$ Twist or angle difference between the angle of attack of plane E (α_{E}) and the angle of attack of plane A (α_{A}), where i takes the values of $i = 1,2,3$ for geometries $\mathrm{S_1}$, $\mathrm{S_2}$ and $\mathrm{S_3}$, respectively
$\delta_{\mathrm{X_iA_i}}$ Local twist or angle difference between the angle of attack of plane X (α_X) and the angle of attack of plane A (α_{A}), where i takes the values of $i = 1,2,3$ for geometries $\mathrm{S_1}$, $\mathrm{S_2}$ and $\mathrm{S_3}$, respectively
$\delta_{\mathrm{E_iE_j}}$ The difference between α_{E_i} and α_{E_j}, where α_{E_i} and α_{E_j} correspond to the same plane but different geometry. For geometries $\mathrm{S_1}$, $\mathrm{S_2}$ and $\mathrm{S_3}$, i and j take values of $i, j = 1,2,3$, respectively.
Δ Local detection criterion
ΔC_{D_W} Wing wake pressure drag
ΔC_{D_B} Body wake pressure drag
ΔT Change in temperature
ε Solid-wake blocking correction

ε_{bias} Bias error

$\varepsilon_{\mathrm{PIV}}$ PIV error

ε_{rms} Random error

ε_{tilt} Tilt error

$\eta_{\mathrm{L/D}}$ Sail angle of rotation providing maximum lift-to-drag ratio coefficient

η_{MD} Sail angle of rotation providing maximum driving force coefficient

η_{L} Sail angle of rotation providing maximum lift coefficient

η Sail angle of rotation around a vertical axis through the head of the sail

γ Global vortex detection criterion

γ_1 Global vortex detection criterion without convection flow field subtracted

γ_2 Global vortex detection criterion with convection flow field subtracted

Γ Circulation

Γ_0 Effective bound circulation, which is the Kutta condition circulation in the absence of external vortices

Γ_{LEV} Circulation of leading-edge vortex

Γ_{LO} Lamb-Oseen vortex circulation

Γ_{b} Bound circulation

$\overline{\Gamma_{\mathrm{b}}}$ Average bound circulation

Γ_{i} Circulation of vortex i

κ Geometric coefficient of free vortices

κ_i Geometric coefficient of vortex i

λ_{o} Wavelength of source

λ_2 Local vortex detection criterion

Λ Sweep angle

ϕ_{h} Heel angle

ϕ Potential function

ψ Stream function

ω_{i} Vorticity in the x, y and z direction (streamwise, normal, spanwise)

Ω_{ij} Rotation tensor

μ Half of maximum camber

ρ_{d} Density of fluid

ρ Location of vortex to centre of cylinder in complex potential model

ρ_{i} Location of free vortex i to centre of cylinder in complex potential model

σ Bevel angle

τ_{ldv} Period of signal recorded by photodetector of LDV system

τ Azimuthal angle of free vortex in complex potential model

τ_i Azimuthal angle of free vortex i
τ_1 Factor to calculate wing wake pressure drag
τ_2 Streamline curvature correction
θ Angle of polar coordinate
θ_{ldv} Angle between the laser beams of a LDV system
ζ Complex variable or complex plane with the real part corresponding to the potential function (ϕ) and the imaginary part corresponding to the stream function (ψ)
ζ_0 Displacement of circle from the origin
ζ_{TE} Location of trailing edge in the circle plane

ACRONYMS

CFD Computational Fluid Dynamics
DES Detached eddy simulation
DT Time between frames
LDV Laser Doppler Velocimetry
LEV Leading-edge vortex
LEV_{av} Time-averaged leading-edge vortex
LE Leading-edge
LSB Laminar separation bubble
PIV Particle Image Velocimetry
RANS Reynolds averaged Navier-Stokes
TE Trailing-edge
TEV Trailing-edge vortex

PART A:
INTRODUCTION

Chapter 1

Introduction

1.1 Downwind sail aerodynamics

Sails are thin wings with a sharp leading edge. For downwind sailing two main types of sails are typically used: the mainsail and the spinnaker (Fig. 1.1). The mainsail, which is on the rear of the yacht, has both the leading edge and the lower edge attached to rigid structures (the mast and the boom, respectively). Conversely, the spinnaker, which is in the front of the yacht, is attached to the yacht by three corners only. Hence, the sharp leading edge could lead to flow separation, at positive angles of attack (Fig. 1.2). This is one of the key features of yacht sails that makes them different from conventional wings.

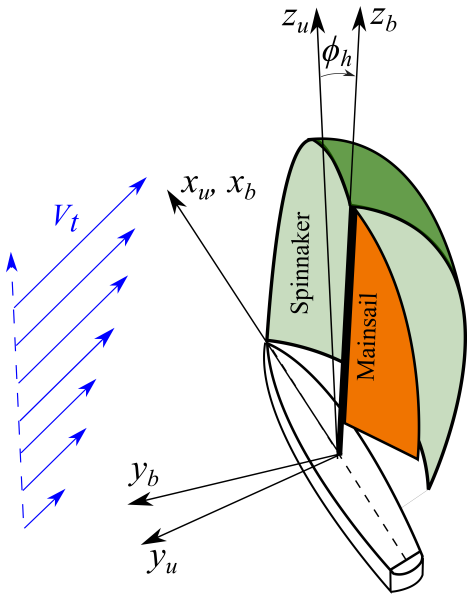

Figure 1.1: Bird's eye view of a yacht sailing downwind, where V_t is the true wind velocity and ϕ_h is the heel angle in the vertical plane perpendicular to the yacht's longitudinal axis. Here x_u, y_u and z_u and x_b, y_b and z_b are the upright and heeled boat frames of reference, respectively

The flow at the leading edge is similar to that of a plate at incidence (Viola and Flay, 2015). Flow reattachment typically occurs downstream of the leading edge, forming a region of separated flow. Although this region is short in the chordwise direction, it grows from the base to the tip of the sail (Viola et al., 2013). Spinnakers are highly-cambered, highly-twisted and low-aspect-ratio sails. The maximum camber of horizontal sections of the sail is typically higher than 20% of the chord length (Flay et al., 2017). The twist angle between the root and top section is about 20°, and the aspect ratio (AR) is between 1.5 and 2. Such sails are designed to generate maximum lift and drag has little effect on the yacht performance when sailing downwind. The large camber enables high lift, but it also leads to trailing edge separation. The rear separated region could cover more than half of the chord. Since its extent is easier to identify than the smaller leading edge separated area, the length of the rear region is typically used to inform the sail designer as to where the shape of the sails can be enhanced. However, virtually all of the driving force is generated near the leading edge. Thus, small changes in the fluid dynamics of the leading edge separated region can result in significant gains in performance. One of the aims of this thesis is to gain new insight into this flow region.

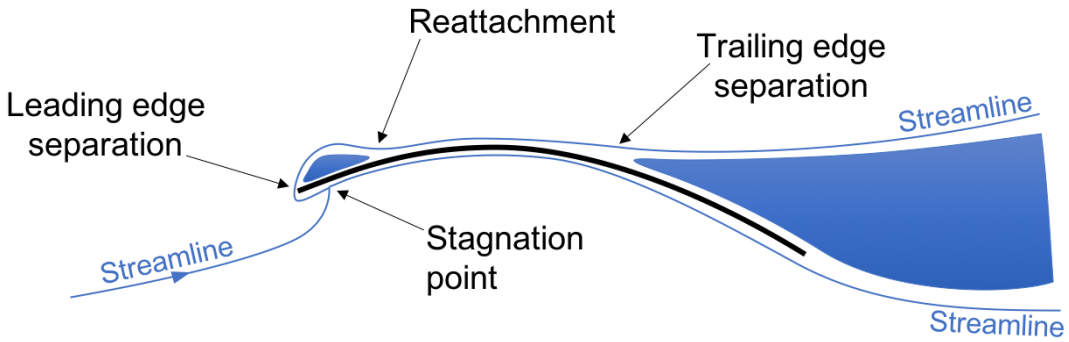

Figure 1.2: Flow around a spinnaker section

Flow separation at the leading edge can occur in the form of a laminar separation bubble (LSB) or a leading edge vortex (LEV). An LSB occurs when a laminar boundary layer encounters a sufficiently strong adverse pressure gradient, causing the flow to separate (O'Meara and Mueller, 1987). The resulting separated shear layer undergoes laminar to turbulent transition and reattachment. Vorticity is continuously shed downstream in the form of vortices, that roll on the surface of the airfoil toward the trailing edge. The time-averaged flow field shows flow reattachment downstream of the point where laminar to turbulent transition occurs.

Alternatively, if separation is accompanied by a concentration of vorticity at the leading-edge and a coherent structure is detected, leading edge separation is related to an LEV type of flow. The LEV is an instantaneous feature of the flow and is resilient to turbulence. Chapter 2 expands the definition of the LEV and its stabilization mechanisms.

Downwind sails are subject to apparent wind (V_a), where V_a is the resultant of the vector addition of the true wind velocity (V_t) and the wind due to the yacht's velocity (V_b). The magnitude of V_t changes with height and follows an atmospheric boundary-layer profile. On the other hand, the magnitude of V_b is not height dependent. The vector addition of V_t and V_b at different heights of the sail results into a twisted V_a, as shown in Fig. 1.3. This effect has led researchers to build or modify wind tunnels (Flay, 1996; Zasso et al., 2005; Fossati et al., 2006) with twisted vanes, to deflect the flow acting on the sail models.

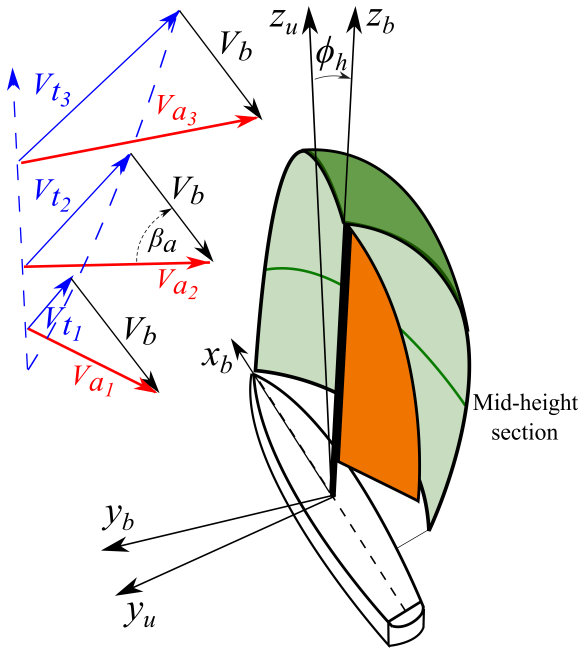

Figure 1.3: Twisted apparent wind V_a at three height stations of the sail, bottom-section (V_{a_1}), mid-section (V_{a_2}) and top-section (V_{a_3})

The orientation of the sail with respect to V_a is key in its performance. Poor alignment is reflected either by the sail collapsing at low angles of attack or by high drag force generation at high angles of attack. Optimum alignment occurs when the spinnaker generates maximum driving force. This happens at an intermediate angle of attack, where the spinnaker produces high lift and low drag. If the angle of attack is too high, the spinnaker produces high drag and the driving force decreases.

Figure 1.4 shows these two scenarios for the mid-height section of the spinnaker. In Fig. 1.4a, the section is at the maximum-driving-force angle of attack. Flow reattachment occurs downstream of the leading edge and upstream of the mid-chord of the section. In Fig. 1.4b the section is poorly aligned. Flow reattachment does not occur, drag increases and the drive decreases.

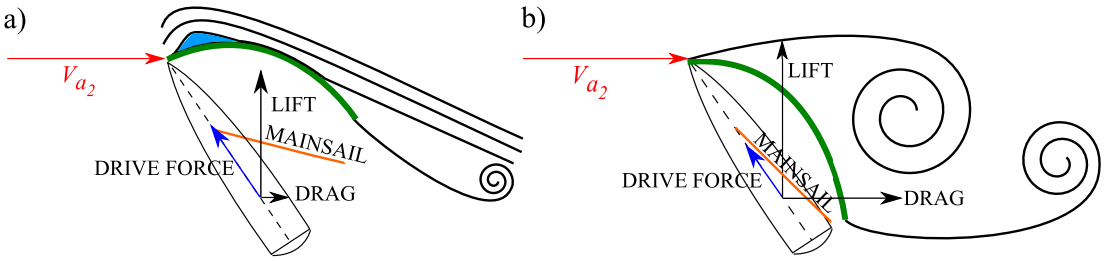

Figure 1.4: Top view of yacht sailing downwind, where the mid-section of the spinnaker is subject to apparent wind velocity (V_{a_2}) and the mid-section is a) at the maximum-driving-force angle of attack and b) at a sub-optimal angle of attack

Downwind sailing at the optimum true wind angle $\beta_{t_{OPT}}$ and at the optimum apparent wind angle $\beta_{a_{OPT}}$

Although it is possible to sail straight downwind along the direction of the wind (Fig. 1.5a), the fastest route to navigate from point A to point B is achieved by sailing at an angle with respect to the true wind direction (Fig. 1.5b).

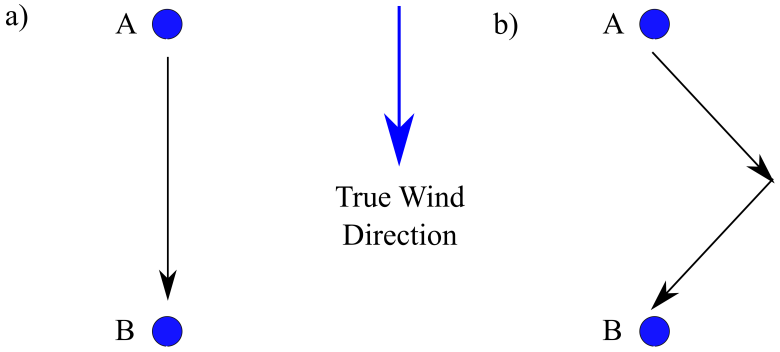

Figure 1.5: a) Shortest route sailing downwind and b) fastest route sailing downwind

Both scenarios can be pictured within a polar plot with the boat direction and the boat speed as angular and radial coordinates, respectively. Figure 1.6a shows a schematic drawing of a polar plot of a high-performance sailing yacht. The polar plot data for the boat, for which the sail investigated in this thesis was designed for, is confidential. However, several examples of polar plots for high-performance yachts can be found in Souppez et al. (2019a).

The red line in Fig. 1.6a indicates how fast the boat can travel at any given direction, with respect to the true wind direction (V_t). By considering point A, the starting point and point B, the destination point, the polar plot shows that it is possible to sail dead downwind from point A to point B. However, the fastest route is achieved by sailing downwind at the optimum true wind angle ($\beta_{t_{\mathrm{OPT}}}$) and changing direction once to reach point B.

By sailing downwind at the optimum true wind angle ($\beta_{t_{\mathrm{OPT}}}$), the optimum apparent wind angle ($\beta_{a_{\mathrm{OPT}}}$) is found as the angle between V_a and V_b at a height of 10 m from the surface of the water (Fig. 1.6b). Figure 1.6c shows that the magnitude of the true wind (V_t) is height dependant and thus the 10 m height is chosen as reference to define $\beta_{a_{\mathrm{OPT}}}$.

The shape of the sail at the optimum apparent wind angle ($\beta_{a_{\mathrm{OPT}}}$) has been studied by Viola et al. (2014) and the same shape is used on this thesis. Further details of the experimental positioning of the sail are found in Chapter 3.

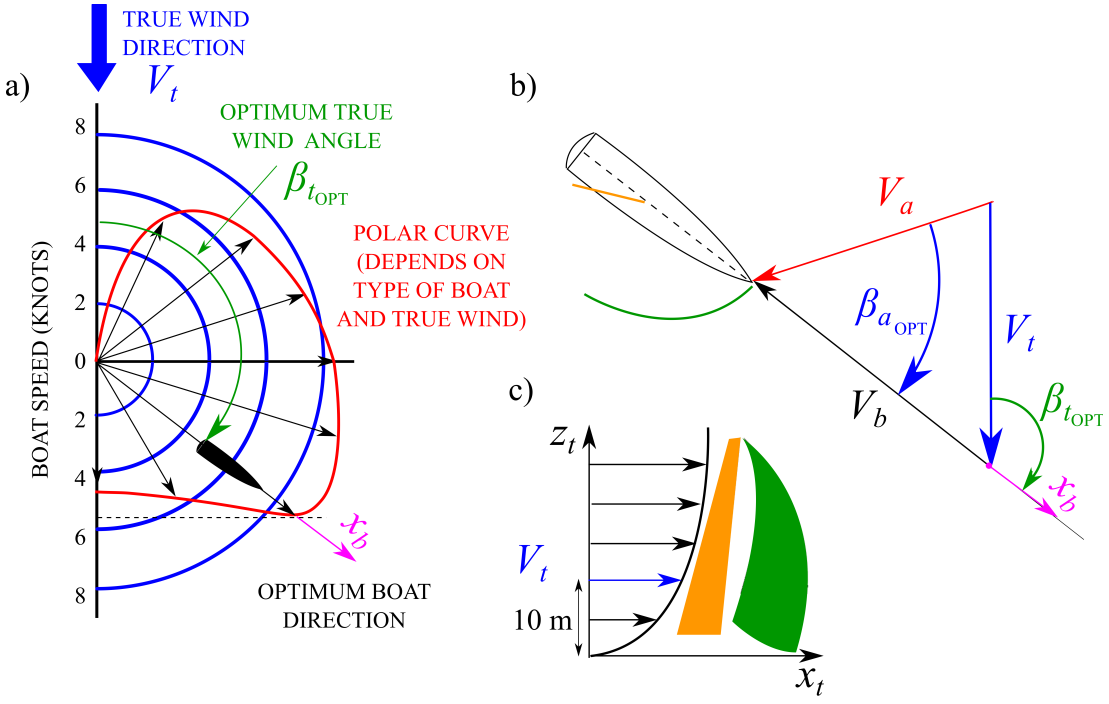

Figure 1.6: a) Schematic drawing of a polar plot of a high-performance sailing yacht showing optimum boat direction (x_b) and optimum true wind angle ($\beta_{t_{\mathrm{OPT}}}$); b) Wind triangle between the true wind velocity (V_t), the apparent wind velocity (V_a) and the wind velocity due to the boat velocity (V_b); c) Vertical profile of the true wind velocity (V_t)

1.2 Recent findings

When the leading edge of a wing is sharp the flow separates, forming a strong shear layer. This results in the production of vorticity that accumulates in the separated region. The surface integral of the vorticity in this region leads to a circulation of the same sign as the bound circulation of the sail; thus this vorticity contributes to the generation of circulatory lift. However, vorticity cannot be accumulated indefinitely. It is either shed downstream with the main flow stream, or else somehow extracted.

At the leading edge of staysails (genoas and jibs), which are higher aspect ratio sails than spinnakers and are used to sail upwind, the vorticity is continuously shed downstream in the form of vortices that roll on the surface of the airfoil toward the trailing edge (Viola and Flay, 2011a, 2015; Nava et al., 2016). The time-averaged flow field shows flow reattachment somewhere downstream of the leading edge and a thick boundary layer that grows towards the trailing edge. Conversely, in asymmetric spinnakers used for downwind sailing, recent Detached Eddy Simulations (DES) have revealed that vorticity is not shed downstream, but convected axially and a stable attached leading-edge vortex (LEV) occurs (Viola et al., 2014).

This was anecdotally anticipated by Bethwaite (Bethwaite, 1993), who sketched the LEV on the asymmetric spinnaker of high-performance dinghies. Figure 1.7 shows the sketch of an LEV on the suction side of a spinnaker. Downwind sails have a sweep angle ($\Lambda \approx 40^o$) at the top part of the sail, similar to a non-slender delta wing. It could be hypothesised that an LEV could be generated at the leeward side of a spinnaker under certain conditions.

Figure 1.7: Sketch of an LEV on a spinnaker

One of the objectives of the present work is to provide experimental evidence that a stable LEV can occur on asymmetric spinnakers, corroborating the previous numerical evidence. Moreover, the work aims to quantify the contribution of the LEV to the performance of the sails.

The same asymmetric spinnaker where the LEV was identified with DES (Viola et al., 2014) is considered in this work. The aerodynamics of this sail has been widely investigated in the last decade and this makes it one of the best available benchmarks for downwind sails. The geometry is available in the yacht engineering section of the website www.ignazioviola.com. This sail was designed for the AC33 class, which was proposed for the 33rd America's Cup. This class was never adopted because the 33rd America's Cup was eventually restricted to multi-hulls (ruled by the Deed of Gift). The optimum apparent wind angle ($\beta_{a_{\mathrm{OPT}}}$) for this geometry has been found experimentally in wind tunnel testing by Viola and Flay (2009) and Viola and Flay (2010). They stated that $\beta_{a_{\mathrm{OPT}}} = 55^{\circ}$ is the angle providing the maximum velocity made good (i.e. the maximum boat velocity component in the direction parallel to that of the wind) for the specific AC33 boat and wind conditions for which the sail was initially designed. This was confirmed in further experiments by Bot et al. (2014). Therefore, this is the optimum apparent wind angle $\beta_{a_{\mathrm{OPT}}}$ shown in Fig. 1.6b and it is the position tested in this thesis, as described later in Chapter 3. Furthermore, the relevance of this geometry is highlighted by previous work, which is now summarised.

A 1:15th-scale model of this sail was tested in a wind tunnel at $\beta_{a_{\mathrm{OPT}}} = 55^{\circ}$ and 10° heel angle. The forces (Viola and Flay, 2009) and pressures (Viola and Flay, 2010) on the sail surfaces were recorded for a range of sail trims and also compared with those measured on similar sails. The sail trim that allowed the maximum driving force was used to build a rigid sail, with embedded pressure taps and both forces and pressures were measured in a wind tunnel (Bot et al., 2014). This sail trim was also modelled with Reynolds-averaged Navier-Stokes (RANS) simulations (Viola and Flay, 2011b) and with DES (Viola et al., 2014). A 1:3rd-scale prototype was built and tested on water on a Platu 25-class yacht (Viola and Flay, 2012), where surface pressures were measured. A three-way comparison between the pressures measured in a wind tunnel, on water and with RANS was presented in Viola and Flay (2011b). The pressures from these three approaches showed a qualitative agreement, with the pressures computed numerically lying in between those measured with the two experimental techniques. Finally, a comparison between wind tunnel tests performed with flexible and rigid sails, and DES, was presented by Bot et al. (2014) and Viola et al. (2014).

Full-scale pressure measurements have, in some instances, provided evidence of the presence of an LEV. Viola and Flay (2011a) identified a suction peak at the trailing edge of full-scale downwind sails at high apparent wind angles. They argued that this is evidence of delta wing-like vortex formation on the top section of the spinnaker. Motta et al. (2015) also performed full-scale pressure measurement, detecting low pressure peaks periodically convecting chordwise; a phenomenon associated to the shedding of an LEV. Richards and Viola (2015) also suggested that in asymmetric spinnakers the inability to sustain an LEV leads to its shedding in the upper sections of downwind sails.

Earlier CFD results by Viola et al. (2014) suggest that a coherent and stationary LEV forms from the foot of the sail to the head; that it grows in size towards the head and vorticity is convected by spanwise flow inside the vortex core, merging with the tip vortex at the head of the sail. They suggest that the LEV is an exceptional lift generator. Based on these observations a hypothesis is developed.

The hypothesis is that there is an LEV attached to the leading edge of a downwind sail and that it increases lift when sailing downwind with the sail trimmed at maximum driving force angle.

To verify if the hypothesis is true the LEV needs to be observed. Following that, the author of this thesis will analyse whether the LEV remains trapped or is shed and will investigate what is the lift contribution of the LEV at the maximum driving force angle.

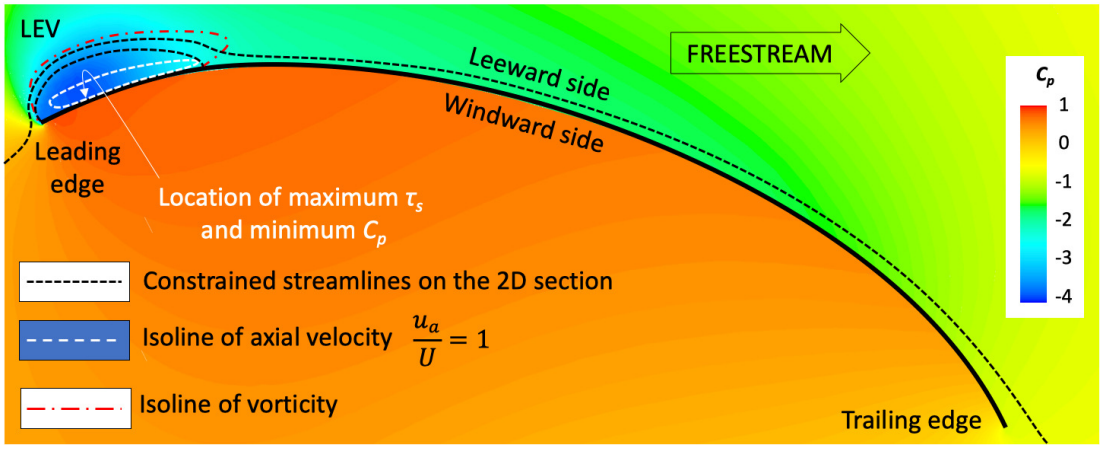

Figure 1.8: CFD results showing leading edge vortex found by Viola et al. (2014) at a section at $7/8^{\text{th}}$ from the span of the sail

1.3 Aim and objectives

The aim of this thesis is to improve the understanding of the vortex flows of downwind sails.

The objectives of the thesis are:

1. Measure the velocity field and vorticity near the leading edge of downwind sails.

2. Track the evolution of the LEV to verify if it is stable or shed downstream.

3. Quantify the circulation of the LEV and estimate its contribution to the sectional lift of the sail.

4. Verify that the results of the above objectives are not affected by the uniform onset flow adopted experimentally, as opposed to the twisted onset flow encountered in full-scale conditions.

5. Provide benchmark data of force measurements and flow visualisation for future studies of downwind sails.

The first objective will determine whether the flow separates at the leading edge or not. If it does, it will clarify whether the flow reattaches to the surface of the sail or remains separated. Subsequently, the second objective will clarify whether the LEV remains stationary at the leading edge or sheds downstream.

Next, the third objective will quantify the circulation of the LEV and compare it to the effective bound circulation (Γ_0), which occurs in attached flow conditions when the Kutta condition is satisfied. The bound circulation (Γ_b) will be computed with an inviscid potential model and using the measured circulation of the LEV (Γ_{LEV}). Here, the model will replicate the two-dimensional results of planar PIV and set the foundations for future downwind sail inviscid approaches.

Testing downwind sails in uniform flow conditions is sometimes the only available option, due to experimental constraints. The fourth objective will reveal whether this is a valid simplification for full-scale sailing conditions, where the apparent wind is twisted. Finally, the last objective will contribute to the field of downwind sails aerodynamics by providing a database of force and flow measurements, to benchmark future numerical or experimental tests.

1.4 Thesis synopsis

Introduction

Chapter 1 provides a background on downwind sail aerodynamics. Chapter 2 discusses the LEV and which parameters affect its stability and dynamics, and prevent vortex shedding.

Methodology

Chapter 3 presents the design of the geometry prototypes and how the experiments were designed. Chapter 4 introduces the force measurements, the laser Doppler velocimetry (LDV) and the particle image velocimetry (PIV) instrumentation. Chapter 5 presents how two vortex detection methods (Q, γ) are applied to the flow field of a Lamb-Oseen vortex.

Results

Chapter 6 shows the time-averaged flow field of a spinnaker at three cross-sections. The presence of an LEV is confirmed in the time-averaged sense at the top of the sail. To understand if the LEV is attached or shedding in time, an instantaneous analysis is carried out with the γ criterion. The LEV is found to alternate between two modes. In the first mode, the LEV remains trapped at the leading edge. In the second mode, the LEV convects downstream. To the author's knowledge, this is the first time the existence of an LEV in a downwind sail has been demonstrated through PIV. The vortex detection algorithms here employed were originally implemented by the author for delta wings (Muir et al., 2017). Chapter 7 introduces the complex potential model used to replicate the vortical flows found around the top section of the sail. It is found that the LEV contributes between 10% to 20% to the sectional lift assuming the Kutta condition. The results in this Chapter and the previous one have been summarised in a journal paper by Arredondo-Galeana and Viola (2018). Chapter 8 discusses the effect of twist in the aerodynamics of sails. To achieve this, three scale model spinnakers are manufactured, each with different twist. PIV results are correlated to force measurements. It is found that twist can be used to manipulate the trajectory of the shedding LEVs, in order to achieve maximum driving force.

Final remarks

Chapter 9 discusses the relevant conclusions of this work. Lastly, Chapter 10 describes what future work can be done to expand the findings achieved in this PhD thesis.

1.5 Publications

The contribution to knowledge developed in this thesis is listed now:

Journal papers:

- Arredondo-Galeana, A., Viola, I. M., 2018. The leading-edge vortex of yacht sails. Ocean Engineering 159, 552-562.
- Muir, R.E., Arredondo-Galeana, A., Viola, I.M., 2017. The leading-edge vortex of swift wing-shaped delta wings. Royal Society Open Science 4.

Conference papers:

- Viola, I.M., Arredondo-Galeana, A. The leading-edge vortex of yacht sails. In: Proceedings of the Innov'Sail International Conference on Innovation in High Performance Sailing Yachts, 4th Edition, Lorient, France, 2017.

Abstracts:

- Arredondo-Galeana, A., Viola, I. M. The leading-edge vortex of yacht sails. In 70th Annual meeting of the APS Division of Fluid Dynamics Meeting Abstracts, volume 62, Denver, Colorado, USA, 2017.
- Arredondo, A., Viola, I. M. (2016). On the leading edge vortex of thin wings. In 69th Annual meeting of the APS Division of Fluid Dynamics Meeting Abstracts, volume 61, Portland, Oregon, USA, 2016.
- Arredondo-Galeana, A., Viola, I. M. Vortex flow of yacht sails. In inaugural UK Fluids Conference, London, UK, 2016.
- Arredondo, A., Viola, I. M. The leading edge vortex of yacht sails. In 29th Scottish Fluid Mechanics Meeting, Edinburgh, UK, 2016.

Metadata:

- Arredondo Galeana, A., Viola, I. M. (2018). PIV dataset for 'The leading-edge vortex of yacht sails' (OE, Arredondo-Galeana and Viola, 2018, Fig. 9, 10, 11, 12). Edinburgh DataShare. University of Edinburgh. School of Engineering. Institute for Energy Systems.
- Viola, I. M., Arredondo Galeana, A. (2017). Flow over a swift shaped wing and delta wing (RSOS, Muir et al., 2017, Fig. 4, 5, 6, 7 and 8). Edinburgh DataShare. University of Edinburgh. School of Engineering. Institute for Energy Systems.

The peer-review publications related to this PhD thesis have been attached at the end of the bibliography.

Chapter 2

The leading edge vortex

2.1 Background studies

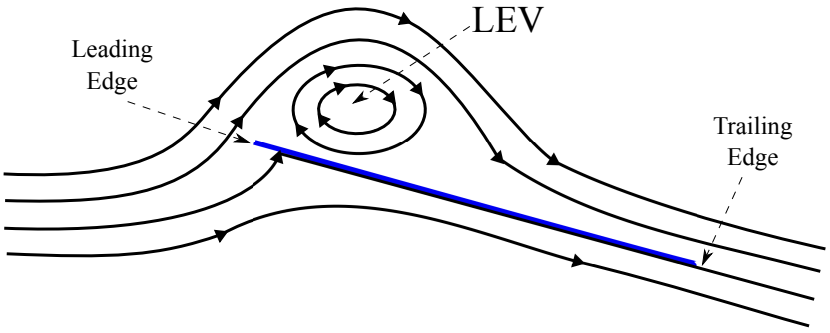

Figure 2.1: Schematic of LEV in a translating flat plate

The leading edge vortex (LEV) is a flow feature formed by the roll up of vorticity, generated at the leading edge of a wing. Here vorticity is convected towards the centre of the vortex, where it accumulates. However, the LEV cannot capture unlimited vorticity at its centre and vortex shedding occurs. If the vorticity is somehow extracted from the axis of the vortex, it is possible to achieve a stable LEV that remains attached to the leading edge indefinitely. In this case, vorticity is typically extracted by axial flow inside the vortex core. In downwind sails, axial flow occurs towards the tip of the sail and the LEV grows in that direction, where it merges with the tip vortex (Viola et al., 2014). At the bottom of the sail, a similar structure to the tip vortex develops from the lower corner of the trailing edge. However, this root vortex has an opposite rotation to the tip vortex (Viola et al., 2014).

The vorticity and circulation of the LEV can significantly increase the lift and thus can be exploited in both man-made and natural flyers (Ellington, 1999; Srygley and Thomas, 2002; Garmann et al., 2013; Jardin and David, 2014). Vorticity is defined as twice the local rotation of a fluid element or as the curl of the velocity. Circulation is defined as the global rotation of a fluid around a closed contour or as the integral of

the velocity around a closed loop. Vorticity and circulation are related to each other, as shown by Stoke's theorem. It is of note that the LEV has been identified across a wide range of Reynolds numbers (*Re*). In fact, the LEV is resilient to different flow regimes. In laminar flow conditions, it has been found on autorotating seeds (Lentink et al., 2009) and on the wings of insects (Muijres et al., 2008) and small birds (Lentink et al., 2007). In transitional and turbulent flow conditions, it has been detected on larger bird wings (Hubel and Tropea, 2010), fish fins (Borazjani and Daghooghi, 2013), and delta wings (Gursul et al., 2005, 2007). In helicopter rotors (Corke and Thomas, 2015) and wind turbines (Larsen et al., 2007) the LEV is a powerful but undesirable flow feature, since it generates large load oscillations. The low pressure region under the LEV grows in magnitude and attenuates as the vortex breaks off and away from the wing, causing the large load oscillations (Eldredge and Jones, 2019). When the LEV is shed downstream it leads to a lift overshoot above the quasi-static maximum lift and to an abrupt and dangerous change in the pitching moment. Conversely, in biological flyers and delta wings, the LEV provides an essential source of lift augmentation.

2.2 Vortex lift

Leading-edge vortex flows gained interest in the late 1950s, through major aircraft development projects such as the British-French Concorde and the Russian TU-144 (Polhamus, 1971). The type of wings used on these aircraft allowed supersonic speeds and the LEV provided additional lift without the requirement for extra high lift devices. Figure 2.2a shows that the suction force C_S acts in the x'-direction at the leading edge of a wing.

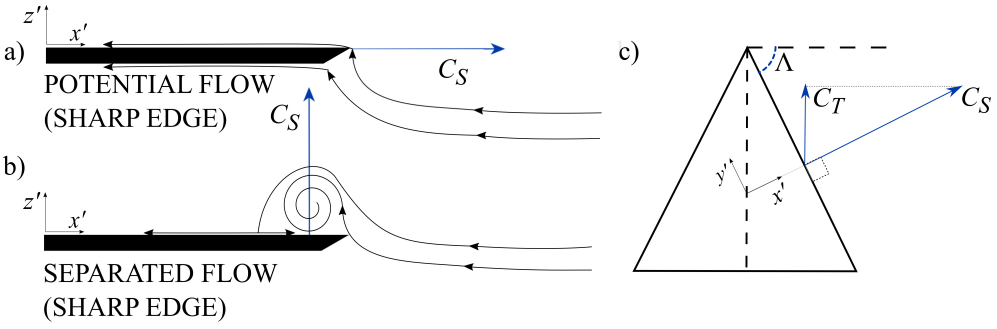

Figure 2.2: a) Suction force (C_S) acting on the leading edge of the wing and b) equivalent force acting on top of the wing; c) suction force (C_S) and thrust force (C_T) schematic of a delta wing

Polhamus (1966) explained that C_S in the x'-direction is zero on a delta wing, where the flow separates at the sharp leading edge. Conversely, an equivalent force to C_S acts along z'. The opposite force exerted on the flow promotes reattachment and the formation of the leading edge vortex (Fig. 2.2b). Figure 2.2c illustrates how the suction force is related to the thrust force by the sweep angle (Λ). The thrust force derivation is found in Polhamus (1966).

Polhamus' method does not require measurement of LEV circulation and uses potential flow concepts to predict the vortex lift on a delta wing. The lift coefficient is described by the zero suction lift, or potential lift, coefficient ($C_{L,p}$) and the vortex lift coefficient ($C_{L,v}$), such that

$$C_L = C_{L,p} + C_{L,v}, \tag{2.1}$$

where $C_{L,p}$ is due to the normal force acting on the wing and a zero suction force contribution. It is given by

$$C_{L,p} = K_p \sin\alpha \cos^2\alpha, \tag{2.2}$$

where K_p is the lift-curve slope of the wing and α is the angle of attack of the wing. K_p is a correction to the average sectional lift-curve slope of the wing for three-dimensional effects, which depends on the spanwise chordwise distribution and the aspect ratio (AR) of the wing. Details can be found in Abbott and Von Doenhoff (1959). $C_{L,v}$ is defined as

$$C_{L,v} = \left(K_p - \frac{K_p^2}{\pi \mathrm{AR}} \right) \frac{\cos\alpha}{\cos\Lambda} \sin^2\alpha, \tag{2.3}$$

such that $C_{L,v}$ is a function of K_p, AR, Λ and α.

A different method used to explain vortex lift was derived with two-dimensional inviscid potential flow and the assumption of the Kutta condition in a flat plate (Saffman and Sheffield, 1977) or in a circular arc (Huang and Chow, 1982). This model is referred to as the 'trapped vortex' analogy by Nabawy and Crowther (2017). A circular arc model based on this approach is developed in Chapter 7 for a sail cross section. The effect of the proximity of the LEV to the airfoil affects lift generation. Neglecting viscosity terms the closer the vortex is to the surface of the foil, the more impact it will have on the bound circulation. Bound circulation (Γ_b) around the airfoil is given by

$$\Gamma_\mathrm{b} = \Gamma_0 - \kappa\Gamma_\mathrm{LEV}, \tag{2.4}$$

where Γ_b is the bound circulation, Γ_0 is the effective bound circulation needed to

satisfy the Kutta condition, κ is a position coefficient of the external vortex with respect to the surface of the wing and Γ_{LEV} is the external vortex circulation. Figure 2.3a shows that in the absence of an external LEV, $\Gamma_{\mathrm{b}} = \Gamma_0$ and the Kutta condition is satisfied. Figure 2.3b shows that the Kutta condition can also be satisfied by the sum of $\kappa\Gamma_{\mathrm{LEV}}$ and Γ_{b}. This method can be used with experimental measurements of Γ_{LEV} to quantify Γ_{b} and can be extended to multiple external vortices.

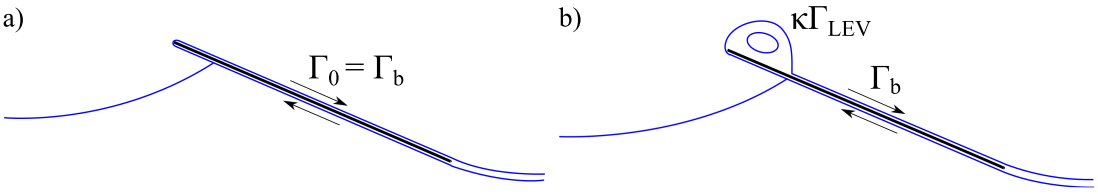

Figure 2.3: a) Flat plate with $\Gamma_0 = \Gamma_{\mathrm{b}}$ and the Kutta condition, b) flat plate with Γ_{b}, Γ_{LEV}, κ and the Kutta condition

2.3 Stabilization mechanisms of the LEV

Different mechanisms have been observed to help maintain a vortex stably attached to the suction side of a wing and to prevent it from convecting downstream. Such mechanisms include spanwise flow, vortex stretching, tip vortex, and vorticity annihilation.

Spanwise convection of vorticity (through spanwise flow) and spanwise vortex stretching appear explicitly in the spanwise component of the vorticity transport equation. The vorticity transport equation is given by

$$\frac{D\boldsymbol{\omega}}{Dt} = (\boldsymbol{\omega}\cdot\nabla)\mathbf{u} + \nu\nabla^2\boldsymbol{\omega}, \tag{2.5}$$

where the first term is the material derivative of the vorticity vector ($\boldsymbol{\omega}$), the second term is the rate of change of $\boldsymbol{\omega}$ due to the stretching and tilting of the vortex, and the third term is the rate of change of $\boldsymbol{\omega}$ due to diffusion of vorticity.

The spanwise component of Eq. 2.5, neglecting the diffusion term, is given by

$$\frac{\partial\omega_z}{\partial t} + u\frac{\partial\omega_z}{\partial x} + v\frac{\partial\omega_z}{\partial y} + w\frac{\partial\omega_z}{\partial z} = \omega_x\frac{\partial w}{\partial x} + \omega_y\frac{\partial w}{\partial y} + \omega_z\frac{\partial w}{\partial z}, \tag{2.6}$$

where the terms from left to right, represent the rate of change of vorticity (ω_z) due to unsteadiness, the advection of ω_z along the streamwise (x), normal (y) and spanwise

(z) directions and, on the right hand side of Eq. 2.6, the vortex tilting term in the x and y-direction and the vortex stretching term in the z-direction.

Wojcik and Buchholz (2014) showed that the spanwise convection of ω_z is not sufficient to balance the flux of vorticity inside the LEV of a revolving plate. They considered an additional term, called vorticity annihilation, to enhance the stability of the LEV. They neglected the tilting and stretching terms, and the streamwise and the normal convection of ω_z. In a different study, Wong and Rival (2015) show through Eq. 2.6 that spanwise flow (due to a wing's sweep angle) and vortex stretching enhance the stability of the LEV and regulate the growth of the vortex.

The aforementioned stability mechanisms are now described. Here spanwise flow will be referred to as axial flow, when the leading edge is not aligned with the z-direction.

Axial flow

Axial flow stabilizes the LEV on a delta wing. It does so by draining vorticity axially along the vortex core (Fig. 2.4). In the case of a delta wing, the axial flow is generated by the component of the onset flow in the direction of the swept leading edge. For a rotating wing the axial flow is generated by a spanwise pressure gradient due to wing rotation and due to the variation of vortex properties from the root to the tip of the wing (Maxworthy, 2007).

Axial flow is not the sole element responsible for LEV attachment in wings in rotation (Birch and Dickinson, 2001) and it is also not sufficient to keep the LEV attached in translating wings, with a plunging motion and with sweep (Beem et al., 2012). However, it increases the relative stability of the LEV in flapping wings with sweep (Wong and Rival, 2015) and it modulates the strength of the LEV.

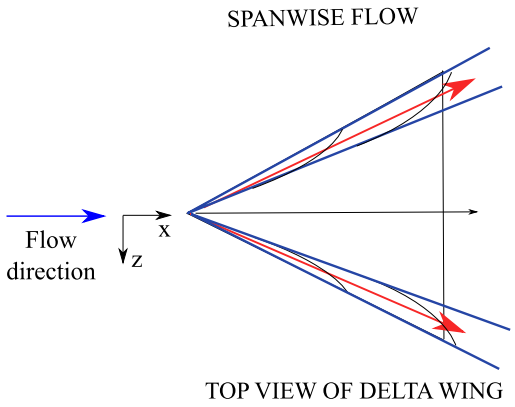

Figure 2.4: Axial flow (red arrow) inside the LEVs of a delta wing

Vortex stretching

Spanwise flow is believed to induce vortex stretching (Birch et al., 2004). To conserve momentum, stretching decreases the moment of inertia of fluid elements inside a vortex, resulting in an increase of their angular rotational speed, as explained in Kundu et al. (2012). An increase in the angular velocity (Ω) of a fluid element generates an increase in the local vorticity (ω_z), given by $\omega_z = 2\Omega$. By modifying the vortex size (i.e. its cross sectional area A) and by keeping a constant circulation (Γ), vortex stretching can improve LEV stability. The stretching of the LEV allows more ω_z to be entrained inside the vortex and its attachment to a wing can be prolonged (Lim et al., 2009). Low vortex area growth rates represent more stable LEVs (Rival et al., 2014). Vortex stretching can help to regulate the vortex area growth rate (Wong and Rival, 2015) and vortex stability can be increased. For a vortex tube and applying Stokes' theorem, ω_z may be defined as

$$\omega_z = \frac{\Gamma}{A}. \tag{2.7}$$

Using Eq. 2.7 for the two vortex tubes of Fig. 2.5 leads to $\omega_{z_1} < \omega_{z_2}$ after stretching. Γ is constant and $A_1 > A_2$ for the two tubes.

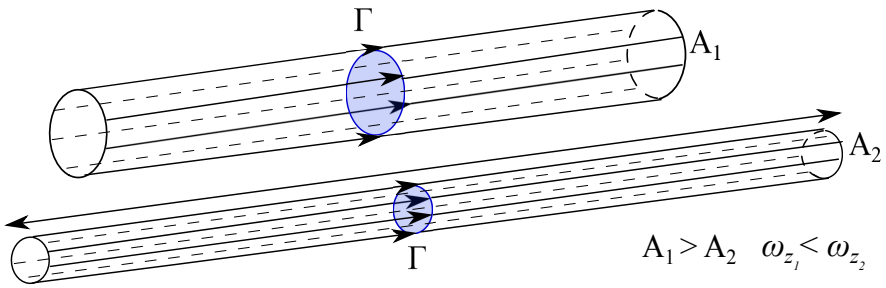

Figure 2.5: Stretching of vortex tubes of constant Γ, where $A_1 > A_2$ and $\omega_{z_1} < \omega_{z_2}$

Tip vortex

The effect of a tip vortex is to decrease the rate of production of vorticity in sections close to the tip of the wing, due to the downwash effect. This has been observed in different experiments by Taira and Colonius (2009); Kim and Gharib (2010); DeVoria and Mohseni (2017). At high incidence, the mean-flow at mid-span of low AR wings reattaches due to the downwash of the tip vortex, as a consequence of the tip vortex proximity to the mid-chord of the wing. DeVoria and Mohseni (2017) speculate that the tip vortex acts mostly on the downstream portion of the leading-edge shear layer. They observe that flat plates with higher AR than 1.5 cannot maintain attached flow and the tip vortex is not as influential as in low AR wings.

On downwind sails, the tip vortex is the largest visible vortical structure (Viola et al., 2014). At the head of the spinnaker, the LEV merges with the tip vortex and it convects downstream in the direction of the far field velocity.

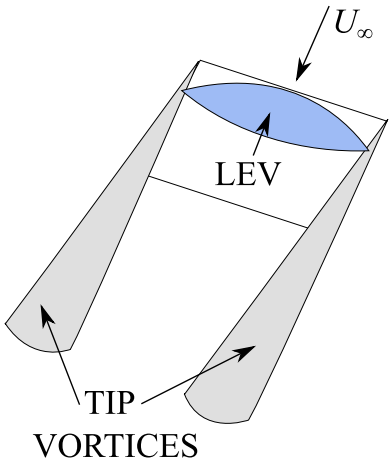

Figure 2.6: Tip vortices in low aspect ratio wing (AR $\leq$ 1.5)

Annihilation

The entrainment of secondary vorticity can help to regulate the strength of the vortex and prevent detachment in plunging (Eslam Panah et al., 2015) and rotating airfoils (Wojcik and Buchholz, 2014). Although annihilation has only been considered for revolving and plunging wings (Wojcik and Buchholz, 2014; Eslam Panah et al., 2015), it is a phenomenon that occurs when the leading edge vortex interacts with the wing and a layer of opposite-sign vorticity is generated on the surface of the wing. Opposite-signed vorticity can counteract or annihilate the original vorticity inside the LEV.

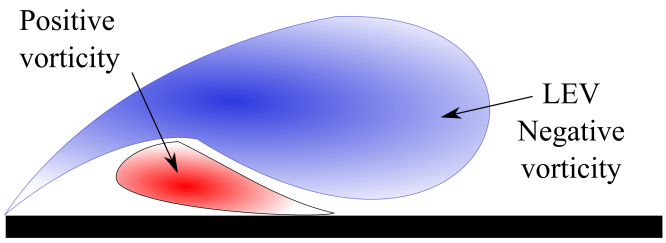

Figure 2.7: Annihilation of vorticity with opposite-sign vorticity inside the LEV of a plunging foil as a mechanism of stabilization

PART B:
METHODOLOGY

Chapter 3

Experiment setup

3.1 Model sails

Four different sail prototypes were generated from a reference surface, the spinnaker available at www.ignazioviola.com. The reference surface is a 1:15$^{\text{th}}$-scale model of an AC33-class yacht, for which an LEV was identified with numerical simulations (Viola et al., 2014). The geometries were resized to fit the water flume dimensions in the Sanderson building at the University of Edinburgh and to set the Reynolds number to a fixed value of $Re = 10^4$. The span ($S = 300$ mm) and the average chord length ($c_{\text{av}} = 150$ mm) were the same for the four geometries. The thickness (t_h) was selected to limit the spanwise deflection and is specified in Table 3.1.

The geometries are referred to as S_0, S_1, S_2 and S_3. Geometry S_0 and geometry S_1 are high twist. Geometry S_2 and S_3 are modified versions of S_1, with a lower twist angle. A summary of each prototype is presented in Table 3.1, where the column 'Coatings' refers to the number of layers applied on the surface of the sail to mitigate the reflection of the PIV laser sheet. A description of the geometries is provided in the following sections.

Table 3.1: Properties of tested prototypes

Geometry	Span (mm)	c_{av} (mm)	t_h (mm)	Twist (°)	Coatings	Bevel LE (°)
S_0	300	15	3	16	3	20
S_1	300	15	3	16	2	20
S_2	300	15	3	8	2	20
S_3	300	15	3	0	2	20

Geometry S_0

Geometry S_0 was used to detect, experimentally, the stable LEV of a spinnaker. The solid geometry was created by using two reference surfaces in the CAD software Solid Edge. The surfaces were scaled down to the dimensions of Table 3.1 and placed 3 mm apart from each other, to provide a thickness to chord ratio of $t_h/c_{\text{av}} = 2.0\%$. Ten cross-sections were used to design the leading and trailing edge bevels to promote flow separation. The cross-sections were lofted along the path of the leading edge to produce the final solid geometry. The tip of the sail was blunt (Fig. 3.1). The surface area of the model was $A = 0.051\,\text{m}^2$. The twist angle from the base to the head was 16°, the maximum chordwise camber was $0.40c_0$ and the maximum spanwise camber was $0.65c_0$, where $c_0 = 0.114\,\text{m}$ is the chord of plane B in Fig. 3.1. The model was 3D printed in ABS by a Fortus 250 3D printer.

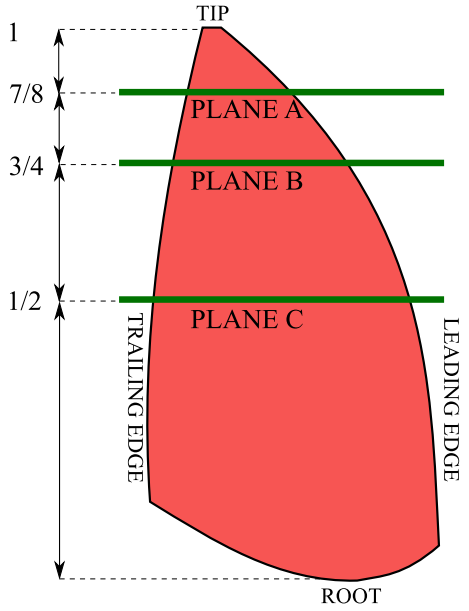

Figure 3.1: Rendering of geometry S_0 and position of PIV measurement planes

Leading edge of geometry S_0

The leading and trailing edge bevels for geometry S_0 were set to $\sigma = 20^\circ$, as shown in Fig. 3.3. At the tip of the sail, it was not possible to keep the bevel at $\sigma = 20^\circ$, because of the increasing curvature of the cross-sections and such a small angle did not intersect the pressure side surface of the sail. Therefore, each bevel was progressively increased from $\sigma = 20^\circ$ to $\sigma = 70^\circ$. This enabled the thickness to be kept constant and to intersect the pressure side surface.

The shape of the leading edge and its effect on the flow dynamics of delta wings and flat plates has been previously investigated. For delta wings, Gursul et al. (2005) compared the effect of sharp and rounded edges (see Fig. 3.2). Gursul et al. (2005) found that round edges of non-slender delta wings ($\Lambda = 50°$) delay stall. The reattachment line around the LEV moves towards the leading edge and away from the symmetry plane. In flat plates, the tendency of the flow to separate can be minimized using a double arc contour at the edge (Davis, 1980) or if the Reynolds number is sufficiently high to have a turbulent boundary layer (Arena and Mueller, 1980). Given that the present work aims to promote flow separation at the leading edge, the sharp bevel shown in Fig. 3.3 is selected for the study.

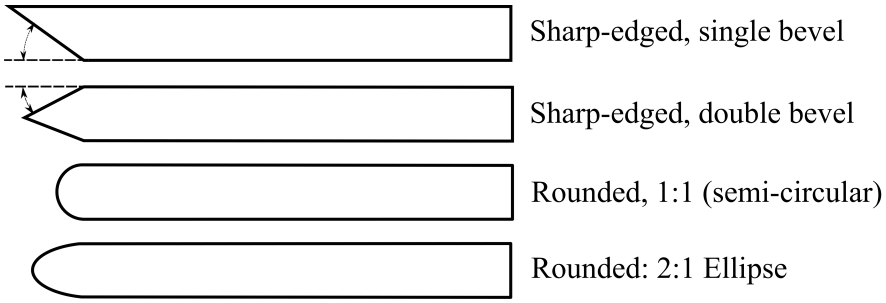

Figure 3.2: Leading edge shapes of delta wings studied by Gursul et al. (2005)

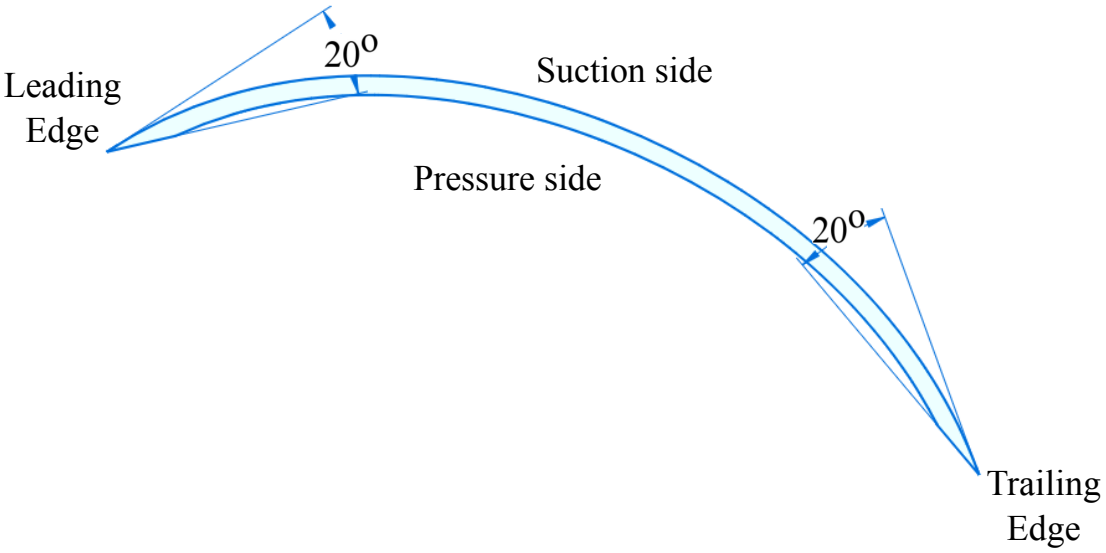

Figure 3.3: Cross-section of geometry S_0 showing sharp-edged, single bevel leading and trailing edges ($\sigma = 20°$)

Geometries S_1, S_2 and S_3

Three geometries, S_1, S_2 and S_3, were created to observe the effect of twist in the flow around spinnakers. The geometries were designed to have high, intermediate and low twist. The definition of twist is expanded upon in the next section. Each geometry was generated with ten cross sections, similar to geometry S_0. Rendering of the surfaces was done with Rhinoceros (Version 5.2) to obtain a continuous profile between the ten cross-sections of the spinnakers. Two surfaces were used to generate each solid. The surfaces were joined at the tip of the sail to provide a sharp peak. Figure 3.4 shows the geometries S_1, S_2 and S_3 and the planes recorded with PIV. The measurement planes were located at $7/8^{th}$, $5/6^{th}$, $3/4^{th}$, $1/2^{th}$ and $1/4^{th}$ the distance from the bottom of the sail to its tip, and labelled as planes A, B, C, D and E, respectively. Solid models were 3D printed in ABS.

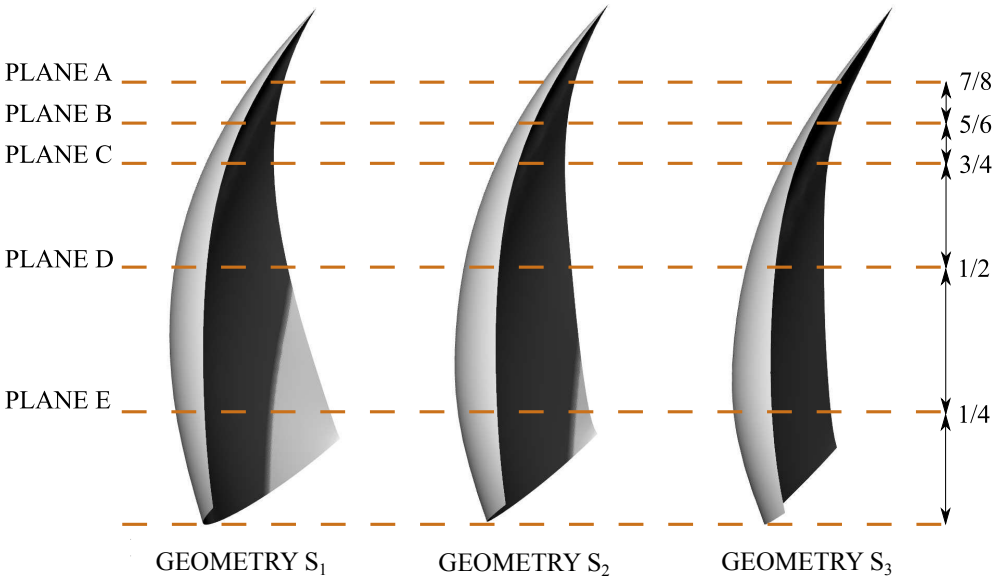

Figure 3.4: Geometries S_1, S_2, and S_3 with high, intermediate and low twist, respectively. Planes A, B, C, D and E are the PIV measurement planes

Twist design of geometries S_1, S_2 and S_3

Sails with different twist were designed to investigate how the conclusions drawn were affected by considering sails, with different spanwise distributions of angles of attack. This is performed because full-scale sails are subject to twisted flow (Fig. 3.5a), whereas sails in a water flume are tested in uniform flow (Fig. 3.5b).

Consider planes E of Fig. 3.5a and Fig. 3.5b, near the foot of the sail. Their top views are superimposed in Fig. 3.5c. Assuming uniform onset flow as in the flume,

the angle of attack of cross-section E (α_{E}) is higher in the flume ($\alpha_{\mathrm{E}}^{\mathrm{FL}}$) than in full-scale conditions ($\alpha_{\mathrm{E}}^{\mathrm{FS}}$). Hence, sails with different spanwise distributions of angle of attack were tested.

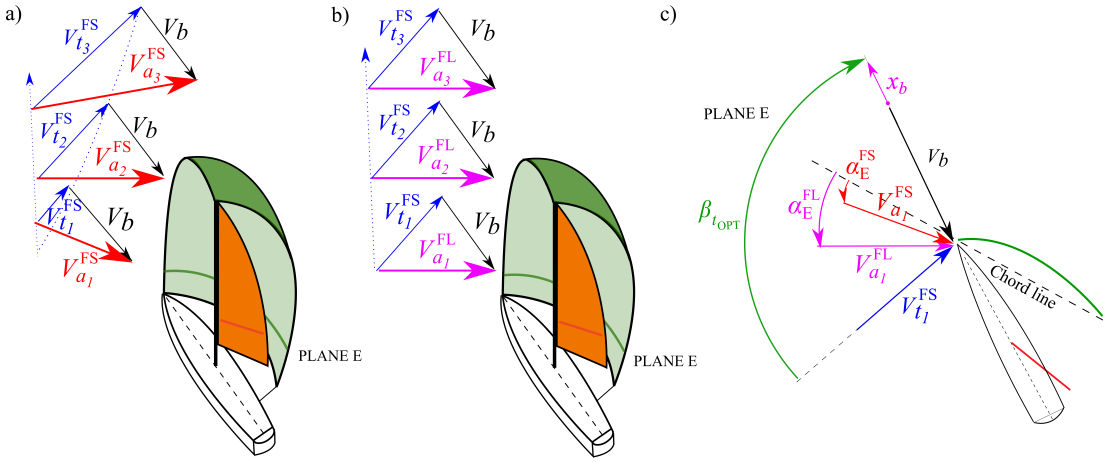

Figure 3.5: a) Full-scale apparent wind V_a^{FS} at three height stations of the sail, bottom-section ($V_{a_1}^{FS}$), mid-section ($V_{a_2}^{FS}$) and top-section ($V_{a_3}^{FS}$) b) Flume apparent wind V_a^{FL} at three height stations of the sail, bottom-section ($V_{a_1}^{FL}$), mid-section ($V_{a_2}^{FL}$) and top-section ($V_{a_3}^{FL}$) c) Top view of bottom-section of sail (plane E) with $V_{a_1}^{FS}$ and $V_{a_1}^{FL}$

Figure 3.6 shows how the angle of attack (α_{X_i}), which is used later in Tab. 3.2 and Tab. 8.1, is defined. This is the angle between the chord line of the X-th cross-section of the i-th sail geometry and the flume flow direction (x-axis direction), where X takes the values of $X = \mathrm{A,B,C,D,E}$ and i takes the values of $i = 1,2,3$ and refers to geometries S_1, S_2 and S_3. In Fig. 3.6, $X = E$ and $i = 1,2$. Therefore, the angles of attack displayed are α_{E_1} and α_{E_2}.

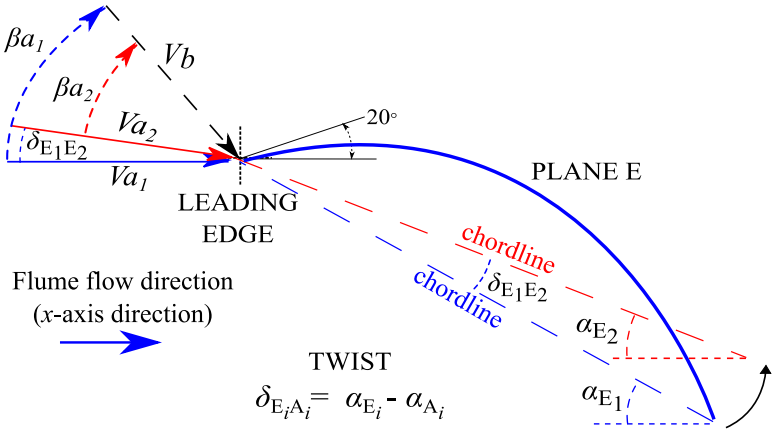

Figure 3.6: Schematic of twist design to define $\delta_{\mathrm{E_1A_1}} = 16°$, $\delta_{\mathrm{E_2A_2}} = 8°$ and $\delta_{\mathrm{E_3A_3}} = 0°$ for geometries S_1, S_2 and S_3, respectively

In Fig. 3.6, twist ($\delta_{\mathrm{E}_i\mathrm{A}_i}$) is defined as the difference between the angle of attack of cross-section E and the angle of attack of cross-section A, i.e., $\delta_{\mathrm{E}_i\mathrm{A}_i} = \alpha_{\mathrm{E}_i} - \alpha_{\mathrm{A}_i}$, where i takes the values of $i = 1,2,3$ and refers to geometries S_1, S_2 and S_3, respectively. Cross-section E is the bottom section and cross-section A is the top section used to render the sails.

$\delta_{\mathrm{E}_i\mathrm{A}_i}$ was modified by changing the angle of attack of cross-section E (α_{E_i}). The change of angle of attack of cross-section E ($\delta_{\mathrm{E}_i\mathrm{E}_j}$) is the difference between α_{E_i} and α_{E_j}, where α_{E_i} and α_{E_j} correspond to the same plane but different geometry. For geometries S_1, S_2 and S_3, i and j take the values of $i, j = 1,2,3$, respectively. In Fig. 3.6, plane E of geometry S_1 is rotated around its leading edge to generate the plane E of geometry S_2, such that $\delta_{\mathrm{E}_1\mathrm{E}_2} = \alpha_{\mathrm{E}_1} - \alpha_{\mathrm{E}_2}$. Figure 3.6 shows that $\delta_{\mathrm{E}_1\mathrm{E}_2}$ is equivalent to a reduction of β_{a_1} to β_{a_2} and a change in the direction of V_{a_1} to V_{a_2}.

Local twist ($\delta_{X_i\mathrm{A}_i}$) is defined as the difference between the angle of attack of any cross-section along the span of the sail and the angle of attack of cross-section A, i.e., $\delta_{X_i\mathrm{A}_i} = \alpha_{X_i} - \alpha_{\mathrm{A}_i}$. $\delta_{X_i\mathrm{A}_i}$ decreases from bottom to top, and it reaches its maximum between plane E and plane A.

Figure 3.7 shows $\delta_{X_iA_i}$, where $X = \mathrm{A},\mathrm{B},\mathrm{C},\mathrm{D},\mathrm{E}$ are the PIV planes and $i = 1,2,3$ are the sails S_1, S_2 and S_3. Sail S_3 is a more realistic sail than the others since its twist was modified to replicate the effects of a twisted inflow.

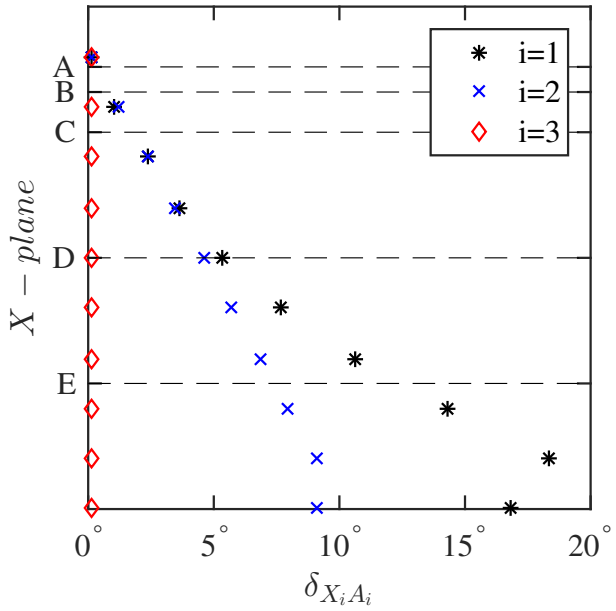

Figure 3.7: Twist profiles of geometries $\mathrm{S}_1(i=1)$, $\mathrm{S}_2(i=2)$ and $\mathrm{S}_3(i=3)$

Design considerations

Two v-shaped attachment legs held the sails and connected them to a shaft that could rotate. Figure 3.8a and Fig. 3.8b show sections through the legs transversal and parallel to the flow. The latter at two cross-sections (A-A' and B-B'). The leg thickness and v-shape were designed to minimise obstruction to the flow. Figure 3.8c shows a photograph of the attachment legs and sail.

Figure 3.9 shows the steel shaft on which the sails were mounted. The diameter of the shaft was 8 mm, and its root was sized to 10 mm. The beam was mounted as a cantilever, from the threaded side.

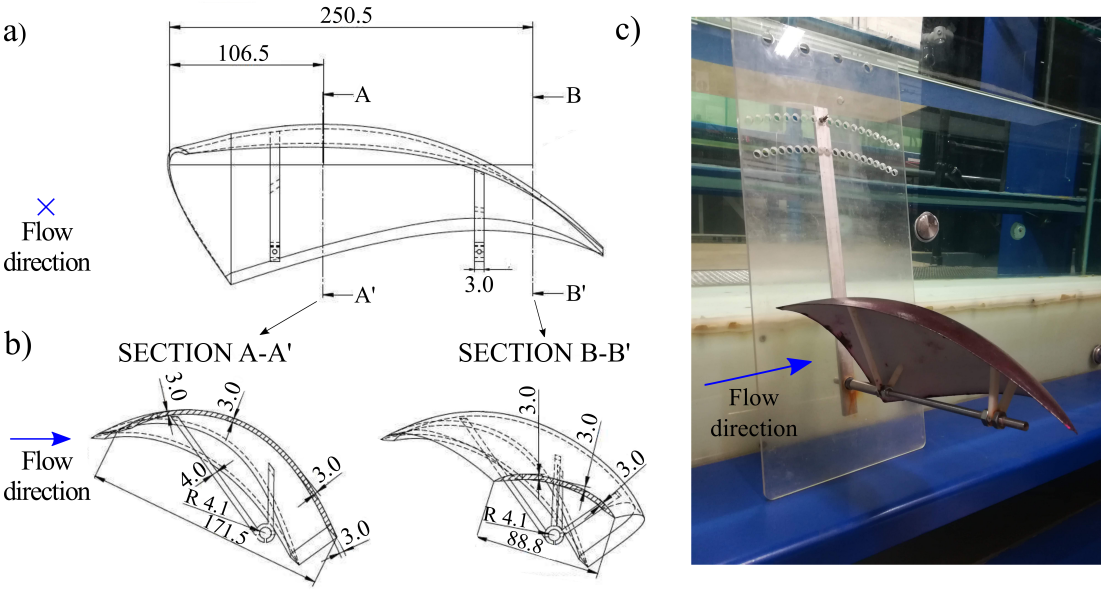

Figure 3.8: Geometry S_0 with attachment legs a) transversal to the flow and b) parallel to the flow at sections A-A' and B-B', c) photograph of attachment legs and sail

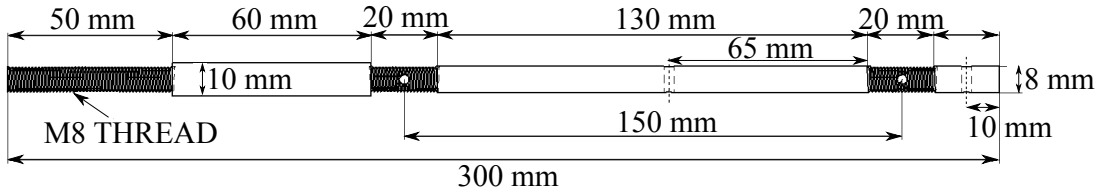

Figure 3.9: 8 mm beam holding the sail models with a 10 mm expansion at the root. All holes are M3 through holes. Threaded parts are coupled to the rig and to the sails

Sweep angle

Figure 3.10a depicts the spinnaker of geometry S_0. Figure 3.10b illustrates the sweep angle of two regions of a planar projection of the same geometry. The top region of the spinnaker has a sweep angle, similar to that of a non-slender delta wing, where vortical structures have been observed at low angles of attack by Yaniktepe and Rockwell (2004); Gursul et al. (2005); Muir et al. (2017). Direct comparison to a non-slender delta wing is not feasible, due to the geometrical differences and the rig setup. However, in a simplified model, the planar projection of the top region of the spinnaker could be considered similar to that of a non-slender delta wing.

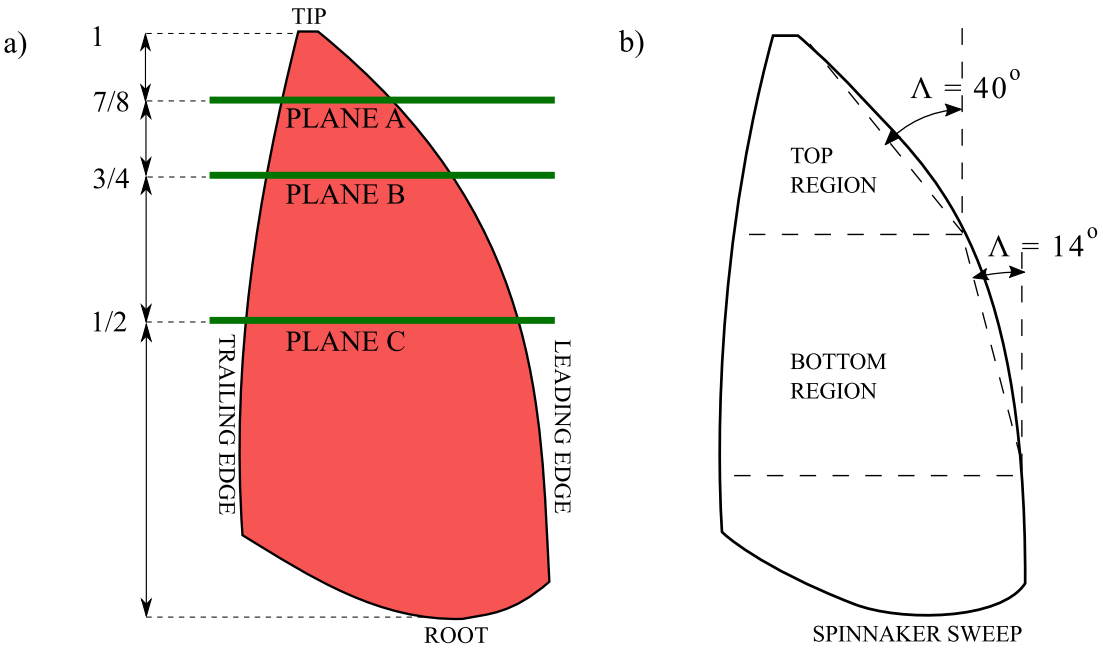

Figure 3.10: a) Spinnaker geometry S_0, b) Planar projection of geometry S_0 showing the sweep angle of two regions: top region ($\Lambda = 40°$) and bottom region ($\Lambda = 14°$)

3.2 The rig

Rig description

The sail prototypes were mounted on a shaft that could rotate and that was controlled by a lever arm for fine control of the angle of attack. The shaft was attached to a 6 mm thick acrylic plate, connected to a pair of 45×45 mm aluminium extrusions. These extrusions were connected to load cells, held in place by a vertical array of extrusions fixed to the flume. The rig allowed the angle of attack of the sail to be altered and it secured the sail's position by locking the rotating system through an arch dial system, displayed in Fig. 3.11. The rig was built to record Particle Image Velocimetry (PIV) measurements across planes of the sail, parallel to the oncoming flow. The laser beam of the PIV system was redirected through two mirrors and an array of underwater LaVision optics to generate a laser sheet, that was fully submerged. The thickness of the laser sheet was approximately 2 mm.

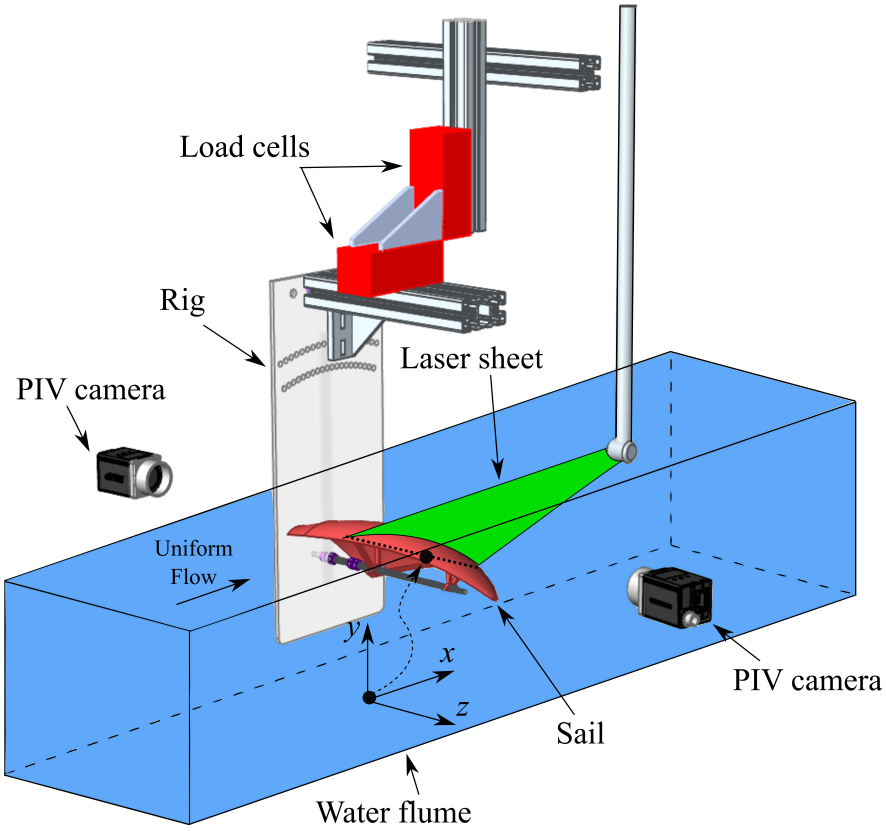

Figure 3.11: Experimental setup showing rig, sail prototype, PIV cameras, laser sheet and flume. The x-, y- and z-axes define the flume frame of reference. The xy-plane corresponds to the plane located at 3/4 of the span of the sail. The origin is located at the midpoint of the chordline

Positioning the sail S_0 at initial testing conditions

Figure 3.12c shows the zero testing condition for the spinnaker S_0 which was set to replicate the same $\beta_{a_{OPT}}$ (55°) investigated with Detached Eddy Simulations (DES) by Viola et al. (2014). The reference boat and spinnaker are found at the website www.ignazioviola.com. The bow of the reference boat is oriented along the negative x-direction, in the reference frame of the flume (Fig. 3.12a). In order to achieve the initial testing conditions, the boat and spinnaker were rotated 55° around the out-of plane axis A to recreate an apparent wind angle equal to $\beta_{a_{OPT}} = 55°$, as shown in Fig. 3.12b. The trim of the sail corresponds to the shape that generates maximum driving force at $\beta_{a_{OPT}}$, as reported by Viola et al. (2014).

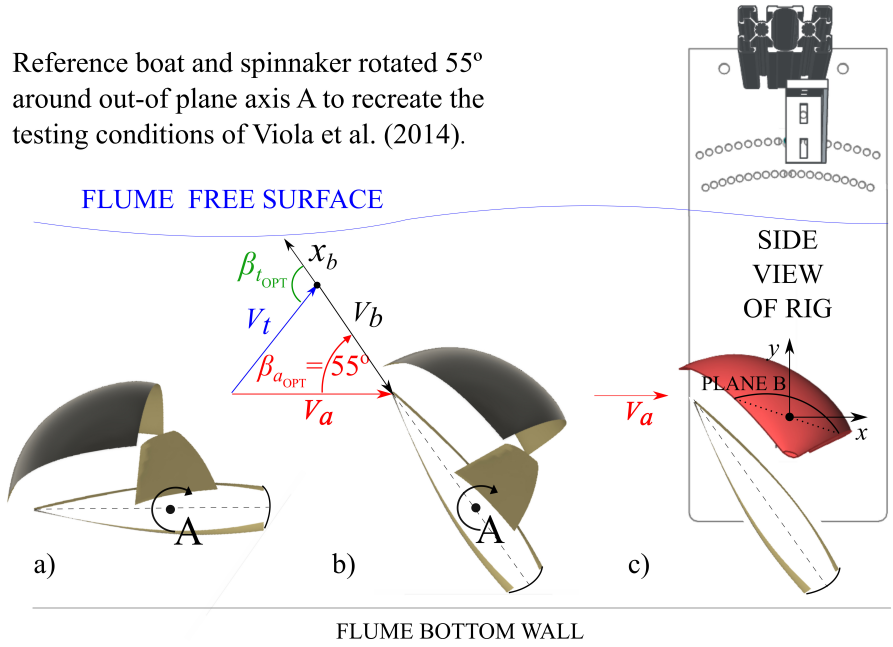

Figure 3.12: a) Reference boat and geometry, b) Rotation of reference boat and geometry c) Side view of rig with geometry S_0 at a zero-testing condition with a constant $\beta_{a_{OPT}} = 55°$ and V_a

Positioning the sails S_1, S_2 and S_3 at initial testing conditions

The sails with the modified twist (S_2 and S_3) have an improved angle of attack distribution, but inevitably have a non-realistic shape, because they are modified versions of a sail with a realistic shape (S_1). Hence, the optimum trim or orientation of S_2 and S_3 is initially unknown. To find out the optimum trim, the sails are rotated around their vertical axis (Fig. 3.13). This rotation is defined as η and $\eta = 0°$ is the angular

position where $\frac{\partial F_{DF}}{\partial \eta} = 0$. $F_{DF}(\eta)$ is the driving force and $F_{SF}(\eta)$ is the side force at an optimum apparent wind angle of $\beta_{a_{\mathrm{OPT}}} = 55^\circ$ and they are defined as

$$F_{DF}(\eta) = L(\eta)\sin(\beta_{a_{\mathrm{OPT}}}) - D(\eta)\cos(\beta_{a_{\mathrm{OPT}}}) \tag{3.1}$$

and

$$F_{SF}(\eta) = L(\eta)\cos(\beta_{a_{\mathrm{OPT}}}) + D(\eta)\sin(\beta_{a_{\mathrm{OPT}}}), \tag{3.2}$$

respectively. Here $L(\eta)$ is the lift force and $D(\eta)$ is the drag force, which are functions of the rotation η and $\beta_{a_{\mathrm{OPT}}}$ is fixed to $\beta_{a_{\mathrm{OPT}}} = 55^\circ$ because the direction of the boat is fixed, as shown in Fig. 3.13. A comparison of force components between S_1, S_2 and S_3 is carried out in Chapter 8, for a range of η from -30° to 30°.

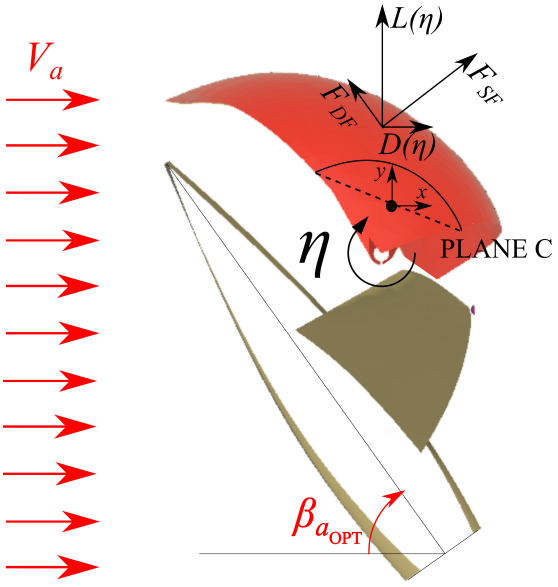

Figure 3.13: Rotation of rig to find $\frac{\partial F_{DF}}{\partial \eta} = 0$, defined as $\eta = 0^\circ$

The angles of attack (α_{X_i}) of planes A, B, C, D and E of the three sails, that correspond to $\eta = 0^\circ$, are provided in Table 3.2, where the sail planes are $X = \mathrm{A}, \mathrm{B}, \mathrm{C}, \mathrm{D}, \mathrm{E}$ and $i = 1, 2, 3$ correspond to sails S_1, S_2 and S_3. In Tab. 3.2, α_{X_i} was measured from raw PIV images, as shown later in Chapter 8.

The error in α_{X_i} ($\varepsilon_{\alpha_{X_i}}$) is found to be up to a maximum of $\pm 2^\circ$ on the lowest sail sections and it is obtained by comparing the experimental twist derived from Table 3.2, with the design twist of Fig. 3.7. The error in η (ε_η) is up to a maximum of $\pm 1^\circ$. This error is included in $\varepsilon_{\alpha_{X_i}}$ and depends on the rig resolution, and the assembly of

the rig. The assembly of the rig is explained in the following section.

Table 3.2: Measurements of α_{A_i}, α_{B_i}, α_{C_i}, α_{D_i} and α_{E_i} at $\eta = 0°$ for geometries S_1, S_2 and S_3, where i corresponds to the index of the geometry

Angle	S_1, High Twist	S_2, Medium Twist	S_3, Low Twist
α_{A_i}	$24° \pm 1°$	$27° \pm 1°$	$29° \pm 1°$
α_{B_i}	$24° \pm 1°$	$27° \pm 1°$	$29° \pm 1°$
α_{C_i}	$25° \pm 1°$	$28° \pm 1°$	$29° \pm 1°$
α_{D_i}	$28° \pm 2°$	$31° \pm 2°$	$31° \pm 2°$
α_{E_i}	$37° \pm 2°$	$34° \pm 2°$	$31° \pm 2°$

Rig assembly

A locking and alignment mechanism was designed to be able to repeat the zero testing condition for every experimental run. This was achieved through locking pins and indicators in the attachment legs. The attachment legs were locked in place with pins, and were secured to both of their sides with hexagonal nuts (Fig. 3.14). The legs had an indicator that pointed downwards to identify the zero position of the sail. The rotating shaft where the sail was mounted, passed through a bearing that was inserted in the acrylic plate. The positions of the shaft and the sail were controlled by an acrylic arm that transmitted a rotation motion through the bearing. The arm could be locked in place at the top of the acrylic plate, with an arch of holes of resolution of 1°.

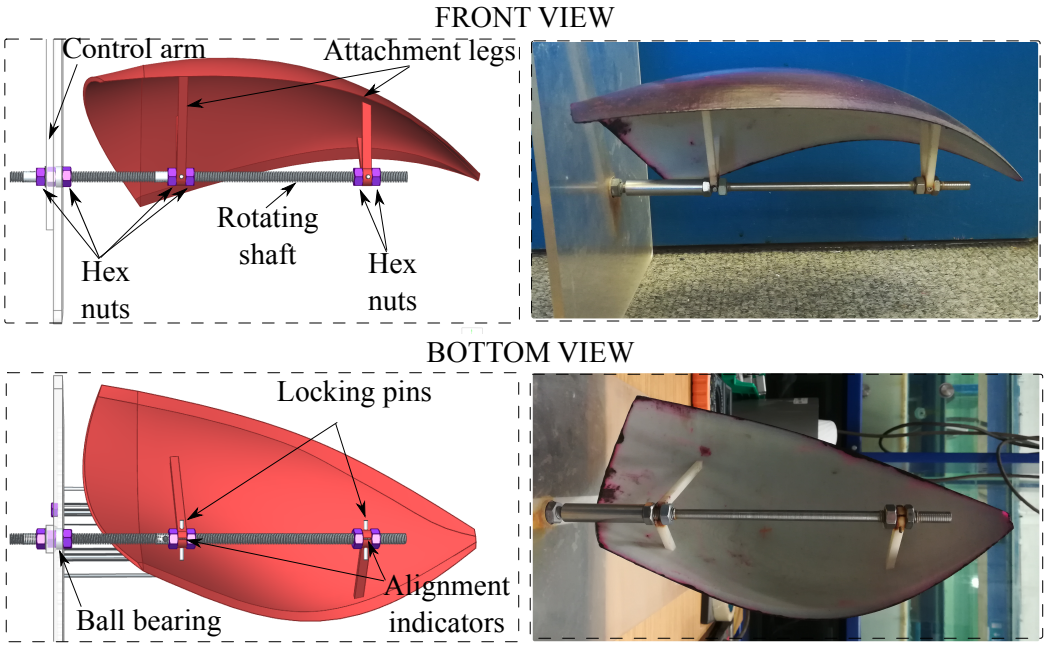

Figure 3.14: Front and bottom view from rotating assembly

3.3 The flume

The water flume is a wave and flow testing facility in the Institute for Energy Systems of the School of Engineering, at the University of Edinburgh. The flume is 9 m long, 0.4 m wide, 0.9 m high with a flat, horizontal bed. The mean water depth was set to 0.5 m and the sail was placed horizontally 0.1 m below the water surface. The gap between the rig and the walls of the flume was 0.05 m at both sides. The flume has a separator that splits the water circuit into an upper level and a lower level (Fig. 3.15). The testing section is located in the upper level. A propeller is connected to the lower level to generate the current in the flume. The flow circulates from lower level to upper level and passes through a set of vanes at the side walls of the flume. The vanes straighten the flow and are described in the next section.

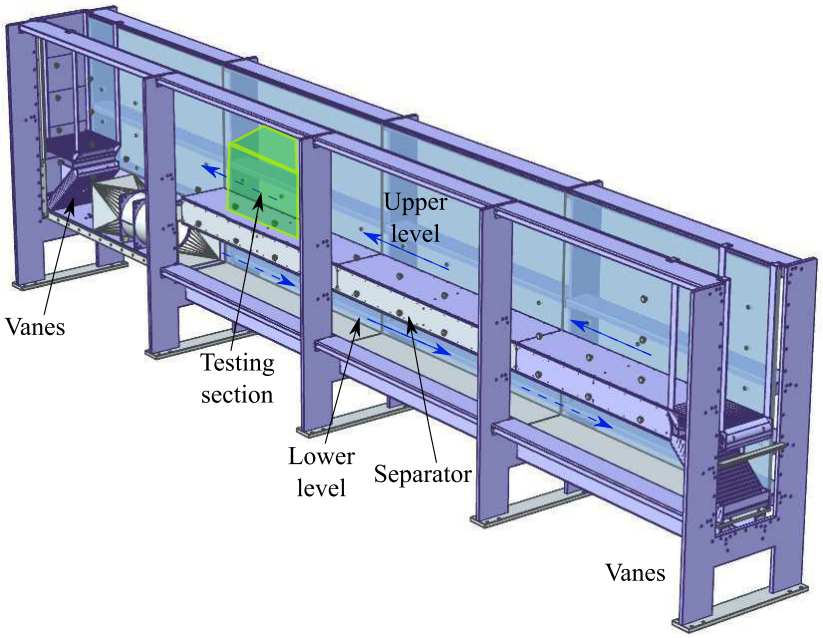

Figure 3.15: Schematic diagram illustrating water flume in the Institute for Energy Systems of the School of Engineering, at the University of Edinburgh

Flow straightening vanes

A pair of flow straightening vanes are placed either end of the flume. The first set of vanes receives flow from the lower level and because of the vertical side wall, the flow curves, and enters a second set of vanes. Finally, the flow is released into the upper level of the flume and parallel to the free surface. The recirculating path of the flow as it passes through the vanes, can be observed in Fig. 3.16. Downstream of the model, the flow travels in the opposite direction, from the upper level to the lower one.

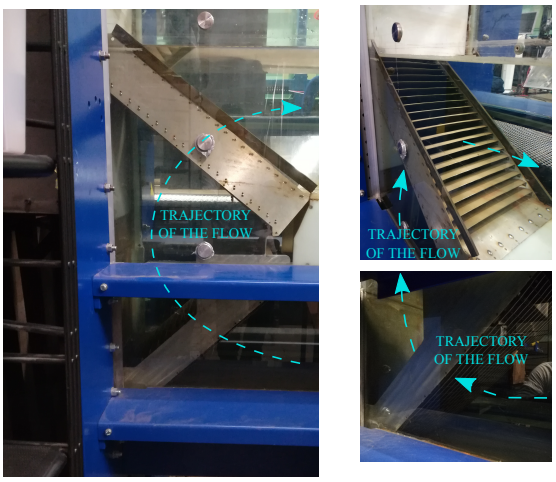

Figure 3.16: Flow straightening vanes at the upstream end of the flume

Honeycomb

An aluminium honeycomb was placed in series at the exit of the upper level vane and upstream of the testing section. The honeycomb reduces turbulence intensity and straightens the flow. The cell size of the honeycomb is 6.4 mm.

HONEYCOMB HONEY COMB IN SERIES WITH VANES

Figure 3.17: Aluminium honeycomb used in series for flow straightening

Turbulence intensity

Turbulence intensity (I) in the flume was measured with LDV. I is defined as the ratio of the root-mean-squared velocity fluctuations (u'_{rms}) and the freestream velocity (U_∞), such that

$$I = \frac{u'_{rms}}{U_\infty}, \tag{3.3}$$

where u'_{rms} is

$$u'_{rms} = \sqrt{\frac{1}{n}\sum (u'_i)^2}, \tag{3.4}$$

in which n is the discrete number of sample points and u'_i is the velocity fluctuation, which is given by

$$u'_i = u_i - \overline{u}, \tag{3.5}$$

where u_i is the velocity component in the x, y and z-directions, and $\overline{u}$ is the mean value of the velocity. A turbulence intensity of 7% was measured with Laser Doppler Velocimetry (LDV) at a location 1 m upstream of the model. Although the high level of turbulence was due to the lack of a contraction section, the value is similar to that experienced by a yacht at full scale (Viola and Flay, 2012).

Velocity profiles

LDV was used to characterise the flow along the spanwise and wall normal directions of the flume for two free stream velocities ($U_\infty = 0.15\,\mathrm{m/s}$ and $0.30\,\mathrm{m/s}$) and normalised for each condition with $\overline{u}$. The profiles in Fig. 3.18 show the effect of the wall on the flow at different speeds. The blue highlighted area is the recommended testing section to have uniform flow.

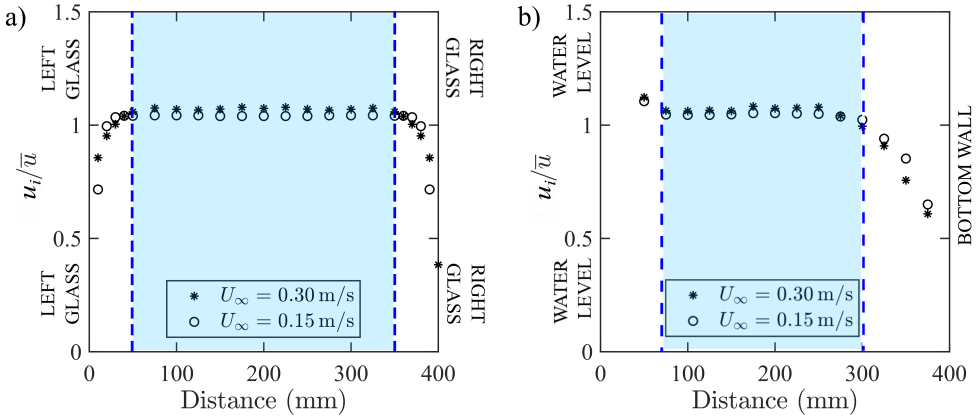

Figure 3.18: Flume characterisation a) spanwise profile and b) wall-normal profile

Uniform flow was quantified within the blue region of Fig. 3.18a and Fig. 3.18b, for the spanwise and wall-normal velocity profiles. It was found that for both profiles, $u_i/\overline{u} = 1.05$ at $U_\infty = 0.15\,\mathrm{m/s}$ and $u_i/\overline{u} = 1.07$ at $U_\infty = 0.30\,\mathrm{m/s}$. At $Re = 10^4$, clearances of 5 cm to each side of the wall and 10 cm below the surface, and above the bottom wall are recommended.

Reynolds effects

The Reynolds number (Re) is the ratio between the inertial forces and the viscous forces of a fluid, and is given by

$$Re = \frac{\rho_d U_\infty c}{\mu}, \tag{3.6}$$

where ρ_d is the fluid density, U_∞ is the freestream velocity, c is the local chord of the sail and μ is the dynamic viscosity of the fluid.

The Reynolds number varies from 10^5 to 10^6 at full-scale conditions. This thesis carries out the experimental tests at $Re = 10^4$. Although this is a smaller Reynolds number than at full-scale conditions, separated flows and vortices occurring from leading edge separation are only marginally affected in the range of Re from 10^4 to 10^6 (Gad-El-Hak and Blackwelder, 1985; Perry and Steiner, 1987; DeVoria and Mohseni, 2017).

Conversely, testing small-scale models in a water flume is a convenient way to characterise the flow around sails. For instance, it allows laser based flow measurement techniques that are currently not possible at full-scale and it allows seeding particles to mix thoroughly and uniformly before measurements are carried out (Melling, 1997). Hence, the drawbacks of water flume testing are overcome by the benefits gained in terms of flow visualisation and measurement capabilities.

This Chapter presents the sail scale models, the rig setup and the water flume that this thesis will use to answer the following research questions. Firstly, if the presence of the leading-edge vortex in a downwind sail can be confirmed experimentally. Secondly, whether the LEV is stable or sheds downstream. Thirdly, if the LEV is contributing to lift by enhancing circulation or by delaying stall. Finally, whether or not, conclusions are affected by assuming a uniform (non twisted) onset flow.

Chapter 4

Instrumentation

4.1 Load cells

The load cell system used in the experiments comprised a wind tunnel dual-balance kit, to measure lift and drag. The system was manufactured by KineOptics. It consisted of two Honeywell strain gauges connected to two SGA/A amplifiers, with a low pass filter, set to 5 Hz to reduce high frequency noise coming from vibrations of the belt driving the flume propeller or electric noise. The excitation voltage for the strain gauges was 10 volts DC and 5 volts DC, for the lift and drag gauges respectively. The amplifiers used a power voltage of 18-25 volts DC. The output analogue signals of the amplifiers were converted to digital signals, with a 16-bit National Instruments 6259 A/D board. Force signals were recorded with Wavelab. Figure 4.1 shows the load cells.

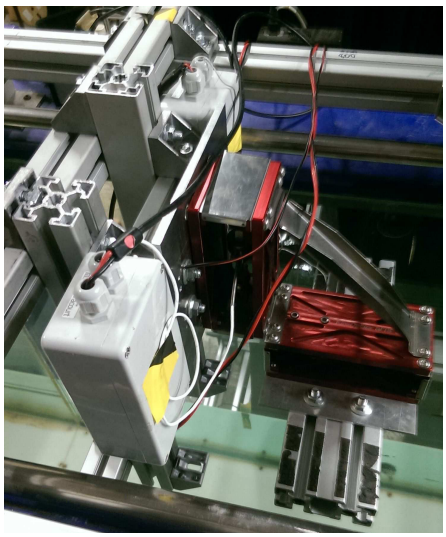

Figure 4.1: KineOptics load cells used to measure lift and drag

Force measurements

The flowchart in Fig. 4.2 summarizes the methodology used to obtain the force acting on the sail. The procedure was applied equally to lift and drag forces. The calibration procedure had two stages. The first involved solely the rig (acrylic plate and rotating shaft). The second stage included the rig and the sail (acrylic plate, rotating shaft and sail). Each stage (rig only and rig + sail) had two zero measurements, taken before and after a measurement with the flow switched on. The average of the zero flow measurements was subtracted from the measurement with the flow on. Finally, the force on the rig in the absence of the sail was subtracted from the force on the rig with the sail, to obtain the resultant force acting on the sail only.

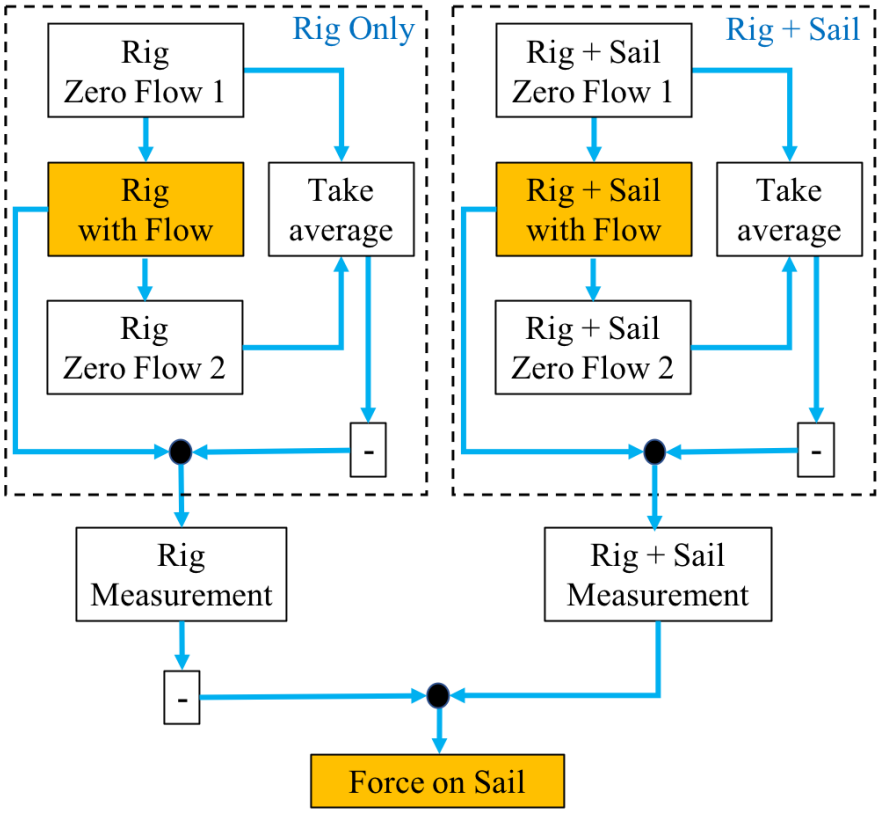

Figure 4.2: Flow chart indicating procedure to measure the forces on the sail

Force measurements calibration

Force calibrations were performed using the setup sketched in Fig. 4.3. Two tensioned strings pulled on the rig. The vertical string pulled on the acrylic side-plate. The horizontal string pulled on the rotating shaft, where the sail was mounted. The vertical string acted on the direction of the lift force and the horizontal string pulled on the direction of the drag.

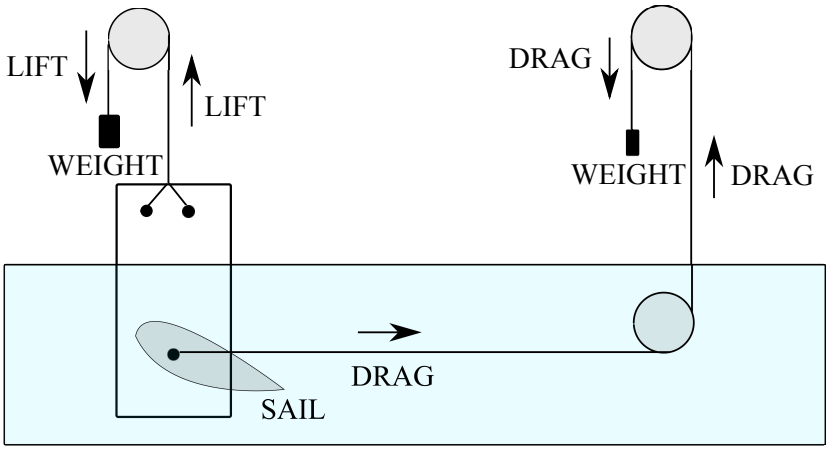

Figure 4.3: Calibration of load cells

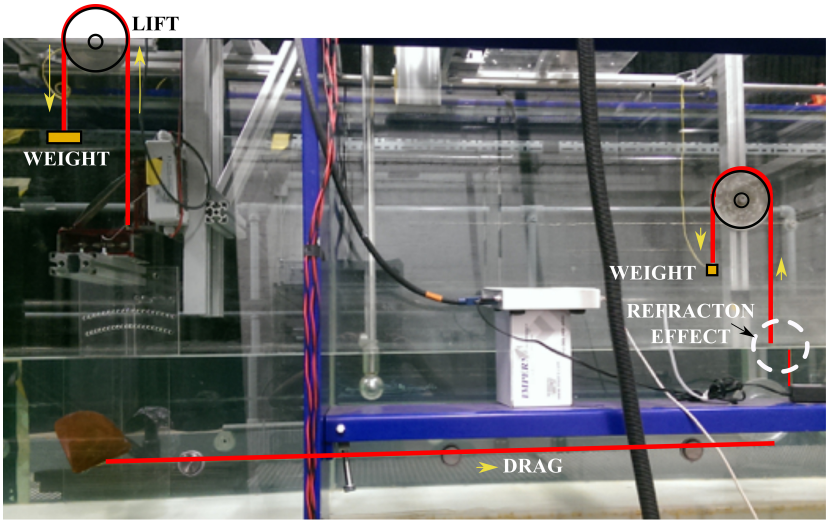

Figure 4.4: Photograph of the calibration setup

The directions of the applied force components are indicated by black arrows in Fig. 4.3. The forces used for calibration were applied by means of a set of weights, in the range from 0 to 1000 gm for lift and 0 to 150 gm for drag, where the acceleration due to gravity is $g = 9.81\,\mathrm{m/s^2}$. Lift and drag calibrations were performed as multiple

point calibrations. The incremental step for the lift calibration was 100 gm and for the drag calibration was a variable incremental step of 0, 5, 10, 20, 40, 50, 100, 150 gm. Figure 4.4 presents a photograph of the actual calibration setup. The rig and tension strings were aligned with a digital level to minimise cross-talk effects. These were recorded during calibration and were negligible within the range of tested forces.

Calibration plots

Figure 4.5 shows the calibration results. The corresponding calibration equations for the lift and drag of geometries S_1, S_2 and S_3 are

$$L_{S_1} = 14.967 v_o + 1.2274, \tag{4.1}$$

$$L_{S_2} = 14.976 v_o + 1.1521, \tag{4.2}$$

$$L_{S_3} = 14.958 v_o + 1.1558, \tag{4.3}$$

$$D_{S_1} = -12.617 v_o - 0.3263, \tag{4.4}$$

$$D_{S_2} = -12.601 v_o - 0.3297, \tag{4.5}$$

and

$$D_{S_3} = -12.657 v_o - 0.3346, \tag{4.6}$$

where v_o is the voltage output of the load cell, L_{S_1}, L_{S_2} and L_{S_3} are lift calibrations and D_{S_1}, D_{S_2} and D_{S_3} are drag calibrations for geometries S_1, S_2 and S_3, respectively. The calibration equations corresponding to L_{S_1}, L_{S_2}, L_{S_3} and D_{S_1}, D_{S_2}, D_{S_3} were averaged and only one calibration equation was utilised for lift and drag.

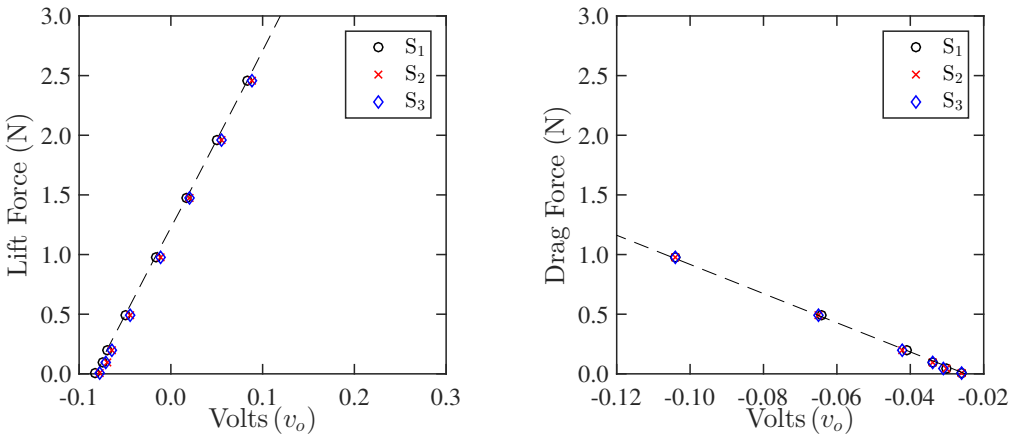

Figure 4.5: Lift and drag calibration curves for geometries S_1, S_2 and S_3

Force measurements corrections

Force corrections were applied for solid, wake blocking and streamline curvature (Pope and Harper, 1966). The corrections were previously developed for aircraft wings and are applied to this study by assuming that the spinnaker is a circular arc of finite AR. The solid and wake blocking effects for a two dimensional section of a sail are illustrated in Fig. 4.6, where U_c is the flow velocity in the vicinity of the object, U_∞ is the freestream velocity and U_{wake} is the velocity in the wake. $U_c > U_\infty$ due to the presence of the solid reducing the cross sectional area around the object and due to the wake effect. The streamline curvature effect refers to an upwash induced by the top and bottom surfaces of the flume, and the sidewalls. The upwash modifies the angle of attack of U_∞. For three dimensional effects, the corrections are the following.

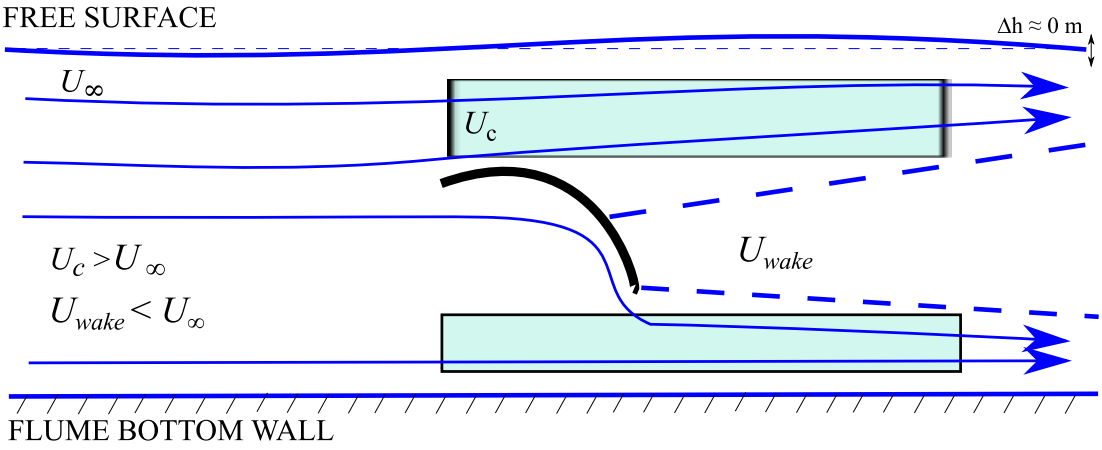

Figure 4.6: Solid and wake blocking effects, where Δh is the change in the free surface level and is approximately $\Delta h \approx 0\,m$

For the lift coefficient, the correction is defined as

$$C_L = C_{L,u}(1-2\varepsilon) - \tau_2 \Delta\alpha a, \tag{4.7}$$

where C_L is the corrected lift coefficient, $C_{L,u}$ is the uncorrected lift coefficient, ε is the solid-wake blocking correction, τ_2 is the streamline curvature correction, a is the wing lift curve slope, and $\Delta\alpha$ (in degrees) is defined as

$$\Delta\alpha = \delta_b \frac{A_m}{A_t} C_{L,u}(57.3), \tag{4.8}$$

where δ_b is the boundary correction factor, A_m is the cross section area of the model, A_t is the cross section area of the test section, $C_{L,u}$ is the measured lift coefficient and

57.3 is $\frac{180}{\pi}$, which is the conversion factor from radians to degrees.

The value of δ_b is taken to be that of a jet with horizontal boundaries, with a jet width to height ratio (r) equal to $r = 1$, hence $\delta_b = 0$.

For unusual shapes

$$\varepsilon = \frac{A_m}{4A_t}, \tag{4.9}$$

where A_m/A_t is the blockage ratio. Three blockage ratios were computed at three rotation angles η, where $\eta = -20°$, $\eta = 0°$ and $\eta = 5°$, correspond to the positions where maximum lift to drag ratio, maximum driving force and maximum lift were recorded for sail S_3. The computed blockage ratios were $A_m/A_t = 0.08, 0.14$ and 0.15 for the three cases presented in Fig. 4.7.

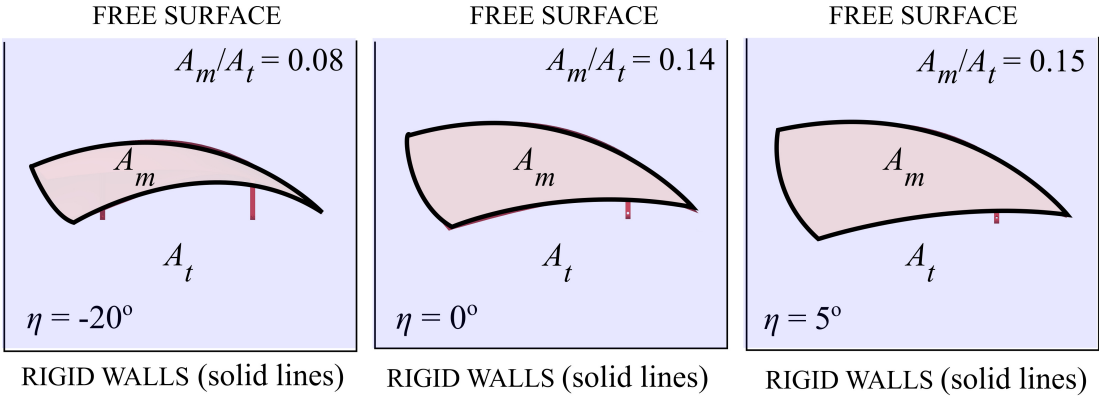

Figure 4.7: Sail cross-section (A_m), testing cross-section (A_t) and blockage ratio (A_m/A_t) for $\eta = -20°$, $\eta = 0°$ and $\eta = 5°$

For the drag coefficient, the correction is defined as

$$C_D = C_{D,u}(1 - 2\varepsilon) - \Delta C_{D_W} - \Delta C_{D_B} + \delta_b \frac{A_m}{A_t} C_L^2, \tag{4.10}$$

where C_D is the corrected drag coefficient, $C_{D,u}$ is the uncorrected drag coefficient, ε is the solid-wake blocking correction, ΔC_{D_W} is the wing wake pressure drag and ΔC_{D_B} is the body wake pressure drag. Here $\Delta C_{D_B} = 0$, since no fuselage is used.

$$\Delta C_{D_W} = \frac{K_1 \tau_1 V_w C_{D,u}}{A_t^{1.5}}, \tag{4.11}$$

where V_w is the volume of the wing, K_1 and τ_1 can be found in (Pope and Harper, 1966). ΔC_{D_W} is usually negligible and for this study $\Delta C_{D_W} = 0$. For the drag coefficient ε is calculated, using Eq. 4.9 and $\delta_b = 0$.

Uncertainty of blockage correction

To ensure that the blockage correction is accurate, experimental data of blockage corrections of a thin circular arc were used for comparison. This is a geometry which is similar to the mid-height section of the scale model spinnakers. The experimental data was provided by Souppez et al. (2019b) and measured in the towing tank of Solent University at $Re = 150k$. The experiments were designed to measure the blockage effect on a finite aspect ratio circular arc at angles of attack of 15° and 20°. The chord of the arc was 0.1 m, the span 0.37 m. Different blockage ratios were tested, by adjusting two side walls to each side of the arc.

Figure 4.8 shows the ratio of the corrected lift coefficient to the uncorrected lift coefficient ($C_L/C_{L,u}$) plotted against blockage ratio (A_m/A_t). Three cases are presented. The black and red markers, correspond to the tests at Solent University at $Re = 150k$ for blockage ratios of $0.020, 0.062, 0.130$ and $0.022, 0.071, 0.153$, tested at $\alpha = 15°$ and $\alpha = 20°$, respectively. The blue markers represent the correction from Pope and Harper (1966). This correction is applied to the lift coefficients of the sail measured at $\eta = -20°$, $\eta = 0°$ and $\eta = 5°$ and is equal to $1-2\varepsilon$, where ε is calculated from Eq. 4.9. Figure 4.8 shows a satisfactory agreement between $1-2\varepsilon$ and the Solent University tests. Two linear fits of the Solent University data for $\alpha = 15°$ and 20° are shown in Fig. 4.8. The distance between these lines is smaller than 8% at $A_m/A_t = 0.20$. The correction applied in this thesis fits between these regression lines and hence the error in the blockage correction factor (ε_B) is estimated to be smaller than 8%.

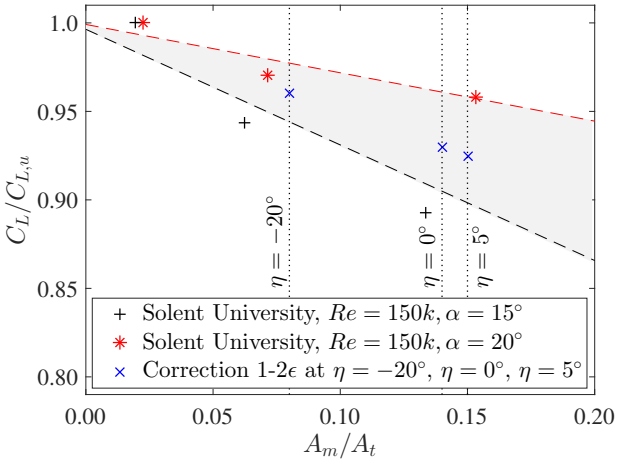

Figure 4.8: Blockage corrections measured at Solent University at $Re = 150k$ for a circular arc of AR = 3.7, at $\alpha = 15°$ (+), $\alpha = 20°$ (*) and correction $1-2\varepsilon$ (x), as applied in this PhD thesis for $\eta = -20°$, $\eta = 0°$ and $\eta = 5°$

Force measurements uncertainty

Experimental results are subject to error due to calibrations, environmental effects, equipment set-up and human factors. The results, however, are expected to remain within an interval around each measurement point.

The uncertainty of an experiment is determined for a number of measurements and represents the possible value that the error might have, within a given confidence interval. The confidence interval is defined as the percentage chance that all of the values measured will lie within the specified range of the error. This value can be obtained statistically. Alternatively, a sensitivity analysis on a function that relates the measured variables, can be performed. Consider the lift coefficient given by

$$C_L = \frac{L}{\frac{1}{2}\rho_d U_\infty^2 A}, \tag{4.12}$$

where L is the lift force on the sail, ρ_d is the density of the fluid, U_∞ is the freestream velocity and A is the surface area of the sail.

The sensitivity of C_L to its constituent variables can be calculated by undertaking a Taylor expansion about the true value of C_L in terms of its parameters (For examples of this method see Anthoine et al. (2009)). In order to eliminate the susceptibility of the calculation to sign, the expansion is squared, so that

$$\Delta C_L^2 = \frac{\partial C_L^2}{\partial x_1}\Delta x_1^2 + \frac{\partial C_L^2}{\partial x_2}\Delta x_2^2 + \frac{\partial C_L^3}{\partial x_3}\Delta x_3^2 + ... \tag{4.13}$$

For small changes and making $x_1 = A, x_2 = L, x_3 = \rho_d$ and $x_4 = U_\infty$, Eq. 4.13 can be rewritten as

$$\delta C_L = \sqrt{\left[\frac{\partial C_L}{\partial A}\delta A\right]^2 + \left[\frac{\partial C_L}{\partial L}\delta L\right]^2 + \left[\frac{\partial C_L}{\partial \rho_d}\delta \rho_d\right]^2 + \left[\frac{\partial C_L}{\partial U_\infty}\delta U_\infty\right]^2}, \tag{4.14}$$

where $\dfrac{\partial C_L}{\partial A} = 0$, since the surface of the sail is constant.

Expanding the derivatives of Eq. 4.14

$$\delta C_L = \sqrt{\left[\frac{2}{\rho_d U_\infty^2 A}(\delta L)\right]^2 + \left[\frac{-2L}{\rho_d^2 U_\infty^2 A}(\delta \rho_d)\right]^2 + \left[\frac{-4L}{\rho_d U_\infty^3 A}(\delta U_\infty)\right]^2}. \tag{4.15}$$

The known values of Eq. 4.15 are the following: $A = 0.051\,\mathrm{m}^2$, $\rho_d = 997\,\mathrm{kg/m}^3$ at $25°C$, $U_\infty = 0.144\,\mathrm{m/s}$. The lift and drag forces are $L = 0.6\,\mathrm{N}$ and $D = 0.23\,\mathrm{N}$. They are calculated with $C_L = 1.31$ and $C_D = 0.5$, which are the coefficient values for a rigid spinnaker reported by Viola et al. (2014).

The lift uncertainty δL and drag uncertainty δD were obtained by comparing results obtained following the flow chart in Fig. 4.2 for sails S_1, S_2 and S_3. The calibrations used the same input voltage (v_o) for each comparison. It was found that $\delta L \leq 0.040\,\mathrm{N}$ and $\delta D \leq 0.003\,\mathrm{N}$.

Density uncertainty $\delta\rho_d$ was determined by measuring the temperature of the water inside the flume, at one hour intervals. The maximum change of temperature measured was $\Delta T = 0.5°C$, which accounted for a change of $\delta\rho_d \leq 0.002\,\mathrm{kg/m}^3$.

Velocity uncertainty δU_∞ was $\delta U_\infty \leq 0.001\,\mathrm{m/s}$, the value obtained by comparing LDV velocity measurements taken 1 m upstream of the sails. The velocity measurements were taken in one continuous day of operation and on the same day that the forces were measured. The propeller was ran at the same power during the measurements.

Replacing values of Eq. 4.15 for the lift and drag coefficients and assuming the changes in $\delta\rho_d$ and δU_∞ were negligible, the squared-values of the force coefficients may be determined for

$$\delta C_L^2 = \left[\frac{2}{(997\,\mathrm{kg/m}^3)(0.144\,\mathrm{m/s})^2(0.051\,\mathrm{m}^2)}(0.04\,\mathrm{N})\right]^2, \tag{4.16}$$

$$\delta C_D^2 = \left[\frac{2}{(997\,\mathrm{kg/m}^3)(0.144\,\mathrm{m/s})^2(0.051\,\mathrm{m}^2)}(0.003\,\mathrm{N})\right]^2. \tag{4.17}$$

The uncertainties for the lift coefficient and the drag coefficient were $\delta C_L = 0.070$, $\delta C_D = 0.005$, and so the uncertainty in the lift coefficient was $C_L = 1.31 \pm 5\%$ and the drag coefficient was $C_D = 0.5 \pm 1\%$.

Systematic errors

Possible sources of systematic errors in the experimental setup include faulty calibrations, incorrect zeroing of instruments, damaged instrumentation or inaccurate readings of results. These type of errors are consistent and repeat themselves. To tackle them, force measurements were validated against literature review values, giving certainty that systematic errors in the blockage correction and force measurements were not detrimental. Velocity measurements were validated with two different instrumentation methods, Laser Doppler Velocimetry (LDV) and Particle Image Velocimetry (PIV), both systems are detailed in the following sections.

4.2 Laser Doppler velocimetry (LDV)

Flow characterisation of the flume was achieved using Laser Doppler velocimetry (LDV), which is a non-intrusive technique. LDV works on the principle that the frequency of scattered light (f_{sc}) is different to that of the source (f_o) and varies as a function of the droplet velocity that scatters the light. The relationship is given by

$$f_D = f_{sc} - f_o = \frac{U_{\text{droplet}}}{\lambda_o}(I_{sc} - I_o), \tag{4.18}$$

which is also known as the Doppler shift, where f_o, λ_o, I_o are the frequency, wavelength and intensity of the source light, f_{sc}, I_{sc} are frequency and intensity of the scattered light, and U_{droplet} is the velocity of the droplet reflecting the light. A basic LDV system is made of a continuous laser, a beam splitter, a brag cell and a lens to intersect the two beams at the measurement point. A schematic of the LDV system is shown in Fig. 4.9

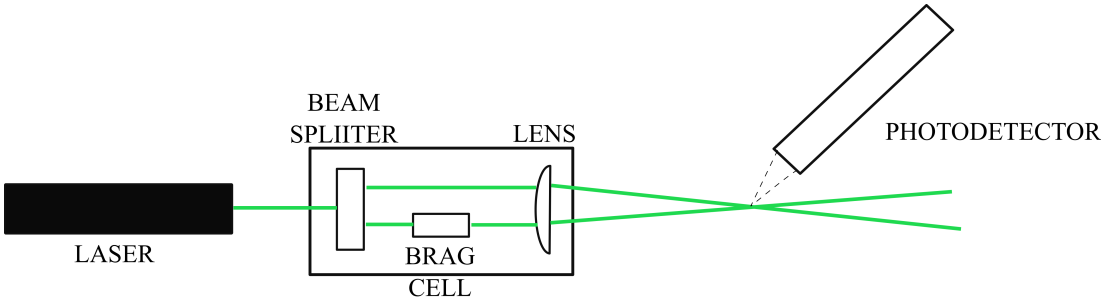

Figure 4.9: LDV components adapted from Anthoine et al. (2009)

The Bragg cell produces a frequency shift between the two intersecting beams (Δf). Provided $f_D < \Delta f$, the velocity is negative, otherwise the velocity is positive.

By intersecting two laser beams, a region of fringes is created (Figure 4.10) and a particle passing through this region will scatter light. The scattered light is detected by a photo-detector. The signal received by the photo-detector has the shape shown in Fig. 4.11. It has a unique period τ_{ldv}, which is the time it takes for the particle to travel from one fringe to the next. The velocity of the particle is calculated with τ_{ldv} and the distance between fringes d_f, such that

$$U_{\text{droplet}} = \frac{d_f}{\tau_{\text{ldv}}}, \tag{4.19}$$

where d_f is the fringe spacing given by

$$d_f = \frac{\lambda_o}{2\sin\theta_{\text{ldv}}/2}. \tag{4.20}$$

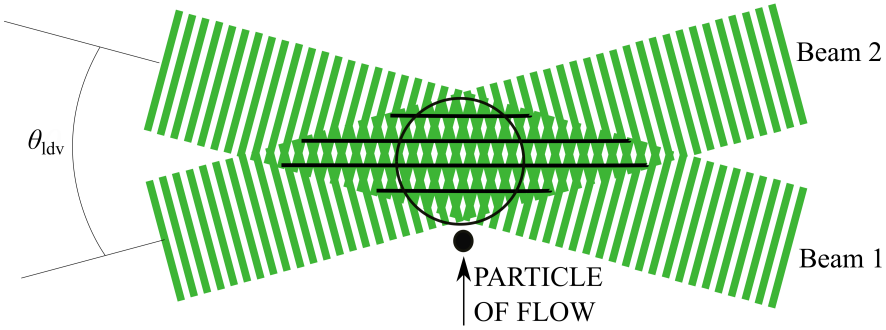

Figure 4.10: Fringe generation by two intersecting light beams

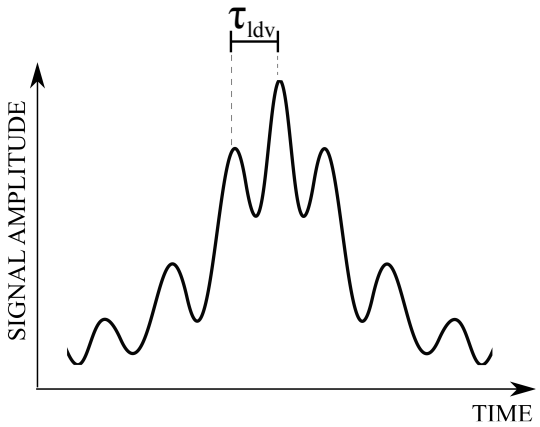

Figure 4.11: Signal captured by photo-detector when particle passes through the fringes and scatters light

4.3 Particle image velocimetry (PIV)

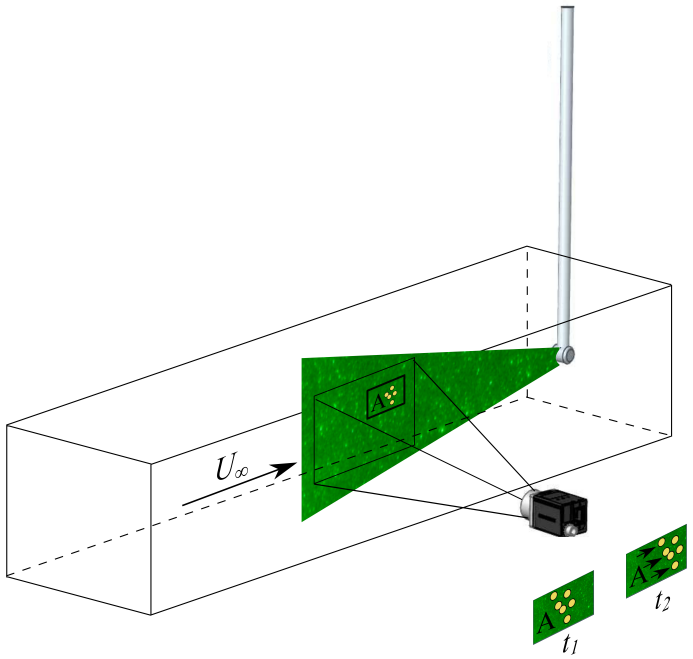

Figure 4.12: PIV system adapted from Raffel et al. (2007)

Particle image velocimetry (PIV) is a non-invasive technique to perform flow velocity measurements, by measuring the velocity of tracer particles that follow the motion of the fluid being studied. A laser sheet is generated with sheet forming optics and a region of the flow is illuminated. Tracer particles reflect the light and images are recorded with a camera. Successive frames are recorded, with two pulses of light emitted by the laser. The separation time between the two pulses is δt and two images are captured at t_1 and t_2. Defining $t_1 = t + \frac{\delta t}{2}$ and $t_2 = t - \frac{\delta t}{2}$, the velocity of a particle can be determined with

$$\mathbf{u}_p(t) = \frac{\mathbf{x}_p(t_1) - \mathbf{x}_p(t_2)}{\delta t} + O(\delta t^2) \tag{4.21}$$

Figure 4.12 shows a PIV system, where two images are captured at t_1 and t_2. Once the frames have been recorded, digital processing is performed of image pairs. The camera plane is divided into interrogation windows. The light intensity of the particle is digitalized and a cross-correlation is performed to determine the displacement of the particles, within the interrogation window. Subsequently, the velocity can be calculated from Eq. 4.21. Details on cross correlation algorithms are given by Raffel et al. (2007).

PIV system specifications

The PIV system used for this thesis consisted of a Solo 200XT pulsed dual-head Nd:YAG laser, with an energy output of 200 mJ at a wavelength of λ = 532 nm. The camera was a CCD Imperx 5MP with a 2448 px $\times$ 2050 px resolution and a Nikkor f/2, 50 mm lens. Seeding particles comprised silver coated hollow glass spheres, with an average diameter of 14 µm and a density of 1.7 g/cc. PIV pair images were sampled at 7.5 Hz. Two-pass adaptive correlation was applied. The first pass had a 64 px $\times$ 64 px interrogation window, with a Gaussian weighting and 50% window overlap. The second pass had a 24 px $\times$ 24 px interrogation window and a 75% window overlap. Averaged fields were generated from the full time series and a 3 $\times$ 3 Gaussian filter was used to smoothen the vector fields.

Figure 4.13a shows the flume set-up mode, where the PIV camera is positioned in front of the spinnaker. Figure 4.13b shows the flume recording mode, where the laser sheet is being fired on the spinnaker for image acquisition.

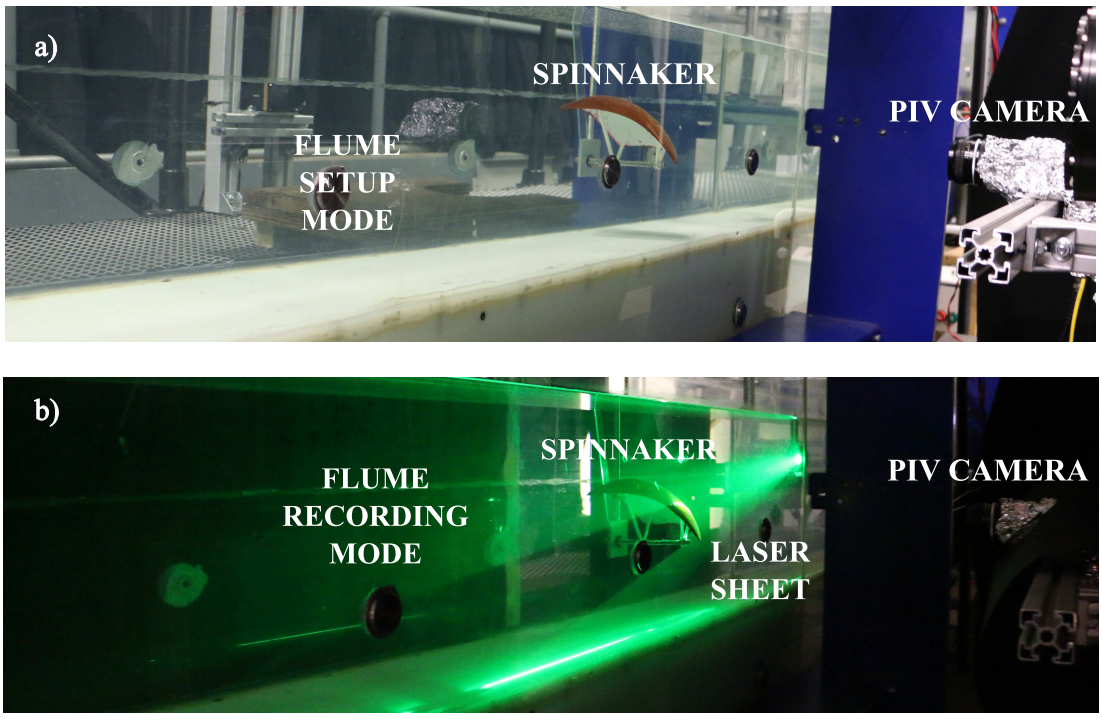

Figure 4.13: PIV setup for spinnaker

PIV uncertainty and error

For this setup, the time between frames (DT) was set to DT $= 2000\,\mu$s, as shown in appendix G, to satisfy the 'one-quarter' rule recommended by Adrian (1997). For an interrogation window of $64\,\text{px} \times 64\,\text{px}$, a particle is allowed to travel 16 pixels or 0.95 mm. For the selected DT and a freestream velocity $U_\infty = 0.25\text{m/s}$ a particle of flow travels 0.5 mm, satisfying the 'one-quarter' rule and giving correlation peak values in the range of 0.4-0.8, corresponding to an uncertainty of 2-3% according to Baum et al. (2014). A decreasing adaptive correlation window, previously described, was selected as part of the PIV algorithm. Hence, the PIV uncertainty measured with DaVis 8.3.0 was $|\delta u_{\text{PIV}}/U_\infty| < 0.05$. The total PIV error can be defined as $\varepsilon_{\text{PIV}} = \varepsilon_{rms} + \varepsilon_{bias}$. The random error ($\varepsilon_{rms}$) is obtained from repeated trials of an experiment, using the same equipment and personnel, where the data should scatter around a mean value. The bias error (ε_{bias}) or fixed error is the difference between the mean value of the measurement and the true value. It is usually constant for equipment and personnel, and it could be referenced from literature review cases. The random error (ε_{rms}) or measurement uncertainty can be estimated by taking a static (quiescent) flow measurement of the tank, after the flow has been left to stabilize. The ε_{rms} measured in the Sanderson flume is $\varepsilon_{rms} = 0.015$, as shown in Fig. 4.14. A bias error of $\varepsilon_{bias} \approx 0.02$ is taken from the reference values given by Raffel et al. (2018), assuming synthetic PIV images with particle image diameters of $d_\tau = 2\,\text{px}$, a particle image density of $N_{\text{ppp}} = 1/64\,\text{ppp}$ and a particle image displacement of $\Delta x = 16\,\text{px}$. Here d_τ is the diameter of the particle as seen by the camera and ppp stands for particle images per pixel. Considering this method and the DaVis uncertainty quantification, the PIV total error is estimated to be in the range of $0.035 < \varepsilon_{\text{PIV}} < 0.050$.

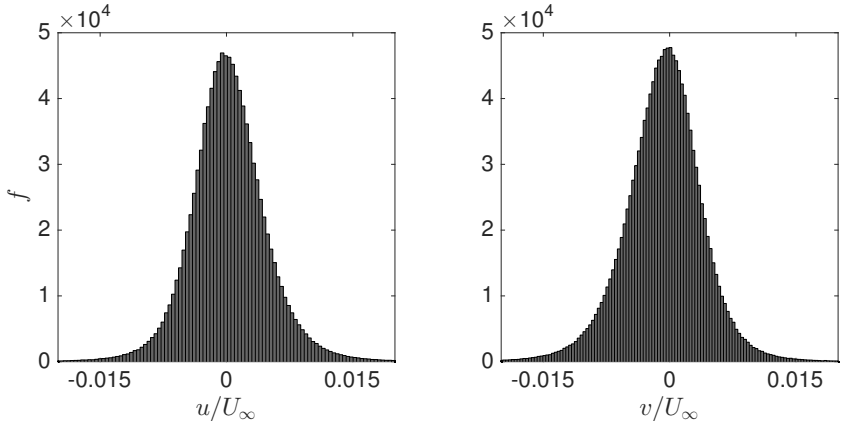

Figure 4.14: PIV measurement of random error (ε_{rms})

Vorticity uncertainty

The out-of-plane vorticity component is given by

$$\omega_z = \frac{\partial v}{\partial x} - \frac{\partial u}{\partial y}. \tag{4.22}$$

With a central difference scheme, vorticity can be approximated as

$$\omega_z = \frac{1}{2d}[v(x+d,y) - v(x-d,y) - u(x,y+d) + u(x,y-d)], \tag{4.23}$$

where d is the distance between uniformly distributed grid points. By propagation of uncertainties (Taylor, 1997), if various quantities $x, ..., w$ are measured with small uncertainties $\delta x, ..., \delta w$ and the measured values are used to calculate some quantity q as a sum or subtraction, then the uncertainties in $x, ..., w$ cause an uncertainty in q as follows:

$$\delta q = \sqrt{\left(\frac{\partial q}{\partial x}\right)^2 (\delta x)^2 + ... + \left(\frac{\partial q}{\partial w}\right)^2 (\delta w)^2}. \tag{4.24}$$

Hence, the vorticity uncertainty is given by

$$\delta {\omega_z}^2 = 2\left(\frac{1}{2d}\right)^2 [\delta u^2 + \delta v^2]. \tag{4.25}$$

The vorticity uncertainty can be reduced by using every second grid point for the finite difference approximation (Sciacchitano and Wieneke, 2016), such that

$$\omega_z = \frac{1}{4d}[v(x+2d,y) - v(x-2d,y) - u(x,y+2d) + u(x,y-2d)], \tag{4.26}$$

and the vorticity uncertainty is

$$\delta {\omega_z}^2 = 2\left(\frac{1}{4d}\right)^2 [\delta u^2 + \delta v^2]. \tag{4.27}$$

The field of view in Fig. 8.11 is 140 mm $\times$ 140 mm. It is focused at the boundary layer of the sail and provides a spatial resolution of $d = 0.005 c_0$, where $c_0 = 114\,\text{mm}$. The velocity uncertainties are $|\delta u/U_\infty| \leq 0.05$ and $|\delta v/U_\infty| \leq 0.05$. Considering Eq. 4.27 and a freestream velocity of $U_\infty = 143\,\text{mm/s}$, the vorticity uncertainty is $|\delta \omega_z c_0/U_\infty| \leq 5$, which corresponds to a range of 5% of the maximum vorticity value.

PIV calibration

PIV calibration was performed for every measurement plane by placing a calibration plate (Fig. 4.15) in front of the PIV camera. The distance between the dots of the calibration plate was 1.5 cm. The fitting algorithm used for the calibration was a 3rd order polynomial, which was selected from the calibration menu provided in DaVis 8.3.0 software. The time between frames (DT) was used as an input into the PIV software to calculate the velocity values. Once the calibration was performed, PIV measurements were validated using alternative LDV measurements, over the range of velocities to be tested. The comparison is shown in Table 4.1.

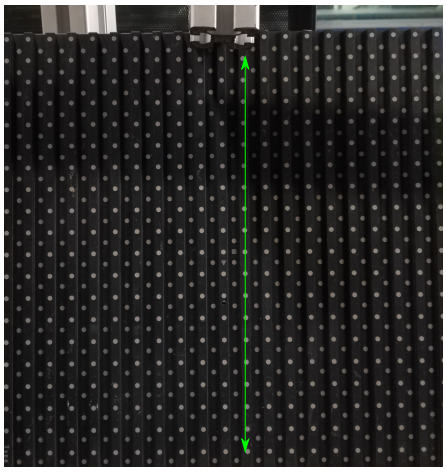

Figure 4.15: PIV calibration plate

Table 4.1: PIV calibration validation with LDV measurements

Flume Power	LDV (m/s)	PIV (m/s)
9 %	0.107	0.106
10 %	0.117	0.120

Laser reflection mitigation

In order to mitigate surface reflections, a coating of Halfords' Matt Black Paint was applied to the sail surface. A second coating of rhodamine B was also applied to the sail, allowing a notch filter on the camera to subtract the wavelength of rhodamine B and minimise the reflected light. A third coating of acrylic was applied to protect the rhodamine B from dissolving in water. The notch filter used on the camera is shown in Fig. 4.16. Additionally, background subtraction enabled measurements in close proximity to the wall. The leading edge region, however, was not affected by

laser reflections due to the curvature of the sail and the direction of the laser sheet. Background subtraction is a technique in which a background image is obtained by averaging a large number of PIV recordings. A random distribution of particles will appear as faint background within the particle field, when taking an ensemble average over a large number of images. However, elements such as the boundaries, contaminants in the glass, particles adhered to the wall or reflections, retain the same brightness on average, because they do not change between individual images and the averaged image. These elements are defined as background noise by Wereley et al. (2002). Therefore subtraction of the averaged image from the instantaneous images is used to remove background noise.

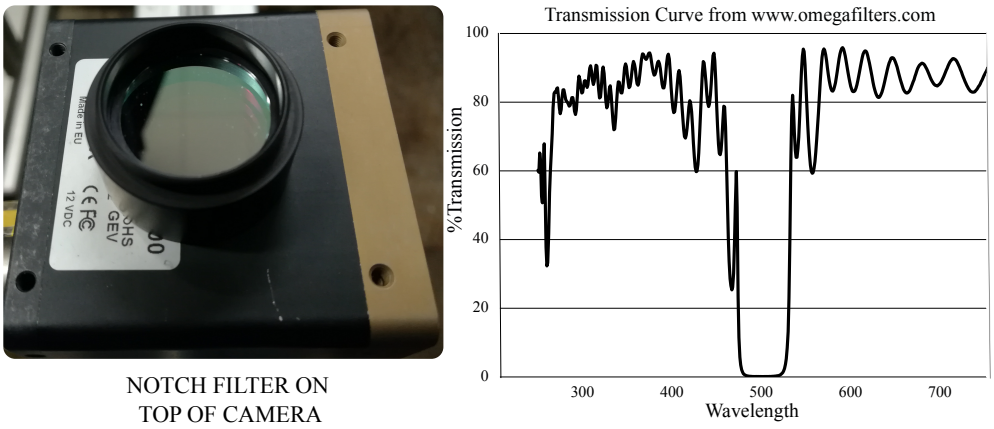

Figure 4.16: Optic filter and transmission curve

Setup limitations

The planar PIV system did not allow measurement of the spanwise velocity component (u_z). Only cross-sections parallel to the flow were recorded. The sweep angle generates vortex tilt and a measurement error due to the orientation of the camera, with respect to the axial flow of the vortex (Fig. 4.17). The measured velocity is a combination of the true tangential velocity and the axial velocity of the vortex. For the subsequent analysis, the true tangential velocity is projected in the y-axis, such that $u_\theta = u_y$. Morgan et al. (2009) define the tangential measured velocity ($u_{y,tilt}$) as

$$u_{y,tilt} = u_y \cos(\Lambda) + u_z \sin(\Lambda), \tag{4.28}$$

where u_y is the true tangential velocity of the vortex, u_z is the axial velocity of the vortex and Λ is the sweep angle of the leading edge. The tilt error (ε_{tilt}) is defined as

$$\varepsilon_{tilt} = 1 - \frac{u_{y,tilt}}{u_y}. \tag{4.29}$$

Figure 4.17 shows the position of the leading edge with respect to the onset flow in the flume. The vortex was transversal to the flow and the tip of the sail was 5 cm away from the wall of the flume. These factors limit the spanwise flow component, as opposed to the axial flow velocity component inside the core of the LEV of a delta wing that can reach values of $u_z = 1.35U_\infty$ (Furman and Breitsamter, 2013) and where the flow is almost parallel to the axial flow.

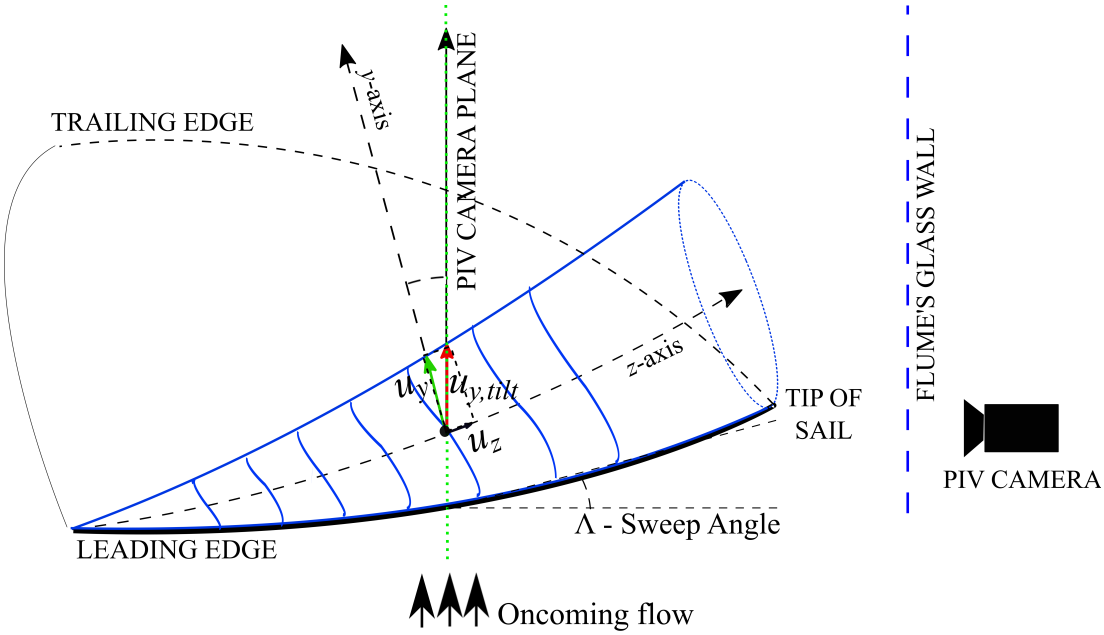

Figure 4.17: Vortex tilt error (ε_{tilt})

On the other hand, when the wing is transverse to the flow, it has been shown that in a translating flat plate, the axial velocity u_z at the leading edge could reach maximum values of $u_z = 0.40U_\infty$ close to midspan and $u_z = 0.20U_\infty$ at $3/4^{th}$ of the span (Kim and Gharib, 2010). At the midspan of swept back ($\Lambda = 45°$) flapping wings, u_z reaches values of $0.20U_\infty \leq u_z \leq 0.25U_\infty$ and in non-swept back wings ($\Lambda = 0°$) values of $0.10U_\infty \leq u_z \leq 0.25U_\infty$ (Wong and Rival, 2015). The difference in the range at midspan is most likely due to different wing motions and end-plate effects.

Considering a range of $0.10U_\infty \leq u_z \leq 0.40U_\infty$, $\Lambda = 40°$ and $u_{y,tilt} = 0.48U_\infty$ (measured in Chapter 6), ε_{tilt} lies within the range of $-0.65 \leq \varepsilon_{tilt} \leq 0.11$. Due to the proximity

of the side walls of the flume to the tip of the sail and because $\Lambda = 40^\circ$ occurs after midspan and at $3/4^{\text{th}}$ of the span of the sail, it is expected that $0.10U_\infty \leq u_z \leq 0.25U_\infty$ and that $-0.15 \leq \varepsilon_{tilt} \leq 0.11$.

Summary of errors and uncertainties

Table 4.2 presents a summary of the errors and uncertainties considered in Chapter 3 and Chapter 4. The error of the circulation computation of a free vortex (ε_Γ) is introduced in Chapter 7.

Table 4.2: Summary of errors and uncertainties

Variable	Error or uncertainty	Range
PIV random error	ε_{rms}	$\varepsilon_{rms} = 0.015$
PIV bias error	ε_{bias}	$\varepsilon_{bias} \approx 0.020$
PIV total error	ε_{PIV}	$0.035 \leq \varepsilon_{\text{PIV}} \leq 0.050$
Tilt error	ε_{tilt}	$-0.15 \leq \varepsilon_{tilt} \leq 0.11$
Angle of attack (α_{X_i}) error	$\varepsilon_{\alpha_{X_i}}$	$-2^\circ \leq \varepsilon_{\alpha_{X_i}} \leq 2^\circ$
Rotation angle (η) error	ε_η	$-1^\circ \leq \varepsilon_\eta \leq 1^\circ$
Blockage correction error	ε_{B}	$\varepsilon_{\text{B}} < 0.08$
Lift uncertainty	δL	$\delta L \leq 0.04\,\text{N}$
Drag uncertainty	δD	$\delta D \leq 0.003\,\text{N}$
Fluid density uncertainty	$\delta\rho_d$	$\delta\rho_d \leq 0.002\,\text{kg/m}^3$
LDV velocity uncertainty	δU_∞	$\delta U_\infty \leq 0.001\,\text{m/s}$
Lift coefficient uncertainty	δC_L	$\delta C_L \leq 0.07$
Drag coefficient uncertainty	δC_D	$\delta C_D \leq 0.005$
PIV velocity uncertainty	$\lvert\delta u_{\text{PIV}}/U_\infty\rvert$	$\lvert\delta u_{\text{PIV}}/U_\infty\rvert < 0.05$
Vorticity uncertainty	$\lvert\delta\omega_z c_0/U_\infty\rvert$	$\lvert\delta\omega_z c_0/U_\infty\rvert \leq 5$

Chapter 5

Vortex detection methods

5.1 Vortex detection methods

Background

Vortices are identified by applying detection algorithms to the velocity fields obtained with PIV or CFD. The algorithms work by processing information contained in the velocity gradient tensor or in the velocity field itself. A brief compilation of these methods is presented in the following paragraphs and two examples are studied for an isolated Lamb-Oseen vortex.

What constitutes a vortex is a topic of long debate and history. Lugt (1979) defined a vortex as a closed spiral of pathlines. However, Jeong and Hussain (1995) noted some problems with this definition. Firstly, a particle might not finish a full rotation around the centre of the vortex, therefore no closed pathline would be generated. Secondly, the Galilean invariance is not fulfilled under different frames of reference.

Summaries of several vortex definitions are given by Jeong and Hussain (1995) and Haller (2005). According to Jeong and Hussain (1995), a vortex should be defined as a region of net vorticity and as a geometry that is Galilean invariant, i.e. it should not change under different frames of reference.

A vortex has also been defined as a region of local pressure minima, but a counter example of this definition is a source or a sink, that also have a pressure minimum at the origin but do not swirl at all. Burgers vortices are also difficult to define with only isopressure contours, as shown by Jeong and Hussain (1995).

Another common definition of a vortex has been given as a region of high vorticity (ω). However, this criterion fails to identify vortices in regions where the background shear vorticity is in the same order of magnitude as the vorticity inside of a vortex. Hence, a vortex can be missed altogether, if vorticity (ω) is used as a detection criterion.

Local schemes

Galilean invariant methods rely on velocity gradient decomposition. Here, the velocity gradient tensor ($\nabla \mathbf{u}$) or Jacobian is defined as

$$J = \nabla \mathbf{u} = \frac{\partial u_i}{\partial x_j} = \begin{bmatrix} \frac{\partial u}{\partial x} & \frac{\partial u}{\partial y} & \frac{\partial u}{\partial z} \\ \frac{\partial v}{\partial x} & \frac{\partial v}{\partial y} & \frac{\partial v}{\partial z} \\ \frac{\partial w}{\partial x} & \frac{\partial w}{\partial y} & \frac{\partial w}{\partial z} \end{bmatrix} \tag{5.1}$$

The elements of the velocity gradient tensor can be approximated with finite difference methods and the tensor itself can be split into a rate of strain tensor (S_{ij}) and a rate of rotation tensor (Ω_{ij}), such that

$$\nabla \mathbf{u} = S_{ij} + \Omega_{ij} = \frac{1}{2}\left[\frac{\partial u_i}{\partial x_j} + \frac{\partial u_j}{\partial x_i}\right] + \frac{1}{2}\left[\frac{\partial u_i}{\partial x_j} - \frac{\partial u_j}{\partial x_i}\right] \tag{5.2}$$

As pointed out by Haller (2005), the first three dimensional vortex criteria using the velocity gradient decomposition were the Q-criterion by Hunt et al. (1988), the Δ-criterion introduced by Chong et al. (1990) and the λ_2-criterion introduced by Jeong and Hussain (1995). These methods have been classified as local schemes by Morgan et al. (2009) because the analysis is undertaken at individual grid points, rather than over a group of grid points.

Global schemes

Non-local schemes for vortex detection have been proposed by Graftieaux et al. (2001) and Chakraborty et al. (2005), among others. Non-local schemes examine the topology of the flow (groups of grid points) rather than the local values of the velocity gradient tensor. In the present study, the Q-criterion (Hunt et al., 1988) will be used as a local scheme and the γ-criterion (Graftieaux et al., 2001) as a global scheme, and the results compared against analytical solutions to quantify which one is best for application to the sail's experimental data.

For instantaneous analysis, global schemes have the advantage of being robust to local fluctuations of the flow that could occur due to turbulence or PIV noise.

Example of local scheme: Q criterion

The Q-criterion is defined as

$$Q = \frac{1}{2}\left(\|\Omega\|^2 - \|S\|^2\right), \tag{5.3}$$

which is the difference between the Euclidean norm of the vorticity tensor squared and the Euclidean norm of the rate of strain tensor squared. The Q-criterion states that a vortex is present when Q is greater than zero, which indicates that the vorticity tensor dominates the rate of strain tensor.

Hence, a region of flow where the rotation dominates the strain qualifies as a vortex. The Q-criterion can also be defined as the second invariant of the Jacobian given by

$$Q = J_{11}J_{22} - J_{12}J_{21} + J_{11}J_{33} - J_{13}J_{31} + J_{22}J_{33} - J_{23}J_{32} \tag{5.4}$$

The second invariant is obtained from the characteristic polynomial of the velocity gradient tensor ($\nabla \mathbf{u}$). The invariants are the coefficients of the characteristic polynomial calculated as the determinant of

$$p(\lambda) = \det(J - \lambda I_3) \tag{5.5}$$

with solution given by

$$\lambda_i^3 - P\lambda_i^2 + Q\lambda_i - R = 0, \tag{5.6}$$

where

$$P = \mathrm{tr}(J) = J_{11} + J_{22} + J_{33}, \tag{5.7}$$

$$Q = \frac{1}{2}(J_{ii}J_{jj} - J_{ij}J_{ji}) \tag{5.8}$$

and

$$R = \det(J). \tag{5.9}$$

The second determinant of Eq. 5.8 is equivalent to Eq. 5.3 and Eq. 5.4. In the sail experiment, only 2D experimental data were available and therefore only 4 out of 9 of the velocity gradients were available to calculate Q. Therefore only cross-sections of a three-dimensional flow feature can be analysed. However, cross-sectional information is still relevant to understand the nature of the vortex and to develop models that reproduce its behaviour.

Example of global scheme: γ criterion

Graftieaux et al. (2001) developed γ_1 and γ_2 vortex detection criteria to overcome the sensitivity to small-scale turbulence of methods that rely on local quantities, such as velocity gradients and vorticity (Graftieaux et al., 2001). The method is defined as a non-local scheme by Morgan et al. (2009) and has been applied successfully to PIV, and CFD data. Examples of its application are given by Rabinovitch et al. (2012), Harbig et al. (2013b) and Pitt Ford and Babinsky (2013).

The difference between γ_1 and γ_2 is that the latter is the Galilean invariant version of the scheme, which involves subtraction of the local convection velocity. Figure 5.1 describes the schematic execution of the algorithm for γ_1.

γ_1 criterion

For every point P on a grid, a region S_w around P is defined. Region S_w has N-number of M points around the central point P. The angle θ_M is defined as that formed between the velocity vector $\boldsymbol{u}_M$ at point M and the directional vector $\boldsymbol{a}_{PM}$ from point P to point M. The corresponding γ_1 value for point P is given by the average of the N-number of $\sin(\theta_M)$ inside region S_w. This is summarised by Eq. 5.10 and Fig. 5.1. If a rotational structure is detected around point P, the value of γ_1 will be close to 1.

$$\gamma_1 = \frac{1}{N}\sum_{S_w}\frac{(\boldsymbol{a}_{PM}\times\boldsymbol{u}_M)\cdot\hat{z}}{||\boldsymbol{a}_{PM}||\,||\boldsymbol{u}_M||} = \frac{1}{N}\sum_{S_w}\sin(\theta_M), \tag{5.10}$$

where $\hat{z}$ is the unit vector normal to the plane formed by $\boldsymbol{a}_{PM}$ and $\boldsymbol{u}_M$.

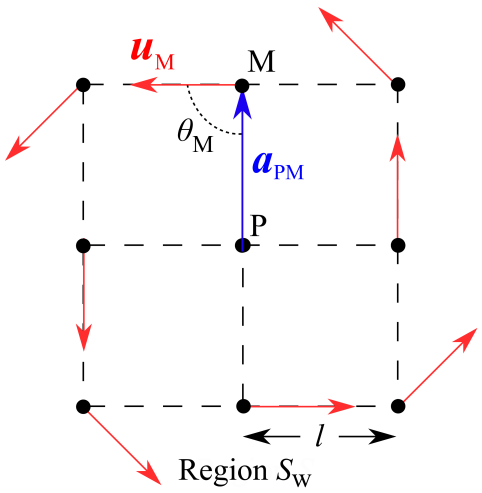

Figure 5.1: Schematic of γ_1 detection algorithm

γ_2 criterion

To compute γ_2, the average convection velocity $\boldsymbol{u}_\mathrm{P}$ is subtracted from $\boldsymbol{u}_\mathrm{M}$ at every point in the interrogation window, such that

$$\gamma_2 = \frac{1}{N}\sum_{S_\mathrm{w}} \frac{(\boldsymbol{a}_\mathrm{PM} \times (\boldsymbol{u}_\mathrm{M} - \boldsymbol{u}_\mathrm{P})) \cdot \hat{z}}{||\boldsymbol{a}_\mathrm{PM}||\,||\boldsymbol{u}_\mathrm{M} - \boldsymbol{u}_\mathrm{P}||} = \frac{1}{N}\sum_{S_\mathrm{w}} \sin(\theta_\mathrm{M}), \tag{5.11}$$

where $\boldsymbol{u}_\mathrm{P}$ is given by

$$\boldsymbol{u}_\mathrm{P} = \frac{1}{N}\sum_{S_\mathrm{w}} \boldsymbol{u}_\mathrm{M}. \tag{5.12}$$

Figure 5.2a shows the schematic representation of the γ_2 criterion and Fig. 5.2b the schematic of the average convection velocity computation.

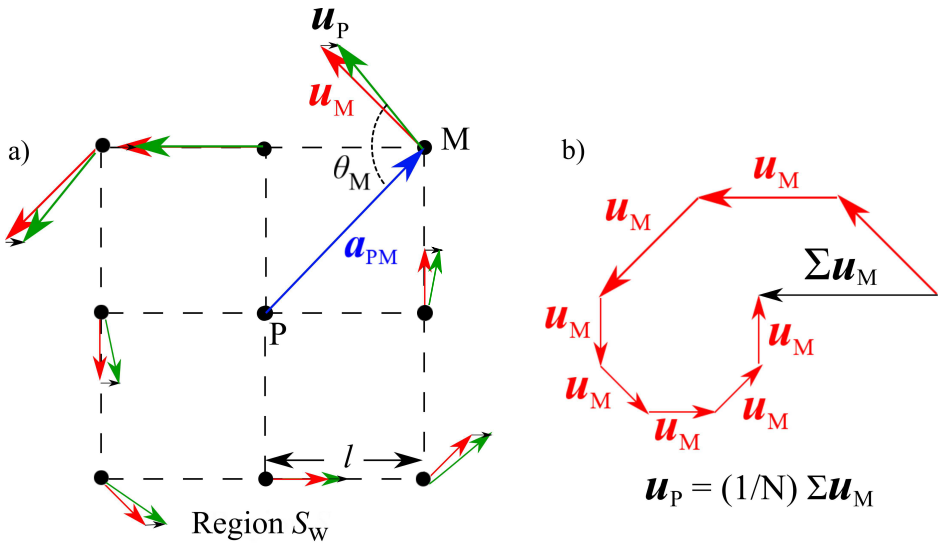

Figure 5.2: a) Schematic of γ_2 detection algorithm, b) schematic of $\boldsymbol{u}_\mathrm{P}$ calculation

5.2 Isolated Lamb-Oseen vortex

The implementations of the Q and the γ criteria are validated for the case of an isolated Lamb-Oseen vortex. A Q criterion code is implemented with first order finite difference and a code is written for the γ criterion. Both codes are included in appendix A. The Lamb-Oseen vortex is used as a test case for the γ criterion by Graftieaux et al. 2001 and Morgan et al. 2009. The tangential velocity of a Lamb-Oseen vortex is defined as

$$u_\theta = \frac{\Gamma_\mathrm{LO}}{2\pi r}\left(1 - \exp\left(-\frac{r^2}{l_0^2}\right)\right), \tag{5.13}$$

where Γ_{LO} is the strength of the vortex, r is radial distance and l_0 is the core vortex radius defined as $l_0 = \sqrt{4\nu t}$, ν is the kinematic viscosity, and t is time. The vortex core radius l_0 grows in time. Vortex detection is carried out at a single instant in time and therefore l_0 has a constant value in the results considered herein.

The velocity profile of a Lamb-Oseen vortex and the contours of the Q-criterion and the γ_2 criterion are shown in Fig. 5.3a and Fig. 5.3b, respectively. It is obvious that both criteria are able to identify the vortex. Addition of a 15% random error (ε) to the velocity profile of the Lamb-Oseen vortex, causes the detection capability of the Q-criterion to deteriorate sharply, as shown in Fig. 5.3c. Figure 5.3d shows how γ_2 is robust to the noise level and remains able to detect the vortex. The error is added to exemplify the effect of PIV noise generated during acquisition and post-processing (Morgan et al. 2009) and the combined effect of PIV uncertainty, and tilt effect. The detection ratio l/l_0 in Fig. 5.3b and Fig. 5.3d is set to $l/l_0 = 0.32$.

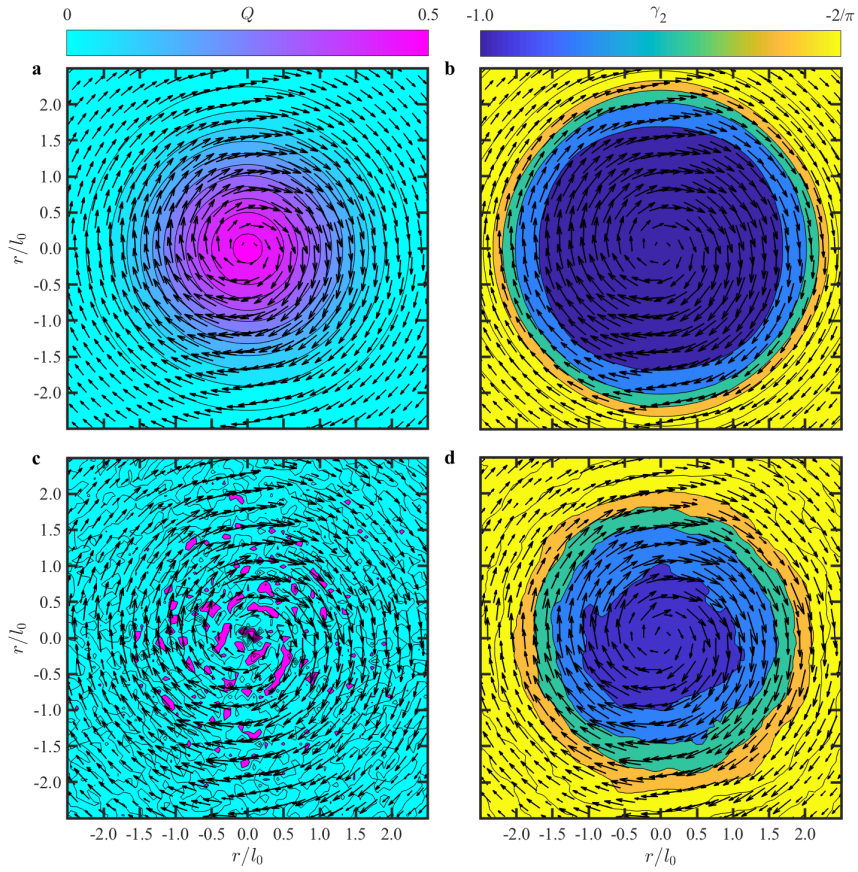

Figure 5.3: a) Q-contours and b) γ_2-contours with $\varepsilon = 0.00$, c) Q-contours and d) γ_2-contours with $\varepsilon = 0.15$ for a clock-wise rotating Lamb-Oseen vortex. Appendix B, shows the criteria applied to the flow of a non slender delta wing (Muir et al., 2017)

Additional considerations for the γ-criterion

For the γ criterion, the vortex core is defined as the region where $2/\pi < |\gamma_2| < 1$ and when $|\gamma_1|$ is maximum. The γ detection window (S_w) should capture the vortex core radius (l_0). By defining l as half of the length of the detection window S_w, shown in Fig. 5.1, the ratio l/l_0 can be defined.

Figure 5.4 shows the results for γ_1 and γ_2, along the centre of a Lamb-Oseen vortex with a 15% random error ($\varepsilon = 0.15$). It can be observed that when the ratio l/l_0 is small, the bell shape of γ_2 decreases in size and the criterion tends to behave more like a local criterion. This can lead to underestimation of the vortex core size and missing out vortices. For γ_1, the smaller the value of l/l_0, the narrower the detection peak becomes (Graftieaux et al. 2001). The effect of noise in γ_1 is to decrease the magnitude of its detection peak. The effect of noise in γ_2 is to decrease the shape of the bell, compared to signals without noise. It is recommended, therefore, for experimental measurements, to set $0.64 < l/l_0 < 1.0$ for γ_2 and $0.1 < l/l_0 < 0.2$ for γ_1. The upper bound in γ_2 and γ_1 prevents the detection curves of Fig. 5.4 from flattening out.

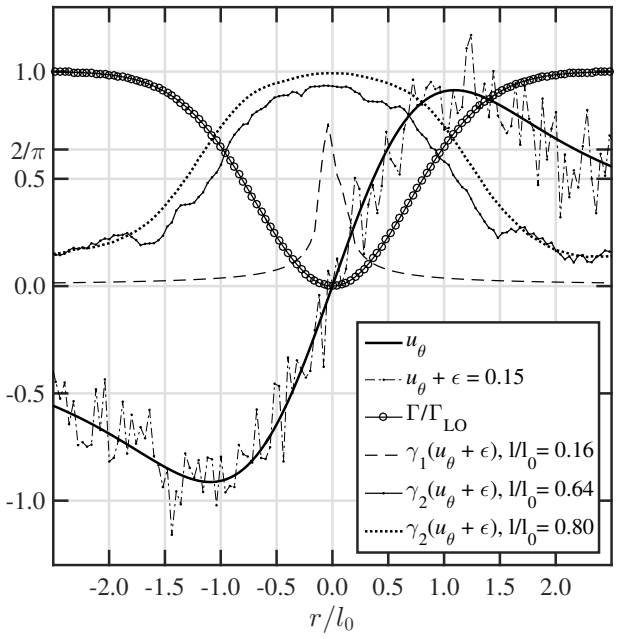

Figure 5.4: Detection curves of γ_1 and γ_2 for an anti-clock wise rotating Lamb-Oseen vortex for different window sizes and Lamb-Oseen vortex circulation

PART C:
RESULTS

Chapter 6

LEV detection

This Chapter presents the time-averaged and instantaneous flow field recorded with PIV, in planes A, B, and C of the spinnaker geometry S_0. Figure 6.1a shows the measurement planes and Fig. 6.1b the experimental setup. The positioning of the sail of Fig. 6.1b replicates the conditions tested by Viola et al. (2014). A detailed explanation is provided in Chapter 3. The time-averaged flow field of each plane consists of a set of 305 PIV image pairs, that were sampled every $t^* = 0.134$, where time t is made non-dimensional, with the chordwise convection period c_0/U_∞, i.e. $t^* \equiv tU_\infty/c_0$. Consider i the index of image pairs, where $1 < i < 305$. An instantaneous analysis was necessary to reveal the nature of the time-averaged structures. In particular, in the time-averaged sense, a shedding vortex might appear as a stable structure. For the instantaneous analysis, resolution near the boundary of the sail was crucial to track the trajectory of shedding vortices near the surface of the sail. Laser-reflection was tackled with background subtraction and an optical filter.

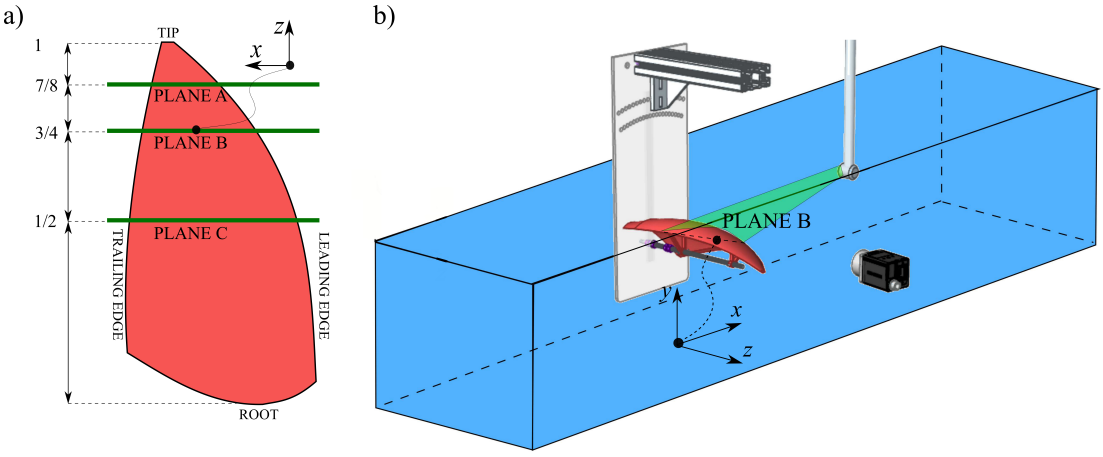

Figure 6.1: a) PIV measurement on plane C of geometry S_0 and b) PIV measurement planes A, B and C, of geometry S_0

6.1 Sail averaged flow field

Figure 6.2 shows the time-averaged vector fields, streamlines and vorticity contours in the planes A, B and C for geometry S_0 in a uniform steady water flow of speed $0.114\,\mathrm{m/s}$. The local angle of attack increases from plane A to plane C due to the twist of the sail. The maximum camber also increases from plane A to plane C.

Planes A and B exhibit flow separation at the leading edge and flow reattachment further downstream. The concentric streamlines of Fig. 6.2e indicate the averaged flow field of a leading-edge vortex. The streamlines are concentric because of the rotational path of the flow particles of flow at the leading edge.

As shown in Section 6.2, some of the vorticity generated at the sharp leading edge becomes convected inside a vortex that is stably attached to the leading edge. The permanent, three-dimensional nature of this flow structure makes it more analogous to the LEV of a delta wing than to a time-averaged laminar separation bubble of a thin foil at transitional Reynolds numbers. These results provide the first experimental evidence that a stable LEV occurs on downwind sails. On plane C, the flow remains attached at the leading edge but separates at $x/c = -0.3$ without reattaching. Vorticity is generated at the leading edge in all three planes. The vorticity contours of planes A (Fig. 6.2g) and B (Fig. 6.2h) follow the curvature of corresponding time-averaged streamlines. The vorticity contour is straighter on plane C (Fig. 6.2i), where trailing edge separation occurs. A region of counter-rotating vorticity is observed on top of plane C (Fig. 6.2i).

The LEV forms at the upper part of the sail (plane B) and grows in size towards the tip. This growth results from vorticity that, at every section, is convected with the axis of the vortex and that accumulates towards the tip. From plane B to plane A, it can be observed that the axis of the vortex moves away from the sail surface and inboard.

The streamline topology of plane C is very different to that of planes A and plane B. This is due to the large separation region dominating plane C. The region of separation and the topology of the streamlines are explored in more detail in Chapter 9, where the near wake of the spinnaker is studied from different angles of attack at different planes.

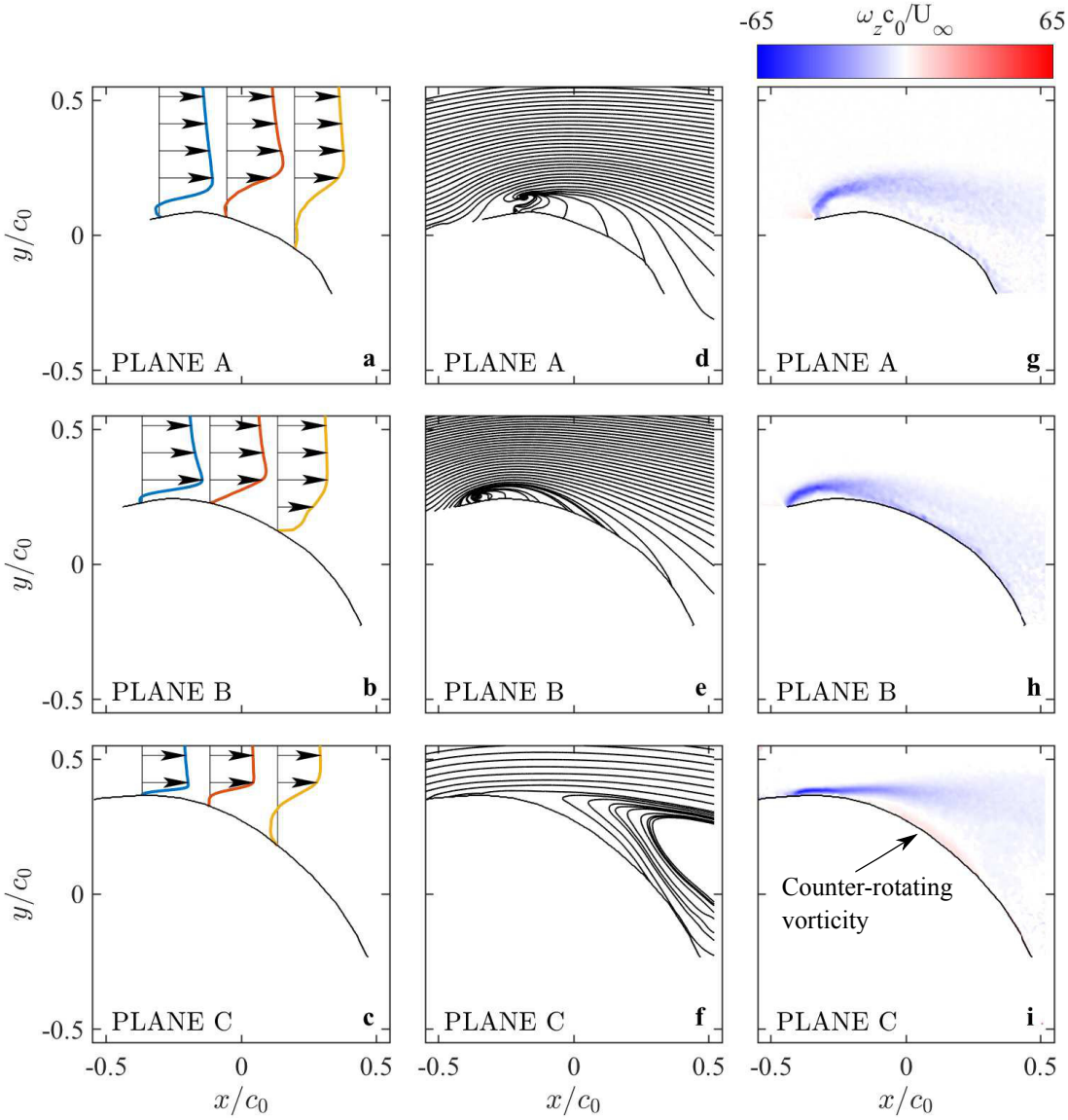

Figure 6.2: Time-averaged velocity profiles (**a, b, c**), streamlines (**d, e, f**) and contours of non-dimensional vorticity (**g, h, i**) on planes A, B and C. Data is averaged over a period $\Delta t^* = 40.736$, in the interval $1 < i < 305$, where i is the number of the PIV image pair

6.2 Sail instantaneous flow field

The γ_2-criterion was used for instantaneous vortex detection, overcoming the sensitivity of the Q-criterion to instantaneous PIV noise. In the time-averaged flow field, both criteria identify a time-averaged LEV in planes A and plane B. Appendix C presents the results and indicates how l/l_0 was set for the γ_1 and γ_2 criteria.

The instantaneous vortex dynamics is investigated using a data set of 305 pairs of images, sampled every $t^* = 0.134$, where time t is non-dimensionalised according to the chordwise convection period c_0/U_∞, such that $t^* \equiv tU_\infty/c_0$. Consider the index i of the pair of images, where $1 < i < 305$.

Mode 1: Stable LEV

Figure 6.3 shows the γ_2 contours for the instantaneous velocity fields on plane B for a period $\Delta t^* = 3.484$ within the interval $16 < i < 42$. A stable LEV which remains attached to the leading edge, can be observed throughout the sequence. The beginning of vortex shedding can be observed towards the end of the sequence. The LEV on this plane is intermittently stable. In particular, it is stable for the sampling periods $1 < i < 65$, $115 < i < 170$ and $264 < i < 305$.

Mode 2: Shedding LEV

Figure 6.4 shows the γ_2 contours for the instantaneous velocity fields on plane A, B and C for a period $\Delta t^* = 1.072$ within the intervals $269 < i < 277$, $195 < i < 203$ and $1 < i < 9$ for planes A, B and C, respectively. The sequences of Fig. 6.4a-i, Fig. 6.4j-r and Fig. 6.4s-aa, represent asynchronous experiments for which the laser sheet location was placed in the corresponding plane. The LEV is not stable and is shed downstream with a convection velocity of approximately $0.6U_\infty$ in plane A and B, and $0.3U_\infty$ in plane C.

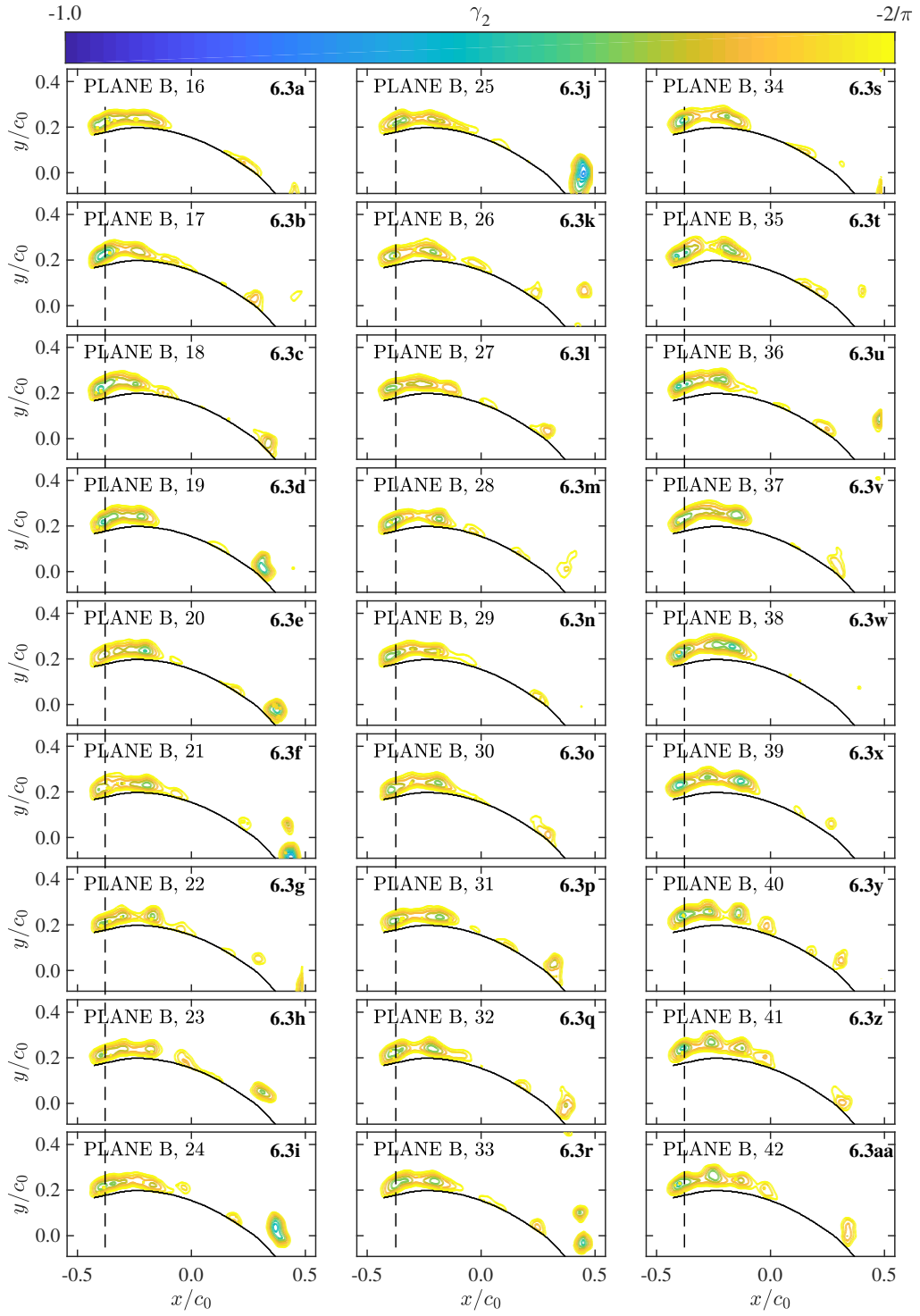

Figure 6.3: Mode 1: Trapped LEV in plane B. Instantaneous velocity fields for plane B. The data show γ_2-contours, for a period of $\Delta t^* = 3.484$, in the interval $16 < i < 42$. The dotted line tracks the LEV in time.

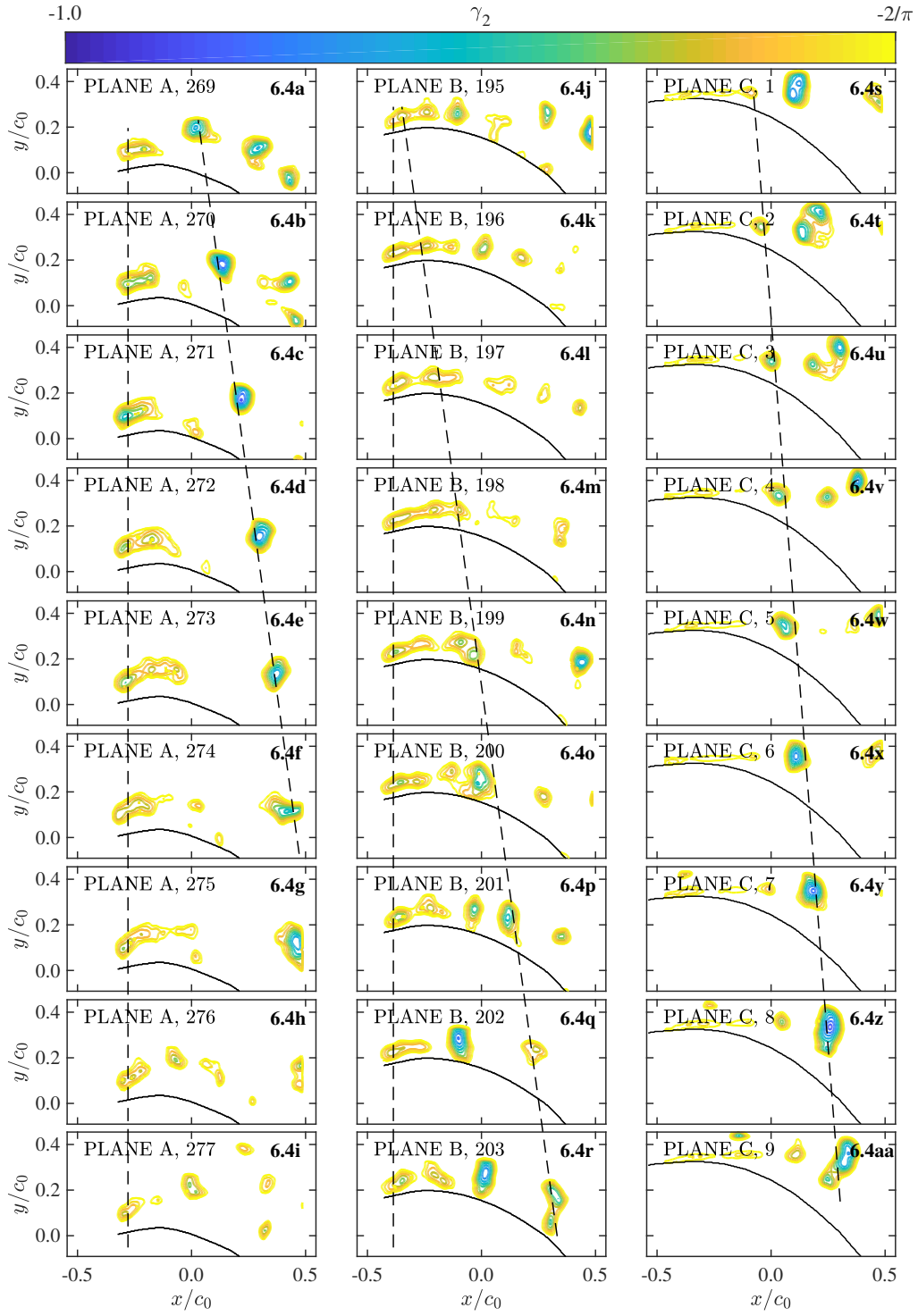

Figure 6.4: Mode 2: Shedding LEVs in planes A, B and C. Instantaneous velocity fields showing vortex shedding for planes A, B and C. The Data show γ_2-contours, for a period of $\Delta t^* = 1.072$, in the intervals $269 < i < 277$, $195 < i < 203$ and $1 < i < 9$ for planes A, B and C, respectively. The dotted line tracks the LEV in time.

Coexistence of the two modes

The vortical structures observed in Fig. 6.3 and 6.4 are the results of Kelvin-Helmholtz instabilities of the vortex sheet generated at the leading edge. This flow field resembles the separated-reattached flow downstream of sharp obstacles (Bradshaw and Wong, 1972) and blunt flat plates (Kiya and Sasaki, 1983; Bradshaw and Wong, 1972; Ota et al., 1981; Stevenson et al., 2016). The coexistence of stationary and unsteady vortices is also observed in other vortex-dominated flows such as, for example, on delta wings. Gad-El-Hak and Blackwelder (1985) were the first to observe experimentally nuclei of unsteady vorticity coexisting with the primary LEV on delta wings. In a later study, Gad-El-Hak and Blackwelder (1987) recognised that these unsteady vortices were due to Kelvin-Helmholtz instabilities of the shear layer. When the LEV is trapped, vorticity is convected through axial flow, similar to a non-slender delta wing.

6.3 LEV structure

Small vorticity concentrations are also observed at the leading edge of non-slender delta wings (Yaniktepe and Rockwell, 2004; Gursul et al., 2005; Muir et al., 2017), which have a sweep angle, more similar to that of a sail. The averaged vorticity of non-slender delta wings shows a dual-vortex substructure system that resembles the elongated vortex structure, near the leading edge of the sail (Fig. 6.3). Yaniktepe and Rockwell (2004) observed that these nuclei of vorticity could be associated either to the fluctuations of the nominally stationary LEV or to instabilities of the shear layer separating from the leading edge. Figure 6.5 shows that a similar multi-structure LEV occurs on yacht sails.

In Sec. 6.2, Mode 1 is defined as a stable LEV that remains attached to the leading edge and Mode 2 as an LEV that sheds. Here, the γ_2 criterion is computed for the time-average flow fields, corresponding to the sequence of Mode 1 of Fig. 6.3(j-r) and Mode 2 of Fig. 6.4(j-r) of plane B, for a period $\Delta t^* = 1.072$. The region near the leading edge is zoomed in to identify the structure of the LEV.

LEV structure of Mode 1:

In Fig. 6.5a, the vortex is trapped at the leading edge and Fig. 6.5b shows that its maximum tangential velocity reaches $u_\theta/U_\infty = 0.48 \pm 0.05$ at $\gamma_2 = -0.75$. The circulation of the LEV is significant and it will be quantified in Chapter 7. The LEV is split into two co-rotating cores, as on a dual LEV (Gursul et al., 2005; Harbig et al., 2013a). Streamwise convection of vorticity does not occur from the dual-core, which remains trapped due to axial flow convecting towards the tip of the sail.

LEV structure of Mode 2:

The LEV breaks down and the time-averaged flow field of Fig. 6.5c appears to contain three sub-cores. Figure 6.5d shows that the maximum tangential velocity reaches $u_\theta/U_\infty = 0.35 \pm 0.05$ at $\gamma_2 = -0.72$. The LEV sheds vorticity downstream, modifying the time-averaged structure from a dual-core to a multiple-core LEV.

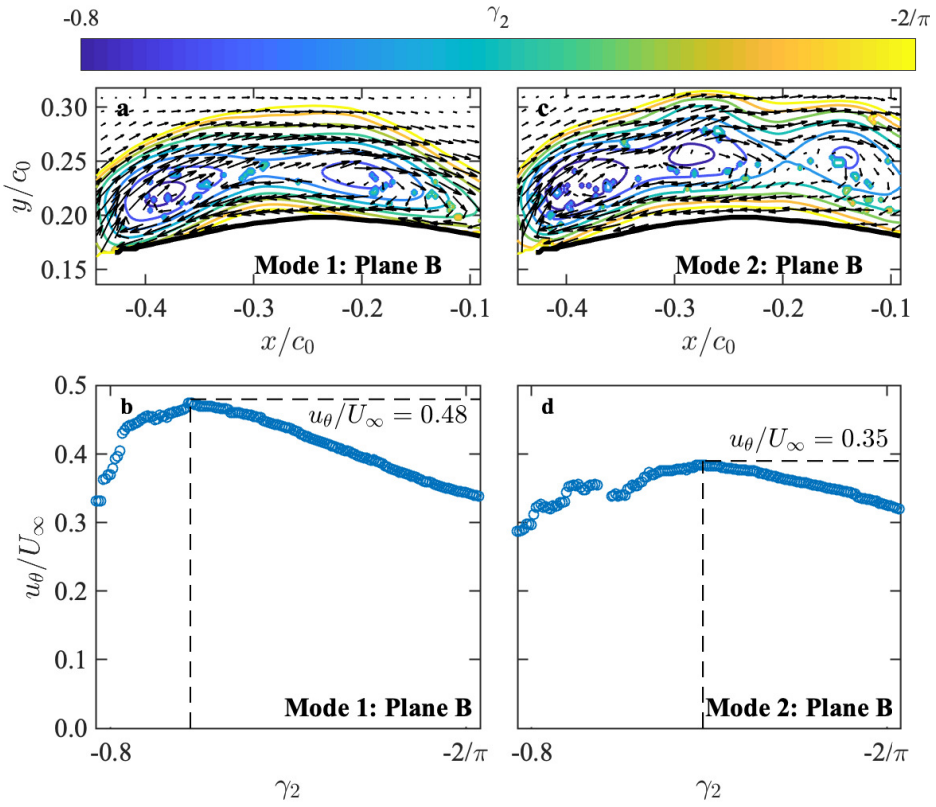

Figure 6.5: Time-average γ_2 contours of Fig. 6.3(j-r) and Fig. 6.4(j-r), corresponding to Mode 1 (trapped vortex) and Mode 2 (shedding vortex) in plane B. The tangential velocity is computed around the γ_2-lines ($-0.8 \leq \gamma_2 \leq -2/\pi$)

6.4 Chapter summary

This Chapter shows, experimental evidence that an LEV occurs in a downwind sail for the first time. PIV image pairs were recorded in three cross-sections of a model-scale spinnaker. Time-averaged analysis and instantaneous vortex detection were carried out. At mid-span of the sail, flow separation occurred downstream of the leading edge and upstream of the mid-chord. At the upper part of the sail, flow separation occurred at the leading edge and reattachment occurred upstream of the mid-chord.

Two modes were found to dominate the flow of the spinnaker in the instantaneous analysis. Mode 1, a stable LEV trapped at the leading edge. Mode 2, a shedding LEV. Mode 1 is found in plane B, where it alternates with Mode 2 for finite periods of time. Mode 2 is found in planes A and C. In plane A, vortex shedding occurs at the leading edge, whereas in plane C, it occurs further downstream, but upstream of the mid-chord. The structure of the stable LEV in Mode 1, is that of a dual-core LEV, similar to the LEV structure of non-slender delta wings at low angles of attack (Yaniktepe and Rockwell, 2004).

An attempt is made in Chapter 7, to model the instantaneous flow fields in Mode 1 (trapped LEV) and Mode 2 (shedding LEV), to assess the contribution of the LEVs to the sectional lift of the sail. A simplification is made and the dual-core LEV is modelled as a single-core LEV, that contains the circulation of the two cores.

Chapter 7

Modelling of the LEV

7.1 Complex potential theory

The physics of flows that separate at the leading edge of thin wings has been captured with two-dimensional inviscid potential models (Pitt Ford and Babinsky, 2013; Xia and Mohseni, 2013). Although the flow around spinnakers is three-dimensional, the relevant physics of their leading edge vortices can be modelled two-dimensionally too, provided that the cross section of the sail is distant from tip vortices and that the spanwise flow is minimal. Such conditions are considered in this Chapter and a potential flow model of a circular arc is developed.

The arc has the same chord c and maximum camber as the section of the sail under consideration and it experiences a uniform flow with the same free stream velocity U_∞, and angle of attack α with respect to the chord. The arc is mapped onto a rotating circular cylinder for ease of analysis. The cylinder is defined in the complex plane ζ, where the complex coordinate

$$\zeta = X + iY \equiv re^{i\theta} \tag{7.1}$$

identifies a position vector in Cartesian coordinates (X,Y) and polar coordinates (r,θ). The velocity potential $\phi = \phi(\zeta)$ and the stream function $\psi = \psi(\zeta)$ are such that the velocity in the X-direction is

$$U = \frac{\partial \phi}{\partial X} \equiv \frac{\partial \psi}{\partial Y}, \tag{7.2}$$

and the velocity in the Y-direction is

$$V = \frac{\partial \phi}{\partial Y} \equiv -\frac{\partial \psi}{\partial X}. \tag{7.3}$$

The complex potential is

$$F(\zeta) \equiv \phi(\zeta) + i\psi(\zeta), \tag{7.4}$$

and the complex velocity in the cylinder plane is

$$W(\zeta) \equiv \frac{\partial F(\zeta)}{\partial \zeta} = U - iV. \tag{7.5}$$

7.2 Circular arc with LEV

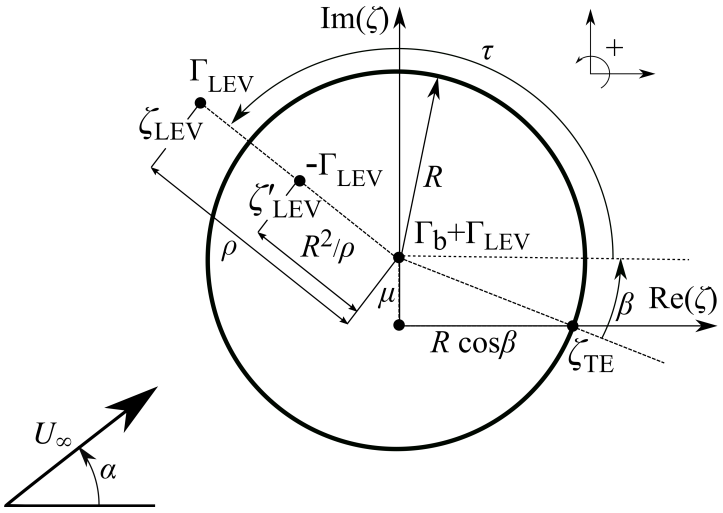

Figure 7.1: Complex potential model of cylinder with circulation and with an external LEV and flow at an angle in the ζ-plane

The complex potential of a rotating cylinder in the ζ-plane is

$$F_0(\zeta) = U_\infty(\zeta - \zeta_0)e^{-i\alpha} + \frac{U_\infty R^2 e^{i\alpha}}{\zeta - \zeta_0} - \frac{i\Gamma_0}{2\pi}\ln(\zeta - \zeta_0), \tag{7.6}$$

where U_∞ is the freestream, R is the radius of the cylinder, α is the incidence angle of U_∞, ζ is the complex variable in the ζ-plane, ζ_0 is the displacement of the cylinder from the origin, Γ_0 is the circulation inside the cylinder. Circulation is defined as positive counter-clockwise. The first term on the right hand side of Eq. 7.6, is the contribution of the free stream, the second term is a doublet and the third term is the circulation in the centre of the cylinder. Here Γ_0 is equal to

$$\Gamma_0 = -4\pi U_\infty R\sin(\alpha + \beta), \tag{7.7}$$

where $\beta = \arctan(4\mu/c)$. For a circular arc of chord c, the cylinder is centred at $\zeta_0 = \mu e^{i\pi/2} = i\mu$ and has a radius $R = c/(4\cos\beta)$. The maximum camber of the circular arc is 2μ (Katz and Plotkin, 2001) and the trailing edge is a stagnation point.

The LEV can be modelled as a free vortex in the ζ-plane and outside the surface of the cylinder. The circulation of the free vortex Γ_{LEV} is computed as explained in Section 7.3. The coordinates of the centre of the LEV, determined with the γ_2 criterion, are used to compute its polar coordinates in terms of ρ and τ in the ζ-plane, as shown in Fig. 7.1 and are given by Eq. 7.8

$$\zeta_{\mathrm{LEV}} = \rho e^{i\tau} + \mu e^{i\pi/2}. \tag{7.8}$$

To retain the impermeable condition of the cylinder surface, a mirror vortex with circulation $-\Gamma_{\mathrm{LEV}}$ must be placed inside of the cylinder at the inverse square point of ζ_{LEV}, given by

$$\zeta'_{\mathrm{LEV}} = \frac{R^2}{\rho} e^{i\tau} + \mu e^{i\pi/2}. \tag{7.9}$$

A circulation Γ_{LEV} is added to the centre of the cylinder to cancel out the mirror vortex circulation. The resulting complex potential is

$$\begin{aligned} F(\zeta) = U_\infty(\zeta - \zeta_0)e^{-i\alpha} + \frac{U_\infty R^2 e^{i\alpha}}{(\zeta - \zeta_0)} - \frac{i(\Gamma_{\mathrm{b}} + \Gamma_{\mathrm{LEV}})}{2\pi} \ln(\zeta - \zeta_0) \\ - \frac{i\Gamma_{\mathrm{LEV}}}{2\pi} \ln \frac{\zeta - \zeta_{\mathrm{LEV}}}{\zeta - \zeta'_{\mathrm{LEV}}}. \end{aligned} \tag{7.10}$$

where the first term on the right is the contribution of the free stream, the second term is the doublet, the third term is the circulation in the centre of the cylinder and the fourth term is the free vortex and its mirror vortex in ζ_{LEV} and ζ'_{LEV}, respectively. Figure 7.1 shows that the total circulation inside the cylinder is Γ_{b}, as the circulation of the mirror vortex $-\Gamma_{\mathrm{LEV}}$ is cancelled by Γ_{LEV}.

Transformations

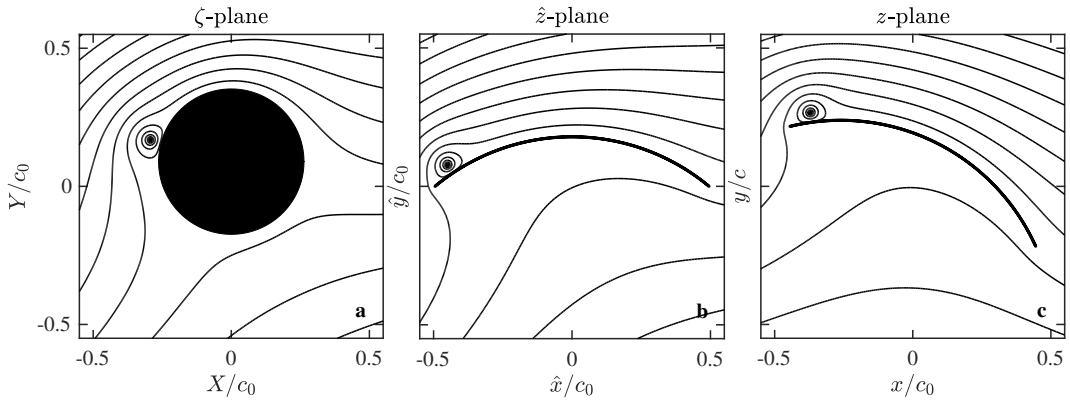

Figure 7.2: Transformations of the ζ- to the $\hat{z}$- and z-planes, for the case of a cylinder with circulation and an external LEV, and flow at an angle

The complex potential in the ζ-plane of the cylinder can be mapped onto the $\hat{z}$-plane of a circular arc with the Joukowski transformation

$$\hat{z} = \zeta + \frac{(R\cos\beta)^2}{\zeta}. \tag{7.11}$$

In the $\hat{z}$-plane, the coordinate system is centred at the middle of the chord, such that the $\hat{x}$-axis is in the direction of the chord and positive toward the trailing edge, and the $\hat{y}$-axis is positive toward the suction side. Finally, a further transformation

$$z = \hat{z}e^{-i\alpha} \tag{7.12}$$

allows a description of the flow field in the flume reference system, where the x-axis is aligned with the free stream velocity U_∞. As shown in Fig. 7.2c.

Velocity fields

The complex velocity in the cylinder plane is given by Eq. 7.13 as

$$W(\zeta) = U - iV = U_\infty e^{-i\alpha} - \frac{U_\infty R^2 e^{i\alpha}}{(\zeta-\zeta_0)^2} - \frac{i(\Gamma_b + \Gamma_{LEV})}{2\pi}\frac{1}{\zeta-\zeta_0} - \frac{i\Gamma_{LEV}}{2\pi}\left[\frac{1}{\zeta-\zeta_{LEV}} - \frac{1}{\zeta-\zeta'_{LEV}}\right]. \tag{7.13}$$

Expressions for the complex velocity in the $\hat{z}$- and the z-planes are obtained with

$$W(\hat{z}) \equiv \frac{\partial F(\zeta)}{\partial \zeta}\frac{\partial \zeta}{\partial \hat{z}} \tag{7.14}$$

and

$$W(z) \equiv \frac{\partial F(\zeta)}{\partial \zeta}\frac{\partial \zeta}{\partial \hat{z}}\frac{\partial \hat{z}}{\partial z}. \tag{7.15}$$

The resultant velocity fields (U, V) for the ζ-, $\hat{z}$- and z-planes are shown in Fig. 7.3

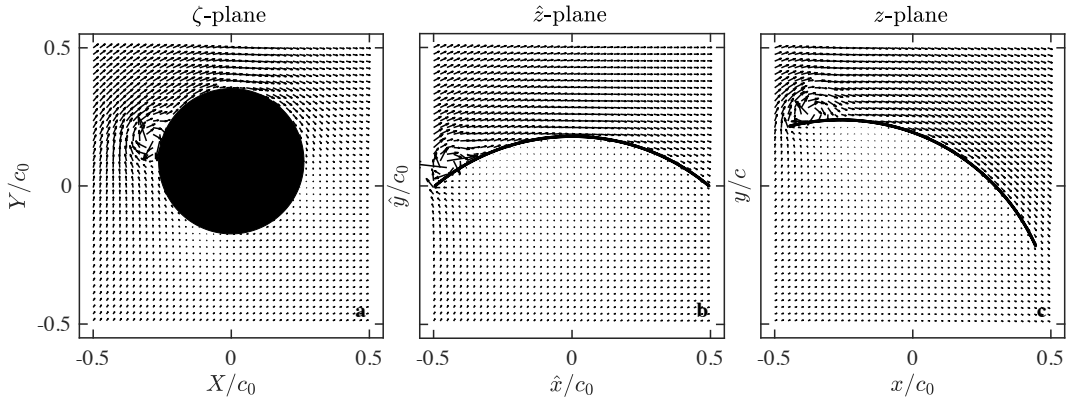

Figure 7.3: Corresponding velocity fields in the ζ-, $\hat{z}$- and z-planes for the cases presented in Fig. 7.2

Circular arc without LEV

A circular arc without external vortices can be modelled with a camber equal to 2μ and making $\Gamma_{\text{LEV}} = 0$. Figure 7.4 shows the modelled streamlines and Fig. 7.5 shows the modelled velocity fields.

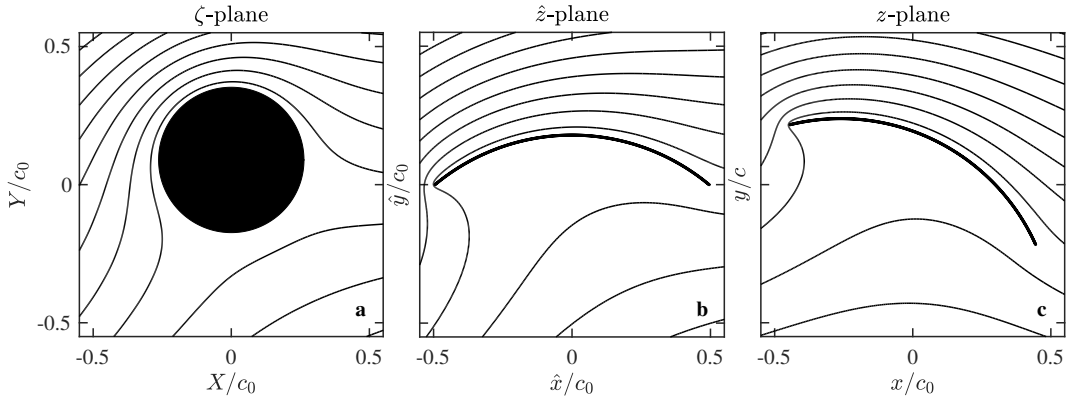

Figure 7.4: Transformations of the ζ- to the $\hat{z}$- and z- planes, for the case of a cylinder with circulation and flow at an angle

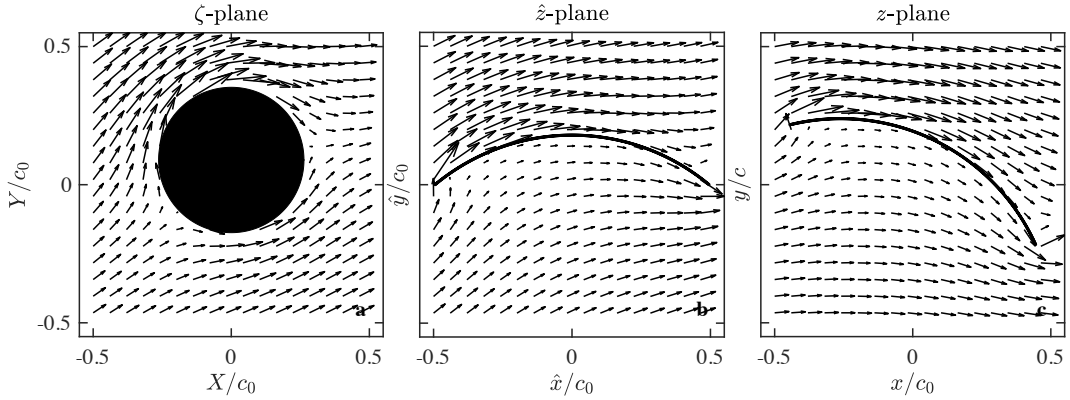

Figure 7.5: Corresponding velocity fields in the ζ-, $\hat{z}$- and z-planes for the cases presented in Fig. 7.4

Flat plate with LEV

By translating the circle to the origin ($\zeta_0 = 0$) and eliminating the camber of the arc ($\beta = 0$), the circle can be mapped onto a flat plate with an external LEV. Figure 7.6 and Fig. 7.7 show the modelled streamlines and velocity fields.

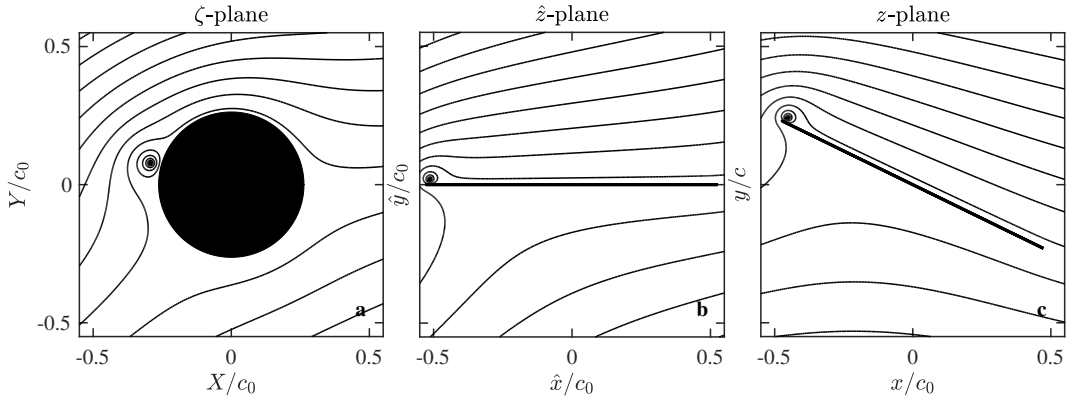

Figure 7.6: Transformations of the ζ- to the $\hat{z}$- and z- planes, for the case of a cylinder centred at the origin ($\zeta_0 = 0$), with circulation, and flow at a prescribed angle

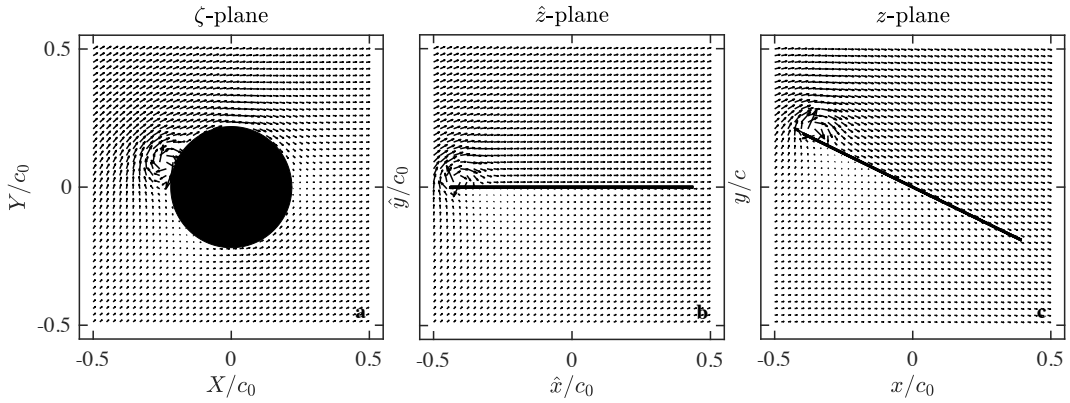

Figure 7.7: Corresponding velocity fields in the ζ-, $\hat{z}$- and z-planes for the cases presented in Fig. 7.6

Multiple vortices

The model can be expanded to multiple vortices shedding from the leading edge and the trailing edge, similar to the works by Pitt Ford and Babinsky (2013) and Xia and Mohseni (2013). Figure 7.8 and Fig. 7.9 show the streamlines and flow fields generated with the model, for six vortices being shed from the leading edge.

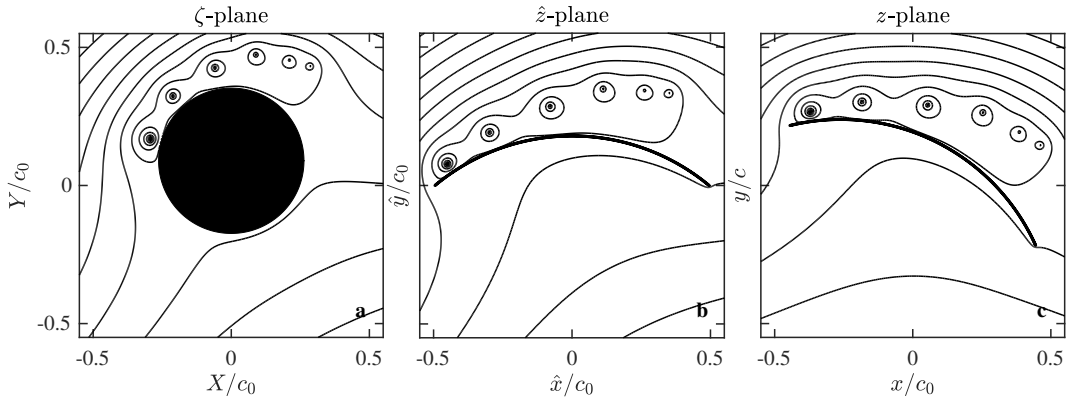

Figure 7.8: Transformations of the ζ- to the $\hat{z}$- and z- planes, for the case of a cylinder, with circulation, with multiple vortices and flow at an angle

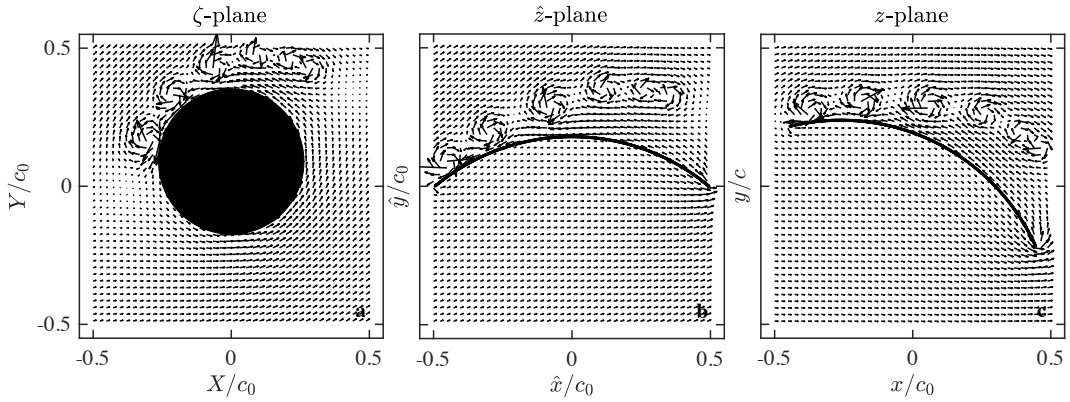

Figure 7.9: Corresponding velocity fields in the ζ-, $\hat{z}$- and z-planes for the cases presented in Fig. 7.8

7.3 Circulatory lift components

Bound circulation

The bound circulation for a circular arc in the absence of external vortices is given by $\Gamma_b = \Gamma_0 = -4R\pi U_\infty \sin(\beta+\alpha)$. To account for the relative position of the LEVs as they convect along the arc, it is possible to compute the Γ_b that satisfies the Kutta condition when multiple LEVs are shed. Figure 7.1 illustrates the cylinder model. The ζ_{TE} coordinate, corresponding to the trailing edge of the circular arc in the $\hat{z}$ plane, must be a stagnation point of the cylinder. Defining $\zeta_{TE} = Re^{-i\beta} + i\mu$, where $\mu = R\sin(\beta)$ and using Eq. (7.13) to evaluate $W(\zeta = \zeta_{TE}) = 0$, it is found (see appendix F), in agreement with Pitt Ford and Babinsky (2013), that

$$\Gamma_b = -4R\pi U_\infty \sin(\beta+\alpha) - \Gamma_{LEV}\left[\frac{2R(R-\rho\cos(\beta+\tau))}{R^2+\rho^2-2R\rho\cos(\beta+\tau)}\right], \tag{7.16}$$

where Γ_{LEV} is the circulation of the LEV and has a value of $\Gamma_{LEV} \leq 0$. The term in brackets is the position factor κ,

$$\kappa = \frac{2R(R-\rho\cos(\beta+\tau))}{R^2+\rho^2-2R\rho\cos(\beta+\tau)}, \tag{7.17}$$

which takes into account the position of the LEV, given by Eq. 7.8. LEVs closer to the leading edge and to the surface of the arc have $\kappa \approx 1$. Equation 7.16 shows that in the scenario where $\kappa = 1$ and $\Gamma_{LEV} = \Gamma_0$, the bound circulation Γ_b is vanished ($\Gamma_b = 0$).

Equation 7.16 is derived for a single LEV with the Kutta condition applied at the trailing edges of a flat plate (Saffman and Sheffield, 1977), a circular arc (Huang and Chow, 1982) and a flat plate with multiple LEVs and TEVs (Pitt Ford and Babinsky, 2013). For multiple LEVs of circulation Γ_i, Eq. 7.16 can be written as

$$\Gamma_b = \Gamma_0 - \sum \kappa_i \Gamma_i, \tag{7.18}$$

where $\Gamma_i \leq 0$, i is an index for each vortex of circulation Γ_i and a position factor κ_i defined as

$$\kappa_i \equiv \frac{2R(R-\rho_i\cos(\beta+\tau_i))}{R^2+\rho_i^2-2R\rho_i\cos(\beta+\tau_i)}. \tag{7.19}$$

This equation is used later to evaluate the relative contribution of the shedding or attached LEVs to the bound circulation of the sail cross-sections.

Effect of LEV in bound circulation

Figure 7.10 shows an LEV located at $\rho/R = 1.15$ and $\tau = 90°$. It also shows a two dimensional contour map of κ, as a function of ρ/R and of τ, in the ζ-plane (Fig. 7.10a) and the z-plane (Figure 7.10b). Recalling that ρ/R is the distance of the free vortex to the centre of the cylinder and τ is the azimuthal position of the vortex, the circular dotted isolines in Fig. 7.10a represent $\rho/R = 2$ and $\rho/R = 3$. The radial dotted lines represent $\tau = 0°, 45°, 90°, 135°, 180°, 225°, 270°$ and $315°$. In Fig. 7.10a, the incidence angle of the flow is $\alpha = 30°$.

The regions where $\kappa = 1$ are the nearest points to the surface of the circular arc. Conversely, κ is negative, at points behind the stagnation point of the trailing edge.

When κ is positive, the presence of the LEV diminishes the bound circulation (Γ_b). The closer the LEV is to the surface of the arc ($\kappa \approx 1$), the more the bound circulation is decreased. Near the trailing edge of the arc, κ becomes negative ($\kappa < 0$). This is the region where the trailing-edge vortex (TEV) occurs. Because the TEV has opposite sign circulation to the LEV, the net effect of the TEV to the bound circulation is also detrimental.

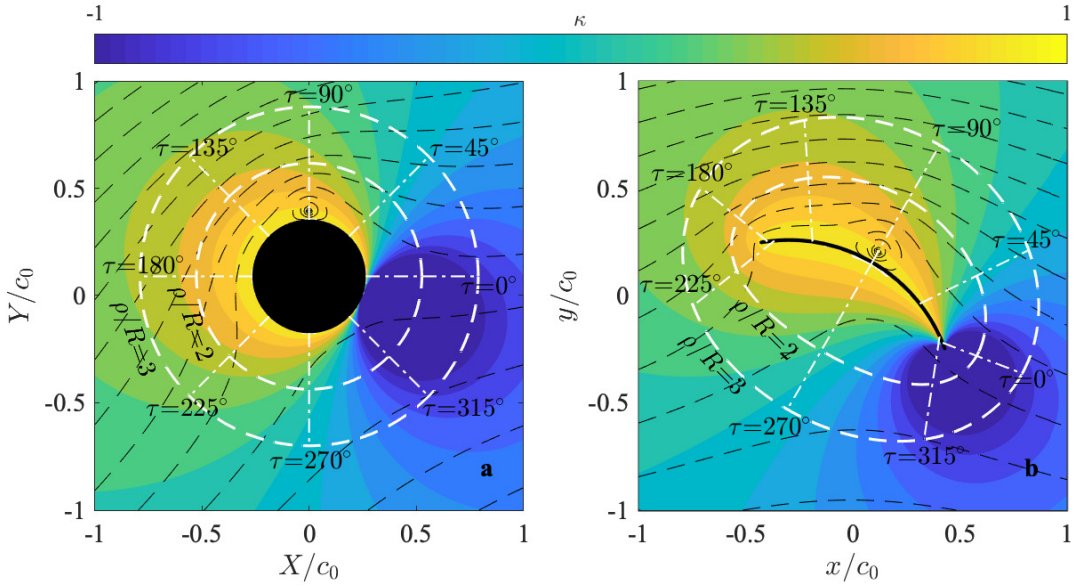

Figure 7.10: a) Coefficient κ as a function of the distance of the LEV to the centre of the cylinder (ρ/R) and of the azimuthal angle τ in the ζ-plane and b) in the z-plane.

LEV circulation

The core radius of an isolated Lamb-Oseen vortex is defined by $|\gamma_2| = 2/\pi$ and is described as the value of $|\gamma_2|$ that corresponds to the maximum tangential velocity of the vortex. However, the edge of the vortex might not coincide with $|\gamma_2| = 2/\pi$ because vorticity is also present outside of the core radius.

Here, low $|\gamma_2|$ values ($|\gamma_2| \leq 0.5$) resulted in large integration paths with unclear distinction between the different nuclei of vorticity due to interference effects or near wall boundaries (Fig. 7.11a). On the other hand, high $|\gamma_2|$ values ($|\gamma_2| \geq 0.8$) did not enable certain vortices to be captured and lost some of the vorticity inside them. The effect of a varying contour size ($0.0 < |\gamma_2| < 0.8$) is shown in Fig. 7.11a and Fig. 7.11b. A proper description of the vorticity field was achieved when $|\gamma_2|$ was close to 0.67, as shown in Fig. 7.11b. This is consistent with values adopted by Pitt Ford and Babinsky (2013) and Eslam Panah et al. (2015).

Therefore, the circulation of the free vortices Γ_i, which are shown in Fig. 7.13, 7.14 and 7.15, could be computed from the measured flow field, as the integral of the tangential velocity over the closed iso-line $\mathbf{l}$ of the γ_2 criterion, where $|\gamma_2| = 0.67$, such that:

$$\Gamma_i = \oint_{|\gamma_2|=0.67} \mathbf{u} \cdot \mathrm{d}\mathbf{l}, \tag{7.20}$$

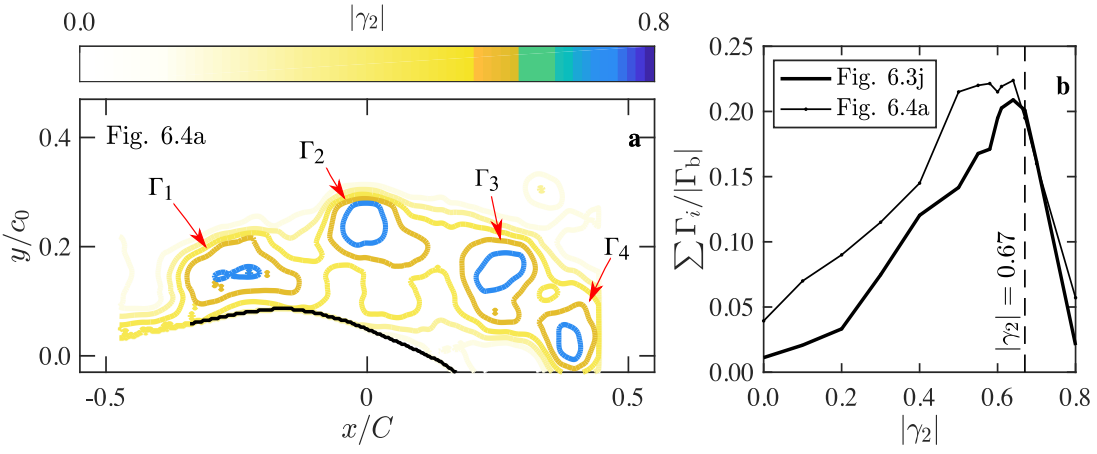

Figure 7.11: a) γ_2 contours of Fig. 6.4a, showing the contours detected by $0.0 < |\gamma_2| < 0.8$ b) Sum of circulation of free vortices $\sum\Gamma_i/|\Gamma_b|$ from Fig. 6.3j and Fig. 6.4a calculated with iso-contour values $0.0 < |\gamma_2| < 0.8$

However, Eq. 7.20 does not account for vorticity that lies outside of the vortex core. For example, integrating along the core of an isolated Lamb-Oseen vortex would yield about 65% of its full circulation. A correction was therefore applied to the circulation computation, to include the vorticity that lied outside the core of the vortex. This was done by fitting the experimental circulation values to the theoretical circulation of a Lamb-Oseen vortex, given by

$$\Gamma = \Gamma_{LO}\left(1 - \exp\left(-\frac{r^2}{l_0^2}\right)\right). \tag{7.21}$$

As shown in Fig. 7.12, $|\gamma_2| = 0.80$ corresponds to a circular contour with $r/l_o = 1.0$ around an ideal Lamb-Oseen vortex. However, to include all of the vorticity of the vortex, it was necessary to integrate over the contour $\gamma_2 = 0.10$ corresponding to $r/l_o = 2.0$. Because the contour $\gamma_2 = 0.10$ was not available in the experimental data (due to proximity to the wall, interference of other vortices, shear layers), a methodology similar to that proposed by Morgan et al. (2009) was followed to estimate the circulation left outside of the iso-contour $\gamma_2 = 0.67$. The circulation of the experimental vortices was computed integrating over different and available γ_2 contours between 0.6 and 0.8, and then these circulations were fitted with those of an ideal Lamb-Oseen vortex (Eq. 7.21).

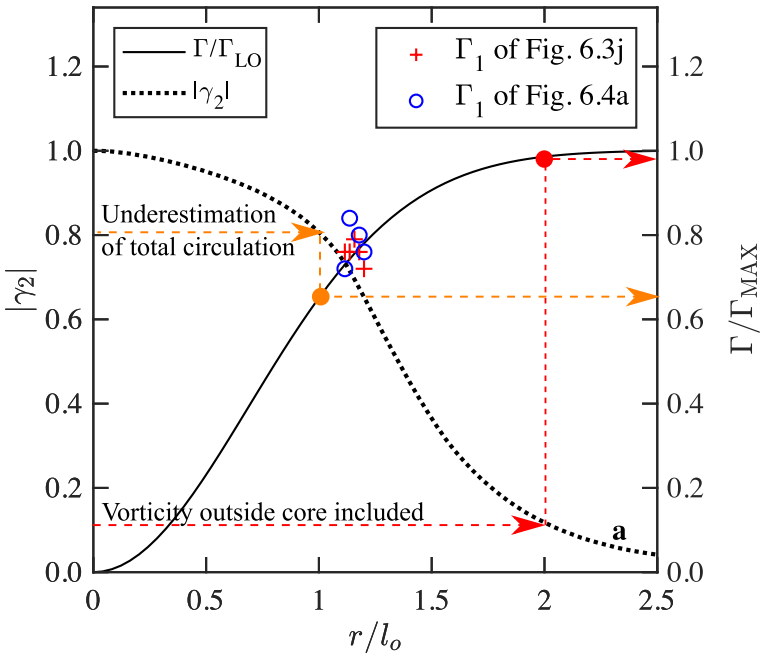

Figure 7.12: Fitting experimental circulations of the first LEV (Γ_1) of Fig. 6.3j and Fig. 6.4a to a Lamb-Oseen vortex

The fitting was performed using a least square method, allowing the total circulation of the vortex to be quantified. It was found that the total circulation was 35% higher than that computed with $\gamma_2 = 0.67$. Therefore, the integrated circulation of each vortex was multiplied by a factor of 1.35. The fitting was achieved using Eq. 7.22, similar to Morgan et al. (2009) and the results are shown in Fig. 7.12. Here, R_{fit} is defined as

$$R_{fit} = 1 - \frac{\sum(\Gamma_{i,j} - \Gamma_{\mathrm{LO},j})^2}{\sum \Gamma_{i,j}^2}, \tag{7.22}$$

where

$$\Gamma_{i,j} = \frac{\Gamma_i|_{|\gamma_2|=a_j}}{\Gamma_{\mathrm{MAX},i}} \tag{7.23}$$

and

$$\Gamma_{\mathrm{LO},j} = \left(\frac{\Gamma}{\Gamma_{\mathrm{LO}}}\right)\Bigg|_{|\gamma_2|=a_j}. \tag{7.24}$$

In Eq. 7.23, $\Gamma_i|_{|\gamma_2|=a_j}$ is the circulation of the i-th vortex computed around a integration contour equal to $|\gamma_2| = a_j$, whereas $\Gamma_{\mathrm{MAX},i}$ is the maximum circulation of the same i-th vortex. This value was iterated until a fit of $R_{fit} = 0.99$ was achieved.

In Eq. 7.24, $(\Gamma/\Gamma_{\mathrm{LO}})|_{|\gamma_2|=a_j}$ is the ratio between the circulation of the Lamb-Oseen vortex (Γ) and its maximum circulation (Γ_{LO}), that corresponds to an integration contour equal to $|\gamma_2| = a_j$. For example, for $a_j = 0.8$, $(\Gamma/\Gamma_{\mathrm{LO}})|_{|\gamma_2|=a_j} = 0.63$, as shown in Fig. 7.12. Table 7.1 shows a_j, $\Gamma_{\mathrm{LO},j}$ and $\Gamma_{i,j}$ for the i-th vortex of Fig. 6.3j and Fig. 6.4a, where $i = 1$.

Table 7.1: Input data to compute R_{fit} for the i-th vortex of Fig. 6.3j and Fig. 6.4a, where $i = 1$

Free Vortex	i	j	a_j	$\Gamma_{\mathrm{LO},j}$	$\Gamma_{i,j}$
Γ_1 of Fig. 6.3j	1	1	0.67	0.73	0.76
	1	2	0.64	0.74	0.76
	1	3	0.62	0.75	0.79
	1	4	0.61	0.76	0.76
	1	5	0.60	0.77	0.72
Γ_1 of Fig. 6.4a	1	1	0.67	0.73	0.72
	1	2	0.64	0.74	0.84
	1	3	0.61	0.76	0.80
	1	4	0.60	0.77	0.76

The standard deviation of the fit was used to estimate the error in the computed circulation. Therefore, the error in the circulation (ε_Γ) is estimated to be $\varepsilon_\Gamma < 0.05$.

7.4 Application of the model

Contribution of LEV circulation to sectional lift

Assuming the steady-state bound circulation of a circular arc (Γ_0) and using Eq. 7.18, derived with the Kutta condition, the lift coefficient for the circular arc in the presence of multiple LEVs can be written as

$$C_{L_0} = -\frac{\Gamma_0}{\frac{1}{2}U_\infty c} = -\frac{\Gamma_b + \sum \kappa_i \Gamma_i}{\frac{1}{2}U_\infty c}. \tag{7.25}$$

The expression can be split into the lift coefficient contribution due to Γ_b

$$C_{L_b} = -\frac{\Gamma_b}{\frac{1}{2}U_\infty c} \tag{7.26}$$

and the lift coefficient contribution due to the LEVs

$$C_{L_{LEV}} = -\frac{\sum \kappa_i \Gamma_i}{\frac{1}{2}U_\infty c}. \tag{7.27}$$

One of the underlying questions that this work aims to address is the effective contribution of the LEV to the sail performance. Using Eq. 7.25 and Eq. 7.27, the contribution of the circulation of the LEVs can be assessed, through the ratio $C_{L_{LEV}}/C_{L_0} = \sum \kappa_i \Gamma_i / \Gamma_0$. A first conservative estimate is made based on the Kutta condition being satisfied when the LEV is present. Given that trailing edge separation actually occurs and the Kutta condition is not satisfied, the computed relative contribution of the LEV is conservative.

To quantify the LEV contribution to the sectional lift, three examples are studied: the stable LEV on plane B in Fig. 6.3(j-r), the shedding LEV on the same plane in Fig. 6.4(j-r) and the shedding LEV on plane A in Fig. 6.4(a-i).

To calculate the κ values of the free vortices, artificial velocity flow fields were generated with the complex potential model to generate γ_2-contours that match the experimental contours. The velocity fields and γ_2-contours of the artificial flow fields are presented in the second and third columns of Fig. 7.13, 7.14 and 7.15, respectively. The first column represents the γ_2-contours of the experimental measurements.

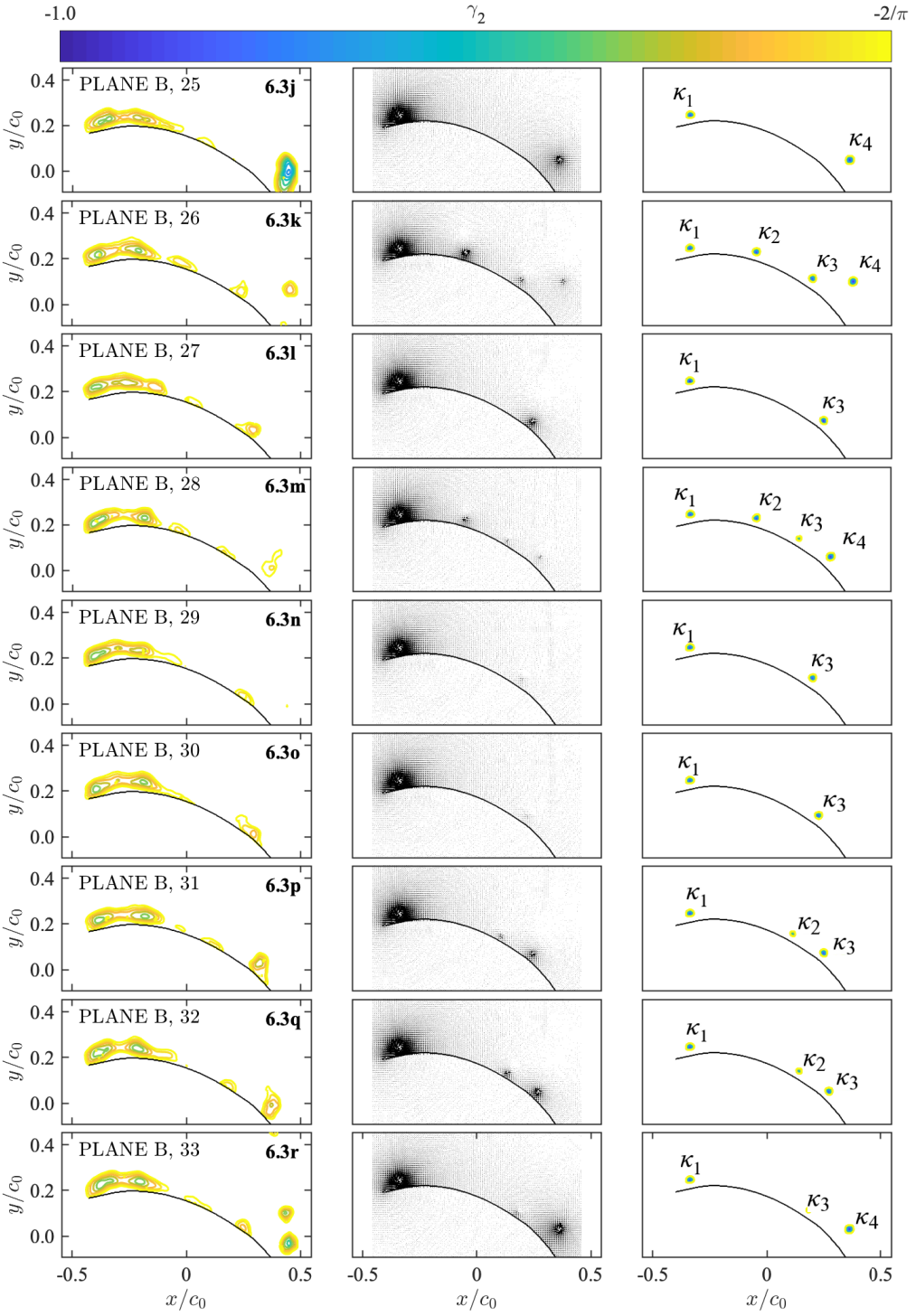

Figure 7.13: γ_2 criterion for instantaneous velocity fields exhibiting the presence of a stable LEV for the sequence of plane B, Fig. (**6.3j**-**6.3r**), with corresponding velocity fields from the model and γ_2-contours resulting from the model. Data correspond to a period of $\Delta t^* = 1.072$, in the interval $25 < i < 33$

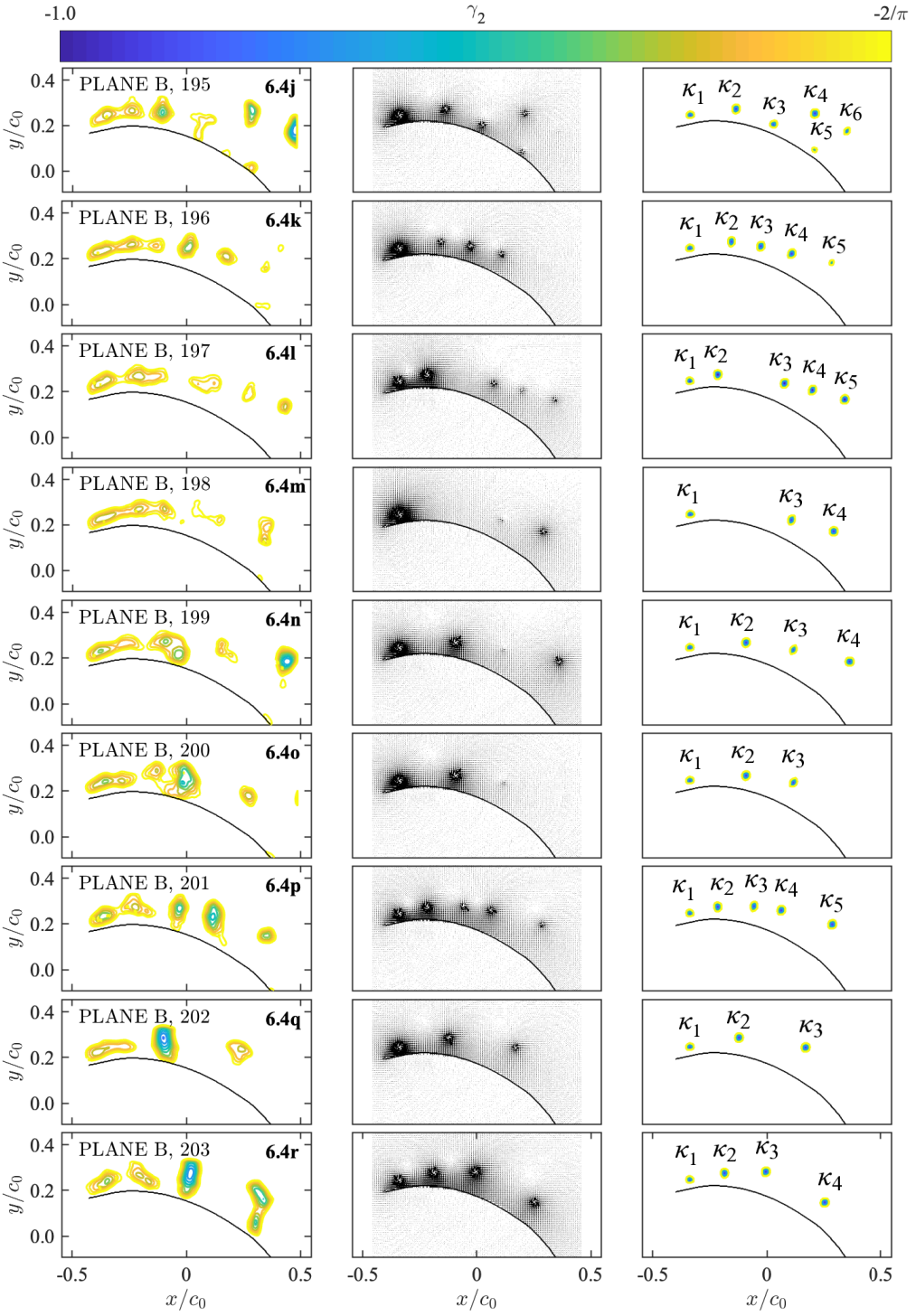

Figure 7.14: γ_2 criterion for instantaneous velocity fields exhibiting a shedding LEV for the sequence of plane B, Fig. (**6.4j**-**6.4r**), with corresponding velocity fields from the model and γ_2-contours resulting from the model. Data correspond to a period of $\Delta t^* = 1.072$, in the interval $195 < i < 203$

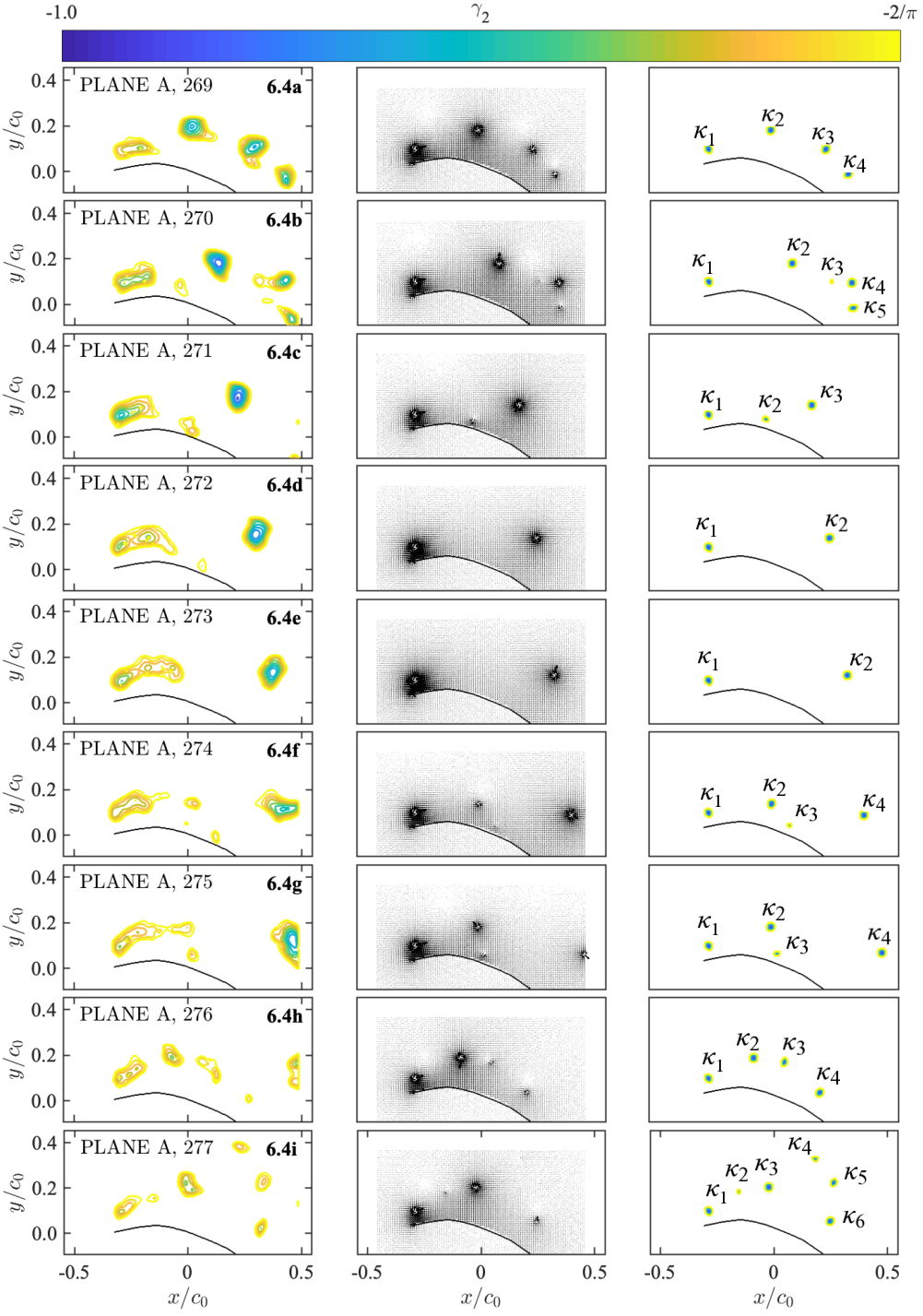

Figure 7.15: γ_2 criterion for instantaneous velocity fields exhibiting the presence of a shedding LEV for the sequence of plane A, Fig. (**6.4a**-**6.4i**), with corresponding velocity fields from the model and γ_2-contours resulting from the model. Data correspond to a period of $\Delta t^* = 1.072$, in the interval $269 < i < 277$

Circulation around each Γ_i measured from the experimental data was input for the model used to calculate Γ_b. Circulation values were computed with the methodology explained in this Chapter, in the subsection LEV circulation. The values are included in Appendix D and correspond to each of the vortices labelled in Fig. 7.13, 7.14 and 7.15. Here Γ_b was calculated with Eq. 7.18. Γ_0 was used to normalise the results. Figure 7.16a shows the ratio $\sum \kappa\Gamma_i/\Gamma_0$ for the sequences of Fig. 7.13, 7.14 and 7.15.

In most of the cases examined, the total contribution of the vortex circulation to the sail's circulation lies between 10% and 20% of the effective bound circulation (Γ_0). At every instant, the contribution of the vortex circulation is higher in plane B, than in plane A and the discrepancy between the results from different planes is larger than the variations between different instants on the same plane.

The time-averaged contribution of the vortex circulation ($\overline{\sum_{a,j}^{i,r} \kappa_i\Gamma_i}$) is presented in Fig. 7.16b for the same cases as in Fig. 7.16a. Here, it is clear that the presence of a stable LEV, as opposed to a series of shedding vortices, provides only a marginally higher averaged circulation.

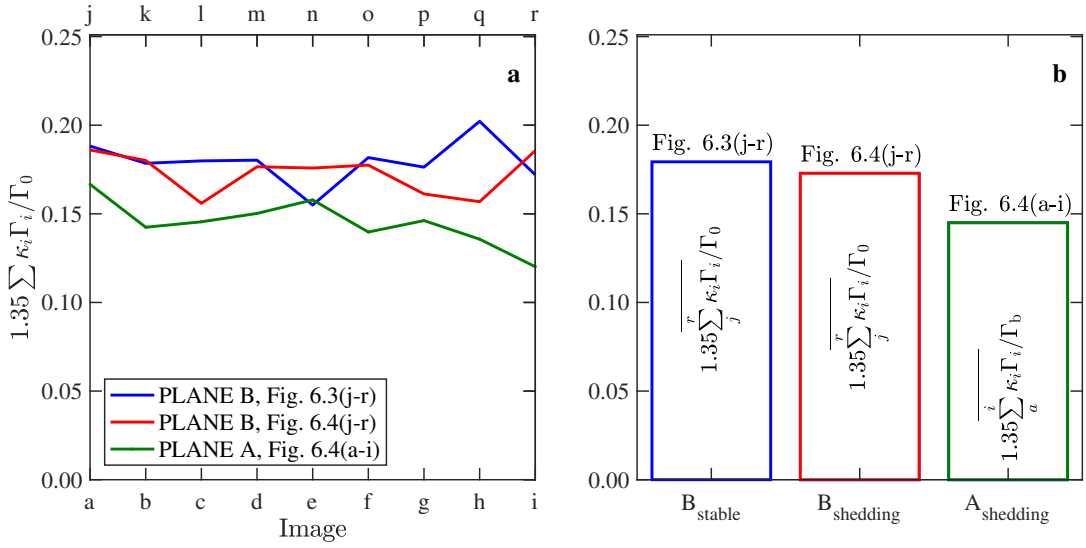

Figure 7.16: a Instantaneous sum of circulation $1.35\sum \kappa_i\Gamma_i/\Gamma_0$ of the free vortices in Fig. 6.3(j-r), 6.4(j-r) and Fig. 6.4(a-i), integrated along $|\gamma_2| = 0.67$. **b** Average circulation for the three cases presented in Fig. 7.16b

Effect of bound circulation value

Figure 7.17 shows the effect of altering the value of Γ_b on the curvature of the streamlines of the complex potential model. The sequences of Fig. 6.4(a-i) and Fig. 6.3(j-r) are taken for planes A and B, respectively. The experimental flow field is taken from the average of these flow fields.

An average bound circulation ($\overline{\Gamma_b}$) is calculated with Eq. 7.18 for plane A and plane B, with the sequences of Fig. 6.4(a-i) and Fig. 6.3(j-r), respectively. The time-averaged flow fields are modelled without any free vortices and by considering that the circulation of the cylinder is $\overline{\Gamma_b} + \overline{\sum \Gamma_i}$, where $\overline{\sum \Gamma_i}$ is the average of the sum of the circulation of the free vortices of Fig. 6.4(a-i) and Fig. 6.3(j-r). The circulation of these free vortices is included in Appendix D.

Figures 7.17a, 7.17c and 7.17e present the experimental time-averaged streamlines of the sequence of Fig. 6.4(a-i) and the modelled flow field of plane A for three cases $1.0\overline{\Gamma_b}$, $0.8\overline{\Gamma_b}$, $0.6\overline{\Gamma_b}$. Figures 7.17b, 7.17d and 7.17f present the experimental time-averaged streamlines of the sequence of Fig. 6.3(j-r) and the modelled flow field of plane B for $0.5\overline{\Gamma_b}$, $0.3\overline{\Gamma_b}$, $0.1\overline{\Gamma_b}$.

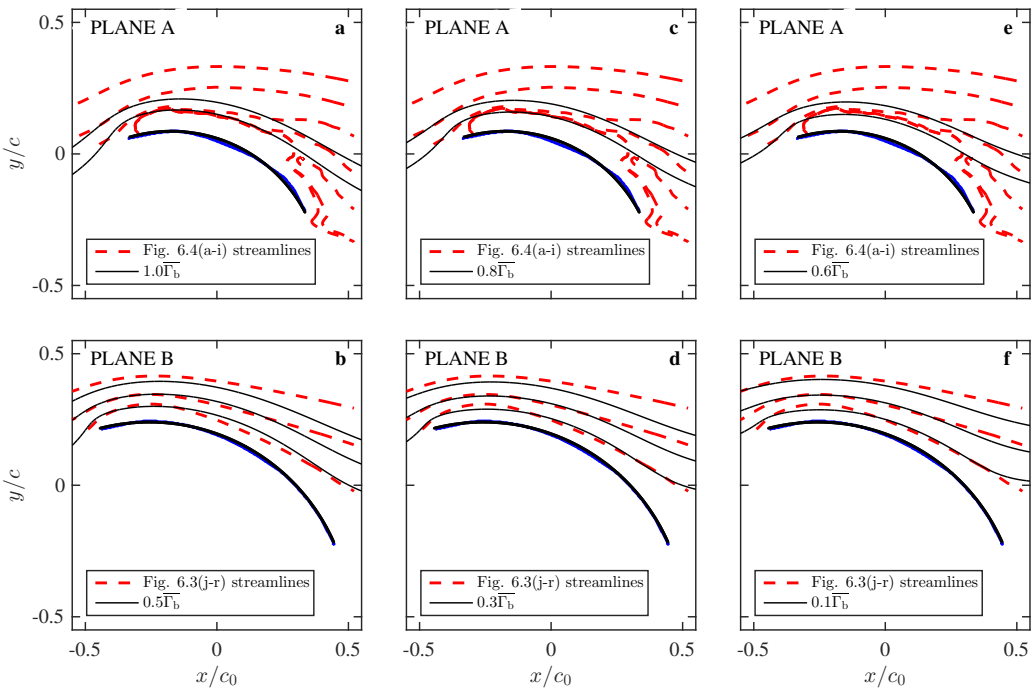

Figure 7.17: Theoretical and experimental streamlines for plane A and plane B, with decreasing value of bound circulation

It should be noted that plane A was approximated solely by the first streamline, whereas plane B was approximated by both the first and second streamlines. The best match for the first streamline in plane A was obtained for a value of $0.8\overline{\Gamma_b}$, whereas for plane B the best match for the first and second streamlines was obtained for a value of $0.3\overline{\Gamma_b}$.

This comparison approach was not suitable for spinnaker geometries, especially close to the tip, where three-dimensional effects are important. However, by carrying out this streamline curvature analysis, it can be inferred that the Kutta condition overestimates the bound circulation value around the cross-section of the sail. This highlights the importance of the contribution of the LEV to the sectional lift.

7.5 Limitations of the model

The present model is two-dimensional and so only applies to the particular PIV measurement plane that is being analysed. This approach neglects out-of-plane momentum fluxes, viscous effects (including trailing edge separation) and unsteady effects. The model accounts only for the strongest nuclei of vorticity included in the PIV window. Once the vortices have been shed downstream, they are no longer included. Here, it is assumed that the main contribution to the effective bound circulation is due to the strong nuclei of vorticity near the arc and thus it is reasonable to neglect the contribution from shed leading-edge and trailing-edge vorticity.

7.6 Chapter summary

This Chapter introduces a complex potential model, for a circular arc, to quantify the contribution of the LEV to the sectional lift of the sail. The Kutta condition is applied to the trailing edge of the circular arc and a bound circulation value is calculated. The bound circulation is a function of the circulation and the position of the LEV. The circulation of the LEV is measured from the experimental flow fields and is used as an input to the complex potential model. The contribution of the LEV to the sectional lift of the top sections of the sail is quantified and it is calculated as the ratio between the LEVs measured circulation and the effective bound circulation (Γ_0). It is found that the LEV contributes between 10% to 20% of the sail's sectional lift. This does not mean that the LEV increases the sectional lift, but instead that it provides a portion of the sectional lift. This is a conservative estimate since the calculated bound circulation is higher than the actual bound circulation value, due to the Kutta condition assumption.

Chapter 8

Different twist spinnakers Forces and PIV analysis

Three sails were manufactured with different twist, in order to explore the effect of twist in the context of sail aerodynamics. Force component and flow field measurements were carried out. Figure 8.1 shows the three sails tested and the corresponding PIV measurement planes. Geometry S_1 provides the maximum driving force and its near wake is analysed. The influence of twist is further studied, by observing the flow at the vicinity of the leading edge and at the maximum-driving-force angle of each sail. Low and high twist effects are characterised by means of time-averaged streamlines, γ_2 and vorticity contours of planes A, B and C. Chordwise convection of vorticity is measured at the leading edges, mid-chords and trailing edges of planes A, B and C of the three geometries to observe the effect of either axial flow or annihilation.

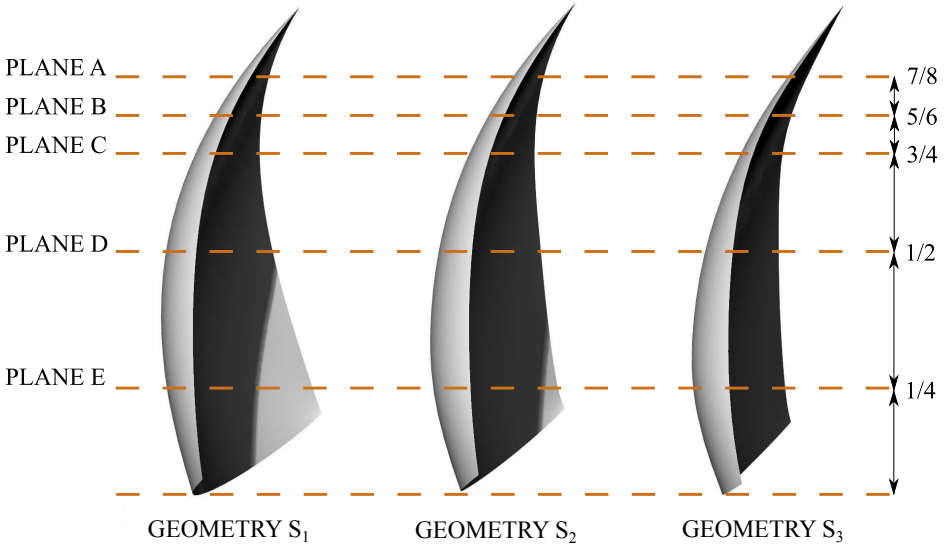

Figure 8.1: Geometries S_1, S_2, and S_3 with high, intermediate and low twist, respectively. Planes A, B, C, D and E are the PIV measurement planes

8.1 Force measurements

Lift (L) and drag (D) force components were measured for the spinnakers S_1, S_2 and S_3, which were manufactured with different twist. The force components were recorded for a range of rotational angles $-30^\circ < \eta < 30^\circ$, where $\eta = 0^\circ$ is the maximum-driving-force rotational angle. Blockage effects due to streamline curvature, wake, and solid bodies were corrected following the methods presented by Pope and Harper (1966) (See Eq.4.7 and Eq. 4.10 in Chapter 4). The lift and drag coefficients (C_L, C_D) were calculated using Eq. 4.12 and by using the corresponding forces. The driving force coefficient (C_{DF}) and the side force coefficient (C_{SF}) on the sails were calculated assuming an optimum apparent wind angle of $\beta_{a_{\mathrm{OPT}}} = 55^\circ$, such that

$$C_{DF} = C_L \sin(\beta_{a_{\mathrm{OPT}}}) - C_D \cos(\beta_{a_{\mathrm{OPT}}}) \tag{8.1}$$

and

$$C_{SF} = C_L \cos(\beta_{a_{\mathrm{OPT}}}) + C_D \sin(\beta_{a_{\mathrm{OPT}}}). \tag{8.2}$$

Figure 8.2 shows the force components on S_1, S_2 and S_3, which correspond to high, intermediate and low twist. Figure 8.2a shows C_L and C_D, and the theoretical lift curve slope ($\partial C_L / \partial \eta$) for a finite aspect ratio wing (AR = 1.5) and for small angles of attack. Figure 8.2b shows C_{SF} against C_{DF}. Figure 8.2c shows the C_L/C_D ratio. Figure 8.2d shows C_L^2 against C_D, which is a useful representation to highlight the induced drag, defined by

$$C_{D,i} = \frac{C_L^2}{\pi AR}, \tag{8.3}$$

where AR is the aspect ratio of the wing. The forces of the three sails show remarkable similarities, despite the very significant difference in the geometry (the twist of the three sails varies from about 2° to 13°). The horizontal position of these curves is set, such that the maximum C_{DF} of each curve is at $\eta = 0^\circ$. This is carried out by rotating sails S_1, S_2 and S_3 around their vertical axis, as explained in the positioning subsection of Chapter 3. However, also at much higher and lower η, the forces do not differ significantly. As discussed in Section 8.4, at $\eta = 0^\circ$, the section at about 1/3rd of the sail span has the same angle of attack for the three sails. Therefore, the three sails show the same behaviour when they experience the same angle of attack at a section near their centre of effort.

The highest maximum lift force coefficient ($C_{L,\max}$) is identified by a red square in the lift-coefficient-curve of S_3 in Fig. 8.2a. The highest maximum driving force ($C_{DF,\max}$)

is identified by a black dot in the driving-against-lateral-force-curve of S_1 in Fig. 8.2b. The highest maximum lift to drag ratio ($C_L/C_{D,\max}$) is identified by a black rhombus in the lift-to-drag-ratio-curve of S_1 in Fig. 8.2c. The markers are displayed in all of the subplots of Fig. 8.2, in order to track their position in the different curves.

Higher C_L and C_D are attained with low twist (S_3). On the contrary, lower C_L and C_D are attained with high twist (S_1). Maximum C_{DF} is achieved with S_1 and minimum with S_3. Recalling that geometries S_2 and S_3 aim to verify that the optimal angle of attack distribution along the span was lower than the one of S_1, these results suggest that S_1 is effectively a good optimal candidate. The characteristics of S_1 provide the highest $C_{DF,\max}$ and $C_L/C_{D,\max}$, and its near wake is now studied.

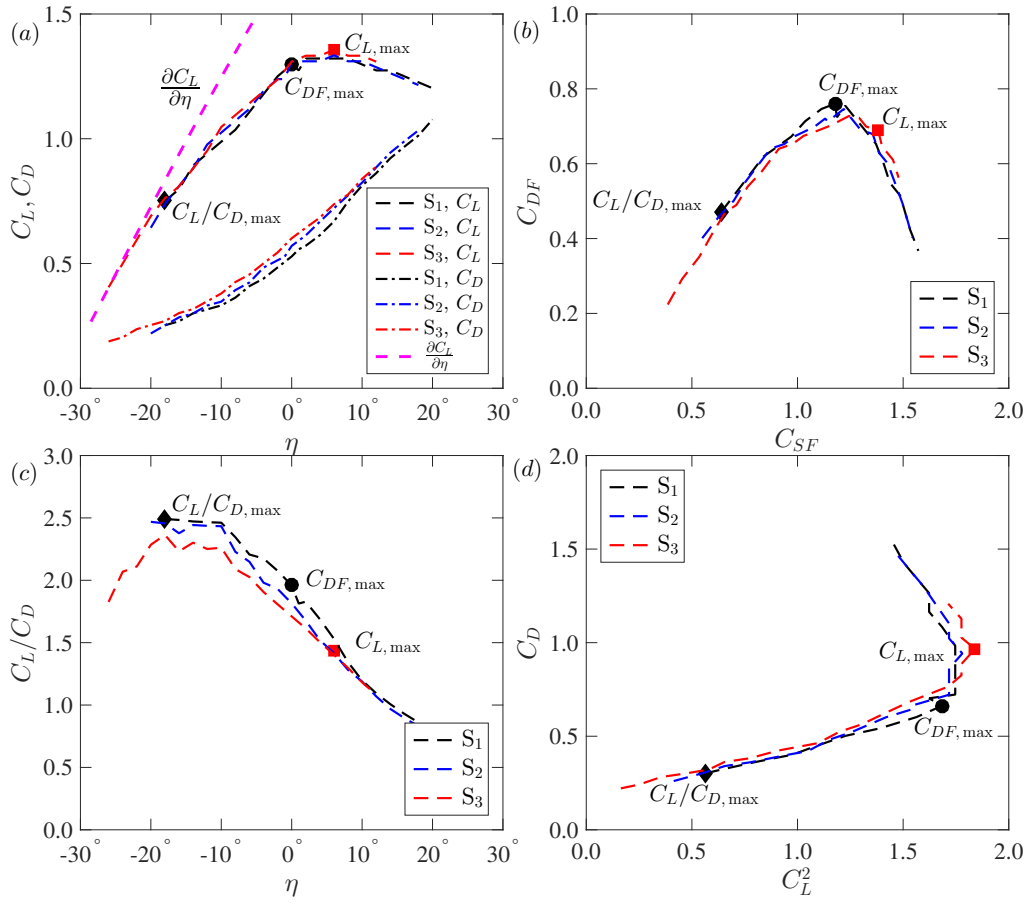

Figure 8.2: Force plots of spinnakers S_1, S_2 and S_3 with high, intermediate and low twist, respectively. Points of maximum C_L/C_D (♦), maximum C_{DF} (●) and maximum C_L (■) are identified.

8.2 Near wake of a high twist sail

Averaged flow field

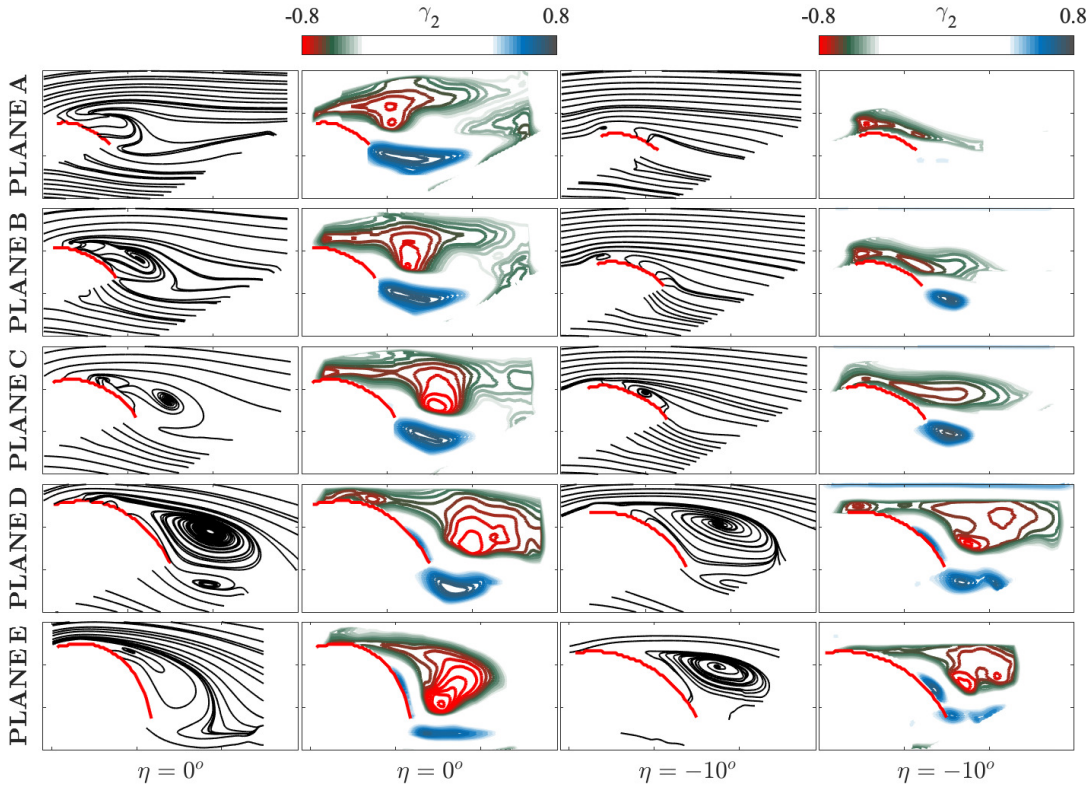

Figure 8.3: Time-averaged near wake streamlines and γ_2-contours of geometry S_1 at $\eta = 0°$ and $\eta = -10°$, where $\eta = 0°$ is the angle of $C_{DF,\max}$. PIV measurement planes A, B, C, D and E, along the span of the sail.

The near wake region is studied for geometry S_1, which provided the highest $C_{DF,\max}$. Averaged streamlines and γ_2-contours are presented for two incidence angles, $\eta = 0°$ and $\eta = -10°$. The sail trim that allows maximum C_{DF} ($\eta = 0°$) is likely to be optimal in low wind speed conditions. Conversely, in strong wind conditions, the optimal trim is the one that allows lower C_{SF} and hence C_{DF}. Hence, there is a condition in strong wind, not known a priori, such that the optimal trim is $\eta = -10°$. Such rotational angle of the sail ($\eta = -10°$) will reduce the side force (C_{SF}) in strong winds and prevent a capsize. Flow fields are presented for 5 PIV measurement planes, which correspond to planes A, B, C, D and E. The streamline patterns of Fig. 8.3 reveal that the flow is highly three dimensional. A time-averaged leading edge vortex (LEV_{av}) appears in the streamlines of planes A, B, C, D and E at $\eta = 0°$. At $\eta = -10°$, an LEV_{av} is present in planes D and E. The γ_2-contours are able to identify a circulation dipole in all the planes at $\eta = 0°$, with a pole emerging from the leading edge and a second pole from

the trailing edge. These types of dipoles have been observed at the midspan of different aspect ratio flat plates at high incidence by DeVoria and Mohseni (2017). Figure 8.4 shows a comparison of the time-averaged flow fields of Sail S_1 at $\eta = 0°$, with the time-averaged streamlines and normalised vorticity results of DeVoria and Mohseni (2017) for a flat plate of aspect ratio AR = 1.5 and AR = 2 at $\alpha = 20°, 25°, 30°, 35°$ and $40°$.

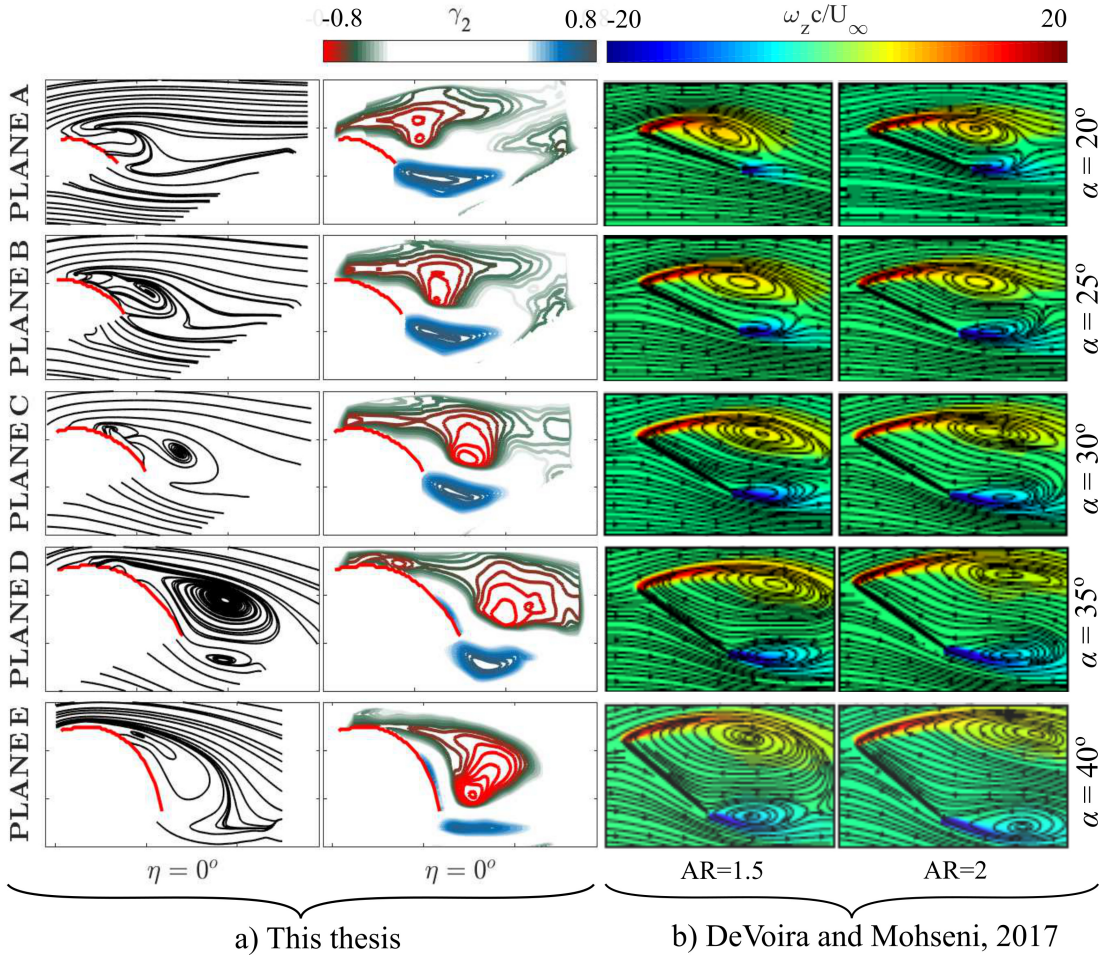

Figure 8.4: a) Time-averaged streamlines and γ_2 contours for planes A, B, C, D and E of Sail S_1 at $\eta = 0°$, b) Time-averaged streamlines and non-dimensional vorticity adapted from DeVoria and Mohseni (2017), at mid-span of flat plates of AR = 1.5 and 2 and at $\alpha = 20°, 25°, 30°, 35°$ and $40°$

Figure 8.3 shows that at $\eta = 0°$, the highest sections of the sail (planes A, B and C) are stalled and have a large trailing edge wake. At $\eta = -10°$, the top sections present less separation and the trailing edge wake shrinks in size. The bottom sections (planes D and E) are stalled at both angles of attack. However at $\eta = 0°$, the curvature of the streamlines and the γ_2-contours is higher than at $\eta = -10°$. This could mean that at

$\eta = 0°$, the circulation of the time-averaged LEV has increased at the bottom sections.

To verify this, the circulation around leading and trailing edge γ_2-contours is quantified. Figure 8.5 quantifies the circulation of the leading edge and trailing edge vortices, delimited by the γ_2-isolines of Fig. 8.3. Results are presented for planes A, B, C and D, for $\eta = 0°$ and $\eta = -10°$. The leading edge circulation grows from $\eta = -10°$ to $\eta = 0°$. This is most evident in planes C and D. At the leading edge, a spanwise drop of circulation occurs from plane D to plane A. This does not occur at the trailing edge, where circulation increases with increasing angle of attack, but remains constant across planes. The circulation of the trailing edge region increases to counteract the effect of the circulation of the leading edge region at high angles of attack. This circulation behaviour has been also observed for flat plates by DeVoria and Mohseni (2017).

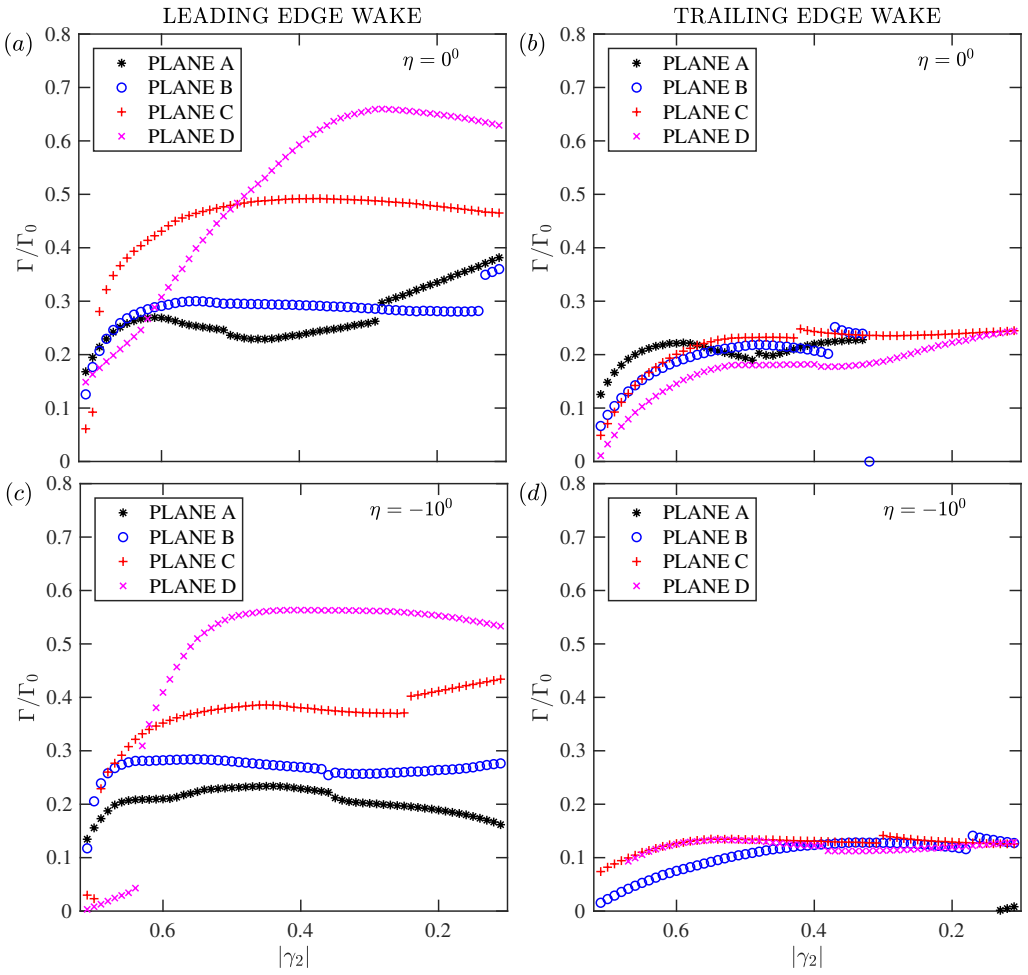

Figure 8.5: Circulation of the time-averaged $|\gamma_2|$-contours of the leading and trailing edges of sail S_1 at two incidence angles, $\eta = 0°$ and $\eta = -10°$. Measurements correspond to planes A, B, C and D.

Instantaneous flow field

A sequence of instantaneous γ_2-contours is plotted for the wakes seen in Fig. 8.3. The flow fields correspond to planes A, B, C, D and E of geometry S_1, at two angles of attack $\eta = 0^\circ$ and $\eta = -10^\circ$. In the vicinity of the trailing edge, the train of leading edge vortices (LEVs) is not in contact with the train of trailing edge vortices (TEVs) in all the planes and at both angles of attack. The size of the LEVs is similar in planes C, D and E for $\eta = 0^\circ$ and $\eta = -10^\circ$. However, for the top planes A and B, the size of LEVs decreases with a decreasing angle of attack ($\eta = -10^\circ$). The convection velocity of the LEVs increases towards the top planes (A, B and C) for the two angles of attack.

Figure 8.6: Instantaneous sequence of γ_2-contours for planes A, B, C and D of sail S_1 at two incidence angles, $\eta = 0^\circ$ and $\eta = -10^\circ$

8.3 Flow field of three different twist model sails

Averaged flow fields

Figure 8.7 shows the effect of adjusting η with respect to the apparent wind (V_A). PIV experimental time-averaged streamlines are presented at the leading edge region of planes A, C and D. Planes A and C correspond to the top of the sail, whereas plane D corresponds to its mid-span. Three values of η were tested to characterise the flow in the vicinity of the leading edge of geometries S_1, S_2 and S_3. The three values of η are those corresponding to the angles of maximum lift to drag ratio ($\eta_{L/D}$), maximum driving force (η_{MD}) and maximum lift (η_L). The columns in Fig. 8.7 relate to the geometries S_1, S_2, and S_3 and the rows to $\eta_{L/D}$, η_{MD}, η_L.

At $\eta_{L/D}$, the flow at the top of S_1, S_2 and S_3 remains mostly attached, as shown by the streamlines of planes A and C. At η_{MD}, the flow exhibits a swirl in planes A and C. At this angle of attack, the flow at the leading edge resembles the time-averaged streamlines of a flat plate at high incidence (Perry and Steiner, 1987; DeVoria and Mohseni, 2017). At η_L, the flow of planes A and C changes to complete stall. In plane D, high separation occurs at the three angles of attack and the flow is not altered significantly by twist. Although topologically the flow behaves similarly for the three sails at the three angles of attack, the swirl of planes A and C at η_{MD} can reveal more qualitative and quantitative information about the effect of twist in sails. In the following paragraphs, the flow conditions at the top of the sails is explored at η_{MD}. Planes A, B and C are studied to understand the effects of twist in the flow around spinnakers.

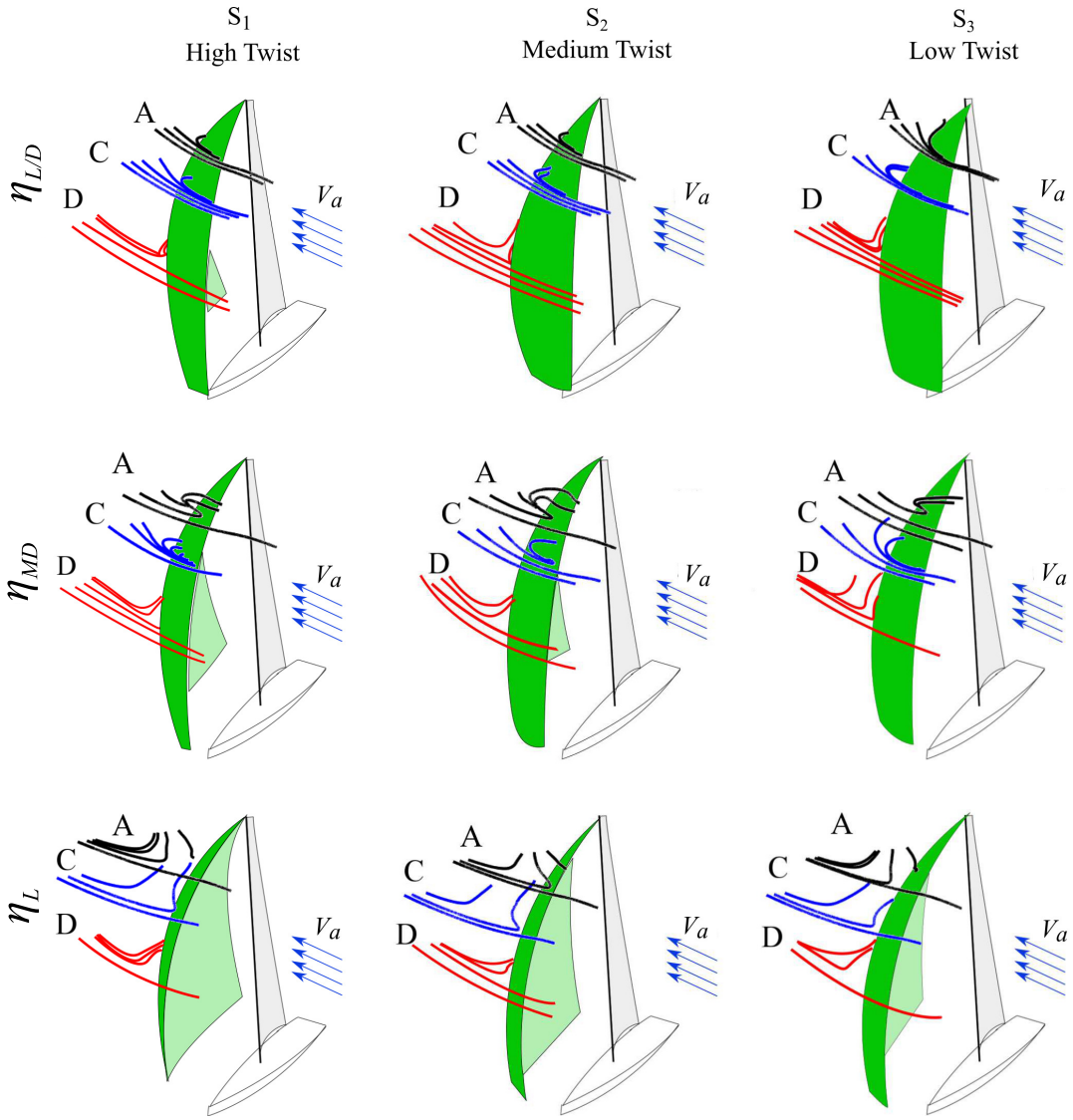

Figure 8.7: Streamlines of leading edge averaged flow fields for spinnakers S_1, S_2, and S_3 (High Twist, Medium Twist, Low Twist) at $\eta_{L/D}$, η_{MD}, and η_L

8.4 Twist effect at maximum-driving-force angle

Figure 8.8 shows the PIV raw images for sails S_1, S_2 and S_3 at η_{MD}. Twist was measured between planes C and A ($\delta_{C_iA_i}$) and D and A ($\delta_{D_iA_i}$), as the angle difference between α_{X_i} and α_{A_i}, where X is plane C or plane D and i refers to the geometry index $i = 1$, 2 and 3.

Laser sheet reflection was used to project a circular arc over planes A, B, C and D. The angle of attack of each plane was measured as the angle between the horizontal plane and the chord of each arc. Table 8.1 lists the measured α_{A_i}, α_{B_i}, α_{C_i}, α_{D_i}. $\delta_{D_iA_i}$ and

$\delta_{C_iA_i}$ values. From Table 8.1, $\delta_{D_1A_1}$ and $\delta_{D_2A_2}$ are higher than $\delta_{D_3A_3}$, which confirms that S_1 and S_2 have higher twist than S_3.

Here α_{C_i} the reference angle with $\alpha_{C_1} = 25°$, $\alpha_{C_2} = 28°$ and $\alpha_{C_3} = 29°$. For the subsequent analysis the positions of geometries S_2 and S_3 are directly compared, due to the minimum difference between α_{C_2} and α_{C_3}. S_1 is used to confirm the flow behaviour observed for S_2, which corresponds to a geometry with twist.

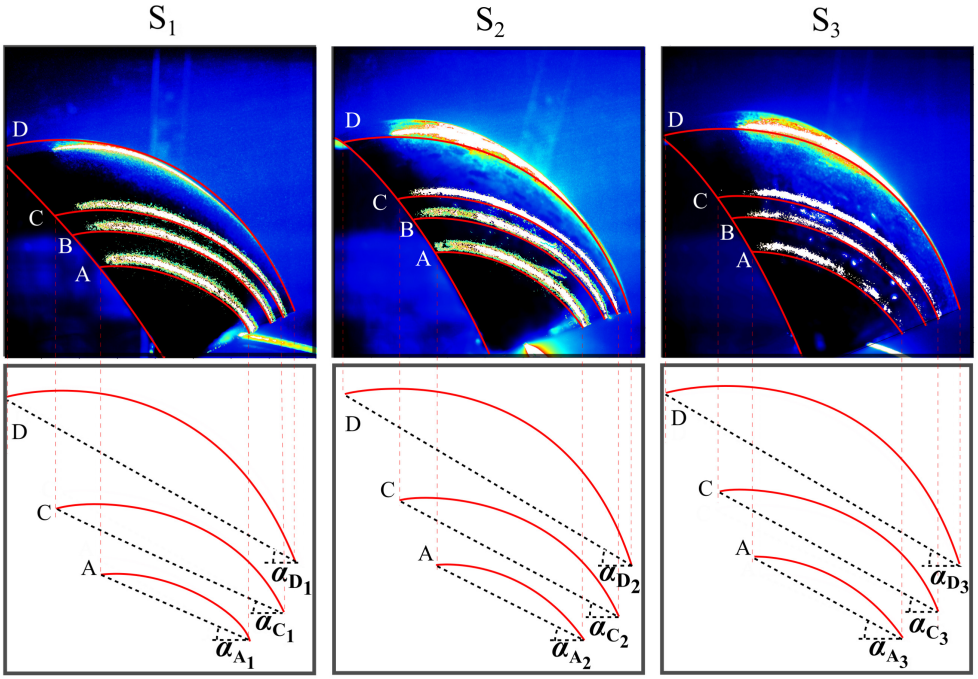

Figure 8.8: Twist measurement for the S_1, S_2 and S_3 geometries

Table 8.1: Measurements of α_{A_i}, α_{B_i}, α_{C_i}, α_{D_i}, $\delta_{C_iA_i}$ and $\delta_{D_iA_i}$ for geometries S_1, S_2 and S_3, where i corresponds to the index of the geometry

Angle	S_1, High Twist	S_2, Medium Twist	S_3, Low Twist
α_{A_i}	$24° \pm 1°$	$27° \pm 1°$	$29° \pm 1°$
α_{B_i}	$24° \pm 1°$	$27° \pm 1°$	$29° \pm 1°$
α_{C_i}	$25° \pm 1°$	$28° \pm 1°$	$29° \pm 1°$
α_{D_i}	$28° \pm 2°$	$31° \pm 2°$	$31° \pm 2°$
α_{E_i}	$37° \pm 2°$	$34° \pm 2°$	$31° \pm 2°$
$\delta_{\alpha_{D_iA_i}}$	4°	4°	2°
$\delta_{\alpha_{C_iA_i}}$	1°	1°	0°

Time averaged streamlines

Figure 8.9 shows the averaged streamlines of planes A, B and C for geometries S_1, S_2 and S_3 at η_{MD}. The flow is highly three dimensional, as evidenced by the foci and the bifurcation lines, following the pictionary definitions given by Perry and Steiner (1987). S_3 shows higher circulation than S_2 and S_1, due to the high curvature of the streamlines in planes B and C. The high curvature of the streamlines shows that S_3 generates the highest sectional lift for planes B and C.

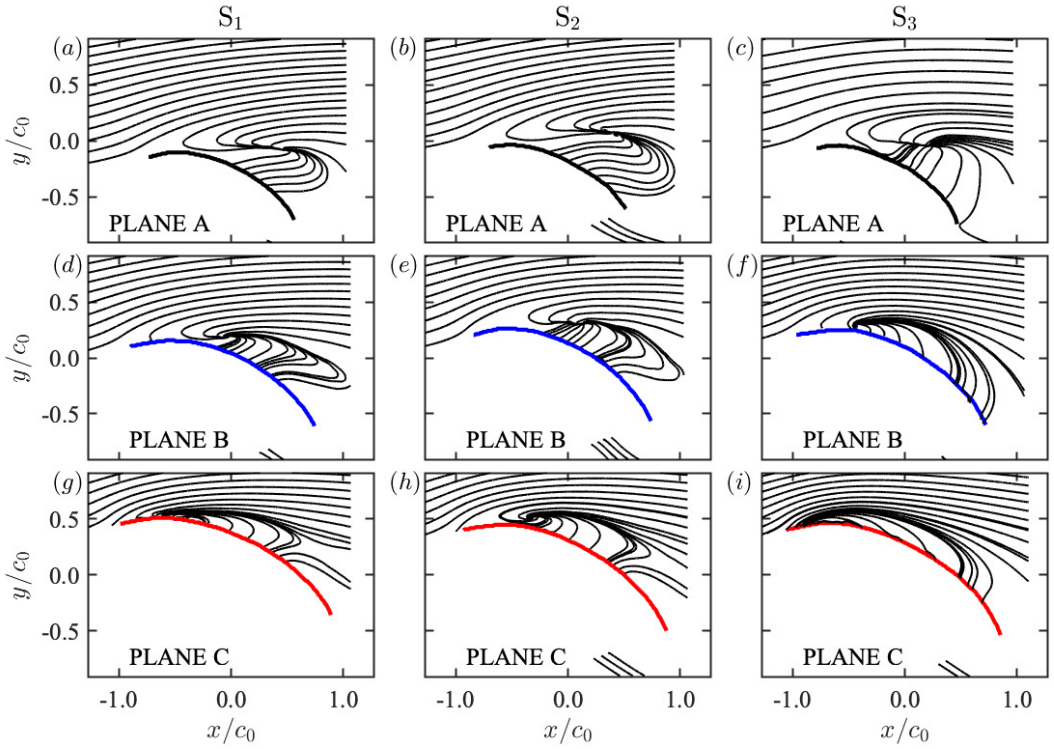

Figure 8.9: Time-averaged streamlines for planes A, B and C for S_1, S_2 and S_3 at the maximum-driving-force angle, η_{MD}

Time averaged γ_2-contours

Figure 8.10 shows the time-averaged γ_2-contours in the vicinity of the leading edge of S_1, S_2 and S_3 at η_{MD}. The γ_2-contours are highly curved in S_3 and they remain in close proximity to the surface of the sail. This is mostly notable in planes B and C. For S_1 and S_2, the γ_2-contours are straight and more distant from the surface of the sail, as shown in planes B and C. Recalling that geometries S_1 and S_2 have higher twist than S_3, the wake pinches off due to twist, because the high angles of attack of planes D and C with respect to planes B and A induce flow separation midspan of the sail.

The γ_2-contours highlight another interesting feature, which is the coherence of a rotating structure in S_3. This hints towards ejection of vorticity in the direction of the tip of the sail. The coherence of the structure is lost in S_1 and S_2, where regions of opposite-signed rotation appear on the surface of the sail. It could be possible in these cases, that two different mechanisms to control the vorticity within the core of the LEV occur for low and high twist. For high twist (S_1, S_2), annihilation could modulate the streamwise convection of vorticity, whereas for low twist (S_3), axial flow could be the dominant factor.

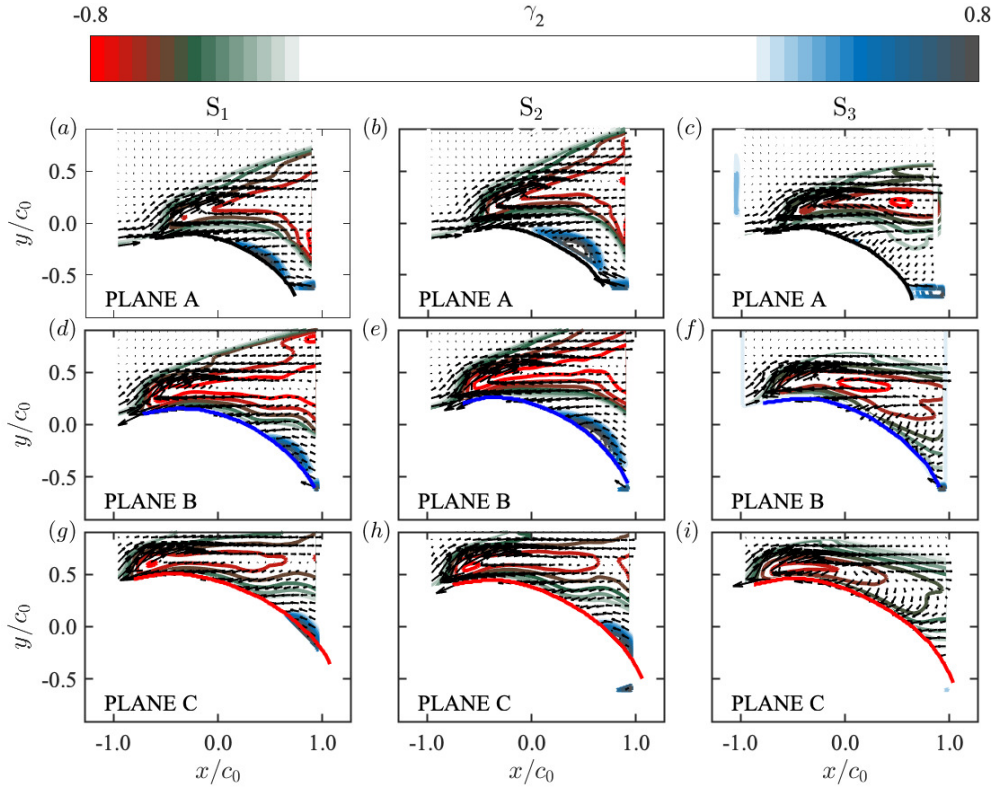

Figure 8.10: γ_2-contours for planes A, B and C for S_1, S_2 and S_3 at the maximum-driving-force angle, η_{MD}

Time averaged vorticity

Figure 8.11 shows the time-averaged vorticity fields in the vicinity of the leading edge of S_1, S_2 and S_3 at η_{MD}. Negative vorticity originates at the leading edge of the three spinnakers in planes A, B and C. Positive vorticity originates on the surface of S_1 and S_2 in planes A, B and C. Positive vorticity regions do not appear in S_3, being prevented by the proximity of the layer of vorticity to the surface of the sail. On the contrary, regions of positive vorticity do appear in S_1 and S_2. From Chapter 4, vorticity uncertainty is $|\omega_z c_0/U_\infty| \leq 5$. Here, the magnitude of the positive vorticity regions is $\omega_z c_0/U_\infty \geq 8$. The regions of positive vorticity are also observed by the γ_2-criterion in Fig. 8.10 and they are similar to the secondary vorticity of non-slender delta wings (Muir et al., 2017). Through twist and by drifting away, the region of negative vorticity permits positive vorticity regions to emerge on the surface of the sail, as shown in Fig. 8.11a, d, g and Fig. 8.11b, e and h. Chordwise convection of vorticity is calculated along the three semi-infinite lines L_1, L_2 and L_3 that extend from the surface of the sail and along the y-direction. The x-coordinates for L_1, L_2 and L_3 are provided by the leading edge, mid-chord and the trailing edge of each of the images in Fig. 8.11. Chordwise convection of vorticity is defined for every L_i as

$$\omega_{z,u_x} = \int_{L_i} u_x \omega_z dy. \tag{8.4}$$

The maximum magnitude of chordwise convection of vorticity increases from S_1 to S_3. Because S_1 and S_2 contain positive regions of vorticity on the surface of the sail, chordwise convection of vorticity is lower than in S_3, where positive vorticity regions do not occur. The generation of positive vorticity on the surface of the sail reduces the circulation around the section of the sail and lift decreases, consequently the induced drag decreases. Positive regions of circulation are observed also with γ_2-contours in S_1 and S_2 in Fig. 8.10.

The three sails experience a drop of chordwise convection of vorticity from leading edge to trailing edge. This drop is a result either of annihilation or ejection of vorticity towards the tip of the sail through axial flow. Because the results show regions of positive vorticity in S_1 and S_2, annihilation might be the dominant effect in geometries with large twist. Conversely, axial flow is likely to be the dominant factor in low twist geometries. Low twist (S_3) does not have opposite signed vorticity on the surface of the sail and instead shows strong coherence between γ_2-contours, which is a sign of consistency between planes. A coherent structure across spanwise planes is an

indication of a LEV that concentrates vorticity at its core and ejects it along its axis through axial flow.

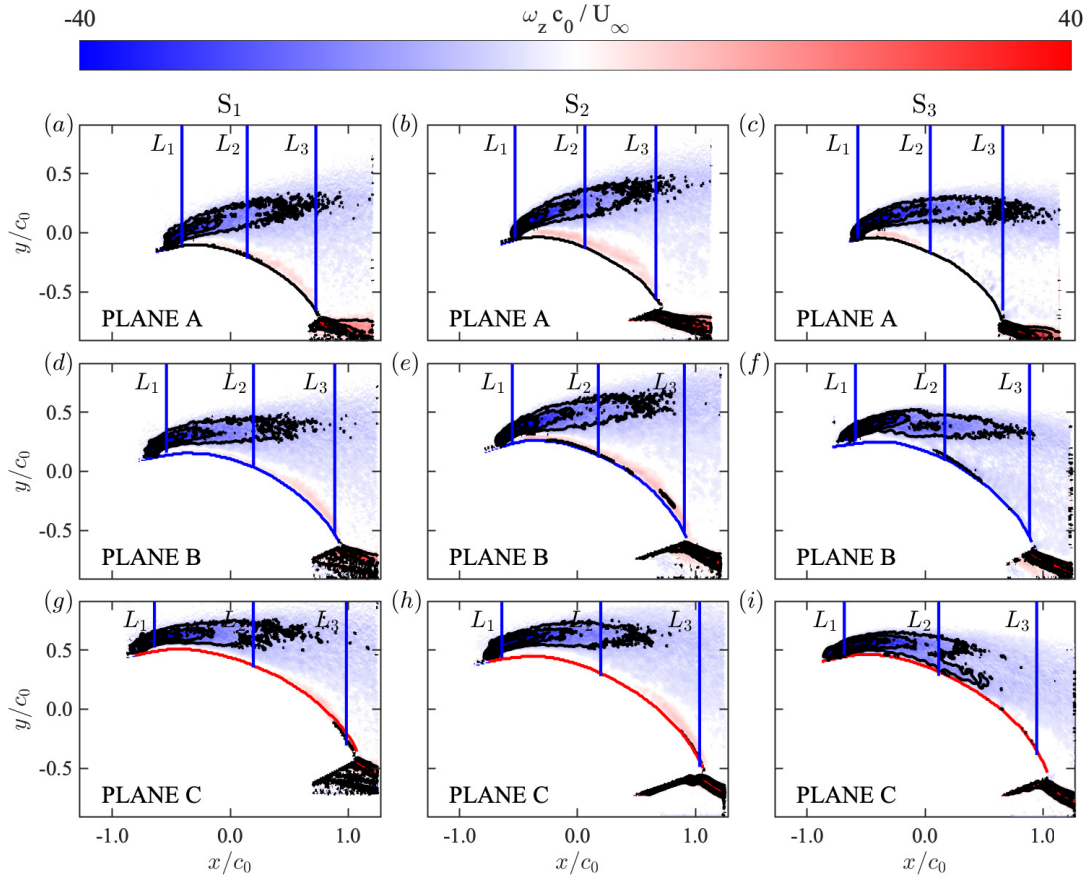

Figure 8.11: ω_z-contours for planes A, B, and C for S_1, S_2, and S_3 at the maximum-driving-force angle, η_{MD}

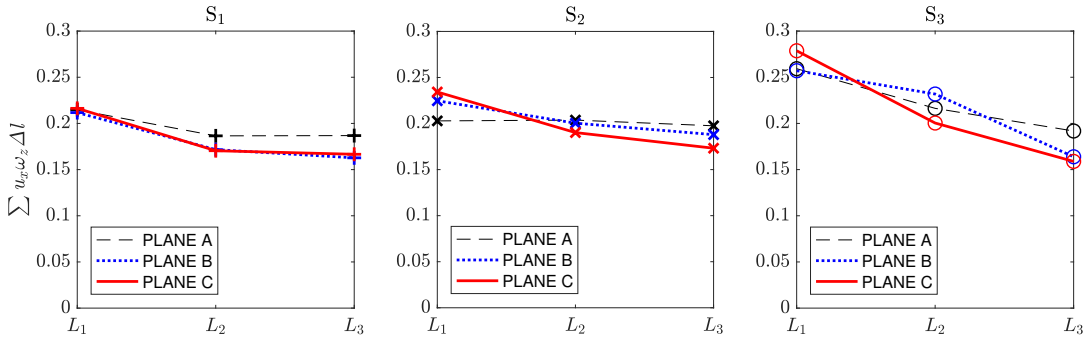

Figure 8.12: Vorticity chordwise convection measured at the leading edge, mid-chord, and trailing edge of planes A, B, and C of S_1, S_2, and S_3 at the maximum-driving-force angle, η_{MD}

Trapped vortex analogy

The proximity of the wake to the body of the sail, affects the bound circulation according to the complex potential model developed in the previous Chapter. Neglecting viscosity terms, the closer the LEVs are to the surface of the foil, the more they reduce the bound circulation. In a time-averaged sense, shedding LEVs can be represented as a single elongated LEV in the vicinity of the surface of the sail. Evidence of time-averaged shedding LEVs is found in Fig. 8.3, where elongated vortex poles are revealed by the γ_2-contours.

The contribution to lift from the LEV is a function of its circulation and position. Assuming a constant circulation Γ_{LEV}, the impact of the LEV to the bound circulation is determined by the coefficient κ. Here $\kappa = 1$ is attributed to an LEV in proximity to the leading edge and to the surface of the sail.

Twist promotes the LEV to move further away from the surface of the sail, allowing the growth of regions of counter-rotating vorticity on the surface of the sail and curbing the strength of the vortex. The effect of counter-rotating vorticity on the surface makes twist in sails an effective tool to control the maximum driving force ($C_{DF,\max}$). It is observed that S_3, is detrimental to the generation of maximum driving force, because it generates a stronger LEV, a higher lift, but also higher induced drag, whereas S_1 and S_2 modify the trajectory of the LEVs away from the surface of the sail, decreasing the strength of the LEV. A weaker LEV reduces C_L and $C_{D,i}$, but results beneficial to the generation of maximum driving force.

Figure 8.13 shows a schematic of the effect of twist in downwind sails. Fig. 8.13a depicts the wake of a high twist sail. Fig. 8.13b represents the wake of a low twist sail.

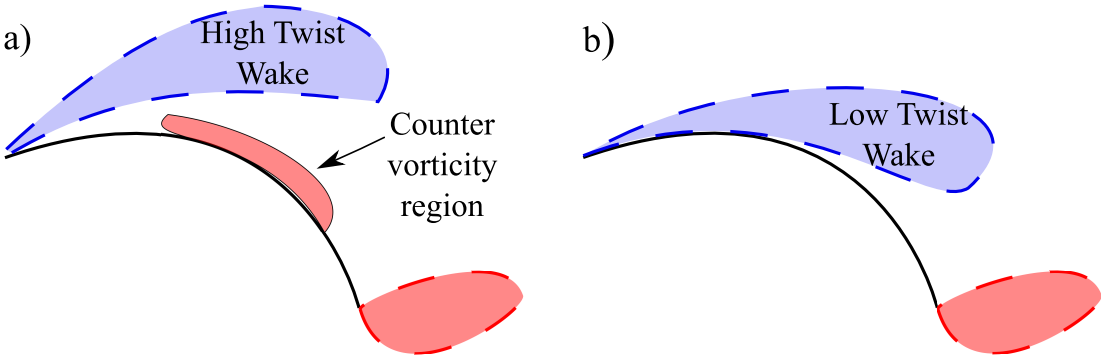

Figure 8.13: Twist effect on a downwind sail

8.5 Twist at maximum L/D ratio and maximum lift

Figure 8.14 shows the averaged streamlines and γ_2-contours of planes A, B and C for geometries S_1, S_2 and S_3 at $\eta_{L/D}$. At this angle of attack, the flow remains mostly attached to the three sails.

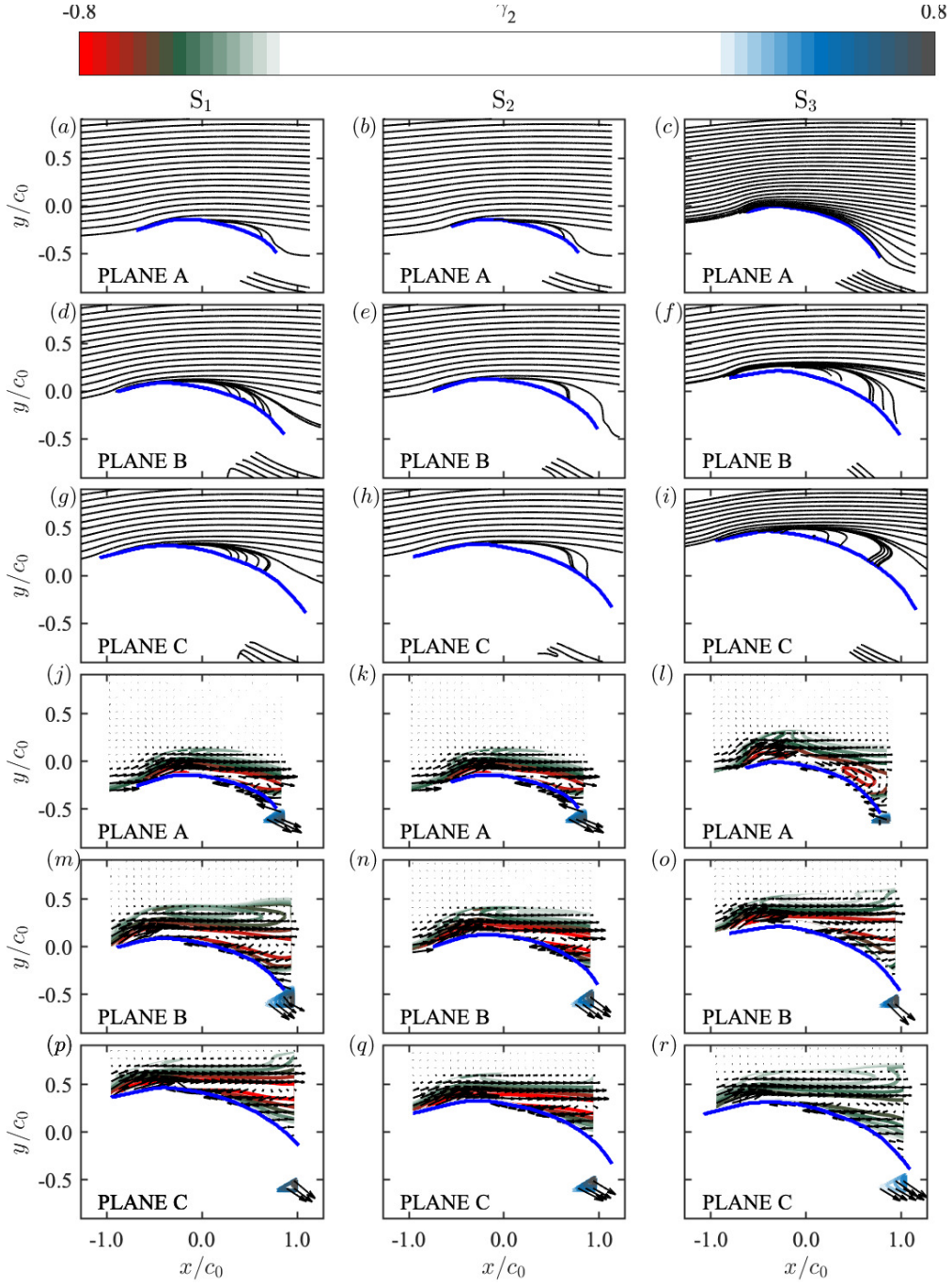

Figure 8.14: Averaged streamlines and γ_2-contours for planes A, B and C, and geometries S_1, S_2, and S_3, at $\eta_{L/D}$

Figure 8.15 shows the averaged streamlines and γ_2-contours of planes A, B and C for geometries S_1, S_2 and S_3 at η_L. At this angle of attack, the flow is stalled and a bubble of counter-rotating vorticity emerges on the surface of the sail.

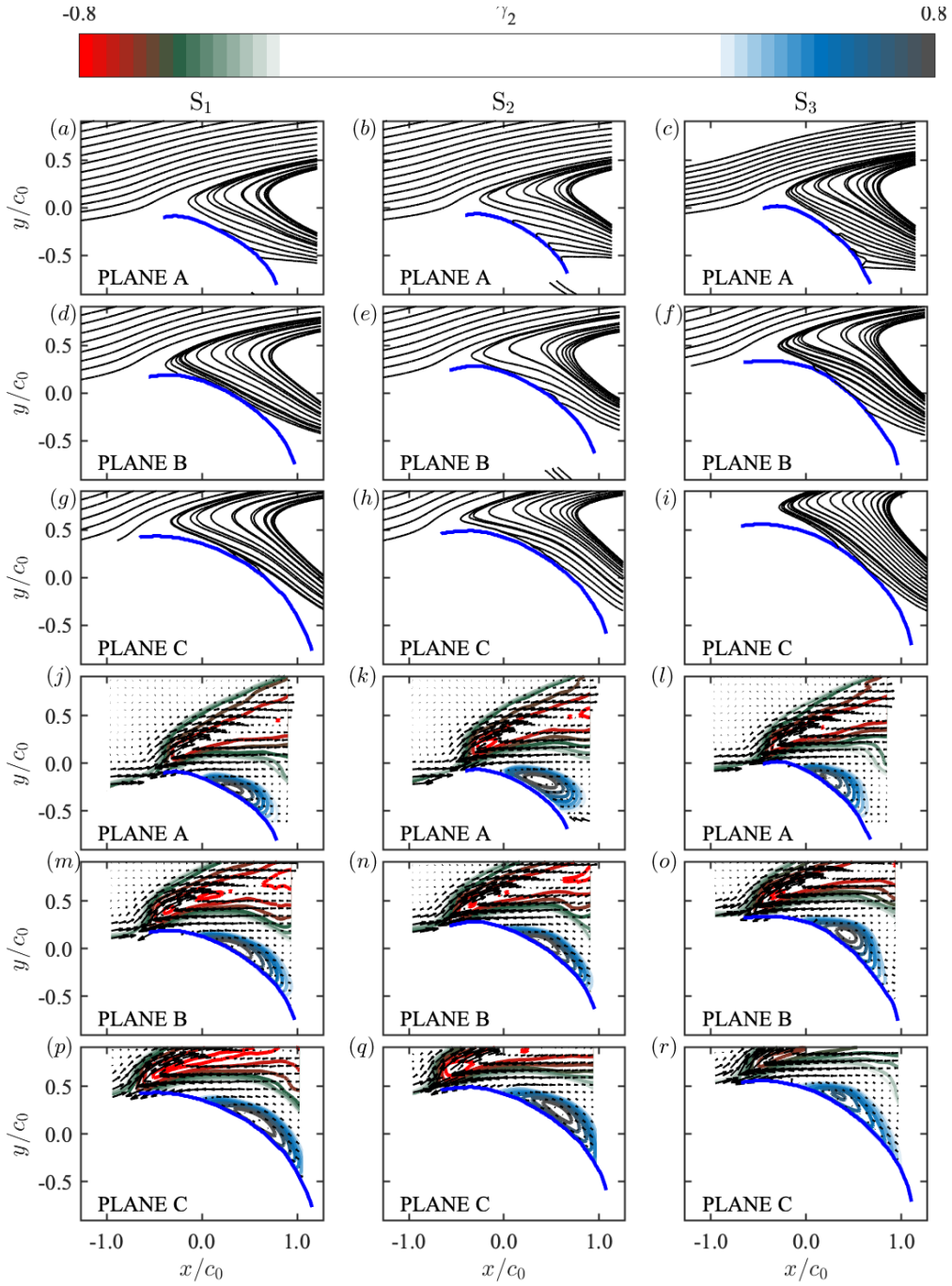

Figure 8.15: Averaged streamlines and γ_2-contours for planes A, B and C, and geometries S_1, S_2, and S_3, at η_L

8.6 Chapter summary

This Chapter presents force components and PIV measurements for spinnaker geometries S_1, S_2 and S_3. These geometries were manufactured with different twist, in order to explore the effect of twist in the context of sail aerodynamics. The sail that provides the maximum driving force is identified and its near wake studied. A comparative assessment is performed between sails, at the maximum-driving-force angle. PIV measurements show that twist promotes the LEV to move further away from the surface of the sail. This increment in distance and the counter-rotating vorticity that generates on the surface of the sail, results in a reduction of lift and induced drag, which is in turn beneficial for maximum driving force generation.

PART D:
FINAL REMARKS

Chapter 9

Conclusions and future work

9.1 Conclusions

Recent high-fidelity numerical simulations (Viola et al., 2014) suggested that an LEV formed at the leading edge of an asymmetric spinnaker. This finding has been investigated in detail in the present PhD thesis.

A model-scale asymmetric spinnaker was tested in uniform flow in a water flume at a Reynolds number of 1.3×10^4. The time-averaged velocity measured with PIV confirmed the numerical results by Viola et al. (2014), which are presented in Fig. 1.8, in Chapter 1. The LEV formed on the upper half of the sail and grew in size towards the head of the sail, where the axis of the LEV moved away from the sail surface and inboard of the sail. Downstream of the LEV, the time-averaged flow reattached and an attached boundary layer formed. Conversely, on the lower half of the sail, where trailing edge separation was dominant, the LEV was absent or of negligible dimensions and the separation point occurred well upstream of the mid-chord.

The time-resolved flow field revealed that the LEV remained attached to the leading edge intermittently and only at a section located 3/4$^{\text{th}}$ along the sail span. The LEV remained attached to the leading edge for time durations of the order of $10c_0/U_\infty$, and broke down into smaller vortices for time periods of similar length. In other words the flow switched between these two states. The convection velocity of the LEV was found to be about 60% of the free stream velocity.

A complex potential model of a circular arc in the presence of an LEV was developed to understand the role of the LEV in downwind sails. The flow field was a representation of the experimental observations carried out with PIV. The model assumed that the Kutta condition was established by the sum of the bound circulation and the circulation of the LEV. Under this assumption, it was found that the LEV contributed between 10% to 20% of the total sectional lift of the sail. These results suggest that the LEV

contributes to lift generation and therefore, quantifying its circulation is key to develop accurate force predictive models. These findings were presented by Arredondo-Galeana and Viola (2018).

The influence of spanwise distribution of the angle of attack was examined by testing three rigid model-scale prototypes and measuring force components, and the local flow fields. It was found that a low twist geometry promoted a wake in close proximity to the sail's surface, whereas high twist geometries generated a distant wake from the sail's surface. In the latter case, counter rotating vorticity was generated on the surface of the sail, which reduced the circulation around the sail. This effect helped to explain the results observed in the force measurements. It was found that a high twist geometry provided a marginally lower lift and a significant lower drag than a low twist geometry. The full wake of the high twist geometry was measured, because it provided the highest maximum drive (C_{DF}). The averaged wake results revealed the existence of two rotating dipoles, one at the leading edge and the other at the trailing edge. Circulation measured around these dipoles revealed that circulation around the LEV was attenuated at high angles of attack, where the TEV grew in strength, causing the geometry to enter a regulated stall mode. The results presented here are similar to that from flat plate studies by DeVoria and Mohseni (2017), as shown in Fig. 8.4 in Chapter 8.

The results presented in this thesis show that the LEV is not infinitely attached to the leading edge of a downwind sail and that it does not increase the lift at the maximum driving force angle. Hence, the hypothesis stated in Chapter 1 is false. However, the presence of the LEV was confirmed and its contribution to the sectional lift of the sail was quantified, highlighting the relevance of studying the LEV of downwind sails.

An understanding of the vortex flows around sails can enhance sail design and sail handling, enabling ship architects and engineers to control the strength and position of vortices to generate optimum lift, and drag forces that generate maximum driving thrust. Additionally, the present work opens up the interesting possibility of implementing sail design discoveries in fields where sail-like geometries can be used for energy extraction, such as in tidal energy devices and aerial vehicles.

9.2 Future work

The author of this thesis identifies these possible avenues of research and remaining questions, after feedback, and revisions received during the PhD.

LEV characterisation and control

It is recommended that future studies be undertaken to quantify the spanwise flow component in the LEV and to investigate to what extent it helps stabilize the LEV. To this end the spanwise component of velocity can be measured using stereo or tomographic PIV.

Finding out why the LEV breaks down and what can be done to keep the LEV trapped infinitely are interesting areas of research. To test these two scenarios, modifications to the geometry and to the flow conditions can be implemented. For example, simplifications of the spinnaker geometry to study the variation of spanwise flow due spanwise camber and sweep could provide insight into LEV stability. Additionally, testing the LEV under different conditions of turbulence and Reynolds numbers could shed light into the robustness of the LEV at different scales.

The role of the LEV is usually taken to be one of lift enhancement (Saffman and Sheffield, 1977; Huang and Chow, 1982); however its purpose has recently been challenged, and new theories have emerged as to exactly what is the function of the LEV. For instance, alternative theories are that the LEV delays separation (Nabawy and Crowther, 2017) and that it is useful for gust alleviation (Muir et al., 2017). Given the complexity of the sail geometry, specific experiments need to be designed to understand whether the LEV is actually enhancing lift or helping to delay stall. By designing experiments to modify the circulation of the LEV, for example, applying suction to promote vortex stretching or modifying the surface roughness to promote annihilation, the effect of the LEV can be further understood in the context of sail aerodynamics.

Modelling the flow of downwind sails with low order models

Vortex modelling of separated flows provide cost effective methods to analyse flow and predict force generation around airfoils. At the moment, industry standards for sailing applications do not include use of downwind sail solvers that analyse separated flow. Cyr and Newman (1996) modelled separation effects in a complex potential model of two dimensional arcs by incorporating a source term. However, this approach was

only reliable for separation points in the vicinity of the trailing edge. For separation that occurs at the leading edge, flow has been represented with discrete point vortices, for example, the complex potential model by (Xia and Mohseni, 2013). Combining these two approaches, a low order model for downwind sails could be developed for industrial use, with the aid of the experimental data gathered in this thesis. Additionally, three dimensional effects such as spanwise flow, could be incorporated through a sink term at the leading edge.

Twist and geometry

Twist effect is found to alter slightly the aerodynamics of sails, but it is significant regarding enhancement or control of sail performance. High twist is able to slightly reduce the lift and the induced drag, and provides the highest driving force for the sail conditions studied here. It is recommended that further investigation be conducted into the the effect of twist, with a wider range of twist focused on the top of the sail. Similarly, dynamic twist should be studied in order to monitor in real time how the vortical flows respond. This would lead to a better understanding of how these changes are reflected in the generated forces of downwind sails.

Sail flexibility and dynamics

Sail dynamics in terms of surface dynamics and body dynamics is another area of research that will lead to improved understanding of flow around downwind sails at motion. The effect of rotational motions such as roll, pitch or yaw, and translation motions such as sway, surge or heave need to be investigated in detail. These motions directly influence the vortex flows and vortex stability.

Surface deformations of flexible membranes opens up new strategies for LEV control, by enhancing stability or delaying flow separation. Controlling the LEV could promote lift enhancement and improve the performance of downwind sails.

Appendix A

Matlab code for Q and γ_2

```
%Q FUNCTION FOR 2D GRID %by Abel Arredondo Galeana
function [Q] = Qcriterion(varargin)

%INPUTS
X = varargin{1};%IN METERS
Y = varargin{2};%IN METERS
u = varargin{3};%IN M/S
v = varargin{4};%IN M/S
msize = varargin{5};%GRID SIZE N, WHERE N IS N X N

%DECLARING VELOCITY GRADIENT TENSOR ARRAYS
dudx = zeros(msize,msize);
dvdx = zeros(msize,msize);
dudx = zeros(msize,msize);
dvdx = zeros(msize,msize);
dwdx = zeros(msize,msize);
dudy = zeros(msize,msize);
dvdy = zeros(msize,msize);
dwdy = zeros(msize,msize);
dudz = zeros(msize,msize);
dvdz = zeros(msize,msize);
dwdz = zeros(msize,msize);
%X AND Y, RENAMED AS x ad y
x = X;
y = Y;

%FIRST ORDER DIFFERENCE SCHEME TO CALCULATE VELOCITY GRADIENT TENSORS IN 2D
j = 2;
delta =  X(4,4+1)-X(4,4-1); %DELTA BETWEEN ADJACENT POINTS
while j < msize;
        i = 2; %RESTARTING THE COLUMN COUNTER
        %LOOP FOR COLUMNS
        while i < msize;%343
                dudx(j,i) = (((u(j,i+1))-(u(j,i-1)))/(delta));
                dvdx(j,i) = (((v(j,i+1))-(v(j,i-1)))/(delta));
                dwdx(j,i) = 0;
                dudy(j,i) = (((u(j-1,i))-(u(j+1,i)))/(delta));
                dvdy(j,i) = (((v(j-1,i))-(v(j+1,i)))/(delta));
                dwdy(j,i) = 0;
                dudz(j,i) = 0;
                dvdz(j,i) = 0;
                dwdz(j,i) = 0;
            i = i+1;
        end
        j = j+1;
end
%CALCULATION OF Q CRITERION
for j=1:msize
    for i=1:msize
    %Q(i) = J11J22-J12J21+J11J33-J13J31+J22J33-J23J32;
    Q(j,i) = dudx(j,i)*dvdy(j,i)-dudy(j,i)*dvdx(j,i)+dudx(j,i)*dwdz(j,i)-
dudz(j,i)*dwdx(j,i)+dvdy(j,i)*dwdz(j,i)-dvdz(j,i)*dwdy(j,i);
    end
end

Q=Q;
Return
```

```
%GAMMA FUNCTION FOR 2D GRID %by Abel Arredondo Galeana
function [Gamma,hi,ho] = GammaTwo(varargin)
X = varargin{1}; %INITIALISATION OF X MATRIX
Y = varargin{2}; %INITIALISATION OF Y MATRIX
u = varargin{3}; %INITIALISATION OF u MATRIX
v = varargin{4}; %INITIALISATION OF v MATRIX
wsize = varargin{5};%INITIALISATION OF L,WHICH IS HALF THE LENGTH OF WINDOW N
msize = varargin{6};%INITIALISATION OF SIZE OF GRID msize x msize
%%%%%%%%%%%%%%%%%%%%%%%%CALCULATE ZERO MATRIX%%%%%%%%%%%%%%%%%%%%%%
x=1; %FILLS WITH ONES MATRIX WITH VALID POINTS, AND WITH ZEROS EMPTY CELLS
y=1;
for x=1:msize;
    for y=1:msize;
        if v(y,x) == 0;
            zero_matrix(y,x) = 0; %not Zero but out of scale
        else
            zero_matrix(y,x) = 1;
        end
        y=y+1;
    end
    x=x+1;
    y=1;
end
hi(msize,msize)=0; %initialize with zeros
ho(msize,msize)=0; %initialize with zeros
%%%%%%%%%%%%%%%%%%%%%%%%GAMMA 2%%%%%%%%%%%%%%%%%%%%%%%%%%%%%%%%%%%%%%%%%%%%%%%%
for g=1:1 %THIS CAN BE CHANGED FOR MULTIPLE FILES
      X = varargin{1}; %INITIALISATION OF X MATRIX
      Y = varargin{2}; %INITIALISATION OF Y MATRIX
      u = varargin{3}; %INITIALISATION OF u MATRIX
      v = varargin{4}; %INITIALISATION OF v MATRIX
      p_x_start =wsize+1;        %X COORDINATE START
      p_x_end = size(X,1)-wsize; %X COORDINATE END
      p_y_start = wsize+1;       %Y COORDINATE START
      p_y_end = size(X,1)-wsize; %Y COORDINATE END
      p_y = p_y_start; %INITIALISATION OF p_y
      p_x = p_x_start; %INITIALISATION OF p_x
      welements = ((wsize*2)+1)^2-1; %NUMBER OF ELEMENTS IN HALF OF WINDOW N
      for p_y = p_y_start:p_y_end %RUN FOR ALL THE GRID IN Y
          for p_x = p_x_start:p_x_end; %RUN FOR ALL THE GRID IN X
                    u = varargin{3}; %REINITIALISE u
                    v = varargin{4}; %REINITIALISE v
                    %definition of Alfa, Beta, Gamma
                    a = p_x-wsize; %STARTING POINT IN X IN WINDOW, AROUND p_x
                    b = p_y-wsize; %STARTING POINT IN Y IN WINDOW, AROUND p_x
                    upx = 0; %upx = 0
                    upy = 0; %upy = 0
                    Gamma_value = 0; %Gamma_value = 0
      %CALCULATION OF CONVECTION VELOCITY AND SUBTRACTION
      upx1 = sum(u(p_y-wsize:p_y+wsize,p_x-wsize:p_x+wsize));%SUMALLUEL. IN N
      upx  = sum(upx1); %SUM ALL U ELEMENTS IN WINDOW N
      upx = upx-u(p_y,p_x); %SUBSTRACT FROM SUM VALUE AT CENTER OF WINDOW N
      upy1 = sum(v(p_y-wsize:p_y+wsize,p_x-wsize:p_x+wsize));%SUMALLVEL. IN N
      upy  = sum(upy1); %SUM ALL V ELEMENTS IN WINDOW N
      upy = upy-v(p_y,p_x); %SUBSTRACT FROM SUM VALUE AT CENTER OF WINDOW N
      upx = (upx)/(welements-1); %AVERAGE VALUE FOR CONVECTION VELOCITY IN U
      upy = (upy)/(welements-1); %AVERAGE VALUE FOR CONVECTION VELOCITY IN V
      A(1:(wsize*2)+1,1:(wsize*2)+1) = upx; % WINDOWN N WITH AV.CONV. VEL U
```

```
      B(1:(wsize*2)+1,1:(wsize*2)+1) = upy; % WINDOWN N WITH AV.CONV. VEL V
      u(p_y-wsize:p_y+wsize,p_x-wsize:p_x+wsize) = u(p_y-wsize:p_y+wsize,p_x-
      wsize:p_x+wsize) - A;  % SUBSTRACT AV.CONV. VEL U FROM FLOW FIELD IN N
      v(p_y-wsize:p_y+wsize,p_x-wsize:p_x+wsize) = v(p_y-wsize:p_y+wsize,p_x-
      wsize:p_x+wsize) - B; % SUBSTRACT AV.CONV. VEL V FROM FLOW FIELD IN N
%%%%%%%%%%%%%%%%%%%%%%%%%%%%%%%%%%%%%%%%%%%%%%%%%%%%%%%%%%%%%%%%%%%%%%%%%%%%%%%
      i = p_x-wsize; %STARTING COORDINATE IN WINDOW N FOR X
      j = p_y-wsize; %STARTING COORDINATE IN WINDOW N FOR Y
      conv_vel=0; %STARTING VALUE FOR CONV_VEL
      Gamma_value2 = 0; %STARTING VALUE FOR GAMMA 2

      %CALCULATION OF GAMMA 2 VALUE
      if zero_matrix(p_y,p_x) == 1 %IF GRID HAS A VALID POINT
            A(1:(wsize*2)+1,1:(wsize*2)+1) = Y(p_y,p_x); %FILL MATRIX A
            B(1:(wsize*2)+1,1:(wsize*2)+1) = X(p_y,p_x); %FILL MATRIX B
            Alfa = atan2d(Y(p_y-wsize:p_y+wsize,p_x-wsize:p_x+wsize)-A,X(p_y-
            wsize:p_y+wsize,p_x-wsize:p_x+wsize)-B); %ANGLE AT ORIGIN
            Beta = atan2d(v(p_y-wsize:p_y+wsize,p_x-wsize:p_x+wsize),u(p_y-
            wsize:p_y+wsize,p_x-wsize:p_x+wsize)); %ANGLE FROM VELOCITYVECTOR
            Omega = Beta-Alfa; %FULL ANGLE
            Omega(wsize+1,wsize+1) = 0; %ELIMINATE POINT IN THE MIDDLE
            Gamma_c = sind(Omega); %GAMMA VALUE IS THE SIN OF THE ANGLE
            REFILL THE ZEROS %MANDATORY ALMOST FOR GAMMA 1%%%%%%%%%%
            aux = u(p_y-wsize:p_y+wsize,p_x-wsize:p_x+wsize);
            i = 1;
            j= 1;
            for j=1:wsize*2+1
               for i=1:wsize*2+1
                   if aux(j,i)==0
                      Gamma_c(j,i) = 0;
                   else
                   end
                end
            end
      %%%%%%%%%%%%%%%%%%%%%%%%%%%%%%%%%%%%%%%%%%%%%%%%%%%%%%%%%%%%%%%%%%%%%%%%%%%%%%%
            Gamma_value1 = sum(Gamma_c,1); %SUM SINE VALUES
            Gamma_value = sum(Gamma_value1,2); %SUM SINE VALUES
            else  %END
                Gamma_value = 0;%IF GRID IS EMPTY OR WITH A ZERO VALUE
            end %END

            Gamma_value = Gamma_value/(welements); %GAMMA VALUE AVERAGE
            Hola(p_y,p_x) = Gamma_value; %GAMMA VALUE FOR EVERY POINT
            hi(p_y,p_x) = u(p_y,p_x); %SAVING SUBSTRACTED FLOW FIELD
            ho(p_y,p_x) = v(p_y,p_x); % SAVING SUBTRACTED FLOW FIELD
            end
      end
    Z = zeros(p_y_end,msize-p_x_end); GAMMA GRID OF EQUAL SIZE AS ORIGINAL
    newa = horzcat(Hola,Z);
    Z2 = zeros(msize-p_y_end,msize);
    newa = vertcat(newa,Z2);
    newa = newa.*zero_matrix;
    A2(:,:,g) = newa;
end
    hi = hi.*zero_matrix;
    ho = ho.*zero_matrix;
    Gamma =  A2;
return
```

Appendix B

Non-slender delta wing

The results of vortex detection are applied to a non slender delta wing. This forms part of the results presented in Muir et al. (2017). Both of the criteria identify the vortices in the region above the wing. These results agree well with numerical and experimental observations done by Gursul et al. (2007), among others. In fact, in this type of wing, a secondary and even a tertiary vortex were detected. The author of this thesis post processed the results for ω, Q and the γ criteria.

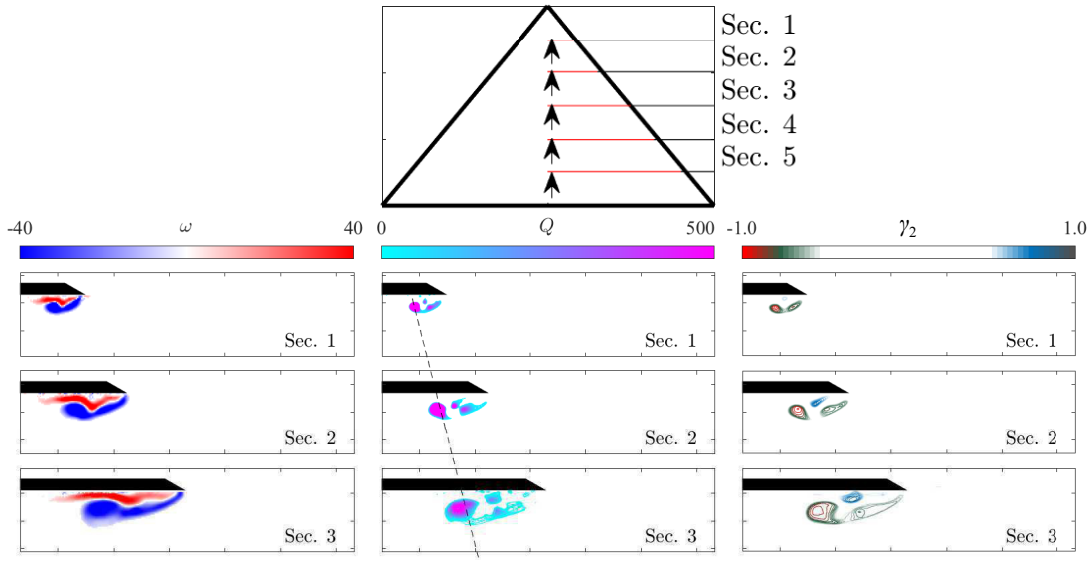

Figure B.1: ω, Q and γ_2 results for the averaged flow field of Sec. 1, 2 and 3, of a non slender delta wing from Muir et al. (2017)

Appendix C

LEV detection settings

The vorticity ω, the Q and the γ_2 criteria are shown for the averaged flow fields of plane A and plane B in Fig. C.1. The sail corresponds to geometry S_0.

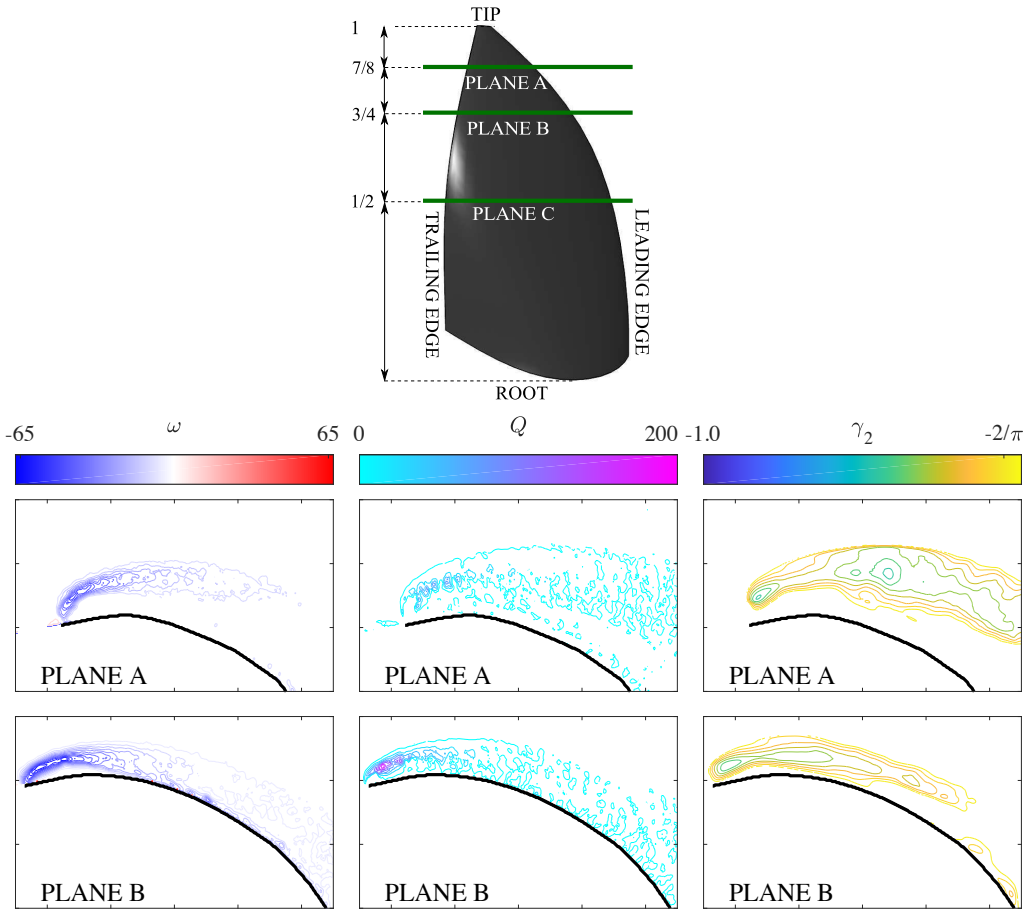

Figure C.1: ω, Q and γ_2 results for averaged flow fields of planes A and B of the spinnaker studied in Arredondo-Galeana and Viola (2018)

It is expected that the LEV core size is $l_0 = 0.1c_0$ and that it does not change in size. The l/l_0 ratio is set to $l/l_0 = 0.80$ for γ_2. Results for the averaged flow field show, that

the γ_2 criterion is able to identify coherent structures on top of the sail, in contrast to the vorticity ω. The Q-criterion identifies the LEV near the leading edge of plane B, while it becomes faint in plane A. The γ_2 identifies rotational structures near the leading edge and downstream, in both planes. An instantaneous analysis is carried out in Sec. 6.2 with the γ_2 due to its robustness to local fluctuations associated to turbulence and noise, and to verify the instantaneous nature of the vortex.

Window size effect in γ_2

The global detection scheme γ_2 can behave as a local detection criterion if the window size (S_w) is set too small, not to include the vortex core size. In other words, if the ratio $l/l_0 < 0.4$, the global detection scheme behaves like a local scheme. The effect of a small window size is show in Fig. C.2. If the detection window is too small, γ_2 does not identify the large scale vortices and resembles the pattern shown by Q. Hence, the window size (S_w) is an important parameter in the γ_2 criterion and needs to be set to include the vortex core size inside the detection window. Figure C.2 shows the difference between setting the detection ratio to $l/l_0 = 0.18$ and $l/l_0 = 0.70$, for a vortex core radius $l_0 = 20\,\text{mm}$.

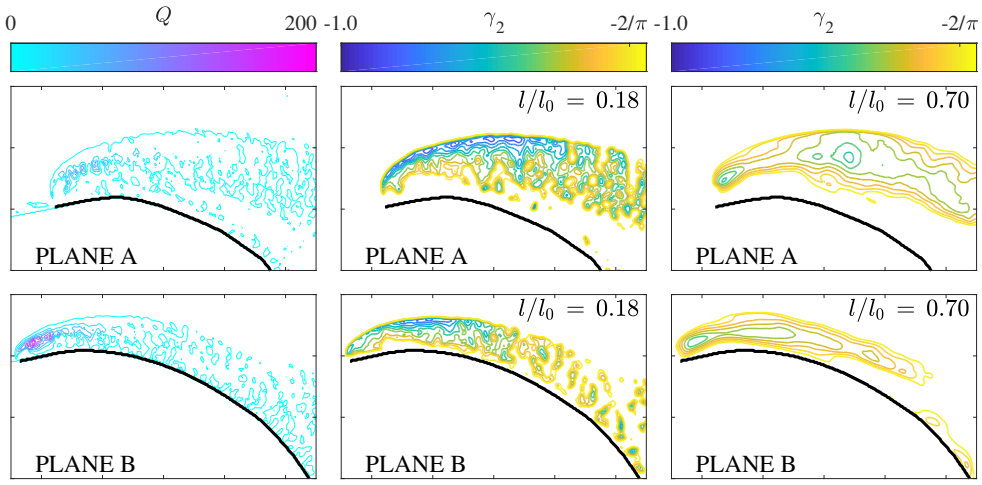

Figure C.2: ω and γ_2 results with different window size (l/l_0) for the averaged flow fields of planes A and B of the Spinnaker used in Arredondo-Galeana and Viola (2018)

Results of γ_1 and γ_2 of averaged flow field

The results for the averaged flow field of γ_1 and γ_2, for planes A and B are compared. The vortex size grows from plane B (Fig. C.3b) to plane A (Fig. C.3a), i.e. in the direction of the tip which is where the vorticity is extracted. The detection ratios are set to $l/l_0 = 0.16$ for γ_1 and $l/l_0 = 0.8$ for γ_2.

The γ_1 criterion has one global maximum at the centre of the LEV. The maximum γ_1 is -0.7 in plane A and -0.8 in plane B. Conversely, the γ_2 criterion has two local maxima on each plane. On plane A, the maxima are both -0.79. On plane B, these are -0.79 near the leading edge and -0.76 at ca. $x/c = -0.2$. Since γ_2 is the Galilean invariant version of the γ-criterion, the instantaneous analysis will be carried out with γ_2.

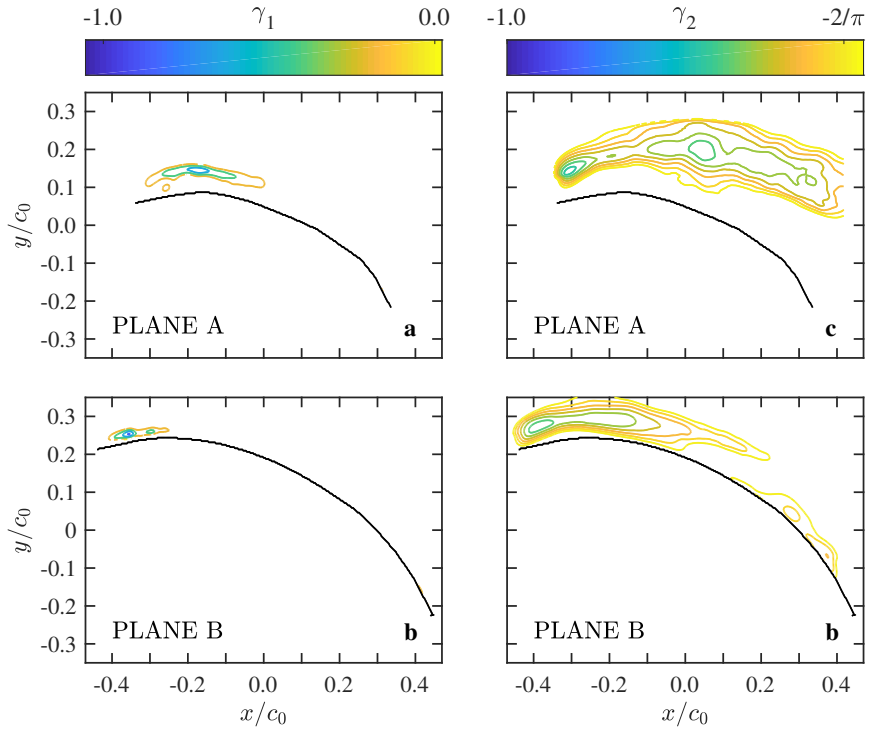

Figure C.3: γ_1 and γ_2 criteria of the time-averaged velocity field measured for $0.000 < t^* < 40.736$ on the planes A and B.

Appendix D

Data for Fig. 7.13, 7.14 and 7.15

Table D.1: Values for κ and Γ used in Fig. 7.13, to reproduce the sequence of Plane B, Fig. 6.3(j-r)

Image	κ_1	Γ_1	κ_2	Γ_2	κ_3	Γ_3	κ_4	Γ_4	κ_5	Γ_5	κ_6	Γ_6
25	0.9301	-0.0042					0.5093	-0.00064216				
26	0.9301	-0.0035	0.9429	-0.00056902	0.9048	-0.00017	0.4364	-0.00015795				
27	0.9301	-0.0039			0.8848	-0.00047						
28	0.9301	-0.0040	0.9429	-0.00022711	0.9584	-0.00007	0.8128	-0.00006692				
29	0.9301	-0.0037			0.9048	-0.00005						
30	0.9301	-0.0041			0.8957	-0.00031						
31	0.9301	-0.0038	0.9612	-0.00012936	0.8848	-0.00035						
32	0.9301	-0.0041	0.9584	-0.00028272	0.8716	-0.00053						
33	0.9301	-0.0035			0.9528	-0.00013	0.5414	-0.00090853				

Table D.2: Values for κ and Γ used in Fig. 7.14, to reproduce the sequence of Plane B, Fig. 6.4(j-r)

Image	κ_1	Γ_1	κ_2	Γ_2	κ_3	Γ_3	κ_4	Γ_4	κ_5	Γ_5	κ_6	Γ_6
195	0.9301	-0.0026	0.9011	-0.0008	0.9365	-0.0005	0.6680	-0.0004	0.9484	-0.00022	0.4796	-0.000037406
196	0.9301	-0.0028	0.9026	-0.0005	0.8894	-0.0007	0.8352	-0.0004	0.6256	-0.00002		
197	0.9301	-0.0015	0.9063	-0.0016	0.8444	-0.0004	0.7424	-0.0002	0.5092	-0.00023		
198	0.9301	-0.0039	0.8352	-0.0001	0.6123	-0.0005						
199	0.9301	-0.0027	0.8971	-0.0012	0.8069	-0.0001	0.4519	-0.0006				
200	0.9301	-0.0025	0.8779	-0.0007	0.8894	-0.0010	0.7630	-0.0002				
201	0.9301	-0.0014	0.9063	-0.0012	0.8700	-0.0005	0.8233	-0.0007	0.6018	-0.00032		
202	0.9301	-0.0025	0.8779	-0.0010	0.7356	-0.0005						
203	0.9301	-0.0014	0.9046	-0.0013	0.8390	-0.0013	0.7292	-0.0008				

Table D.3: Values for κ and Γ used in Fig. 7.15, to reproduce the sequence of Plane A, Fig. 6.4(a-i)

Image	κ_1	Γ_1	κ_2	Γ_2	κ_3	Γ_3	κ_4	Γ_4	κ_5	Γ_5	κ_6	Γ_6
269	0.8321	-0.0017	0.722	-0.0012	0.4979	-0.0006	0.1923	-0.00040				
270	0.8321	-0.0016	0.6448	-0.0011	0.4284	-0.0001	0.2096	-0.00080	0.0794	-0.00022		
271	0.8321	-0.0015	0.942	-0.0003	0.5775	-0.0013						
272	0.8321	-0.0023	0.4328	-0.0011								
273	0.8321	-0.0027	0.2701	-0.0010								
274	0.8321	-0.0017	0.7948	-0.0004	0.9272	-0.0001	0.3227	-0.00120				
275	0.8321	-0.0018	0.7220	-0.0007	0.9365	-0.0002	0.2096	-0.00060				
276	0.8321	-0.0012	0.7447	-0.0011	0.6973	-0.0002	0.6458	-0.00030	0.1124	-0.00020		
277	0.8321	-0.0012	0.7584	-0.0001	0.6932	-0.0010	0.3955	-0.00003	0.3579	-0.00002	0.4890	-0.00028

Appendix E

Data to calculate κ_i of appendix D

The κ_i values from appendix D were calculated with the following values of ρ_i and τ_i.

Table E.1: Values used to calculate κ of Table D.1

Image	ρ_1	τ_1	ρ_2	τ_2	ρ_3	τ_3	ρ_4	τ_4	ρ_5	τ_5	ρ_6	τ_6
25	1.15	165					1.35	45				
26	1.15	165	1.1	112	1.1	70	1.5	50				
27	1.15	165			1.1	60						
28	1.15	165	1.1	112	1.05	80	1.15	55				
29	1.15	165			1.1	70						
30	1.15	165			1.1	65						
31	1.15	165	1.05	85	1.1	60						
32	1.15	165	1.05	80	1.1	55						
33	1.15	165			1.05	72	1.3	43				

Table E.2: Values used to calculate κ of Table D.2

Image	ρ_1	τ_1	ρ_2	τ_2	ρ_3	τ_3	ρ_4	τ_4	ρ_5	τ_5	ρ_6	τ_6
195	1.15	165	1.2	127	1.1	100	1.5	80	1.05	67	1.6	60
196	1.15	165	1.2	130	1.2	110	1.25	90	1.45	67		
197	1.15	165	1.2	140	1.25	95	1.35	78	1.55	60		
198	1.15	165	1.25	90	1.45	65						
199	1.15	165	1.2	120	1.3	90	1.65	60				
200	1.15	165	1.25	125	1.2	110	1.30	75				
201	1.15	165	1.2	140	1.25	115	1.3	98	1.5	68		
202	1.15	165	1.25	125	1.4	84						
203	1.15	165	1.2	135	1.3	108	1.3	67				

Table E.3: Values used to calculate κ of Table D.3

Image	ρ_1	τ_1	ρ_2	τ_2	ρ_3	τ_3	ρ_4	τ_4	ρ_{51}	τ_5	ρ_6	τ_6
269	1.4	170	1.6	110	1.7	68	1.7	43				
270	1.4	170	1.7	95	1.8	65	2.1	55	1.8	40		
271	1.4	170	1.1	110	1.7	80						
272	1.4	170	1.9	70								
273	1.4	170	2.1	60								
274	1.4	170	1.4	108	1.1	88	2.1	65				
275	1.4	170	1.6	110	1.1	100	2.1	55				
276	1.4	170	1.6	123	1.6	100	1.4	65	2.2	50		
277	1.4	170	1.6	135	1.7	112	2.6	90	2.3	75	1.6	61

Appendix F

Derivation of bound circulation

The complex potential of the rotating cylinder in Fig. 7.1 is given by Eq. F.1

$$F(\zeta) = U_\infty(\zeta-\zeta_0)e^{-i\alpha} + \frac{U_\infty R^2 e^{i\alpha}}{(\zeta-\zeta_0)} - \frac{i(\Gamma_b+\Gamma_{LEV})}{2\pi}\ln(\zeta-\zeta_0) - \frac{i\Gamma_{LEV}}{2\pi}\ln\frac{\zeta-\zeta_{LEV}}{\zeta-\zeta'_{LEV}}. \tag{F.1}$$

The complex velocity in the cylinder plane is given by differentiating Eq. F.1 with respect to ζ

$$W(\zeta) = U - iV = U_\infty e^{-i\alpha} - \frac{U_\infty R^2 e^{i\alpha}}{(\zeta-\zeta_0)^2} - \frac{i(\Gamma_b+\Gamma_{LEV})}{2\pi}\frac{1}{\zeta-\zeta_0} - \frac{i\Gamma_{LEV}}{2\pi}\left[\frac{1}{\zeta-\zeta_{LEV}} - \frac{1}{\zeta-\zeta'_{LEV}}\right]. \tag{F.2}$$

Following Pitt Ford and Babinsky (2013), except the trailing edge coordinates in the ζ-plane here are defined as $\zeta_{TE} = Re^{-i\beta} + i\mu$, where $\mu = R\sin(\beta)$ is the displacement of the cylinder in the vertical axis; the Kutta condition is satisfied at the trailing edge of a circular arc, if a stagnation point exists at the equivalent point in the cylinder plane, such that

$$W(\zeta)\Big|_{\zeta=Re^{-i\beta}+i\mu=0.} \tag{F.3}$$

In the presence of an LEV at an arbitrary position $\zeta_{LEV} = \rho e^{i\phi}$, the value for the bound circulation (Γ_b) for a circular arc to keep the Kutta condition is

$$\Gamma_b = -4R\pi U_\infty \sin(\beta+\alpha) - \Gamma_{LEV}\left[\frac{2R(R-\rho\cos(\beta+\tau))}{R^2+\rho^2-2R\rho\cos(\beta+\tau)}\right]. \tag{F.4}$$

Appendix G

PIV Diagram Schematic and Triggering Sequence

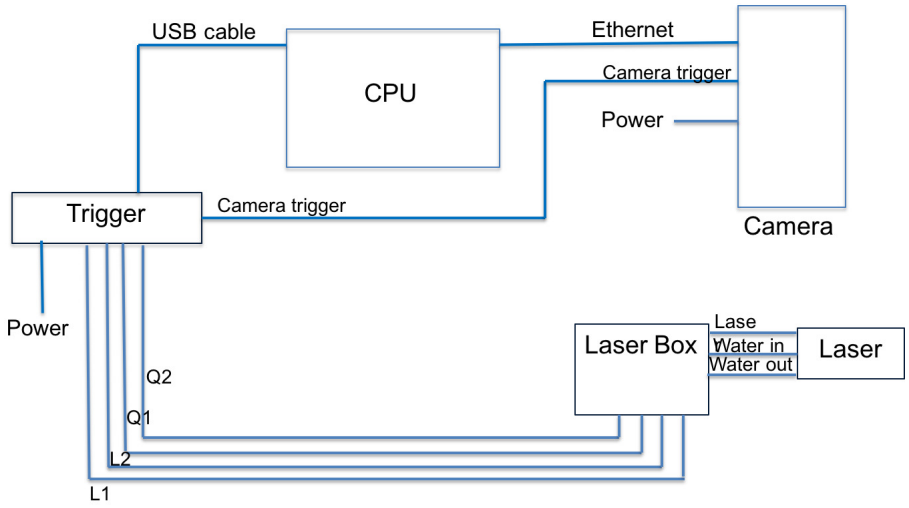

Figure G.1: PIV Diagram Schematic

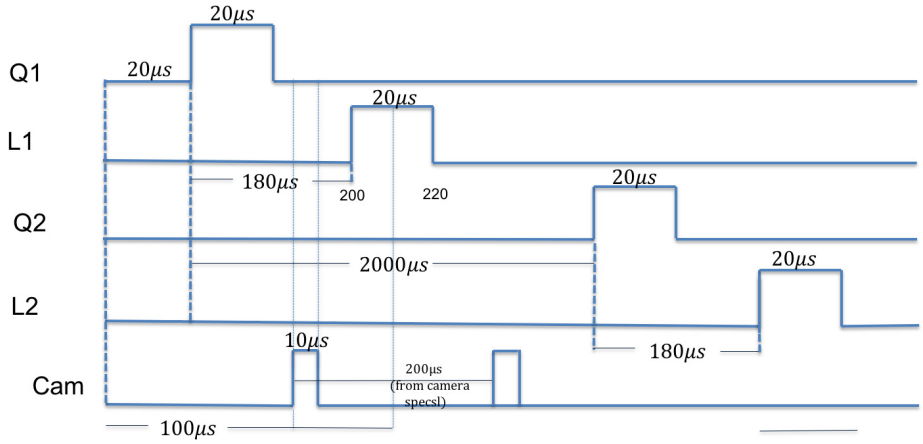

Figure G.2: PIV Triggering Sequence

Bibliography

Abbott, I., Von Doenhoff, A., 1959. Theory of wing sections. Including a summary of airfoil data. Dover Publications, New York, US.

Adrian, R.J., 1997. Dynamic ranges of velocity and spatial resolution of particle image velocimetry. Measurement Science and Technology 8, 1393.

Anthoine, J., Arts, T., H.L., B., J.-M., B., Carbonaro, M., Degrez, G., Dénos, R., Fletcher, D., Olivari, D., Riethmuller, M.L., Van Den Braembussche, R.A., 2009. Measurement Techniques in Fluid Dynamics - An Introduction.

Arena, A.V., Mueller, T.J., 1980. Laminar separation, transition, and turbulent reattachment near the leading edge of airfoils. AIAA Journal 18, 747–753.

Arredondo-Galeana, A., Viola, I.M., 2018. The leading-edge vortex of yacht sails. Ocean Engineering 159, 552–562.

Baum, E., Peterson, B., Böhm, B., Dreizler, A., 2014. On the validation of LES applied to internal combustion engine flows: Part 1: Comprehensive experimental database. Flow, Turbulence and Combustion 92, 269–297.

Beem, H.R., Rival, D.E., Triantafyllou, M.S., 2012. On the stabilization of leading-edge vortices with spanwise flow. Experiments in Fluids 52, 511–517.

Bethwaite, F., 1993. High Performance Sailing. Waterline Books, UK.

Birch, J.M., Dickinson, M.H., 2001. Spanwise flow and the attachment of the leading-edge vortex on insect wings. Nature 412, 729.

Birch, J.M., Dickson, W.B., Dickinson, M.H., 2004. Force production and flow structure of the leading edge vortex on flapping wings at high and low reynolds numbers. Journal of Experimental Biology 207, 1063–1072.

Borazjani, I., Daghooghi, M., 2013. The fish tail motion forms an attached leading edge vortex. Proceedings. Biological sciences / The Royal Society 280, 20122071.

Bot, P., Viola, I.M., Flay, R.G., Brett, J.S., 2014. Wind-tunnel pressure measurements on model-scale rigid downwind sails. Ocean Engineering 90, 84–92.

Bradshaw, P., Wong, F.Y.F., 1972. The reattachment and relaxation of a turbulent shear layer. Journal of Fluid Mechanics 52, 113–135.

Chakraborty, P., Balachandar, S., Adrian, R.J., 2005. On the relationships between local vortex identification schemes. Journal of Fluid Mechanics 535, 189–214.

Chong, M.S., Perry, A.E., Cantwell, B.J., 1990. A general classification of three-dimensional flow fields. Physics of Fluids A: Fluid Dynamics 2, 765–777.

Corke, T.C., Thomas, F.O., 2015. Dynamic stall in pitching airfoils: aerodynamic damping and compressibility effects. Annu Rev Fluid Mech 47, 479–505.

Cyr, S., Newman, B.G., 1996. Flow past two-dimensional membrane aerofoils with rear separation. Journal of Wind Engineering and Industrial Aerodynamics 63, 1–16.

Davis, M., 1980. Design of flat plate leading edges to avoid flow separation. AIAA Journal 18, 598–600. Cited By 15.

DeVoria, A.C., Mohseni, K., 2017. On the mechanism of high-incidence lift generation for steadily translating low-aspect-ratio wings. Journal of Fluid Mechanics 813, 110–126.

Eldredge, J.D., Jones, A.R., 2019. Leading-edge vortices: Mechanics and modeling. Annual Review of Fluid Mechanics 51, 75–104.

Ellington, C.P., 1999. The novel aerodynamics of insect flight: applications to micro-air vehicles. Journal of Experimental Biology 202, 3439 LP – 3448.

Eslam Panah, A., Akkala, J.M., Buchholz, J.H.J., 2015. Vorticity transport and the leading-edge vortex of a plunging airfoil. Experiments in Fluids 56, 160.

Flay, R.G.J., 1996. A twisted flow wind tunnel for testing yacht sails. Journal of Wind Engineering and Industrial Aerodynamics 63, 171–182.

Flay, R.G.J., Piard, A., Bot, P., 2017. Aerodynamics of a highly cambered circular arc aerofoil: Experimental investigations, in: Proceedings of the 4th Innov'Sail International Conference on Innovation in High Performance Sailing Yachts, Lorient, France.

Fossati, F., Muggisca, S., Viola, I.M., Zasso, A., 2006. Wind tunnel techniques for investigation and optimization of sailing yachts aerodynamics, in: In the proceedings of the 2nd High Performance Yacht Design Conference, Auckland, New Zealand.

Furman, A., Breitsamter, C., 2013. Turbulent and unsteady flow characteristics of delta wing vortex systems. Aerospace Science and Technology 24, 32 – 44. VFE-2.

Gad-El-Hak, M., Blackwelder, R.F., 1985. The discrete vortices from a delta wing. AIAA Journal 23, 961–962.

Gad-El-Hak, M., Blackwelder, R.F., 1987. Control of the discrete vortices from a delta wing. AIAA Journal 25, 1042–1049.

Garmann, D.J., Visbal, M.R., Orkwis, P.D., 2013. Three-dimensional flow structure and aerodynamic loading on a revolving wing. Physics of Fluids 25.

Graftieaux, L., Michard, M., Grosjean, N., 2001. Combining PIV, POD and vortex identification algorithms for the study of unsteady turbulent swirling flows. Meas Sci Technol 12, 1422–1429.

Gursul, I., Gordnier, R., Visbal, M., 2005. Unsteady aerodynamics of nonslender delta wings. Progress in Aerospace Sciences 41, 515–557.

Gursul, I., Wang, Z., Vardaki, E., 2007. Review of flow control mechanisms of leading-edge vortices. Progress in Aerospace Sciences 43, 246–270.

Haller, G., 2005. An objective definition of a vortex. Journal of Fluid Mechanics 525, 1–26.

Harbig, R.R., Sheridan, J., Thompson, M.C., 2013a. Relationship between aerodynamic forces, flow structures and wing camber for rotating insect wing planforms. Journal of Fluid Mechanics 730, 52–75.

Harbig, R.R., Sheridan, J., Thompson, M.C., 2013b. Reynolds number and aspect ratio effects on the leading-edge vortex for rotating insect wing planforms. Journal of Fluid Mechanics 730, 52–75.

Huang, M.K., Chow, C.Y., 1982. Trapping of a free vortex by Joukowski airfoils. AIAA Journal 20, 292–298.

Hubel, T.Y., Tropea, C., 2010. The importance of leading edge vortices under simplified flapping flight conditions at the size scale of birds. J Exp Biol 213, 1930–1939.

Hunt, J.C.R., Wray, A.A., Moin, P., 1988. Eddies, stream, and convergence zones in turbulent flows. Center for Turbulence Research Report CTR-S88 , 193–208.

Jardin, T., David, L., 2014. Spanwise gradients in flow speed help stabilize leading-edge vortices on revolving wings. Phys Rev E 90, 13011.

Jeong, J., Hussain, F., 1995. On the identification of a vortex. Journal of Fluid Mechanics 285, 69–94.

Katz, J., Plotkin, A., 2001. Low-speed aerodynamics. Cambridge Aerospace Series. 2 ed., Cambridge University Press.

Kim, D., Gharib, M., 2010. Experimental study of three-dimensional vortex structures in translating and rotating plates. Experiments in Fluids 49, 329–339.

Kiya, M., Sasaki, K., 1983. Structure of a turbulent separation bubble. Journal of Fluid Mechanics 137, 83–113.

Kundu, P.K., Cohen, I.M., Dowling, D.R., 2012. Fluid Mechanics. Fifth edit ed., Elsevier.

Larsen, J.W., Nielsen, S.R.K., Krenk, S., 2007. Dynamic stall model for wind turbine airfoils. Journal of Fluids and Structures 23, 959–982.

Lentink, D., Dickson, W.B., van Leeuwen, J.L., Dickinson, M.H., 2009. Leading-edge vortices elevate lift of autorotating plant seeds. Science 324, 1438–1440.

Lentink, D., Müller, U.K., Stamhuis, E.J., de Kat, R., van Gestel, W., Veldhuis, L.L.M., Henningsson, P., Hedenström, A., Videler, J.J., van Leeuwen, J.L., 2007. How swifts control their glide performance with morphing wings. Nature 446, 1082–1085.

Lim, T.T., Teo, C.J., Lua, K.B., Yeo, K.S., 2009. On the prolong attachment of leading edge vortex on a flapping wing. Modern Physics Letters B 23, 357–360.

Lugt, H.J., 1979. The dilemma of defining a vortex. Springer Berlin Heidelberg, Berlin, Heidelberg. pp. 309–321.

Maxworthy, T., 2007. The formation and maintenance of a leading-edge vortex during the forward motion of an animal wing. Journal of Fluid Mechanics 587, 471–475.

Melling, A., 1997. Tracer particles and seeding for particle image velocimetry. Measurement Science and Technology 8, 1406–1416.

Morgan, C.E., Babinsky, H., Harvey, J.K., 2009. Vortex detection methods for use with PIV and CFD data, in: Proceedings of the 47th AIAA Aerospace Sciences Meeting, Orlando, Florida, USA.

Motta, D., Flay, R.G., Richards, P.J., Le Pelley, D., Bot, P., Deparday, J., 2015. An investigation of the dynamic behaviour of asymmetric spinnakers at full-scale, in: Proceedings of the 5th High Performance Yacht Design Conference, Auckland, New Zealand.

Muijres, F.T., Johansson, L.C., Barfield, R., Wolf, M., Spedding, G.R., Hedenström, A., 2008. Leading-edge vortex improves lift in slow-flying bats. Science 319, 1250–1253.

Muir, R., Arredondo-Galeana, A., Viola, I., 2017. The leading-edge vortex of swift wing-shaped delta wings. Royal Society Open Science 4.

Nabawy, M.R.A., Crowther, W.J., 2017. The role of the leading edge vortex in lift augmentation of steadily revolving wings: a change in perspective. Journal of The Royal Society Interface 14, 20170159.

Nava, S., Cater, J., Norris, S., 2016. A comparison of RANS and LES for upwind sailing aerodynamics, in: Proceedings of the 22nd Chesapeake Sailing Yacht Symposium, Annapolis, Mryland, USA.

O'Meara, M., Mueller, T.J., 1987. Laminar separation bubble characteristics on an airfoil at low Reynolds numbers. AIAA Journal 25, 1033–1041.

Ota, T., Asano, Y., Okawa, J.i., 1981. Reattachment length and transition of the separated flow over blunt flat plates. Bulletin of JSME 24, 941–947.

Perry, A.E., Steiner, T.R., 1987. Large-scale vortex structures in turbulent wakes behind bluff bodies. Part 1. Vortex formation processes. Journal of Fluid Mechanics 174, 233–270.

Pitt Ford, C., Babinsky, H., 2013. Lift and the leading-edge vortex. Journal of Fluid Mechanics 720, 280–313.

Polhamus, E.C., 1966. A concept of the vortex lift of sharp-edge delta wings based on a leading-edge suction analogy. NASA Tech. Rep. TND-3767 .

Polhamus, E.C., 1971. Predictions of vortex-lift characteristics by a leading-edge suction analogy. Journal of Aircraft 8, 193–199.

Pope, A., Harper, J.J., 1966. Low-Speed Wind Tunnel Testing. John Wiley & Sons, Inc. New York.

Rabinovitch, J., Brion, V., Blanquart, G., 2012. Effect of a splitter plate on the dynamics of a vortex pair. Physics of Fluids 24.

Raffel, M., Willert, C.E., Scarano, F., Kähler, C.J., Wereley, S.T., Kompenhaus, J., 2018. Particle image velocimetry: A practical guide. Third ed., Springer.

Raffel, M., Willert, C.E., Wereley, S.T., Kompenhaus, J., 2007. Particle image velocimetry: A practical guide. Second ed., Springer.

Richards, P.J., Viola, I.M., 2015. Leading edge vortex dynamics, in: Proceedings of the 17th Australasian Wind Engineering Society Workshop, Wellington, New Zealand.

Rival, D.E., Kriegseis, J., Schaub, P., Widmann, A., Tropea, C., 2014. Characteristic length scales for vortex detachment on plunging profiles with varying leading-edge geometry. Experiments in Fluids 55, 1660.

Saffman, P.G., Sheffield, J.S., 1977. Flow over a wing with an attached free vortex. Studies in Applied Mathematics 57, 107–117.

Sciacchitano, A., Wieneke, B., 2016. PIV uncertainty propagation. Measurement Science and Technology 27, 084006.

Souppez, J.B.R.G., Dewavrin, J.M.M.A., Gohier, F., Borba Labi, G., 2019a. Hydrofoil configurations for sailing superyachts: Hydrodynamics, stability and performance, in: Proceedings of the 7th Design & Construction of Super & Mega Yachts, The Royal Institution of Naval Architects, Genoa, Italy.

Souppez, J.B.R.G., Arredondo-Galeana, A., Viola, I.M., 2019b. Recent advances in experimental downwind sail aerodynamics, in: Proceedings of the 23rd Chesapeake Sailing Yacht Symposium, The Society of Naval Architects and Marine Engineers, Annapolis, Maryland, USA.

Srygley, R.B., Thomas, A.L.R., 2002. Unconventional lift-generating mechanisms in free-flying butterflies. Nature 420, 660–664.

Stevenson, J.P., Walsh, E.J., Nolan, K.P., 2016. Visualization of the vortex and reverse-flow structure of a separation bubble. J. Vis. 19, 175–177.

Taira, K., Colonius, T., 2009. Three-dimensional flows around low-aspect-ratio flat-plate wings at low Reynolds numbers. Journal of Fluid Mechanics 623, 187–207.

Taylor, J.R., 1997. An Introduction to Error Analysis. The Study of Uncertainties in Physical Measurements. University Science Books, USA.

Viola, I.M., Bartesaghi, S., Van-Renterghem, T., Ponzini, R., 2014. Detached eddy simulation of a sailing yacht. Ocean Engineering 90, 93–103.

Viola, I.M., Bot, P., Riotte, M., 2013. Upwind sail aerodynamics: A RANS numerical investigation validated with wind tunnel pressure measurements. International Journal of Heat and Fluid Flow 39, 90–101.

Viola, I.M., Flay, R.G.J., 2009. Force and pressure investigation of modern asymmetric spinnakers. Transactions of the Royal Institution of Naval Architects Part B: International Journal of Small Craft Technology 151, 31–40.

Viola, I.M., Flay, R.G.J., 2010. Pressure distributions on modern asymmetric spinnakers. International Journal of Small Craft Technology Transaction RINA Part B1 152, 41–50.

Viola, I.M., Flay, R.G.J., 2011a. Sail aerodynamics: Understanding pressure distributions on upwind sails. Experimental Thermal and Fluid Science 35, 1497–1504.

Viola, I.M., Flay, R.G.J., 2011b. Sail pressures from full-scale, wind-tunnel and numerical investigations. Ocean Eng 38, 1733–1743.

Viola, I.M., Flay, R.G.J., 2012. Sail aerodynamics: on-water pressure measurements on a downwind sail. J Ship Res 56, 197–206.

Viola, I.M., Flay, R.G.J., 2015. Aerodynamics of headsails: a review of measured surface pressures and expected flow fields, in: Proceedings of the 5th High Performance Yacht Design Conference, Auckland, New Zealand.

Wereley, S.T., Gui, L., Meinhart, C.D., 2002. Advanced algorithms for microscale Particle Image Velocimetry. AIAA J 40, 1047–1055.

Wojcik, C.J., Buchholz, J.H.J., 2014. Vorticity transport in the leading-edge vortex on a rotating blade. Journal of Fluid Mechanics 743, 249–261.

Wong, J.G., Rival, D.E., 2015. Determining the relative stability of leading-edge vortices on nominally two-dimensional flapping profiles. Journal of Fluid Mechanics 766, 611–625.

Xia, X., Mohseni, K., 2013. Lift evaluation of a two-dimensional pitching flat plate. Physics of Fluids 25, 91901.

Yaniktepe, B., Rockwell, D., 2004. Flow structure on a delta wing of low sweep angle. AIAA Journal 42, 513–523.

Zasso, A., Fossati, F., Viola, I.M., 2005. Twisted flow wind tunnel design for testing Yacht Sails., in: In the proceedings of the 4th European and African Conference on Wind Engineering (EACWE4), Prague, Czech Republic.

Ocean Engineering 159 (2018) 552–562

Contents lists available at ScienceDirect

Ocean Engineering

journal homepage: www.elsevier.com/locate/oceaneng

The leading-edge vortex of yacht sails

Abel Arredondo-Galeana, Ignazio Maria Viola *

School of Engineering, Institute for Energy Systems, University of Edinburgh, Mayfield Road, Edinburgh, EH9 3DW, UK

ARTICLE INFO

Keywords:
Yacht sails
Spinnakers
Vortex flows
Leading edge vortex
Particle image velocimetry
Circular arc

ABSTRACT

It has been suggested that a stable Leading Edge Vortex (LEV) can be formed from the sharp leading edge of asymmetric spinnakers, which are high-lift sails used by yachts to sail downwind. If the LEV remains stably attached to the leading edge, it provides an increase in the thrust force. Until now, however, the existence of a stable and attached LEV has only been shown by numerical simulations. In the present work we experimentally verify, for the first time, that a stable LEV can be formed on an asymmetric spinnaker. We tested a 3D printed rigid sail in a water flume at a chord-based Reynolds number of ca. 10^4. The sail was tested in isolation without hull and rigging. The flow field was measured with Particle Image Velocimetry (PIV) over horizontal cross sections. We found that on the leeward side of the sail (the suction side), the flow separates at the leading edge reattaching further downstream and forming a stable LEV. The LEV grows in diameter from the root to the tip of the sail, where it merges with the tip vortex. We detected the LEV using the γ criterion, and we verified its stability over time. The lift contribution provided by the LEV was computed solving a complex potential model of each sail section. This analysis indicated that the LEV provides more than 20% of the total sail's lift. These findings suggest that the maximum lift of low-aspect-ratio wings with a sharp leading edge, such as spinnakers, can be enhanced by promoting the formation of a stable LEV.

1. Introduction

Sails are thin wings with a relatively sharp leading edge. A common configuration for downwind sailing includes two sails: the mainsail and the spinnaker (Fig. 1). The mainsail, which is on the rear of the yacht, has both the leading edge and the lower edge attached to rigid structures (the mast and the boom, respectively). Conversely, the spinnaker, which is in the front of the yacht, is attached to the boat only by the three corners. The free, sharp leading edge leads to flow separation at any non-zero angle of attack (Fig. 2). This is one of the key features of yacht sails that makes them different from conventional wings. In fact, the flow at the leading edge is similar to that of a plate at incidence (Viola and Flay, 2015). Flow reattachment occurs somewhere downstream of the leading edge, forming a region of separated flow. This region is short in the chordwise direction, but it extends from the base to the tip of the sail (Viola et al., 2013). When sailing downwind, the most efficient fore sails are asymmetric spinnakers, which are highly-cambered, highly-twisted and low-aspect-ratio sails. The maximum camber in both the chordwise and spanwise directions is typically higher than 20% and 50% of the chord length, respectively. The twist angle between the root and top section is higher than 20°, and the aspect ratio is between 1.5 and 2. These sails are designed to allow the maximum lift, and the drag has little effect on the yacht performance because it is almost perpendicular to the sail course.

The large camber enables high lift, but it also leads to trailing edge separation. The rear separated region could cover more than half of the chord. Since the extent of it is easier to identify than the smaller leading edge separated area, the length of the rear region is typically used to inform the sail designer on where the sails' shape can be enhanced. However, virtually all of the driving force is generated near the leading edge. Thus, small changes in the fluid dynamics of the leading edge separated region can result in significant gains in performance. This work aims to gain new insight on the flow in this section.

The impact of this work, however, extends beyond sail design. In particular, there is an increasing interest for very thin wings, and also membrane-wings, for Unmanned Aerial Vehicles (UAV). These operate at moderate Reynolds numbers (*Re*) of the order of 10^4 - 10^5. At this *Re* regime, either a large angle of attack or a high camber must be used to generate lift. Therefore, the flow around this highly cambered sail is relevant for the design of UAV wings.

* Corresponding author.
E-mail address: I.M.Viola@ed.ac.uk (I.M. Viola).

https://doi.org/10.1016/j.oceaneng.2018.02.029
Received 29 September 2017; Received in revised form 2 February 2018; Accepted 15 February 2018
Available online 24 February 2018

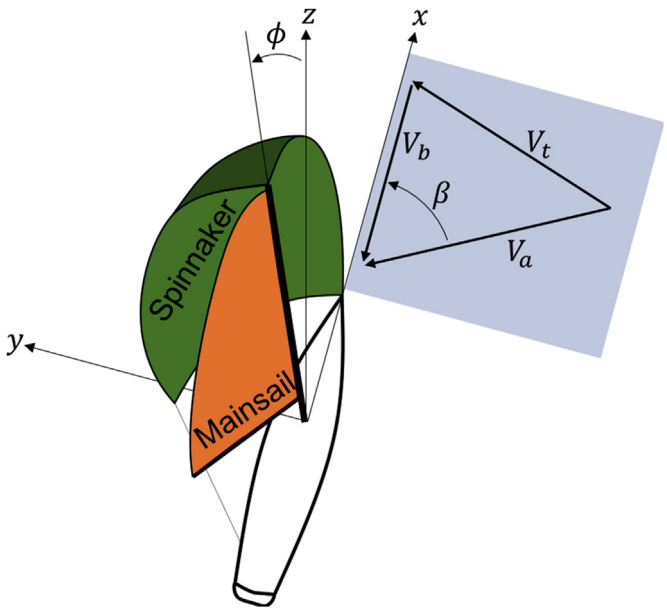

Fig. 1. Bird eye view of a yacht sailing downwind, where ϕ is the heel angle in the vertical plane perpendicular to the yacht, V_b is the wind due to the boat speed, while V_t and V_a are the true and apparent wind, respectively; β is the apparent wind angle.

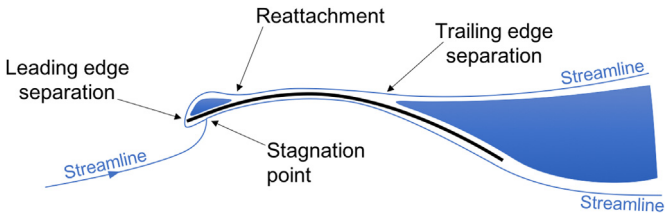

Fig. 2. Schematic view of the flow over a horizontal section of a spinnaker.

1.1. The flow of sharp-edge sails

When the leading edge of a wing is sharp and the incidence angle is high, the flow separates forming a strong shear layer. This results in the production of vorticity that is accumulated in the separated region. The integral of the vorticity in this region leads to a circulation that has the same sign as the circulation of the sail; thus this vorticity contributes to the generation of lift. However, vorticity cannot be accumulated indefinitely. It can be either shed downstream with the main flow stream, or it must be somehow extracted. At the leading edge of genoas and jibs, which are higher aspect ratio sails than spinnakers and are used to sail upwind, the vorticity is continuously shed downstream in the form of vortices that roll on the surface of the airfoil toward the trailing edge (Viola and Flay, 2011a, 2015; Nava et al., 2016). The time-averaged flow field shows flow reattachment somewhere downstream of the leading edge, and a thick boundary layer that grows towards the trailing edge.

Recent Detached Eddy Simulations (DES) (Viola et al., 2014) have revealed that a stable attached LEV might also occur on the asymmetric spinnakers of sailing yachts. This was anecdotally anticipated by Bethwaite (1993), who sketched the LEV on the asymmetric spinnaker of high-performance dinghies. The LEV is a coherent vortex formed by the roll up of vorticity, generated at the leading edge. The vorticity is not continuously shed downstream, but is instead convected towards the centre of the vortex. If the vorticity is somehow extracted from the axis of the vortex, it is possible to achieve a stable LEV that remains attached to the leading edge indefinitely. The vorticity is typically extracted by axial flow inside of the vortex core, towards the wing tip. A stable LEV grows in the direction in which the vorticity is extracted. The vorticity and circulation of the LEV can significantly increase the lift and thus it is exploited on both man-made and natural flyers (Ellington, 1999; Srygley and Thomas, 2002; Garmann et al., 2013; Jardin and David, 2014). Remarkably, it has been identified across a wide range of *Re*. In laminar flow conditions, it has been found on autorotating seeds (Lentink et al., 2009), and on the wings of insects (Muijres et al., 2008) and small birds (Lentink et al., 2007). In transitional and turbulent flow conditions, it has been found on larger bird wings (Hubel and Tropea, 2010), fish fins (Borazjani and Daghooghi, 2013) and delta wings (Gursul et al., 2005, 2007). In helicopter rotors (Corke and Thomas, 2015) and wind turbines (Larsen et al., 2007), the LEV is a powerful but undesirable flow feature. This is due to the large angle of attack oscillations. At every period, the LEV is shed downstream leading to a lift overshoot above the quasi-static maximum lift and to an abrupt, and dangerous change in the pitching moment. Conversely, in biological flyers and delta wings, the LEV provides an essential source of lift augmentation.

This work aims to provide experimental evidence that a stable LEV can occur on asymmetric spinnakers, corroborating the numerical evidence. Moreover, the work aims to quantify the contribution of the LEV to sails' performances.

1.2. A benchmark for downwind sails

The asymmetric spinnaker where the LEV was identified with DES (Viola et al., 2014) is considered in this work. The aerodynamics of this sail have been widely investigated in the last decade and this makes it one of the best available benchmarks for downwind sails. The geometry and the experimental, and numerical data are available on the Edinburgh DataShare (datashare.is.ed.ac.uk). This sail was designed for the AC33 class, which was proposed for the 33rd America's Cup. This class has never been adopted, as the 33rd America's Cup was eventually disputed with multi-hulls (ruled by the Deed of Gift). A 1:15th-scale model of this sail was tested in a wind tunnel at 55° apparent wind angle and 10° heel angle. The apparent wind angle is the supplementary angle between the wind velocity experienced by the yacht and the sailed course. The forces (Viola and Flay, 2009) and pressures (Viola and Flay, 2010) on the sail surfaces were recorded for a range of sail trims, and also compared with those measured on similar sails. The sail trim that allowed the maximum driving force, was used to build a rigid sail with embedded pressure taps and both forces, and pressures were measured in a wind tunnel (Bot et al., 2014). This sail trim was also modelled with Reynolds-averaged Navier-Stokes (RANS) simulations (Viola and Flay, 2011b) and with DES (Viola et al., 2014). A 1:3rd-scale prototype was built and tested on water on a Platu25-class yacht (Viola and Flay, 2012), where surface pressures were measured. A three-way comparison between the pressures measured in a wind tunnel, on water and with RANS was presented in Viola and Flay (2011b). While a comparison between wind tunnel tests performed with flexible and rigid sails, and DES, was presented in both Bot et al. (2014) and Viola et al. (2014). The pressures from these three approaches showed a qualitative agreement, with the pressures computed numerically lying in between those measured with the two experimental techniques.

1.3. Overview of the present work

In order to test in highly controlled flow conditions and to identify the main mechanisms enabling the formation, and stability of the LEV, the asymmetric spinnaker is tested in isolation (without the mainsail and the hull). Consider the chord measured on a section at 3/4th of the mitre from the base of the sail, where the mitre is the line on the sail surface equally far from the leading and trailing edge. Based on this reference chord, the Reynolds number of the sail tested in this work is $Re = 1.3 \times 10^4$. The actual flow of a real sail is certainly more complex than the one of this simplified model. The enhanced turbulent mixing and boundary

layer effects at higher Reynolds numbers are not accounted for in this model. However, the LEV has been found to be very resilient to the effects of Reynolds numbers (Gordnier et al., 2009). Also, the effect of the other sails and the hull is neglected. The rear sail generates upwash and increases the effective angle of attack. Therefore, these effects can be mostly accounted for by adjusting the angle of attack. The proximity to the hull and the sea surface leads to a local variation of the flow near the bottom of the sail. The effect of this variation is marginal on the LEV because the LEV is mostly developed at the highest sections of the sail. The onset flow is uniform and does not take into account the variation in height of the apparent wind velocity experienced by a sail at full scale. However, also this effect is moderate and can mostly be accounted for by a different trim of the sail. For this reason, the benchmark experiments and simulations described in section 1.2 consider a uniform onset flow. Therefore, while this investigation does not provide a quantitative description of the full-scale flow, it enables the understanding of the key features of downwind sail flow.

The rest of the paper is organised as follows: in Section 2, Methodology, the details of the methodology is presented, including the geometry of the sail, the experimental rig, the flow conditions, the instrumentation used to measure the flow field and how the data is analysed. In Section 3, Results, the flow measurements are presented, including the analysis of the LEV and an estimate of the contribution of the LEV to the sail's performance. Finally, Section 4, Conclusions, the key findings are summarised.

2. Methodology

2.1. Sail model

The geometry of the 3D-printed model used for this investigation is available on www.ignazioviola.com. The model has an area of $A = 0.045\ m^2$. The twist angle from the base to the head is 16°, the maximum chordwise camber is $0.40c_0$ and the maximum spanwise camber is $0.65c_0$, where $c_0 = 0.114$ m is the chord of a sail section at 3/4th of the span from the base (Fig. 3).

The model is 3 mm thick. Separation at the leading edge is promoted chamfering the edges. The chamfer at the leading and trailing edges is 20° for the first 3/4th of the span from the base to the head. At the top 1/4th of the sail's span, the chamfer grows progressively from 20° to 70°, allowing the thickness to remain constant on the mitre. The head of the sail is blunt.

The model is 3D printed in ABS with a Fortus 250 3D printer. It is mounted on a rotating shaft controlled by a lever arm for the fine control of the angle of attack. The shaft is attached to a 6 mm thick acrylic plate connected to a pair of 45 × 45 mm aluminium extrusions attached to the flume's side walls. The rig allows to change the angle of attack and to secure its testing position through an arch dial system (Fig. 4). The shaft is set to replicate the same apparent wind angle (55°) and heel angle (10°) as tested with DES (Viola et al., 2014).

2.2. Water flume

The water flume is a current-wave testing facility in the Institute of Engineering Systems of the School of Engineering, University of Edinburgh. It is 2 m long, 0.4 m wide and 0.9 m high. The water depth is set to 0.5 m and the sail is placed horizontally 0.1 m below the water surface. The free space between the rig and the walls of the flume is 0.05 m at both sides. The model is tested in a uniform current with $U_\infty = 0.1146$ m/s. A turbulence intensity of 7% is measured with laser Doppler velocimetry at a location 1 m upstream of the model. The high level of turbulence is due to the lack of a contraction section, and it is similar to that experienced by a yacht at full scale. Therefore, the vortical flow structures here investigated convect within a turbulent stream as they would do at full scale. As shown by McWilliams (1984), coherent vortices are highly resilient to the turbulent perturbations.

2.3. Particle image velocimetry

Flow visualisation is performed with a Particle Image Velocimetry (PIV) system, which consists of a Solo 200XT pulsed dual-head Nd:YAG laser, with an energy output of 200 mJ at a wavelength of $\lambda = 532$ nm. The camera is a CCD Imperx 5 MP with a 2448 px × 2050 px resolution and a Nikkor f/2, 50 mm lense. The seeding particles are silver coated hollow glass spheres with an average diameter of 14 μm and a density of 1.7 g/cc. In order to mitigate surface reflections, a coating of matt black paint is applied to the sail with a second coating of rhodamine B. A third coating of acrylic is applied to protect the rhodamine B coating from the water. An optical filter is used on the camera to subtract the wavelength of rhodamine B and minimise the reflected light. Background subtraction (Wereley et al., 2002) enables measurements in close proximity to the wall. The leading edge region, however, is not affected by laser reflections due to the curvature of the sail and the direction of the laser sheet.

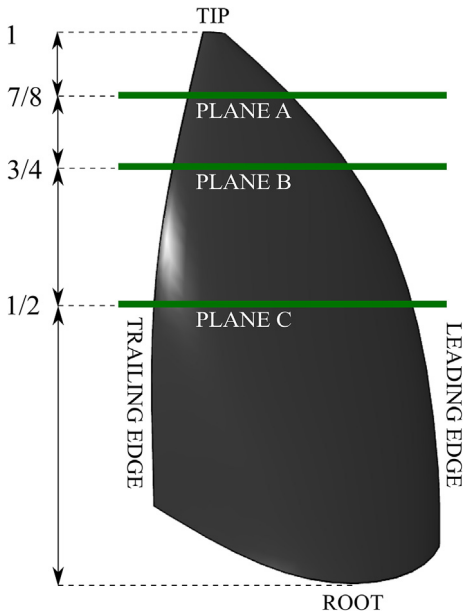

Fig. 3. Rendering of the sail model and position of the measurement planes.

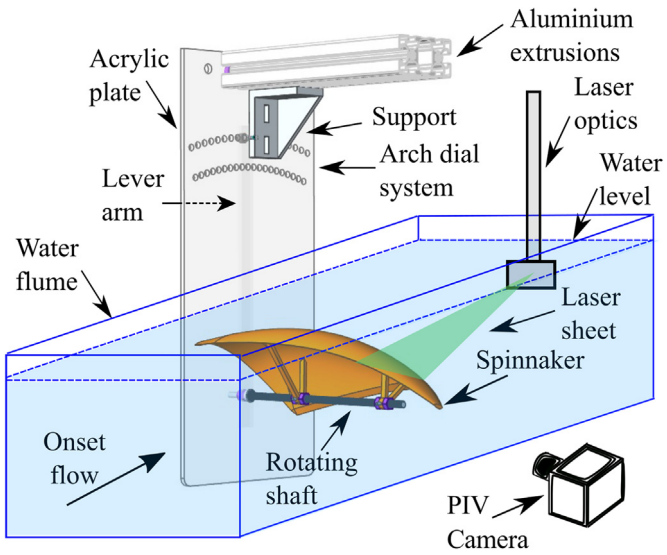

Fig. 4. Schematic diagram of the experimental setup.

The laser beam is redirected through two mirrors and an array of underwater LaVision optics to generate a laser sheet parallel to the flow. The laser sheet is fully submerged as shown in Fig. 4. The thickness of the laser sheet is approximately 2 mm. Three cross sections of the sail are recorded: plane A, B and C (Fig. 3). These are located respectively at 7/8, 3/4 and 1/2 of the distance from the root of the sail to the tip.

PIV pair images are sampled at 7.5 Hz. A two pass adaptive correlation is applied. The first pass has a 64 px × 64 px interrogation window, with a Gaussian weighting and 50% window overlap. The second pass has a 24 px × 24 px interrogation window and a 75% window overlap. Averaged fields are generated from the full time series and a 3 × 3 filter is used to smoothen the vector fields.

2.4. Vortex detection criteria

Vortices are detected with the γ_1 and the γ_2 criteria (Graftieaux et al., 2001), which have been successfully applied to PIV data (Rabinovitch et al., 2012; Harbig et al., 2013; Pitt Ford and Babinsky, 2013). The γ_2 criterion is the non-Galilean invariant version of the γ_1 criterion, as the local convection velocity is subtracted. Fig. 5 shows a schematic drawing of the γ_1 algorithm. The γ_1 criterion at a point P is computed using the PIV data within a square window S of size $2l \times 2l$ centred in P. At each point M within S, the sine of the angle θ_M between the vector **PM** and the velocity $\mathbf{u}_M$ is computed. The γ_1 value in P is given by

$$\gamma_1 = \frac{1}{N}\sum_S \frac{\mathbf{PM} \times \mathbf{u}_M}{||\mathbf{PM}||\cdot||\mathbf{u}_M||} = \frac{1}{N}\sum_S \sin(\theta_M), \tag{1}$$

where N is the number of grid points in S.

In the γ_2 criterion, the average convection velocity $\langle \mathbf{u} \rangle$ in the region S is subtracted from every velocity point in the interrogation window, such that

$$\gamma_2 = \frac{1}{N}\sum_S \frac{\mathbf{PM} \times (\mathbf{u}_M - \langle \mathbf{u} \rangle)}{||\mathbf{PM}||\cdot||\mathbf{u}_M - \langle \mathbf{u} \rangle||}, \tag{2}$$

where

$$\left\langle \mathbf{u} \right\rangle = \frac{1}{N}\sum_S \mathbf{u}_M. \tag{3}$$

2.5. Calibration of the vortex detection criteria

To calibrate the γ_1 and γ_2 criteria, these are tested on an isolated Lamb-Oseen vortex. The tangential velocity of the Lamb-Oseen vortex is

$$u_\theta = \frac{\Gamma_{LO}}{2\pi r}\left(1 - \exp\left(-\frac{r^2}{l_0^2}\right)\right), \tag{4}$$

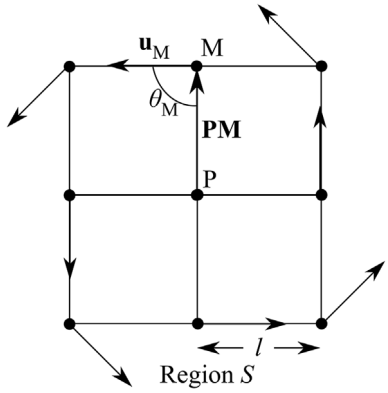

Fig. 5. Vortex detection algorithm.

where Γ_{LO} is the strength of the vortex, r is the radial coordinate and l_0 is the core vortex radius, defined as the radial coordinate where the tangential velocity is maximum. Its circulation is given by

$$\Gamma = \Gamma_{LO}\left(1 - \exp\left(-\frac{r^2}{l_0^2}\right)\right). \tag{5}$$

The γ_1 and γ_2 criteria for the Lamb-Oseen vortex are shown in Fig. 6. The γ_2 criterion is computed for two different sizes l of the interrogation window S: $l/l_0 = 0.64$ and 0.80; for γ_1, $l/l_0 = 0.16$. The centre of the vortex is identified by the maximum of both the γ_1 and γ_2 criteria, while the radius of the vortex core is identified by $|\gamma_2| = 2/\pi$.

A random error $\varepsilon = 15\%\, u_\theta$ is included to model the effect of PIV noise that is generated during acquisition and post-processing (Morgan et al., 2009). A 15% noise in γ_1 is found to decrease the magnitude of the detection peak by 30%. When l/l_0 decreases, γ_2 shows greater fluctuations and it behaves more like a local criterion. This leads to the underestimation of the vortex core size. For the γ_1 criterion, the smaller the l/l_0 is set, the narrower the detection peak becomes (Graftieaux et al., 2001). Varying the window size of the γ_2 criterion results in different γ_2 contours, but the threshold $|\gamma_2| = 2/\pi$ that corresponds to the core size of the Lamb-Oseen vortex is almost independent of the window size.

In the present experiment, the LEV core size is found to be ca. $l_0 = 0.1c$. The size l of the interrogation window is set to $l/l_0 = 0.16$ and 0.80 for γ_1 and γ_2, respectively. The noise level in the experiment is estimated to be ca. 15% u_θ. In fact, the maximum $|\gamma_1|$ on the sail is 0.7.

2.6. Complex potential model

In order to estimate the contribution of the LEV to the lift of the sail, a potential flow model of a circular arc is developed. The arc has the same chord c and maximum camber 2μ than the considered sail's section, and it experiences a uniform flow with the same free stream velocity U_∞ and angle of attack α with respect to the chord. The arc can be mapped onto a rotating circular cylinder whose external flow has the same circulation than the arc. The cylinder is defined in the complex plane ζ, where the complex coordinate

$$\zeta \equiv X + iY \equiv re^{i\theta} \tag{6}$$

identifies a position vector in the Cartesian coordinates (X, Y) and in the polar coordinates (r, θ). The velocity potential $\phi = \phi(\zeta)$ and the stream function $\psi = \psi(\zeta)$ are such that the velocity in the $X-$ direction is

$$U \equiv \frac{\partial \phi}{\partial X} \equiv \frac{\partial \psi}{\partial Y}, \tag{7}$$

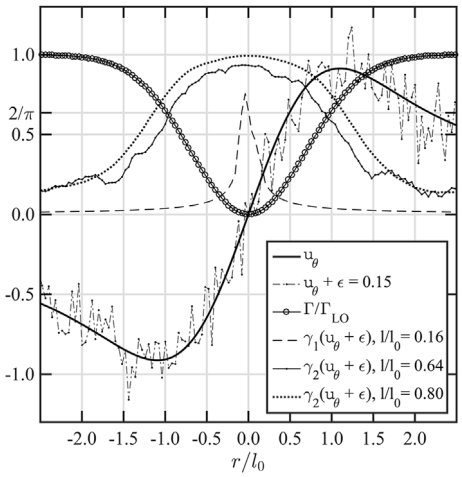

Fig. 6. γ_1 and γ_2 criteria for a Lamb-Oseen vortex.

and the velocity in the $Y-$ direction is

$$V \equiv \frac{\partial \phi}{\partial Y} \equiv -\frac{\partial \psi}{\partial X}. \tag{8}$$

The complex potential is

$$F(\zeta) \equiv \phi(\zeta) + i\psi(\zeta), \tag{9}$$

and the complex velocity is

$$W(\zeta) \equiv \frac{\partial F(\zeta)}{\partial \zeta} = U - iV. \tag{10}$$

The complex velocity provides the velocity field around the rotating cylinder. The cylinder is centred in $\zeta_0 = \mu e^{i\pi/2} = i\mu$ and has a radius $R = c/(4\cos\beta)$, where $\beta = \arctan(4\mu/c)$ (Fig. 7). And the maximum camber is 2μ.

The velocity field in the ζ plane of the cylinder can be mapped onto the plane $\hat{z}$ of the circular arc with the Joukowski transformation

$$\hat{z} = \zeta + \frac{(R\cos\beta)^2}{\zeta}. \tag{11}$$

In the $\hat{z}$ plane, the coordinate system is centred in the middle of the chord, such that the $\hat{x}-$ axis is in the direction of the chord and positive toward the trailing edge, and the $\hat{y}-$ axis is positive toward the suction side.

Finally, a further transformation

$$z = \hat{z}e^{-i\alpha} \tag{12}$$

allows a description of the flow field in the flume reference system, where the $x-$ axis is aligned with the free stream velocity U_∞. These two transformations are shown in Fig. 8.

The complex potential of the cylinder in the ζ plane is

$$F_0(\zeta) = U_\infty(\zeta - \zeta_0)e^{-i\alpha} + \frac{U_\infty R^2 e^{i\alpha}}{\zeta - \zeta_0} - \frac{i\Gamma_0}{2\pi}\ln(\zeta - \zeta_0), \tag{13}$$

where

$$\Gamma_0 = -4\pi U_\infty R\sin(\alpha + \beta) \tag{14}$$

is the circulation of the cylinder. Circulation values are defined positive anticlockwise.

The LEV can be modelled as a free vortex in the ζ plane. The circulation of the free vortex Γ_{LEV} is computed from the measured flow field, as the integral of the tangential velocity over the closed iso-line $\mathbf{l}$ of the γ_2 criterion, where $\gamma_2 = 0.67$:

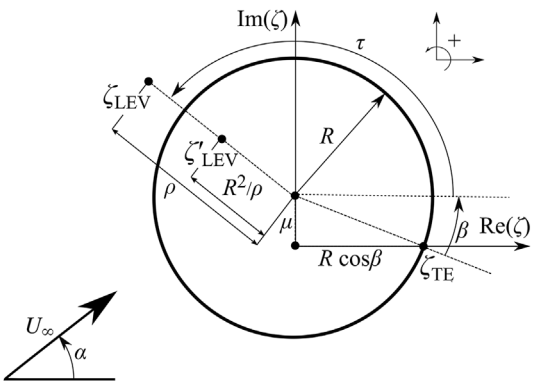

Fig. 7. Complex potential model in the ζ plane.

$$\Gamma_{\mathrm{LEV}} = \oint_{|\gamma_2|=0.67} \mathbf{u}\cdot\mathrm{d}\mathbf{l}. \tag{15}$$

A correction is then applied as described in the following Sec. 2.7.

The coordinates of the centre of the LEV, determined with the γ_2 criteria, are used to compute its polar coordinates in terms of ρ and τ in the ζ plane

$$\zeta_{LEV} = \rho e^{i\tau} + \mu e^{i\pi/2}. \tag{16}$$

If only one free vortex was added, the cylinder would no longer be impermeable and in the $\hat{z}$ plane, the Kutta condition would not be satisfied at the trailing edge. In order to restore the impermeability of the cylinder, a mirror vortex with circulation $-\Gamma_{\mathrm{LEV}}$ must be placed inside of the cylinder at the inverse square point

$$\zeta'_{LEV} = \frac{R^2}{\rho}e^{i\tau} + \mu e^{i\pi/2}. \tag{17}$$

The resulting complex potential is

$$\begin{aligned} F(\zeta) &= U_\infty(\zeta - \zeta_0)e^{-i\alpha} \\ &+ \frac{U_\infty R^2 e^{i\alpha}}{(\zeta - \zeta_0)} - \frac{i(\Gamma_b + \Gamma_{\mathrm{LEV}})}{2\pi}\ln(\zeta - \zeta_0) \\ &- \frac{i\Gamma_{\mathrm{LEV}}}{2\pi}\ln\frac{\zeta - \zeta_{\mathrm{LEV}}}{\zeta - \zeta'_{\mathrm{LEV}}}. \end{aligned} \tag{18}$$

where the first line is the contribution of the free stream, the second line is due to the cylinder and the circulation in the centre of the cylinder and the third line is due to the free vortices in ζ_{LEV} and ζ'_{LEV}. By derivation of the complex potential, we compute the complex velocity as

$$\begin{aligned} W(\zeta) &= U_\infty e^{-i\alpha} \\ &- \frac{U_\infty R^2 e^{i\alpha}}{(\zeta - \zeta_0)^2} - \frac{i(\Gamma_b + \Gamma_{\mathrm{LEV}})}{2\pi}\frac{1}{\zeta - \zeta_0} \\ &- \frac{i\Gamma_{\mathrm{LEV}}}{2\pi}\frac{\zeta - \zeta'_{\mathrm{LEV}}}{\zeta - \zeta_{\mathrm{LEV}}}. \end{aligned} \tag{19}$$

Having derived the complex velocity for a generic Γ_b, it is now possible to compute the Γ_b that satisfies the Kutta condition. The ζ_{TE} coordinate, corresponding to the trailing edge of the circular arc in the $\hat{z}$ plane, must be a stagnation point of the cylinder. Using Eq. (19) to evaluate $W(\zeta = \zeta_{TE}) = 0$, we find that for multiple vortices

$$\Gamma_b = \Gamma_0 - \sum \kappa_i \Gamma_i, \tag{20}$$

where

$$\kappa_i \equiv \frac{1 - \frac{\rho_i}{R}\cos(\beta + \tau_i)}{\frac{1}{2}\left[\left(\frac{\rho_i}{R}\right)^2 + 1\right] - \frac{\rho_i}{R}\cos(\beta + \tau_i)}, \tag{21}$$

is a geometric coefficient that takes into account the relative position of the i-th LEV with respect to the arc. For the vortices that are on the arc, $\rho_i = R$ and $\kappa_i = 1$.

Using the Kutta-Joukowski theorem, the lift coefficient for the circular arc in the presence of the LEV is written as

$$C_L = -\frac{\Gamma_b + \Gamma_{\mathrm{LEV}}}{\frac{1}{2}U_\infty c} = -\frac{\Gamma_b}{\frac{1}{2}U_\infty c} - \frac{\Gamma_{\mathrm{LEV}}}{\frac{1}{2}U_\infty c}. \tag{22}$$

In the Results, the lift coefficient contribution due to the bound circulation

$$C_{L_b} \equiv -\frac{\Gamma_b}{\frac{1}{2}U_\infty c} \tag{23}$$

and the lift coefficient contribution due to the LEV

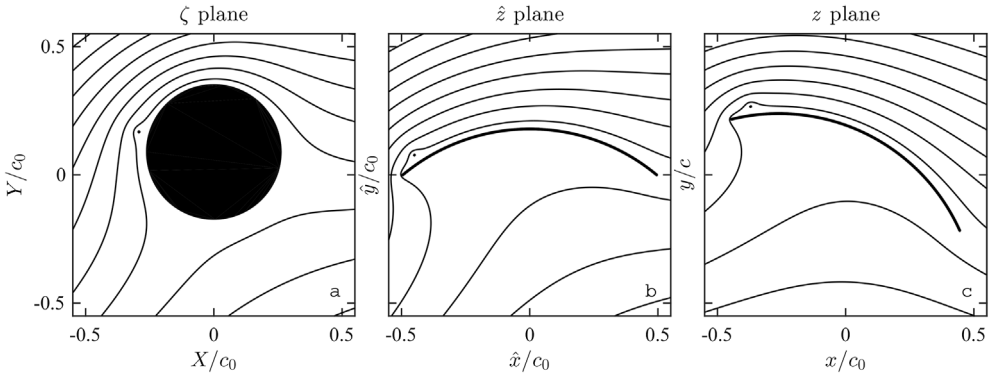

Fig. 8. Velocity potential streamlines in the ζ plane (**a**) and the transformations in Eq. (11) (**b**) and Eq. (12) (**c**).

$$C_{L_{\mathrm{LEV}}} \equiv -\frac{\Gamma_{\mathrm{LEV}}}{\frac{1}{2}U_\infty c} \tag{24}$$

will be compared.

It is important to recall that this is a two-dimensional model that only applies to the particular PIV measurement plane that is being analysed. With this approach we neglect the out-of-plane momentum fluxes, the effect of viscosity (including trailing edge separation) and unsteady effects. The model accounts only for the strongest nuclei of vorticity included in the PIV window, as well as their mirror vortices. Once the vortices have been shed downstream, these are no longer included, nor are their image vortices. For Kelvin's theorem, the circulation shed downstream with an LEV must be balanced by an equal production and shedding of counter-rotating vorticity from the trailing edge. As long as the bound circulation remains almost constant, as in the tested conditions, the net vorticity shed in the wake must be small. Here we assume that the main contribution to the effective bound circulation is due to the strong nuclei of vorticity near the arc, and thus we neglect the contribution of the shed leading-edge and trailing-edge vorticity. Therefore, the lift that is obtained with the model is a first order estimate of the cross-sectional lift.

2.7. Computation of vortex circulation

The circulation of the vortex was computed by integration of the velocity over the iso-contours of (Eq. (15)). Low γ_2 values resulted in large integration paths with unclear distinction between the different nuclei of vorticity. On the other hand, high γ_2 values do not allow capturing some of the vortices. A clear description of the vorticity field is achieved when γ_2 ranges between 0.6 and 0.8. On average, the maximum value of the circulation is achieved with $\gamma_2 \approx 0.67$. This is consistent with the values adopted by Pitt Ford and Babinsky (2013) and by Eslam Panah et al. (2015).

As shown in Fig. 6, $\gamma_2 = 0.67$ corresponds to a circular contour with $r/l_o = 1.1$ around an ideal Lamb-Oseen vortex. However, to include all of the vorticity of the vortex, it should be necessarily to integrate over a $\gamma_2 = 0.20$ that corresponds to $r/l_o = 2.5$. Because the contour $\gamma_2 = 0.20$ was not available, a methodology similar to that proposed by Morgan et al. (2009) was followed to estimate the circulation left outside of the iso-contour $\gamma_2 = 0.67$. The circulation was computed integrating over different γ_2 contours between 0.6 and 0.8, and then these circulations were fitted with those of an ideal Lamb-Oseen vortex (Eq. (5)). The fitting, which was performed with a least square method, allowed to identify the total circulation of the vortex. The total circulation was found to be 35% higher than that computed with $\gamma_2 = 0.67$. Therefore, the integrated circulation of each vortex was multiplied by 1.35.

3. Results

3.1. Velocity and vorticity fields

Fig. 9 shows the time-averaged vector fields, streamlines and vorticity contours for the planes A, B and C. The local angle of attack increases from plane A to plane C due to the twist of the sail. The maximum camber also increases from plane A to plane C. Planes A and B show flow separation at the leading edge and flow reattachment further downstream. The concentric streamlines of Fig. 9e show the averaged flow field of a leading-edge vortex. The streamlines are concentric because part of the onset flow is trapped inside the vortex core and ejected out of the plane of the figure toward the head of the sail. As showed in the following section (3.2), some of the vorticity which is generated at the sharp leading edge, is convected inside a vortex that is stably attached to the leading edge. The permanent and three-dimensional nature of this flow structure make it more similar to the LEV of a delta wing, rather than the laminar separation bubble, which is defined in a time-averaged sense, of a thin foil at transitional Reynolds numbers.

On plane C, the flow remains attached at the leading edge but separates at $x/c = -0.3$ without reattaching. Vorticity contours show the shear layer generated at the leading edge for the three planes. The separated shear layer curves down in planes A (Fig. 9g) and B (Fig. 9h) showing the effect of the high circulation on these planes, while it is straighter on plane C (Fig. 9i) where trailing edge separation occurs.

The LEV is formed in the upper part of the sail (plane B) and grows in size towards the tip. The growth of the vortex is the result of the vorticity that, at every section, is convected in the axis of the vortex and that, hence, accumulates towards the tip. From plane B to plane A, it can be observed that the axis of the vortex moves away from the sail surface and inboard.

3.2. Unsteady flow

The vortex dynamics is investigated using a data set of 305 pair of images sampled every $t^* = 0.134$, where time t is made non-dimensional with the chordwise convection period c_0/U_∞, i.e. $t^* \equiv tU_\infty/c_0$. Consider i the index of the pair of images, where $1 < i < 305$. Fig. 10 shows the γ_2 contours for the instantaneous velocity fields on plane B for a period $\Delta t^* = 3.484$ within the interval $16 < i < 42$. A stable LEV, which remains attached to the leading edge, can be observed throughout this sequence. The incipiency of vortex shedding can be observed towards the end of the sequence. The LEV on this plane is, in fact, intermittently stable. In particular, it is stable for the sampling periods $1 < i < 65$, $115 < i < 170$ and $264 < i < 305$.

Examples of shedding LEV are presented in Fig. 11 on the planes A, B and C. Each sequence has a time length $\Delta t^* = 1.072$, but the sequences are taken at different times on each plane, since the experimental setup does not allow simultaneous recording of the planes. It can be observed that the LEV is not stable and it is shed downstream with a convective velocity of approximately $0.6U_\infty$ in plane A and B, and $0.3U_\infty$ in plane C.

The vortical structures observed in Figs. 10 and 11 are the results of Kelvin-Helmholtz instabilities of the vortex sheet generated at the leading edge. This flow field resemble the separated-reattached flow downstream of sharp obstacles (Bradshaw and Wong, 1972) and blunt flat

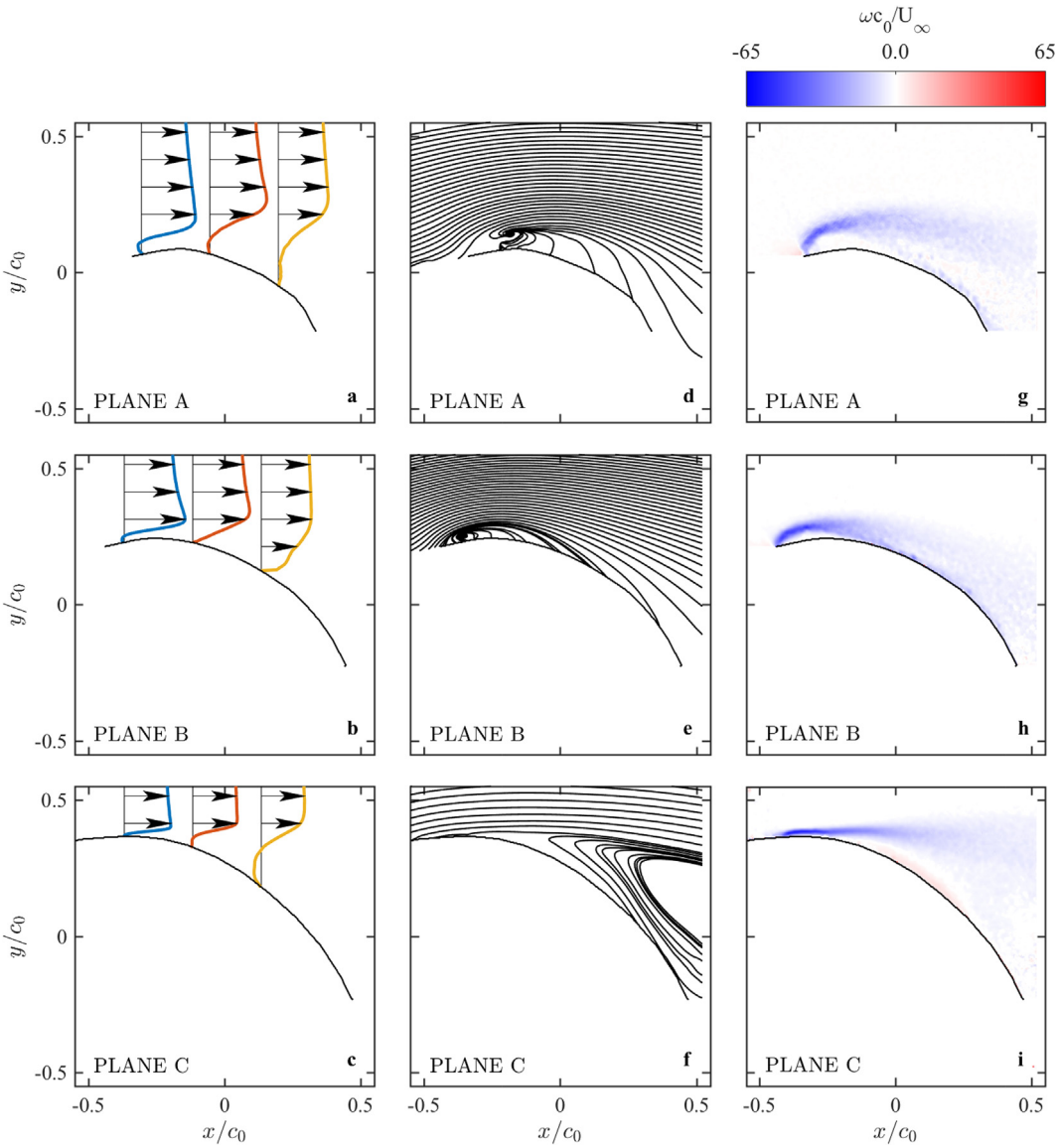

Fig. 9. Time-averaged velocity profiles (**a, b, c**), streamlines (**d, e, f**) and contours of non-dimensional vorticity (**g, h, i**) on the planes A, B and C. Data is averaged over a period $\Delta t^* = 40.736$, in the interval $1 < i < 305$, where i is the number of the PIV image pair.

plates (Kiya and Sasaki, 1983; Bradshaw and Wong, 1972; Ota et al., 1981; Stevenson et al., 2016). The coexistence of a stationary and unsteady vortices is also observed in other vortex dominated flows such as, for example, on delta wings. Gad-El-Hak and Blackwelder (1985) were the first to observed experimentally nuclei of unsteady vorticity coexisting with the primary LEV on delta wings. In a successive work, (Gad-El-Hak and Blackwelder, 1987), the same authors recognised that these unsteady vortices were due to Kelvin-Helmholtz instabilities of the shear layer. Small vorticity concentrations were also observed on non-slender delta wings (Yaniktepe and Rockwell, 2004; Gursul et al., 2005; Muir et al., 2017), which have a swept angle more similar to that of a sail. The averaged vorticity of non-slender delta wings shows a dual-vortex substructure system that resemble the elongated vortex structure near the leading edge of the sail (Fig. 10). Yaniktepe and Rockwell (2004) observed that these nuclei of vorticity could be associated to either jitter of the nominally stationary LEV or to instabilities of the shear layer separating from the leading edge.

Consistently with the observations made in Sec.3.1 on the time averaged flow field, the stationary vortex system near the leading edge in plane A is larger, more distant from the sail surface and more inboard than in plane B.

3.3. Contribution of the vortex circulation to the total circulation

The underlying question that this work aims to address, is the effective contribution of the LEV to the sail performance. Recalling that the total lift coefficient can be broken down into the contribution of the bound circulation C_{L_b} and the contribution of the vortex circulation $C_{L_{LEV}}$, the ratio $C_{L_{LEV}}/C_{L_b} = \Gamma_{LEV}/\Gamma_b$ is computed. A first conservative estimate is made that the Kutta condition is satisfied when the LEV is present. Since trailing edge separation actually occurs and the Kutta condition is not satisfied, the computed bound circulation is higher than the real value and thus the computed relative contribution of the LEV is conservative.

The coefficient κ in Eq. (21) takes into account the distance of the vortices from the sail. Therefore, the total contribution to the sail's circulation provided by the vortices is $\sum \kappa_i \Gamma_i$.

Fig. 12b shows how this varies across a sequence of image pairs. Three examples are presented: the stable LEV on plane B in Fig. 10j-r, the shedding LEV on the same plane in Fig. 11j-r, and the shedding LEV on plane A in Fig. 11a-i. More results are included in the supplementary data available in the Edinburgh digital repository (datashare.is.ed.ac.uk). In most of the cases examined, the total contribution of the vortex

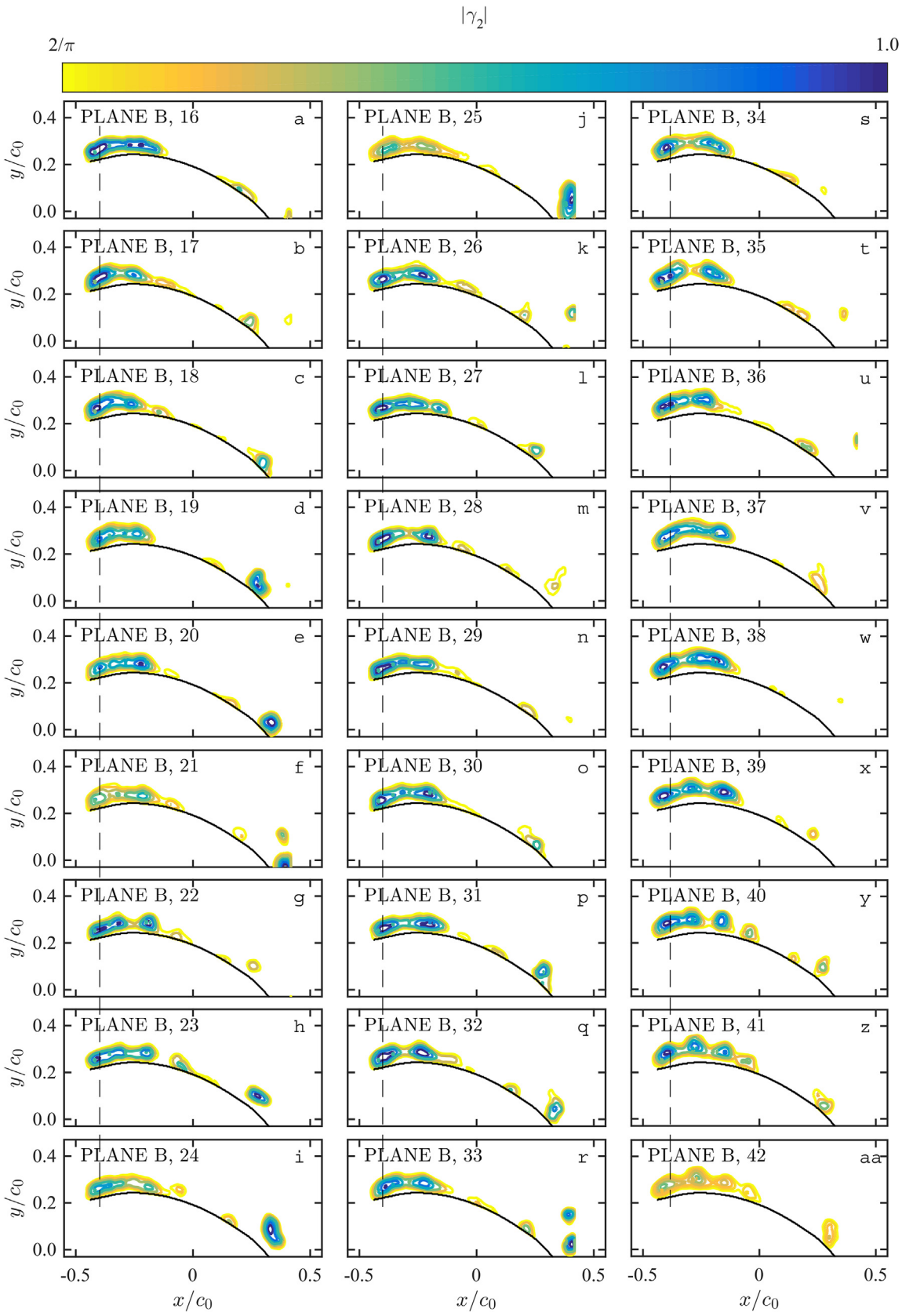

Fig. 10. γ_2 criterion on instantaneous velocity fields for plane B (**a**-**aa**). Data corresponds to a period of $\Delta t^* = 3.484$, in the interval $16 < i < 42$.

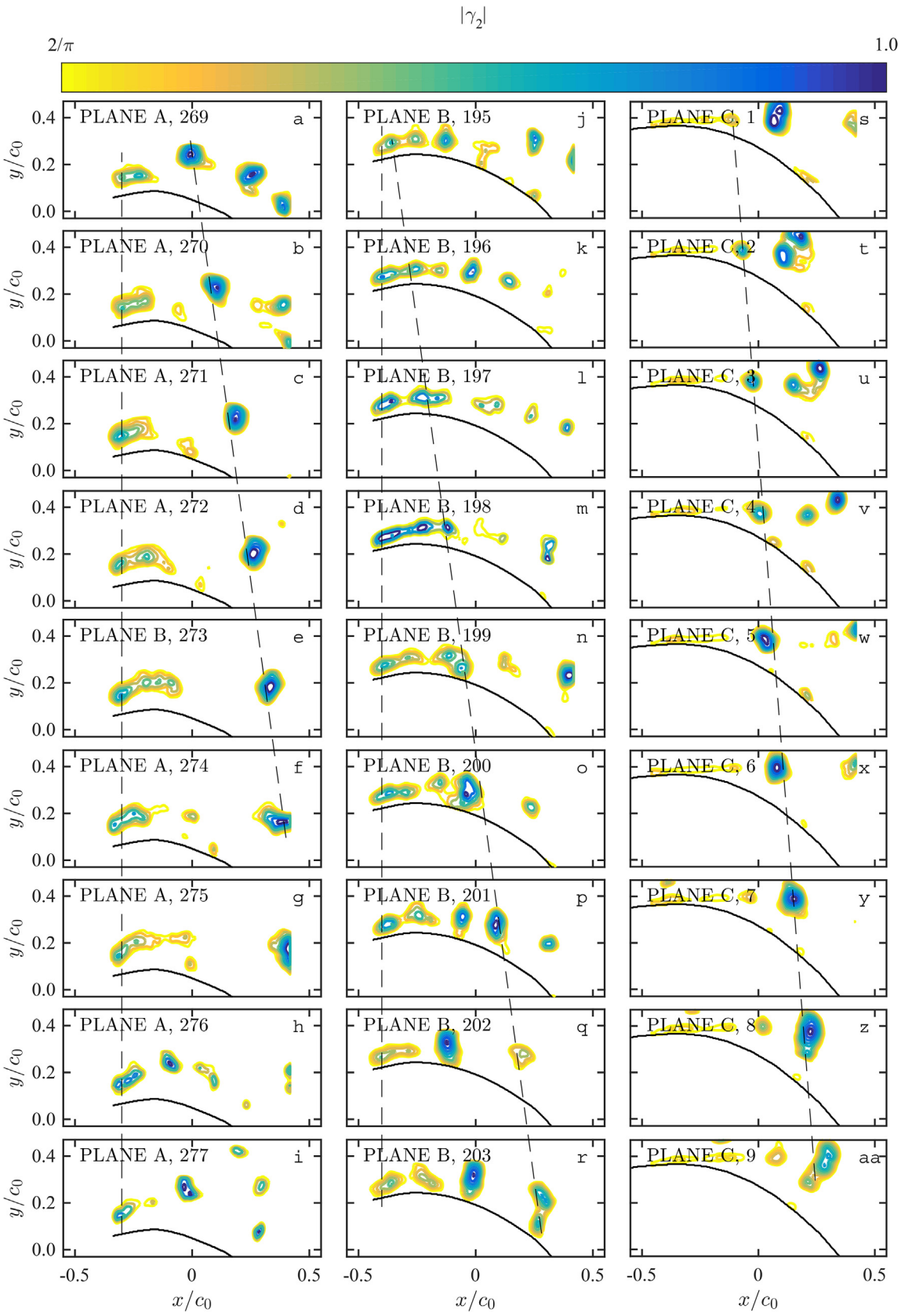

Fig. 11. γ_2 criterion on instantaneous velocity fields showing vortex shedding for planes A (**a**–**i**), B (**j**–**r**) and C (**s**-**aa**). Data corresponds to a period of $\Delta t^* = 1.072$, in the intervals $269 < i < 277$, $195 < i < 203$ and $1 < i < 9$ for planes A, B and C, respectively.

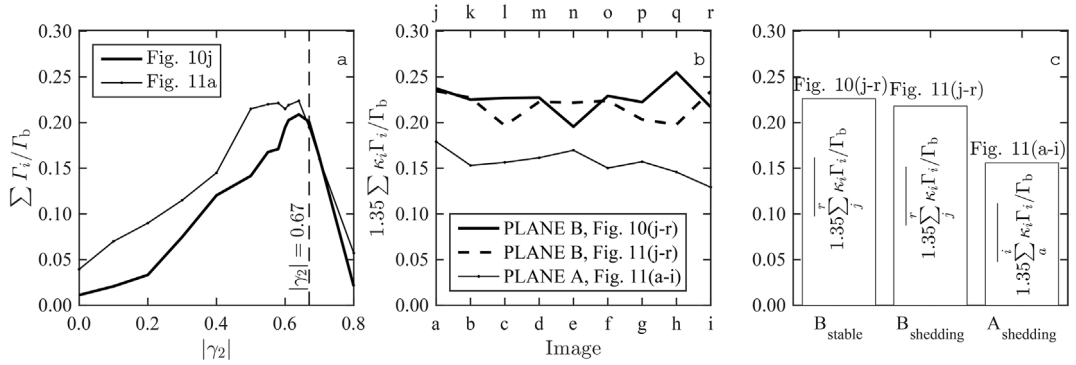

Fig. 12. **a** Sum of circulation of free vortices $\sum \Gamma_i/\Gamma_b$ from Figs. 10j and 11a calculated with different γ_2 iso-contour values. **b** Instantaneous sum of circulation $\sum \kappa_i \Gamma_i/\Gamma_b$ (adjusted by the correction factor 1.35) of the free vortices in Fig. 10(j–r), 11(j–r) and Fig. 11(a–i), integrated along $|\gamma_2| = 0.67$. **c** Average circulation for the three cases presented in Fig. 12b.

circulation to the sail's circulation is between 10% and 20% of the bound circulation. At every instant, the contribution of the vortex circulation is higher in B than in plane A, and the difference between the planes is larger than the variations between different instants on the same plane.

The time-averaged contribution of the vortex circulation ($\overline{\sum_{a,j}^{i,r} \kappa_i \Gamma_i}$) is presented in Fig. 12c for the same cases as in Fig. 12b. Here it is clear that the presence of a stable LEV, as opposed to a series of shedding vortices, provides only a marginally higher averaged circulation. It must be remembered, however, that increasing the vortex circulation in the front of the sail, as with a stable LEV, rather than on the rear, would lead to a higher driving force. This effect, however, cannot be assessed with the present analysis.

4. Conclusions

Recent high-fidelity numerical simulations (Viola et al., 2014) suggested that a LEV is formed at the leading edge of asymmetric spinnakers and that it remains stably attached to the sail providing lift augmentation. This finding is investigated in the present paper. A model-scale asymmetric spinnaker is tested in uniform flow in a water flume at a Reynolds number of U_∞ is 1.3×10^4. The time-averaged velocity field measured with PIV confirms the numerical results. On the highest half of the sail, the LEV is formed and it grows in size towards the head of the sail, while its axis moves away from the sail surface and inboard of the sail. Downstream of the LEV, the time-averaged flow reattaches and an attached boundary layer is formed. Conversely, on the lowest half of the sail, where trailing edge separation is dominant, the LEV is absent or of negligible dimensions and the separation point is well upstream of the mid-chord.

The time-resolved flow field reveals that the LEV remains attached to the leading edge intermittently and only on a section at 3/4th of the sail span. For a period of time of the order of $10c/U_\infty$, the LEV is stably attached, and then for a period of similar length the LEV is shed and convects downstream at 60% of the free stream velocity. The contribution to the sail sectional lift of the vortices is higher than 15%–25%, where the estimation is very conservative because a Kutta condition has been assumed to compute the bound circulation. These results suggest that the performance of asymmetric spinnakers could be enhanced significantly by controlling the formation and stability of the LEV.

Acknowledgements

This work was funded by the Consejo Nacional de Ciencia y Tecnología (CONACYT (329623/384490)).

Appendix A. Supplementary data

Supplementary data related to this article can be found at https://doi.org/10.1016/j.oceaneng.2018.02.029.

References

Bethwaite, F., 1993. High Performance Sailing. Waterline Books, UK.
Borazjani, I., Daghooghi, M., 2013. The fish tail motion forms an attached leading edge vortex. Proc R Soc B 280, 20122071. https://doi.org/10.1098/rspb.2012.2071.
Bot, P., Viola, I.M., Flay, R.G.J., Brett, J.S., 2014. Wind-tunnel pressure measurements on model-scale rigid downwind sails. Ocean. Eng. 90, 84–92. https://doi.org/10.1016/j.oceaneng.2014.07.024.
Bradshaw, P., Wong, F.Y.F., 1972. The reattachment and relaxation of a turbulent shear layer. J. Fluid Mech. 52, 113135. https://doi.org/10.1017/S002211207200299X.
Corke, T.C., Thomas, F.O., 2015. Dynamic stall in pitching airfoils: aerodynamic damping and compressibility effects. Annu. Rev. Fluid Mech. 47, 479–505. https://doi.org/10.1146/annurev-fluid-010814-013632.
Ellington, C.P., 1999. The novel aerodynamics of insect flight: applications to micro-air vehicles. J. Exp. Biol. 202, 3439–3448.
Eslam Panah, A., Akkala, J.M., Buchholz, J.H.J., 2015. Vorticity transport and the leading-edge vortex of a plunging airfoil. Exp. Fluid 56, 160. https://doi.org/10.1007/s00348-015-2014-7.
Gad-El-Hak, M., Blackwelder, R.F., 1985. The discrete vortices from a delta wing. AIAA J. 23, 961–962. https://doi.org/10.2514/3.9016. https://doi.org/10.2514/3.9016.
Gad-El-Hak, M., Blackwelder, R.F., 1987. Control of the discrete vortices from a delta wing. AIAA J. 25, 1042–1049. https://doi.org/10.2514/3.9740. https://doi.org/10.2514/3.9740.
Garmann, D.J., Visbal, M.R., Orkwis, P.D., 2013. Three-dimensional flow structure and aerodynamic loading on a revolving wing. Phys. Fluids 25. https://doi.org/10.1063/1.4794753.
Gordnier, R.E., Visbal, M.R., Gursul, I., Wang, Z., 2009. Computational and experimental investigation of a nonslender delta wing. AIAA J. 47, 1811–1825. https://doi.org/10.2514/1.37848.
Graftieaux, L., Michard, M., Grosjean, N., 2001. Combining PIV, POD and vortex identification algorithms for the study of unsteady turbulent swirling flows. Meas. Sci. Technol. 12, 1422–1429. https://doi.org/10.1088/0957-0233/12/9/307.
Gursul, I., Gordnier, R., Visbal, M., 2005. Unsteady aerodynamics of nonslender delta wings. Prog. Aero. Sci. 41, 515–557. https://doi.org/10.1016/j.paerosci.2005.09.002.
Gursul, I., Wang, Z., Vardaki, E., 2007. Review of flow control mechanisms of leading-edge vortices. Prog. Aero. Sci. 43, 246–270. https://doi.org/10.1016/j.paerosci.2007.08.001.
Harbig, R.R., Sheridan, J., Thompson, M.C., 2013. Reynolds number and aspect ratio effects on the leading-edge vortex for rotating insect wing planforms. J. Fluid Mech. 717, 166–192. https://doi.org/10.1017/jfm.2012.565.
Hubel, T.Y., Tropea, C., 2010. The importance of leading edge vortices under simplified flapping flight conditions at the size scale of birds. J. Exp. Biol. 213, 1930–1939. https://doi.org/10.1242/jeb.047886.
Jardin, T., David, L., 2014. Spanwise gradients in flow speed help stabilize leading-edge vortices on revolving wings. Phys. Rev. E 90, 013011. https://doi.org/10.1103/PhysRevE.90.013011.
Kiya, M., Sasaki, K., 1983. Structure of a turbulent separation bubble. J. Fluid Mech. 137, 83113. https://doi.org/10.1017/S002211208300230X.
Larsen, J.W., Nielsen, S.R.K., Krenk, S., 2007. Dynamic stall model for wind turbine airfoils. J. Fluid Struct. 23, 959–982. https://doi.org/10.1016/j.jfluidstructs.2007.02.005.
Lentink, D., Dickson, W.B., van Leeuwen, J.L., Dickinson, M.H., 2009. Leading-edge vortices elevate lift of autorotating plant seeds. Science 324, 1438–1440. https://doi.org/10.1126/science.1174196.
Lentink, D., Müller, U.K., Stamhuis, E.J., de Kat, R., van Gestel, W., Veldhuis, L.L.M., Henningsson, P., Hedenström, A., Videler, J.J., van Leeuwen, J.L., 2007. How swifts control their glide performance with morphing wings. Nature 446, 1082–1085. https://doi.org/10.1038/nature05733.

McWilliams, J.C., 1984. The emergence of isolated coherent vortices in turbulent flow. J. Fluid Mech. 146, 2143. https://doi.org/10.1017/S0022112084001750.
Morgan, C.E., Babinsky, H., Harvey, J.K., 2009. Vortex detection methods for use with PIV and CFD data. In: Proceedings of the 47th AIAA Aerospace Sciences Meeting, Orlando, Florida, USA. https://doi.org/10.2514/6.2009-74.
Muijres, F.T., Johansson, L.C., Barfield, R., Wolf, M., Spedding, G.R., Hedenström, A., 2008. Leading-edge vortex improves lift in slow-flying bats. Science 319, 1250–1253. https://doi.org/10.1126/science.1153019.
Muir, R.E., Arredondo-Galeana, A., Viola, I.M., 2017. The leading-edge vortex of swift wing-shaped delta wings. Royal Society Open Science 4. https://doi.org/10.1098/rsos.170077.
Nava, S., Cater, J., Norris, S., 2016. A comparison of RANS and LES for upwind sailing aerodynamics. In: Proceedings of the 22nd Chesapeake Sailing Yacht Symposium, Annapolis, Mryland, USA.
Ota, T., Asano, Y., ichi Okawa, J., 1981. Reattachment length and transition of the separated flow over blunt flat plates. Bulletin of JSME 24, 941–947. https://doi.org/10.1299/jsme1958.24.941.
Pitt Ford, C., Babinsky, H., 2013. Lift and the leading-edge vortex. J. Fluid Mech. 720, 280–313. https://doi.org/10.1017/jfm.2013.28.
Rabinovitch, J., Brion, V., Blanquart, G., 2012. Effect of a splitter plate on the dynamics of a vortex pair. Phys. Fluids 24. https://doi.org/10.1063/1.4737878.
Srygley, R.B., Thomas, A.L.R., 2002. Unconventional lift-generating mechanisms in free-flying butterflies. Nature 420, 660–664. https://doi.org/10.1038/nature01223.
Stevenson, J.P., Walsh, E.J., Nolan, K.P., 2016. Visualization of the vortex and reverse-flow structure of a separation bubble. J. Vis. 19, 175–177. https://doi.org/10.1007/s12650-015-0306-x. https://doi.org/10.1007/s12650-015-0306-x.
Viola, I.M., Bartesaghi, S., Van-Renterghem, T., Ponzini, R., 2014. Detached eddy simulation of a sailing yacht. Ocean. Eng. 90, 93–103. https://doi.org/10.1016/j.oceaneng.2014.07.019.
Viola, I.M., Bot, P., Riotte, M., 2013. Upwind sail aerodynamics: a RANS numerical investigation validated with wind tunnel pressure measurements. Int. J. Heat Fluid Flow 39, 90–101. https://doi.org/10.1016/j.ijheatfluidflow.2012.10.004.
Viola, I.M., Flay, R.G.J., 2009. Force and pressure investigation of modern asymmetric spinnakers. Int. J. Small Craft Technol. Trans. RINA Part B2 151, 31–40. https://doi.org/10.3940/rina.ijsct.2009.b2.98.
Viola, I.M., Flay, R.G.J., 2010. Pressure distributions on modern asymmetric spinnakers. Int. J. Small Craft Technol. Trans. RINA Part B1 152, 41–50. https://doi.org/10.3940/rina.ijsct.2010.b1.103.
Viola, I.M., Flay, R.G.J., 2011a. Sail aerodynamics: understanding pressure distributions on upwind sails. Exp. Therm. Fluid Sci. 35, 1497–1504. https://doi.org/10.1016/j.expthermflusci.2011.06.009.
Viola, I.M., Flay, R.G.J., 2011b. Sail pressures from full-scale, wind-tunnel and numerical investigations. Ocean. Eng. 38, 1733–1743. https://doi.org/10.1016/j.oceaneng.2011.08.001.
Viola, I.M., Flay, R.G.J., 2012. Sail aerodynamics: on-water pressure measurements on a downwind sail. J. Ship Res. 56, 197–206. https://doi.org/10.5957/JOSR.56.4.110003.
Viola, I.M., Flay, R.G.J., 2015. Aerodynamics of headsails: a review of measured surface pressures and expected flow fields. In: Proceedings of the 5th High Performance Yacht Design Conference, Auckland, New Zealand.
Wereley, S.T., Gui, L., Meinhart, C.D., 2002. Advanced algorithms for microscale particle image velocimetry. AIAA J. 40, 1047–1055.
Yaniktepe, B., Rockwell, D., 2004. Flow structure on a delta wing of low sweep angle. AIAA J. 42, 513–523. https://doi.org/10.2514/1.1207. https://doi.org/10.2514/1.1207.

ROYAL SOCIETY OPEN SCIENCE

rsos.royalsocietypublishing.org

Research

Cite this article: Muir RE, Arredondo-Galeana A, Viola IM. 2017 The leading-edge vortex of swift wing-shaped delta wings. *R. Soc. open sci.* **4**: 170077. http://dx.doi.org/10.1098/rsos.170077

Received: 27 January 2017
Accepted: 27 July 2017

Subject Category:
Physics

Subject Areas:
biomechanics/fluid mechanics

Keywords:
delta wing, bird wing aerodynamics, common swift *Apus apus*, leading-edge vortex, swept wing, particle image velocimetry

Author for correspondence:
Ignazio Maria Viola
e-mail: i.m.viola@ed.ac.uk

The leading-edge vortex of swift wing-shaped delta wings

Rowan Eveline Muir, Abel Arredondo-Galeana and Ignazio Maria Viola

Institute for Energy Systems, School of Engineering, University of Edinburgh, Edinburgh, UK

IMV, 0000-0002-3831-8423

Recent investigations on the aerodynamics of natural fliers have illuminated the significance of the leading-edge vortex (LEV) for lift generation in a variety of flight conditions. A well-documented example of an LEV is that generated by aircraft with highly swept, delta-shaped wings. While the wing aerodynamics of a manoeuvring aircraft, a bird gliding and a bird in flapping flight vary significantly, it is believed that this existing knowledge can serve to add understanding to the complex aerodynamics of natural fliers. In this investigation, a model non-slender delta-shaped wing with a sharp leading edge is tested at low Reynolds number, along with a delta wing of the same design, but with a modified trailing edge inspired by the wing of a common swift *Apus apus*. The effect of the tapering swift wing on LEV development and stability is compared with the flow structure over the unmodified delta wing model through particle image velocimetry. For the first time, a leading-edge vortex system consisting of a dual or triple LEV is recorded on a swift wing-shaped delta wing, where such a system is found across all tested conditions. It is shown that the spanwise location of LEV breakdown is governed by the local chord rather than Reynolds number or angle of attack. These findings suggest that the trailing-edge geometry of the swift wing alone does not prevent the common swift from generating an LEV system comparable with that of a delta-shaped wing.

1. Introduction

The leading-edge vortex (LEV) is a commonly found mechanism that, under the correct conditions, can significantly augment the lift generation of both manufactured and natural fliers [1–4]. The LEV is robust to kinematic change [1] and has been identified across a wide range of Reynolds numbers (Re) (table 1), from the laminar flow conditions ($10 < Re < 10^4$) of autorotating

THE ROYAL SOCIETY PUBLISHING

Table 1. Non-dimensional quantities are made non-dimensional using l, U_0 and the density of the water.

AR	aspect ratio (b^2/S)
b	span (m)
C_l	lift coefficient
c_r	root chord of the swift wing-shaped delta wing (m)
l	chordwise length of the wing (m)
N	number of grid points within the domain Π
P and M	two grid points within Π
Q	second invariant of the non-dimensional velocity-gradient tensor
Re	Reynolds number
S	area of the wing (m^2)
U_0	free stream velocity ($m\,s^{-1}$)
x	chordwise coordinate (m)
α	angle of attack (deg.)
Γ_2	vortex identification criterion (equation (2.1))
Λ	sweep back angle (deg.)
ω	non-dimensional vorticity
Π	two-dimensional, rectangular domain around P
$\mathbf{U_M}$	velocity vector at the grid point M ($m\,s^{-1}$,$m\,s^{-1}$, $m\,s^{-1}$)
$\tilde{\mathbf{U}}_\mathbf{P}$	mean velocity vector within Π ($m\,s^{-1}$, $m\,s^{-1}$, $m\,s^{-1}$)
$\hat{\mathbf{z}}$	unit vector normal to the measured plane (m, m, m)

seed pods [5] and in insect [1], bat [6] and small bird [7] flight, to the transitional and turbulent conditions over larger bird wings [8], fish fins [9], delta wings [10,11], helicopter rotors [12], sailing yachts [13] and wind turbines [14]. Increasingly driven by the potential exploitation of this effective lift mechanism for micro air vehicles (MAV), and facilitated by improvements in flow visualization and computational techniques, aerodynamicists and biologists alike now seek further understanding of aircraft and natural fliers at low to medium Re ($10 < Re < 10^5$), as the LEV is increasingly understood to be a valuable flight mechanism to apply by design.

Across the broad spectrum of delta-wing aircraft and natural fliers, an LEV's stability and ability to augment lift depend on numerous variables. Certain variables such as wing shape, sweep back angle (Λ) and angle of attack (α) can be identified and replicated, providing the potential for comparison between the two types of fliers. The determination and modelling of the wing kinematics of a natural flier, however, poses a more complex problem than that of man-made aircraft. Vortex lift is recorded at the same α, 30°, on both the extensively studied slender delta wing (e.g. [15], where $\Lambda = 75°$) and the more complex case of a bird wing, where a blunt-nosed, flapping model wing is tested at $\Lambda = 10°$ [8]. The number of variables in the latter study makes a comparison challenging, however, the simpler act of gliding flight can more readily be studied via the existing relative wealth of delta wing research; such a comparison may allow the examination of key variables in isolation.

Research into the aerodynamics of non-slender or 'low sweep' ($\Lambda < 60°$) delta wings is more limited than that available on slender ($\Lambda \geq 60°$) delta wings, despite the increased relevance of the non-slender configuration, as research into MAVs becomes increasingly active [16]. Many (e.g. [16–20]) have experimentally and computationally explored non-slender delta wings of $\Lambda = 50°$, with varying leading-edge radii and at a range of Re and α. These delta wings have a wing configuration comparable with that of the impressive natural fliers, the common swift *Apus apus*, when in non-diving, gliding flight. With a 'hand wing' sweep of $\Lambda = 50°$ [7], the narrow, protruding, anterior vein of the primary feather provides a sharp leading-edge [21], as is typical in delta wing design to promote leading-edge separation. The trailing-edge shape and surface area of a swift wing clearly differs from a delta-shaped wing, as the wing tapers to a point from the body to the tip. The wing shape and configuration during non-diving

gliding therefore conveniently allows comparison with a normal delta-shaped wing; the tapered wing of the swift can be simply represented by a modified trailing edge, and its effect on the flow structure can thus be elucidated.

This fundamental difference in trailing-edge shape should be explored if an analogy between the intricate LEV system of a natural flier and that of a more readily examined delta wing is to be made (e.g. [22]); such an analogy has in fact been identified as critical in enhancing understanding of natural flight (e.g. [23]). The lift produced by bird wings can be described by the circulation around a streamlined body, supported in specific circumstances by the circulation of the LEV. The delta wing provides a paradigm example of the latter, where the wing lift can be almost entirely due to LEV circulation. The formation and stability of the LEV on natural fliers can therefore be studied with this simplified geometry; the absence of more complex bird wing geometry, kinematics, flexibility, etc., facilitating understanding of the underlying aerodynamic mechanisms, as the accurate testing of natural fliers continues to challenge researchers who seek to apply this robust, high-lift mechanism by design.

Taylor *et al.* [16] tested a sharp leading-edge delta wing model at $\Lambda = 50^\circ$ and low *Re* in a water tunnel. Using particle imaging velocimetry (PIV) and ink injection, they present the first experimental evidence of the development, not of a single LEV, but a dual LEV, from $2.5^\circ \leq \alpha \leq 15^\circ$ at $Re = 13\,000$. A dual LEV is a system now commonly described on non-slender delta wings at low incidence [24], though, to date, it is not known to have been identified on bird wings. It comprises a larger, primary leading-edge vortex along with a second, minor, co-rotating vortex, separated by a region of counter-rotating vorticity generated between the vortices and the wing suction surface. They further show that, at $\alpha = 7.5^\circ$, the dual LEV is recorded across a range of low to moderate *Re*, from 8700 to 34 700. Interestingly, at $Re = 26\,700$ neither a dual nor single LEV is present at a lower α of 5°, suggesting a strong sensitivity to *Re*. In contrast to this finding, Gordnier & Visbal [17] use a sixth-order compact differencing scheme to computationally reveal the existence of a dual LEV at $\alpha = 5^\circ$, at the same Λ of 50°, at $Re = 20\,000, 26\,000$ and 50 000. In further contradiction to Taylor *et al.* [16], Gordnier & Visbal [17] reveal a classic primary, secondary and tertiary vortex system, more typical to a slender delta wing, at $\alpha = 15^\circ$. At this α the flow becomes unsteady and vortex breakdown is seen. They corroborate the observation of Taylor *et al.* [16], that a dual LEV exists at 26 000 and $\alpha = 10$.

The experimental results of Videler *et al.* [21], who test model wings of a common swift at a characteristic slender delta wing sweep $\Lambda = 60^\circ$, show that a model swift wing can also generate an LEV in 'gliding flight'. They use PIV to record flow separation, as would be expected on a slender delta wing under the same conditions, where a single LEV is noted at low α (5°–10°). It is asserted that while the 'arm wing' generates lift conventionally, being similar in cross-sectional shape to a conventional aerofoil, the hand wing section is used to generate lift via an LEV. The generation of a single rather than a dual LEV is likely to be a result of the increased sweep; however, the additional effect of the tapering of the swift wing on the flow is not known.

No force measurements are undertaken by Videler *et al.* [21], and their assertion that the LEV is used by the swift for lift augmentation is challenged by Lentink *et al.* [7]. They test real, inherently flexible, swift wings with a maximum sweep of 50°; a more representative wing position during normal, non-diving gliding. They too find a single LEV over the swift wing, but only at higher α. When $Re = 25\,000$, an LEV is only identified where $\alpha \geq 11^\circ$, a result in contrast to the delta wing findings presented earlier in this section; Taylor *et al.* [16] reveal a dual LEV at $\alpha = 7.5^\circ$ from $Re = 8700$ to 34 700, and Gordnier & Visbal [17] find a dual LEV at $\alpha = 5^\circ$ when $Re = 26\,000$. Lentink *et al.* [7] also test the swift wings at $Re = 50\,000$ and only find an LEV where $\alpha \geq 14^\circ$, which again contrasts with the results of Gordnier & Visbal [17] who test at the same *Re*, and present a dual LEV at $\alpha = 5^\circ$. In the research presented on both fliers, the existence and form of the LEV depends on factors not yet understood. A systematic approach is therefore required to understand the influence, on the flow, of the numerous variables at play.

To isolate the effect of trailing-edge geometry, which provides an approximation of the fundamental difference in wing shape, we perform flow measurements at *Re* typical of the gliding swift, between 12 000 and 67 000 [25], over two geometrically equivalent model delta-shaped wings. One of the wings was modified to crudely mimic a swift wing by removing material from the trailing edge, providing a tapering wing from the apex to the tip. The form and evolution of the LEV across a range of α and *Re* are revealed on both planforms using PIV. The aim of this investigation is to identify whether a swift wing-shaped delta wing can generate a comparable LEV system to that of a normal delta wing, to explore the effect of the trailing-edge shape of the swift wing on LEV generation and stability. The results will also be discussed in relation to known swift flight aerodynamics.

2. Material and methods

2.1. Model specification and facility

The tested delta wing (figure 1) has $\Lambda = 50^\circ$, chordwise length $l = 0.15$ m and span $b = 0.25$ m, which with area S gives the wing an aspect ratio (AR $= b^2/S$) of 3.36. The delta wing design was then replicated and, using the trailing-edge taper and AR provided in Lentink *et al.* [7], for a swift wing at 50° sweep, modified to produce a simple, rigid, swift wing-shaped delta wing planform. The wing shape is constructed with $\Lambda = 50^\circ$, root chord $c_r = 0.43\,l$, a span of 0.25 and an aspect ratio of 6.

The wing sections were laser cut from 10 mm thick acrylic. A sharp leading edge is provided on both wings by applying a 60° bevel on the windward side, as is common practice in delta wing investigations (e.g. [18,26]). The leading-edge bevel also results in the wing gaining an effective camber [10,27]. Camber can, however, be seen on the cross section of bird wings (e.g. [21]), and as aerodynamic forces are not explored in this instance, this was not thought to be unduly detrimental to the study. Both models were painted matt black to reduce reflection of the laser.

The wing was rigidly located in a low-speed, free surface, water flume at the University of Edinburgh (figures 2 and 3). The glass-walled flume is 8 m long and 0.4 m wide with a water depth of 0.55 m; it is of closed circuit, recirculating current design, and includes a series of meshes around 4 m upstream of the model to reduce turbulence. The maximum blockage ratio (the ratio between the projected area of the model and the cross-sectional area of the volume of flowing water) was lower than 3.5% for the delta wing at $\alpha = 15^\circ$, and thus no corrections were made. While there was a relatively small clearance of $0.5\,l$ between the wing tips and the flume wall, any consequence of this would have a parallel effect on both models, so no notable impact on the comparison between the two was anticipated. The water speed is controlled by an electric motor driving a propeller providing a flow speed (U_0) at the model location of up to 1 m s^{-1}. In the present investigation, $0.10\,\mathrm{m\,s^{-1}} < U_0 < 0.44\,\mathrm{m\,s^{-1}}$, resulting in a chord-based Re range of around 15 800 to 65 500, with the turbulence intensity ranging from 6.8% to 3.1%, respectively. Where possible, the test section of the flume was covered externally in thick matt black fabric to reduce reflection.

The models were supported by a frame securely mounted on the top of the flume, and via a 12 mm diameter cylindrical sting attached to the upper, bevelled surface of the wing (figures 2 and 3). The wing was attached with a screw countersunk into, and flush with, the suction surface; the suction surface was therefore the lower surface of the wing. The sting was attached to the frame via an adjustable bracket that allowed the angle of attack of the wing to be modified. The angle was measured and set by a digital level with an accuracy of $\pm 0.01^\circ$.

A set of images were taken of the cross-sectional flow field over the swift wing-shaped delta wing at five different sections, namely Sec. 1 to Sec. 5 in figure 1. These sections are at a distance x/l from the apex of 0.17, 0.33, 0.50, 0.67 and 0.83, where x is a chordwise coordinate from the apex of the wing, and l is the chordwise length of the wing. Sec. 2 was selected to be sufficiently far from the apex to allow development of the flow feature, however, upstream of vortex breakdown in most cases.

The flow field was recorded at the angle at which a vortex was identified by Lentink *et al.* [7], $\alpha = 15^\circ$; then again at steps reducing the angle of attack to $\alpha = 0^\circ$. $\alpha = 0^\circ$, 5°, 10° and 15° are presented. A set of images was also taken at $\alpha = 7.5^\circ$ on both the normal and swift wing-shaped delta wings, a previously documented flow regime on non-slender delta wings, to allow comparison with previously published literature (e.g. [16]). The first and second set of images were taken across the range of Re; however, only the lowest ($Re = 15\,800$) and highest ($Re = 65\,500$) cases are presented because the flow field was found to vary virtually linearly with Re. A third set of images were again taken at $\alpha = 7.5^\circ$, but at all five locations along the length of each wing at $Re = 17\,500$, to elucidate vortex development along the leading edge of each planform more fully.

2.2. Particle imaging velocimetry

A dual-pulse Nd:YAG laser (15–200 mJ at 532 nm, 200 Hz) was used to generate a 3 mm thick light sheet illuminating seeding particles in selected planes at each α. The seeding particles used are Conduct-O-Fil silvered spheres, with an average diameter of 14 µm and average density of 1.7 g cc^{-1}. A LaVision Imager pro SX 5M camera fitted in a waterproof housing was secured in the flume around 1 m downstream from the wing support rig. In order to improve resolution, only one half of each model was imaged. All images and raw data are available on the Edinburgh DataShare repository (http://datashare.is.ed.ac.uk).

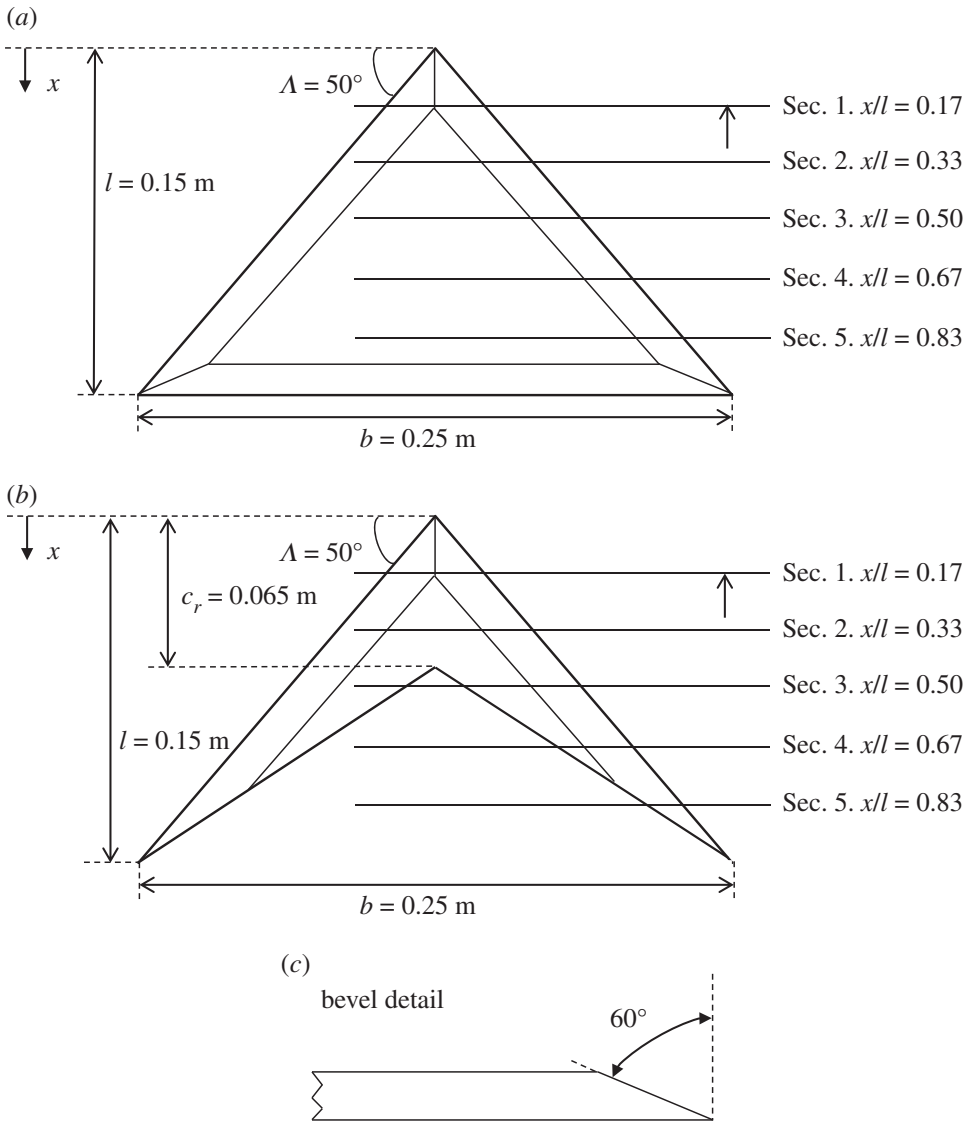

Figure 1. Schematic diagram of the tested models, showing the imaged sectional cross-flow planes at different chordwise coordinates x/l. (*a*) delta-shaped wing, (*b*) swift wing-shaped delta wing and (*c*) bevel detail.

2.3. Image processing and vortex detection

Analysis was undertaken using the LaVision software, DaVis 8.3.0. The images were preprocessed using image subtraction, subtracting the average image of each sample set, in order to reduce light reflections and increase particle definition close to the wing surface [28]. The preprocessed images (field of view of around 150 × 125 mm) were then broken into interrogation windows, and the wing model masked from the image and analysed using a multipass cross-correlation algorithm.

An FFT algorithm was applied with a window size of 64 pix × 64 pix and a 50% overlap, and refined with three passes at 32 pix × 32 pix window size and a 75% overlap. Outliers were removed in post-processing with a median filter, and a 3 × 3 Gaussian smoothing was applied. Results presented are averages of 100 image pairs taken at a frequency of 7.5 Hz, with a resolution of 2448 pix × 2050 pix. Velocity vectors and vorticity contours are presented; the vorticity field is computed from the curl of the velocity field, and only 1 in 4 velocity vectors are displayed, for clarity.

Two vortex identification algorithms were used to further elucidate the flow field. Vortical structures are identified using the Q criterion [29], where Q is the second invariant of the velocity gradient tensor. A positive value of Q results when the local magnitude of rotation dominates that of strain. Vortex boundaries were also computed using the Γ_2 criterion as defined by Graftieaux *et al.* [30], which derives a solution not from the magnitude of the velocity field, but from the topology. For every point P, Γ_2 is defined as follows:

$$\Gamma_2(\mathrm{P}) = \frac{1}{N}\sum_{\Pi}\frac{[\mathbf{PM}\wedge(\mathbf{U_M}-\tilde{\mathbf{U}}_\mathbf{P})]\cdot\hat{\mathbf{z}}}{\|\mathbf{PM}\|\cdot\|\mathbf{U_M}-\tilde{\mathbf{U}}_\mathbf{P}\|}, \tag{2.1}$$

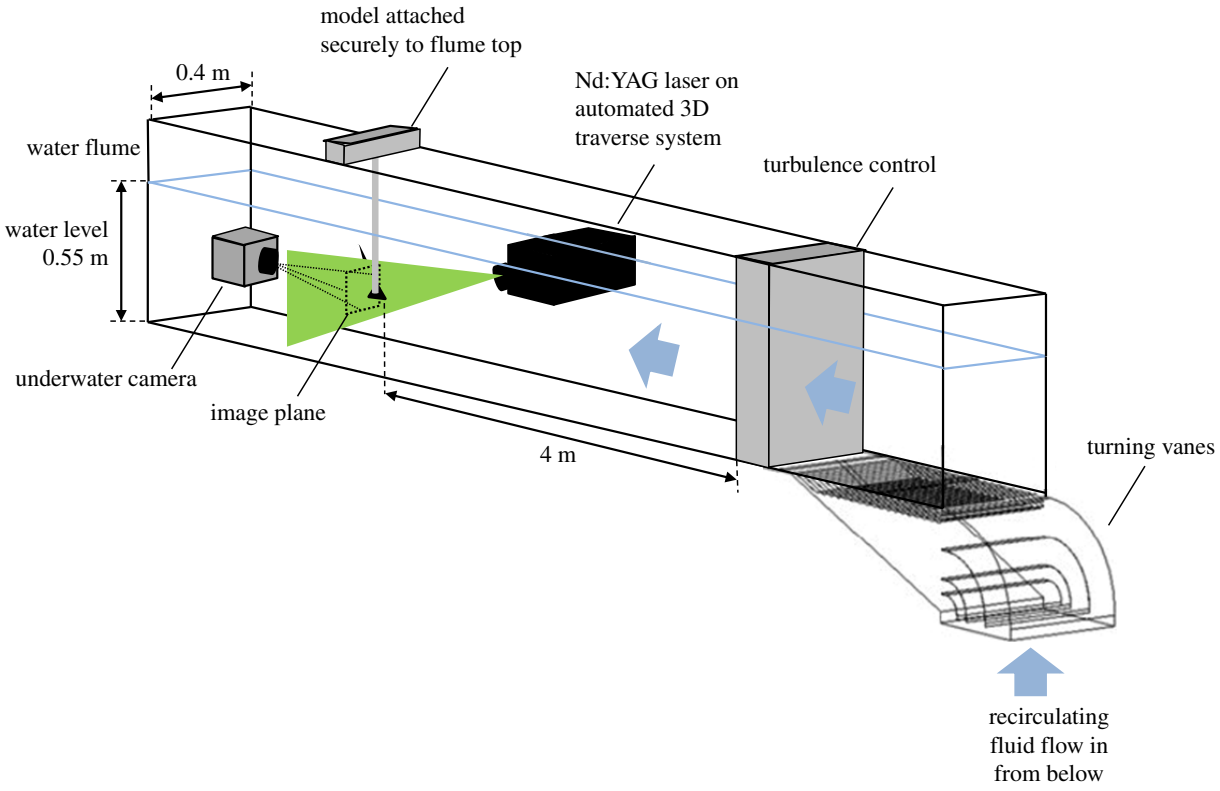

Figure 2. Schematic diagram of the experimental rig. The figure shows the general position of the laser, the model and the downstream location of the underwater camera.

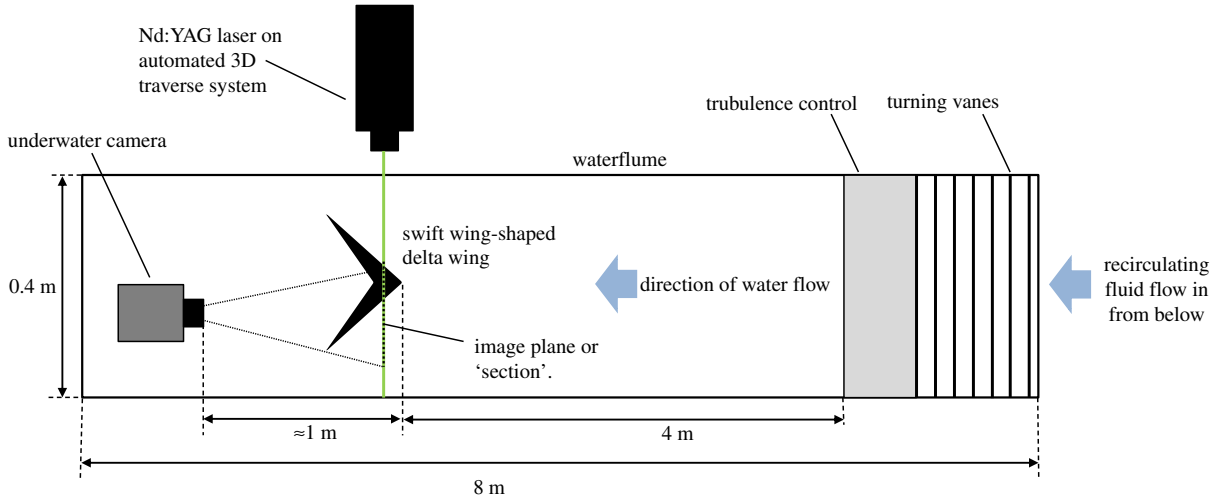

Figure 3. Plan view schematic of the experimental rig.

where Π is a rectangular, two-dimensional domain around P. The point M, identified by the position vector **PM**, is one of the N points in Π. At the point M, $\mathbf{U_M}$ is the measured velocity and $\hat{\mathbf{z}}$ is the unit vector normal to the measured plane. The mean convection velocity $\tilde{\mathbf{U}}_\mathbf{P}$ within Π is subtracted from $\mathbf{U_M}$ to make the algorithm Galileian invariant, as is the Q criterion.

3. Results

3.1. Primary and secondary leading-edge vortex

Figure 4 shows the flow field on Sec. 2 ($x/l = 0.33$) of the swift wing-shaped delta wing at $\alpha = 0°$, 5°, 10°, 15° and $Re = 15\,800$. The time-averaged, in-plane, vector velocity field is presented together with the vorticity contours, the Q criterion and the Γ_2 criterion. Figure 5 shows the same but for $Re = 65\,500$.

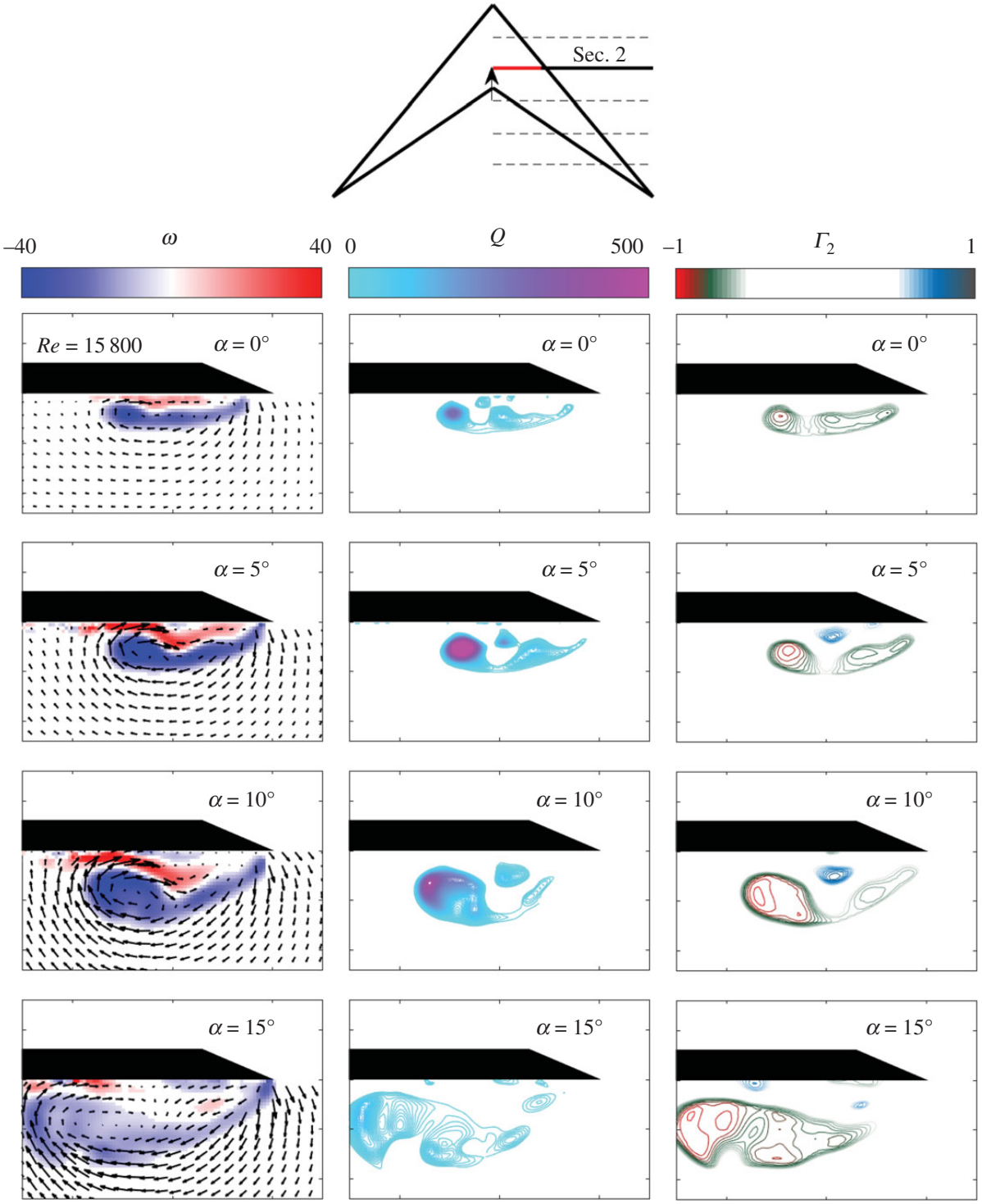

Figure 4. In-plane mean velocity vectors and vorticity contours, Q and Γ_2 around the swift wing-shaped delta wing at $Re = 15\,800$, for a range of α.

At $Re = 15\,800$, a dual vortex system comprising a primary and second, minor LEV, along with a counter-rotating secondary vortex, is recorded in all cases tested, until vortex breakdown is imaged at $\alpha = 15°$. Breakdown was also revealed by the increased unsteadiness of the flow field. As reported previously (e.g. [10,31,32]), the LEV system increases in size and strength with increased α, resulting in a reduced proximity to the leading edge. In each case presented, the minor vortex (nearer to the leading edge) contains notably reduced vorticity than the primary vortex (inbound on the wing). At $\alpha = 10°$, the minor vortex is significantly weaker, suggesting breakdown. That breakdown may affect the minor vortex in advance of the primary vortex is also reported by Ol & Gharib [18], and Taylor *et al.* [16].

At $Re = 65\,500$ (figure 7), the same primary and second, minor dual vortex system is found at low α (0° and 5°). The minor vortex is now more similar in strength to the primary vortex. At higher α (10° and 15°), the vortex system appears to display a tertiary vortex as is reported by Gordnier & Visbal [17] at $Re = 26\,000$ and $\alpha = 15°$. By $\alpha = 15°$, the system shows notable unsteadiness as the breakdown moves

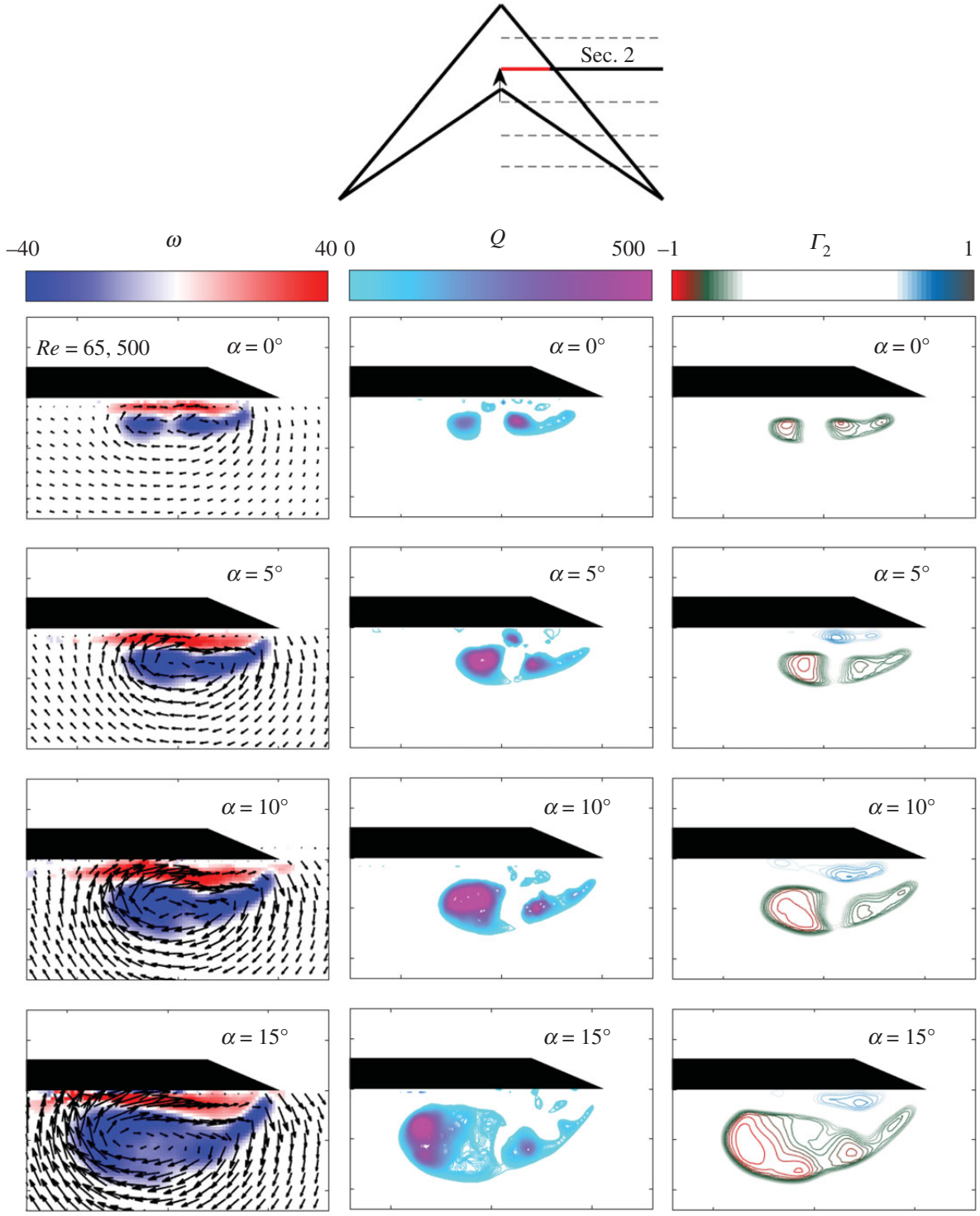

Figure 5. In-plane mean velocity vectors and vorticity contours, Q and Γ_2 around the swift wing-shaped delta wing at $Re = 65\,500$, for a range of α.

upstream with increase in α. The area of secondary separation is less distinct than at $Re = 15\,800$; however, this could be a function of reduced resolution at the surface of the wing with slight movement of the wing due to the increased flow rate and related hydrodynamic forces. In line with Taylor *et al.* [16], the increase in Re also results in a slight movement of the vortex system outboard, towards the leading edge, as the effects of viscosity are reduced. The proximity of the system to the wing surface is largely unchanged.

3.2. Comparison between delta wing and swift wing-shaped delta wing vortex structures

Figure 6 shows that under the same hydrodynamic conditions, the flow around the delta wing and the swift wing-shaped delta wing is highly comparable, both developing a coherent dual vortex flow structure located around the same horizontal and vertical position over the suction surface of the wing. In both cases, the primary LEV and second, minor, co-rotating vortex can be seen clearly in the Q and Γ_2 vorticity contour plots, along with the distinct secondary counter-rotating vortex. The primary difference

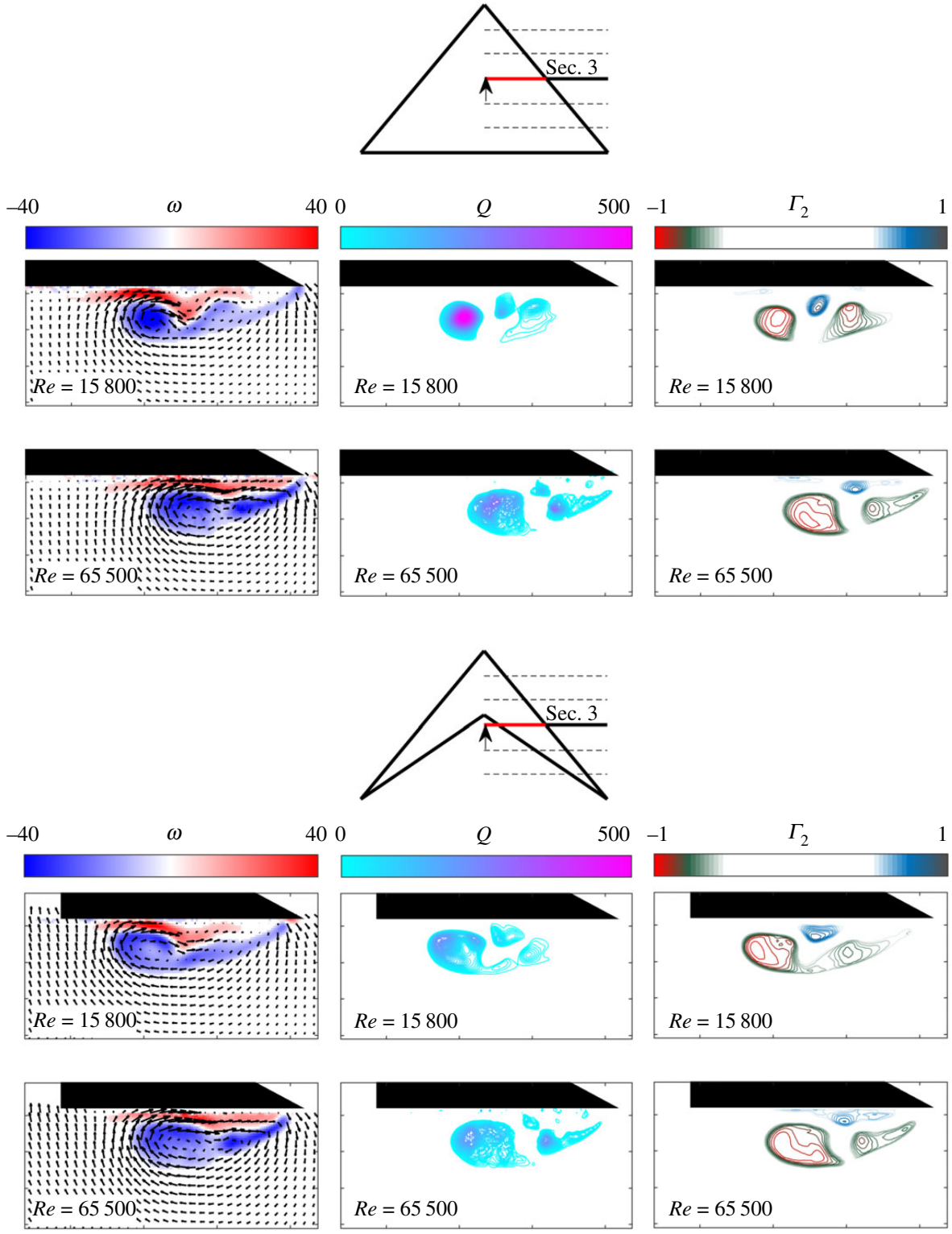

Figure 6. In-plane mean velocity vectors and vorticity contours, Q and Γ_2 around the delta- and the swift-shaped wing. Tests performed at $\alpha = 7.5^\circ$ and $Re = 15\,800$ and 65 500.

appears to be the increased size, but reduced coherence and strength, of the swift wing-shaped delta wing vortex structure compared with that of the delta wing. This is particularly apparent at the lower *Re*. The strength and magnitude of the secondary vortex in the swift wing-shaped case is also reduced, again most notably for $Re = 15\,800$. At higher *Re*, the difference between the two systems is reduced but still may be perceived. As previously described for figures 4 and 5, the vortex structures shift position outboard slightly as expected [16] with increase in *Re*.

3.3. Vortex breakdown

Figures 7 and 8 show the vortex development along the span of normal and the swift wing-shaped delta wings, respectively, at $\alpha = 7.5^\circ$ and $Re = 17\,500$. While the flow field towards the root of the wing

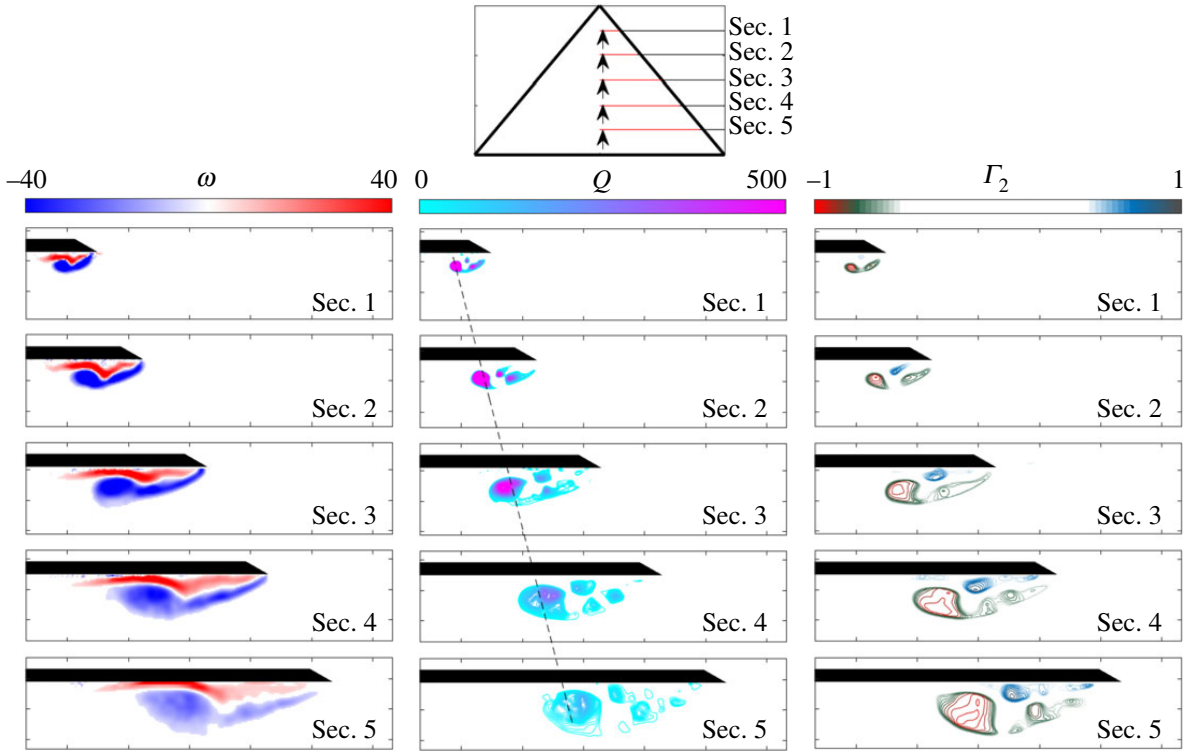

Figure 7. In-plane mean velocity vectors and vorticity contours, Q and Γ_2 around the delta-shaped wing. Tests performed at $Re = 17\,500$ and $\alpha = 7.5°$.

models is highly comparable in vorticity magnitude, location and coherence, differences are seen from around Sec. 3 ($x/l = 0.5$). In the case of the swift wing-shaped delta wing, the vortex system appears to suffer the loss of coherence and increase in size associated with breakdown, as the width of the vortex system exceeds that of the local wing chord beneath it, and flow reattachment is no longer possible. This transition is seen clearly by reviewing Sec. 3 and Sec. 4 on both models; while the vortex system of the delta wing (figure 7) at Sec. 3 continues to be supported by the delta wing surface in Sec. 4, the tapering swift wing (figure 8) no longer supports the necessary flow reattachment and at Sec. 4, vortex breakdown is seen. Following breakdown, a larger region of vorticity made of small-scale, unsteady vortical structures is seen, with a concentration in the region of the primary LEV. The delta wing vortex system, on the other hand, largely retains coherence. The trajectory of the delta wing primary vortex is tracked, showing the location of the vortex along the wing. The trajectory of the swift wing-shaped primary vortex is also tracked; however, it can be seen from Sec. 4 that the vortex deviates notably from its upstream trajectory. In line with the experimental results of Ol & Gharib [18], and Taylor *et al.* [16], the second minor vortex displays the greatest reduction in coherence; it is proposed that this may serve to provide an early indication of LEV breakdown.

4. Discussion

The trailing edge of a delta wing was modified to produce a swift wing-shaped delta wing. The figures presented show that the modification does not intrinsically prevent the development of a leading-edge vortex system under typical gliding conditions of a swift, at low α and Re, that is highly comparable to that of a classic delta wing.

Figures 4 and 5 present the averaged flow field towards the apex of the modified, swift wing-shaped delta wing. In line with the computational study of non-slender delta wings at $\Lambda = 50°$ and $\alpha = 5°, 10°$ and $15°$ [17], a shallow separated shear layer can be seen at low α, which increases in prominence and strength with increase in α. The flow separates from the sharp leading edge forming a shear layer which rolls up into a coherent LEV. At lower Re, secondary separation of opposite sign can be seen between the LEV and the wing surface, formed by the interaction between the LEV and the boundary layer (e.g. [10, 16,18]). Dual vortices are more readily developed on non-slender rather than slender delta wings due to the increased proximity of the LEV to the wing suction surface with reduced sweep [10]. At $Re = 15\,800$, the minor vortex is not clearly defined by vorticity contours alone, as it is almost entirely embedded in the shear layer (in line with [17]); however, isolines of positive Q and Γ_2 show three distinct vortices until

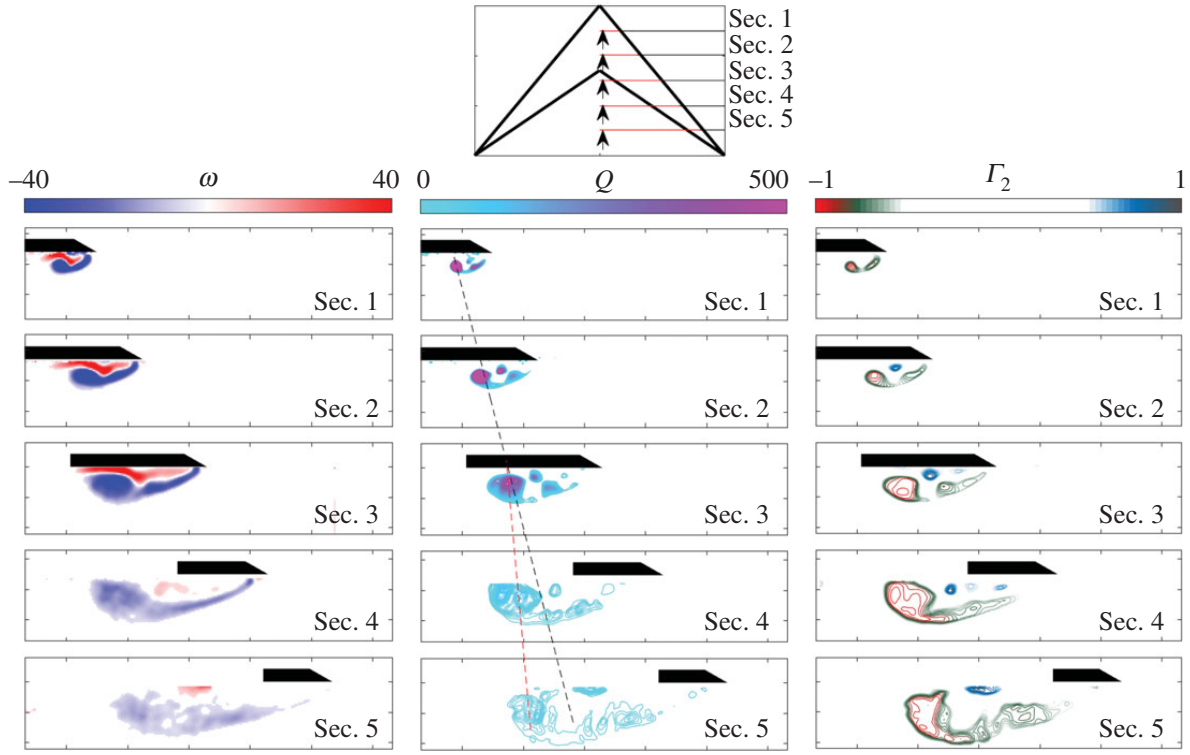

Figure 8. In-plane mean velocity vectors and vorticity contours, Q and Γ_2 around the swift wing-shaped delta wing. Tests performed at $Re = 17\,500$ and $\alpha = 7.5^\circ$.

breakdown at $\alpha = 15^\circ$. Vortex breakdown progresses upstream with increase in α (e.g. [18]); as seen in similar investigations on delta wings (e.g. [16]), the broken-down vortex remains located over the wing, with the vertical position of the vortex axis largely unaffected.

The primary, secondary and tertiary co-rotating vortex system identified at $\alpha = 10^\circ$ and $\alpha = 15^\circ$ at $Re = 65\,500$ is an interesting observation when compared with Gordnier & Visbal [17]. They find this system only where $\alpha = 15^\circ$ at $Re = 26\,000$, so their assertion that the vortex system on non-slender wings (as opposed to that of slender wings) is sensitive to changing Re would appear to be supported. In this case, it may be that increase in Re promotes the development of the tertiary structure at a lower α.

Figure 6 allows a comparison between the vortex system on the delta wing and the swift-shaped delta wing, where perhaps the most noteworthy outcome is their similarity in form, particularly at lower Re. The vortex of the swift wing-shaped wing suffers greater disturbance through advanced breakdown; however, this does not seem to notably impact the form and location of the vortex system upstream of the point of breakdown. This suggests that an analogy between the vortex systems on a delta wing and a more realistic swift wing may not fail due to the wing trailing-edge shape alone. The noted reduction in coherence of the swift wing-shaped delta wing vortex system is typically associated with reduced lift, while the increase in size increases drag.

The relationship between the spanwise position of vortex breakdown and the local chord length of the wing is elucidated in figures 7 and 8. While the swift-wing shape does not in itself prevent the generation of a vortex system, it does appear to provide a physical limit that is not experienced by a delta wing. This limit provides a maximum LEV size, after which point any increase in α or advance ratio, for example, would result in vortex breakdown, reducing lift and increasing drag. Breakdown can therefore be mediated by controlling the width of the vortex system; an increase in Re, for example, has been shown to increase coherence and shift the vortex system outboard, thereby delaying the width of the system from reaching that of the local chord length. The proposed relationship between vortex size and wing chord is aligned with the previous work of Rival *et al.* [33], who find that, for plunging profiles, with varying leading-edge geometries, vortex detachment occurs at an LEV length scale of one chord length. While the vortex system does not detach in this study, the point of breakdown is governed by the spanwise location at which the width of the LEV system reaches one local chord length.

The identification of a dual LEV at low Re is in contrast to both the PIV results of Videler *et al.* [21] and the tuft flow visualization of Lentink *et al.* [7], who provide the closest comparative experimentation on wings which more closely replicate natural fliers. While the PIV measurements of Videler *et al.* [21] found a prominent but single LEV on a model swift wing at $\alpha > 5^\circ$, their model had a slender sweep of $\Lambda = 60^\circ$, bringing improved vortex stability. Had they tested at $\Lambda = 50^\circ$, as in the present work, it is likely

that they would not have found an LEV at a lower α due to reduced LEV stability of non-slender wings at low α. The probable lack of a vortex at low α, and that no dual vortex was recorded in any case, are both in contrast to the results presented in this paper. Similarly, Lentink *et al.* [7] did not record an LEV at low angles of attack, when they tested real swift wings at $\Lambda = 50^\circ$, finding evidence only at $\alpha \leq 11^\circ$. They also did not record a dual vortex in any case.

These results suggest that the increase in α required to generate an LEV on the swift wings tested previously is not due to the wing trailing-edge geometry, but to another variable. It is easily conceivable that the differences in results noted here are due to varying sharpness of the leading edge or wing thickness across the respective models tested. In the case of the dual LEV, the surface texture or structure of the bird wing could affect the nature of the secondary separation and its influence on the vortex structure.

It may also be that the flow visualization method used is key in identifying the smaller, weaker vortex structure at low α and Λ. Videler *et al.* [21] do not state the resolution of their PIV analysis, however their use of a thick laser sheet of 30 mm (on a hand wing section of average chord length 50 mm) may have prevented any finer flow features from being resolved. Lentink *et al.* [7] use a tuft grid survey, originally developed for testing flow over slow-flying delta wings [34]. The tuft grid method places a tuft (or single hair) at regular intervals across the wing which can then be imaged as it moves according to the local flow regime. Where the size, strength, position etc. of the flow feature is not known, it can be difficult to suitably define the length, stiffness and position of the tuft to highlight the sought feature. It may be possible that a weak LEV did exist in the cases presented, but that the flow visualization technique used was not sensitive enough to capture it. Similarly, a dual vortex may have existed at higher angles of attack with the weaker minor vortex not identified for the same reason.

The present results on the flow structure over a tapering swift wing-shaped delta wing allow speculation on the flow structure over a real swift wing, and its potential use. The effect of the swift wing geometry is exaggerated in the test case presented here by the more pronounced reduction in chord length of the model, compared with that of a typical swift wing planform [35]. A twisted leading edge and wing flexibility would also affect the breakdown location; a spanwise reduction in the effective angle of attack via twist or flexibility would attenuate vortex development towards the wing tip, delaying the onset of vortex breakdown, despite the tapered wing.

The many differences between the wing of a real swift, such as that tested by Lentink *et al*. [7], and the model presented here have arguably been 'selected' in natural fliers to improve their aerodynamic and flight ability. The leading-edge detail, in particular the sharpness, is known not only to promote flow separation, but also to define the relationship between α and the force coefficients generated [36], while the behaviour of the LEV is increasingly dependent on leading-edge shape at low sweep [37]. If a vortex can be generated at low α, promoted by the sharp leading edge of the swift wing and stabilized in part by leading-edge twist and wing flexibility, it is interesting to consider what function it may serve if not one of lift augmentation, or lift-to-drag ratio improvement. While Henningsson *et al.* [38] conclude that the swift wing is best adapted for flapping rather than gliding flight, the ability to generate and maintain a stable leading-edge vortex across a wide range of α may be a useful addition to the suite of flight optimization tools deftly deployed by the swift. As alluded to by their genus name *Apus* (from the Greek 'a pous', meaning 'without foot'), swifts spend the majority of their lives in the air; hunting, eating, collecting water, mating and even roosting [7], and they have necessarily evolved to be one of the most aerodynamically refined bird species [25]. The optimization of energy required to undertake these necessary activities is clearly essential, and with the swift spending a significant portion of its flight time gliding, often in complex air flows, any reduction in gliding energy requirement would be of significant benefit.

While the LEV is typically referred to as a high-lift mechanism [1–5], it is known that the component of total lift provided by vortex lift reduces with decreasing sweep [39]. It may be that the ability to generate an LEV and/or LEV system on a swift wing can provide another function. Along with potentially enhancing lift and manoeuvrability at high α and during flapping flight, the LEV system may help to manage wing loading and aerodynamic force fluctuations at lower α, by acting as a dampening mechanism. The 'robustness to kinematic change' noted by Ellington [1] may allow the LEV to react more slowly to sudden changes in the angle of attack that might otherwise have resulted in a sharp increase in lift, or in flow separation and stall. Rather, the LEV may grow or reduce in size at a rate mediated by inertia of the vortex system, altering the lift-to-drag ratio, but preventing the severe loading fluctuations associated with stall. The ability to exploit the LEV in this way could save the bird significant expenditure of energy, and may be a useful addition to a suite of flow control techniques used by MAVs seeking to fly in complex or turbulent weather conditions.

5. Conclusion

The flow structure over a model delta wing and a model swift wing-shaped delta wing has been characterized, with the aim of elucidating the effect of the tapering of the swift wing on the wing's aerodynamics. The models have identical sharp leading edges, with a non-slender sweep angle of 50°. The swift wing-shaped delta wing has a modified trailing edge, resulting in a crude tapering wing planform.

A leading-edge vortex system was found in all cases tested, from $\alpha = 0°$ to 15° and from $Re = 15\,800$ to 65 500, on both the normal and modified delta wing models. The cross-flow planes present the mean velocity vectors and vorticity contours, along with iso-surfaces of Q and Γ_2. At lower α and Re, a clear primary and second minor co-rotating vortex structure is present, along with an area of counter-rotating vorticity between the dual LEV and the wing surface. At higher α and Re, a tertiary co-rotating vortex is identified, as is typical on slender delta wings. The size and strength of the vortex system increases with α, while increased Re improves coherence, and results in the vortex system moving outboard.

The results presented demonstrate that the flow developed over the two-wing platforms is highly comparable, despite the tapering of the swift wing-shaped wing. The notable difference between the two is the location of vortex breakdown along the wing span. On the swift wing-shaped delta wing, this is governed by the width of the vortex system in relation to the local wing chord length; where the size of the vortex system exceeds that of the local wing chord, flow is no longer able to reattach and the vortex breaks down. The vortex system upstream of the point of breakdown is not significantly impacted in the cases presented. The broken-down vortex remains attached to the wing suction surface, with the proximity to the surface remaining largely unaltered, compared with that of the delta wing. The results presented confirm the sensitivity of the non-slender wing shapes to changing Re. An increase in Re results in increased coherence of the vortex system, and also a movement of the system towards the leading edge, both serving to reduce the overall width of the system. It is hypothesized that an increase in Re would also therefore delay vortex breakdown for the swift wing-shaped delta wing, as the width of the vortex system compared with the local wing chord is mediated.

A dual LEV is commonly reported over non-slender delta wings at low α, however, no dual vortex has been found over swift wings, despite their broadly comparable geometry. While numerous variables separate these two fliers, this study demonstrates that, at the same α and Re, relevant for swifts in gliding flight, a highly comparable vortical flow structure is generated by the model delta wing and the model swift wing-shaped delta wing. This suggests that if the flow fields reported over swift wings do differ from those of delta wings, it is due not to the tapering of the wing, but to other variables such as wing surface texture or leading-edge geometry.

Data accessibility. The metadata underpinning these results and electronic supplementary material for this article can be found online on the Edinburgh DataShare repository: http://datashare.is.ed.ac.uk.

Authors' contributions. R.E.M. and I.M.V. jointly conceived and designed the study. R.E.M. was responsible for the construction of the model, the execution of the experiments and the data analysis; she prepared the original draft of the manuscript. I.M.V. was responsible for supervision and administration of the project, and funding acquisition; he contributed to the critical analysis and interpretation of the results; and reviewed and edited the manuscript. Both authors gave their final approval for publication. A.A.G. contributed to the data analysis.

Competing interests. The authors declare that the research was conducted in the absence of any commercial or financial relationships that could be construed as a potential conflict of interest.

Funding. This work received funding from the Engineering and Physical Sciences Research Council (EP/M506515/1) and the Consejo Nacional de Ciencia y Tecnología (CONACYT).

Acknowledgements. The authors thank Susan Tully and Jean-Baptiste Richon for their experimental insight and guidance throughout.

References

1. Ellington CP. 1999 The novel aerodynamics of insect flight: applications to micro-air vehicles. *J. Exp. Biol.* **202**, 3439–3448.
2. Garmann DJ, Visbal MR, Orkwis PD. 2013 Three-dimensional flow structure and aerodynamic loading on a revolving wing. *Phys. Fluids* **25**, 034101. (doi:10.1063/1.4794753)
3. Jardin T, David L. 2014 Spanwise gradients in flow speed help stabilize leading-edge vortices on revolving wings. *Phys. Rev. E* **90**, 013011. (doi:10.1103/PhysRevE.90.013011)
4. Srygley RB, Thomas ALR. 2002 Unconventional lift-generating mechanisms in free-flying butterflies. *Nature* **420**, 660–664. (doi:10.1038/nature01223)
5. Lentink D, Dickson WB, van Leeuwen JL, Dickinson MH. 2009 Leading-edge vortices elevate lift of autorotating plant seeds. *Science* **324**, 1438–1440. (doi:10.1126/science.1174196)
6. Muijres FT, Johansson LC, Barfield R, Wolf M, Spedding GR, Hedenström A. 2008 Leading-edge vortex improves lift in slow-flying bats. *Science* **319**, 1250–1253. (doi:10.1126/science.1153019)
7. Lentink D, Müller UK, Stamhuis EJ, de Kat R, van Gestel W, Veldhuis LLM, van Leeuwen JL. 2007 How swifts control their glide performance with

morphing wings. *Nature* **446**, 1082–1085. (doi:10.1038/nature05733)

8. Hubel TY, Tropea C. 2010 The importance of leading edge vortices under simplified flapping flight conditions at the size scale of birds. *J. Exp. Biol.* **213**, 1930–1939. (doi:10.1242/jeb.040857)
9. Borazjani I, Daghooghi M. 2013 The fish tail motion forms an attached leading edge vortex. *Proc. R. Soc. B* **280**, 20122071. (doi:10.1098/rspb.2012.2071)
10. Gursul I, Gordnier R, Visbal M. 2005 Unsteady aerodynamics of nonslender delta wings. *Prog. Aerosp. Sci.* **41**, 515–557. (doi:10.1016/j.paerosci.2005.09.002)
11. Gursul I, Wang Z, Vardaki E. 2007 Review of flow control mechanisms of leading-edge vortices. *Prog. Aerosp. Sci.* **43**, 246–270. (doi:10.1016/j.paerosci.2007.08.001)
12. Corke TC, Thomas FO. 2015 Dynamic stall in pitching airfoils: aerodynamic damping and compressibility effects. *Annu. Rev. Fluid Mech.* **47**, 479–505. (doi:10.1146/annurev-fluid-010814-013632)
13. Viola IM, Bartesaghi S, Van-Renterghem T, Ponzini R. 2014 Detached eddy simulation of a sailing yacht. *Ocean Eng.* **90**, 93–103. (doi:10.1016/j.oceaneng.2014.07.019)
14. Larsen JW, Nielsen SRK, Krenk S. 2007 Dynamic stall model for wind tubine airfoils. *J. Fluids Struct.* **23**, 959–982. (doi:10.1016/j.jfluidstructs.2007.02.005)
15. Visbal MR. 1996 Computed unsteady structure of spiral vortex breakdown on delta wings. In *AIAA 27th Fluid Dynamics Conf., New Orleans, LA, 17–20 June*, paper 96-2074. Reston, VA: AIAA. (doi:10.2514/6.1996-2074)
16. Taylor GS, Schnorbus T, Gursul I. 2003 An investigation of vortex flows over low sweep delta wings. In *AIAA 33rd Fluid Dynamics Conf., Orlando, FL, 23–26 June*, pp. 1–13. Reston, VA: AIAA.
17. Gordnier RE, Visbal MR. 2005 Compact difference scheme applied to simulation of low-sweep delta wing flow. *AIAA J.* **43**, 1744–1752. (doi:10.2514/1.5403)
18. Ol MV, Gharib M. 2003 Leading-edge vortex structure of nonslender delta wings at low Reynolds number. *AIAA J.* **41**, 16–26. (doi:10.2514/2.1930)
19. Verhaagen NG. 2011 Flow over 50° delta wings with different leading-edge radii. In *AIAA 49th Aerospace Sciences Meeting including the New Horizons Forum and Aerospace Exposition, Orlando, FL, 4–7 January*, pp. 1–14. Reston, VA: AIAA.
20. Jin-Jun W, Wang Z, 2008 Experimental investigations on leading-edge vortex structures for flowover non-slender deltawings. *Chin. Phys. Lett.* **25**, 2550–2553. (doi:10.1088/0256-307X/25/7/060)
21. Videler JJ, Stamhuis EJ, Povel GDE. 2004 Leading-edge vortex lifts swifts. *Sci. New Ser.* **306**, 1960–1962. (doi:10.1126/science.1104682)
22. Ellington CP, Van Den Berg C, Willmott AP, Thomas AL. 1996 Leading-edge vortices in insect flight. *Nature* **384**, 626–630. (doi:10.1038/384626a0)
23. Garmann DJ, Visbal MR. 2014 Dynamics of revolving wings for various aspect ratios. *J. Fluid Mech.* **748**, 932–956. (doi:10.1017/jfm.2014.212)
24. Taylor G, Wang Z, Vardaki E, Gursul I. 2007 Lift enhancement over flexible nonslender delta wings. *AIAA J.* **45**, 2979–2993. (doi:10.2514/1.31308)
25. Lentink D, de Kat R. 2014 Gliding swifts attain laminar flow over rough wings. *PLoS ONE* **9**, e99901. (doi:10.1371/journal.pone.0099901)
26. Wang J, Zhao X, Liu W, Tu J. 2007 Experimental investigation on flow structures over nonslender delta wings at low Reynolds numbers. *J. Exp. Fluid Mech.* **21**, 1–7.
27. Verhaagen NG. 2012 Leading-edge radius effects on aerodynamic characteristics of 50-degree delta wings. *J. Aircr.* **49**, 521–531. (doi:10.2514/1.C031550)
28. Honkanen M, Nobach H. 2005 Background extraction from double-frame PIV images. *Exp. Fluids* **38**, 348–362. (doi:10.1007/s00348-004-0916-x)
29. Hunt JCR, Wray AA, Moin P. 1988 Eddies, streams and convergence zones in turbulent flows. In *Proc. of the Summer Program 1988, Report CTR-S88*, pp. 193–208. Stanford, CA: Center for Turbulence Research.
30. Graftieaux L, Michard M, Grosjean N. 2001 Combining PIV, POD and vortex identification algorithms for the study of unsteady turbulent swirling flows. *Meas. Sci. Technol.* **12**, 1422–1429. (doi:10.1088/0957-0233/12/9/307)
31. Ozen CA, Rockwell D. 2011 Flow structure on a rotating plate. *Exp. Fluids* **52**, 207–223. (doi:10.1007/s00348-011-1215-y)
32. Wojcik CJ, Buchholz JHJ. 2014 Parameter variation and the leading-edge vortex of a rotating flat plate. *AIAA J.* **52**, 348–357. (doi:10.2514/1.J052381)
33. Rival DE, Kriegseis J, Schaub P, Widmann A, Tropea C. 2014 Characteristic length scales for vortex detachment on plunging profiles with varying leading-edge geometry. *Exp. Fluids* **55**, 1660. (doi:10.1007/s00348-013-1660-x)
34. Bird JD. 1969 Tuft-grid surveys at low speeds for delta wings. NASA Technical Note D-5045.
35. Henningsson P, Hedenström A. 2011 Aerodynamics of gliding flight in common swifts. *J. Exp. Biol.* **214**, 382–393. (doi:10.1242/jeb.050609)
36. Usherwood JR, Ellington CP. 2002 The aerodynamics of revolving wings I. Model hawkmoth wings. *J. Exp. Biol.* **205**, 1547–1564.
37. Miau JJ, Kuo KT, Liu WH, Hsieh SJ, Chou JH. 1995 Flow developments above 50-deg sweep delta wings with different leading-edge profiles. *J. Aircr.* **32**, 787–794. (doi:10.2514/3.46792)
38. Henningsson P, Hedenström A, Bomphrey RJ. 2014 Efficiency of lift production in flapping and gliding flight of swifts. *PLoS ONE* **9**, e90170. (doi:10.1371/journal.pone.0090170)
39. Polhamus EC. 1966 A concept of the vortex lift of sharp-edge delta wings based on a leading-edge-suction analogy. National Aeronautics and Space Administration, NASA TN D-3767.

THE LEADING-EDGE VORTEX OF YACHT SAILS

I. M. Viola, Institute for Energy Systems, School of Engineering, University of Edinburgh, UK, i.m.viola@ed.ac.uk
A. Arredondo-Galeana, Institute for Energy Systems, School of Engineering, University of Edinburgh, UK, a.arredondo@ed.ac.uk

It has been suggested that a stable Leading Edge Vortex (LEV) can be formed from the sharp leading edge of asymmetric spinnakers. If the LEV remains stably attached to the leading edge, it provides an increase in the thrust force. Until now, however, the existence of a stable and attached LEV has only been shown by numerical simulations. In the present work we experimentally verify, for the first time, that a stable LEV can be formed on an asymmetric spinnaker. We tested a 3D printed rigid sail in a water flume at a chord-based Reynolds number of ca. 10^4. The sail was tested in isolation (no hull and rigging) at an incidence with the flow equivalent to an apparent wind angle of $55°$ and a heel angle of $10°$. The flow field was measured with particle image velocimetry over horizontal cross sections. We found that on the leeward side of the sail, the flow separates at the leading edge reattaching further downstream and forming a stable LEV. The LEV grows in diameter from the root to the tip of the sail, where it merges with the tip vortex. We detected the LEV using the γ_1 and γ_2 criteria, and we verified its stability over time. The lift contribution provided by the LEV was computed solving a complex potential model of each sail section. This analysis showed that the LEV provides more than 10% of the total sail's lift. These findings suggests that the performance of asymmetric spinnakers could be significantly enhanced by promoting a stable LEV.

1 INTRODUCTION

Sails are thin wings with a relatively sharp leading edge. On headsails, where the leading edge is not attached to the mast, the sharp leading edge leads to flow separation at any non-zero angle of attack. This is one of the key features of yacht sails that makes them different from conventional wings. While wing designers try to prevent flow separation, in sail aerodynamics flow separation is a fact. Flow reattachment occurs somewhere downstream of the leading edge, forming a region of separated flow. This region is short in the chordwise direction, but it extends from the base to the tip. On downwind sails, the flow separates again before reaching the trailing edge; this is known as trailing edge separation. This larger separated region that could cover more than half of the chord, is easier to identify than the smaller leading edge separated region. Therefore, the extent of this region is typically used to inform the sail designer on where the sails' shape can be enhanced. However, virtually all of the driving force is generated near the leading edge. Thus small changes in the fluid dynamics of the leading edge separated region can result in significant gains in performance. This work aims to gain new insight on the flow in this region.

The flow separates at the leading edge, forming a strong separated shear layer. This results in the production of vorticity. At the typical Reynolds numbers (Re) of a yacht sail, from 5×10^5 to 5×10^7, the vorticity dissipation due to the viscosity is negligible. Therefore, the vorticity is accumulated in the separated region. The integral of the vorticity in this region leads to a circulation that has the same sign as the circulation of the sail; thus this vorticity contributes to the generation of lift. However, vorticity cannot be accumulated indefinitely. It can be either shed downstream with the main flow stream, or it must be somehow extracted. These two mechanisms are employed by the laminar separation bubble (LSB) and the leading edge vortex (LEV), respectively.

1.1 THE LAMINAR SEPARATION BUBBLE

The LSB occurs on the suction side of thin airfoils at transitional Reynolds numbers ($10^4 < Re < 10^6$). The laminar boundary layer that has grown from the leading edge, separates due to the adverse pressure gradient somewhere downstream of the foil's suction peak. The resulting separated shear layer promotes the laminar to turbulent transition and the generation of vorticity. The vorticity is continuously shed downstream in the form of vortices that roll on the surface of the airfoil toward the trailing edge. The time-averaged flow field shows flow reattachment downstream of the point where laminar to turbulent transition occurs. A thick turbulent boundary layer grows downstream of the reattachment point. This results in lower suction and lift, and also in higher momentum deficit in the wake and drag. A LSB-type of flow with continuous shedding of vorticity occurs at the leading edge of genoas and jibs [27, 30].

1.2 THE LEADING EDGE VORTEX

The LEV is a coherent vortex formed by the roll up of vorticity, generated at the leading edge. The vorticity is not continuously shed downstream, but is instead convected towards the centre of the vortex. If the vorticity is somehow extracted from the axis of the vortex, it is possible to achieve a stable LEV that remains attached to the leading edge indefinitely. The vorticity is typically extracted by axial flow inside of the vortex core, in the direction of the wing tip. A stable LEV grows in the direction in which the vorticity is extracted. The vorticity and circulation of the LEV can significantly increase the lift and thus it is exploited on both man-made and natural flyers [5, 23, 6, 15]. Remarkably, it has been identified across a wide range of Re. In laminar flow conditions, it has been found on autorotating seeds [17] and on the wings of insects [20] and small birds [18]. In transitional and turbulent flow conditions, it has been found on larger bird wings [14], fish fins [2] and delta wings [9, 10]. In helicopter rotors [4] and wind turbines [16], the LEV is a powerful but undesirable flow feature. This is due to the large angle of attack oscillations. At every period, the LEV is shed downstream leading to a lift overshoot above the quasi-static maximum lift and to an abrupt, and dangerous change in the pitch moment. Conversely, in biological flyers and delta wings, the LEV provides an essential source of lift augmentation.

Recent Detached Eddy Simulations (DES) [24] have revealed that a stable attached LEV might also occur on the asymmetric spinnakers of sailing yachts. This was anecdotally anticipated by Bethwaite [1], who sketched the LEV on the gennaker of a skiff. This exiting finding is the motivation for this work. In fact, the exploitation of the LEV by design has enabled a step change in the performance of a wide range of applications, from micro aerial vehicles to rockets and supersonic planes [10]. The understanding of how to promote and stabilise the LEV on downwind sails can enable a major step in the sails' performances. In this study, therefore, we aim to prove experimentally the existence of the LEV on a downwind sail, to identify its main features, and to quantify its contribution to sails' performances.

1.3 A BENCHMARK FOR DOWNWIND SAILS

The asymmetric spinnaker where the LEV was identified with DES [24] is considered in this work. The aerodynamics of this sail have been widely investigated in the last decade and this makes it one of the best available benchmarks for downwind sails. The geometry and the experimental, and numerical data are available on www.ignazioviola.com. This sail was designed for the AC33 class, which was proposed for the 33$^{\text{rd}}$ America's Cup. This class has never been adopted, as the 33$^{\text{rd}}$ America's Cup was eventually disputed under the Deed of Gift. A 1:15$^{\text{th}}$-scale model of this sail was tested in a wind tunnel at 55° AWA and 10° heel angle. The forces [25] and pressures [26] on the sail surfaces were recorded for a range of sail trims, and also compared with those measured on similar sails. The sail trim that allowed the maximum driving force, was used to build a rigid sail with embedded pressure taps and both forces, and pressures were measured in a wind tunnel [3]. This sail trim was also modelled with Reynolds-averaged Navier-Stokes (RANS) simulations [28] and with DES [24]. A 1:3$^{\text{rd}}$-scale prototype was built and tested on water on a Platu25-class yacht [29], where surface pressures were measured. A tri-way comparison between the pressures measured in a wind tunnel, on water and with RANS was presented in Viola and Flay [28]. While a comparison between wind tunnel tests performed with flexible and rigid sails, and DES, was presented in both [3] and [24]. The pressures from these three approaches showed a qualitative agreement, with the pressures computed numerically lying in between those measured with the two experimental techniques.

1.4 OVERVIEW OF THE PRESENT WORK

In order to test in highly controlled flow conditions and to identify the main mechanisms enabling the formation, and stability of the LEV, we tested the asymmetric spinnaker in isolation (without the mainsail and the hull), in low Re conditions. The Reynolds number based on the sail chord measured on a section at 3/4$^{\text{th}}$ of the mitre (measured from the sail's base) is $Re = 1.3 \times 10^4$. The actual flow of a real sail is certainly more complex than the one of this simplified model. The effects of the mainsails are primarily to generate upwash and to increase the effective angle of attack. Therefore, their effects can be mostly accounted for by adjusting the angle of attack. We do not take into account the effects of the enhanced turbulent mixing and boundary layer effects at higher Reynolds numbers. However, the LEV has been found to be very resilient to the effects of Reynolds numbers [7]. Therefore, while this investigation does not provide a quantitative description of the full-scale flow, it enables the understanding of the key features of downwind sail flow.

The rest of the paper is organised as follows: in Section 2, Methodology, we present the details of the methodology, including the geometry of the sail, the experimental rig, the flow conditions, the instrumentation used to measure the flow field and how we analysed the data. In Section 3, Results, we present the flow measurements, the analysis of the LEV and an estimate of the contribution of the LEV to the sail's performance. Finally, in Section 4, Conclusions, we summarise the key findings.

2 METHODOLOGY

2.1 SAIL MODEL

The geometry of the 3D-printed model used for this investigation is available on www.ignazioviola.com. The model has an area of $A = 0.045\,\text{m}^2$. The twist angle from the base to the head is 16°, the maximum chordwise camber is $0.40c_0$ and the maximum spanwise camber is $0.65c_0$, where $c_0 = 0.11\,\text{m}$ is the chord of a sail section at 3/4$^{\text{th}}$ of the span from the base (1).

The model is 3 mm thick. Separation at the leading edge is promoted chamfering the edges. The chamfer at the leading and trailing edges is 0° for the first 3/4$^{\text{th}}$ of the span from the base to the head. At the top 1/4$^{\text{th}}$ of the sail's span, the chamfer grows progressively from 20° to 70°, allowing the

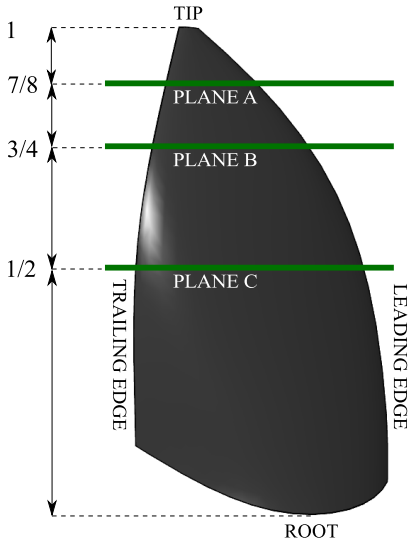

Figure 1: Schematic diagram of the experimental setup.

thickness to remain constant on the mitre. The head of the sail is blunt.

The model was 3D printed in ABS with a Fortus 250 3D printer. The model was mounted on a rotating shaft controlled by a lever arm for the fine control of the angle of attack. The shaft was attached to a 6 mm thick acrylic plate connected to a pair of $45 \times 45\,\mathrm{mm}$ aluminium extrusions attached to the flume's side walls. The rig allows to change the angle of attack and to secure its testing position through an arch dial system (Fig. 2). The shaft was set to replicate the same AWA ($55°$) and heel angle ($10°$) as tested with DES by [24].

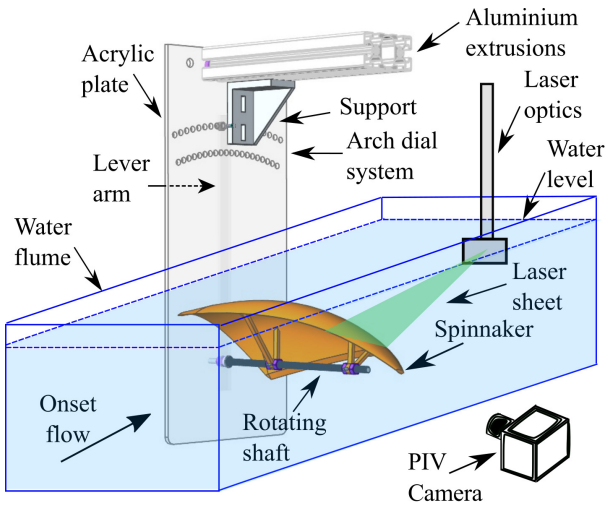

Figure 2: Schematic diagram of the experimental setup.

2.2 WATER FLUME

The water flume is a current-wave testing facility in the Institute of Engineering Systems of the School of Engineering, University of Edinburgh. It is $2\,\mathrm{m}$ long, $0.4\,\mathrm{m}$ wide and $0.9\,\mathrm{m}$ high. The water depth was set to $0.5\,\mathrm{m}$ and the sail was placed horizontally $0.1\,\mathrm{m}$ below the water surface. The free space between the rig and the walls of the flume was $0.05\ \mathrm{m}$ at both sides. The model was tested in a uniform current with $U_\infty = 0.1146\,\mathrm{m/s}$. A turbulence intensity of 7% was measured with Laser Doppler Velocimetry $1\,\mathrm{m}$ upstream of the model.

2.3 PARTICLE IMAGE VELOCIMETRY

We used a Particle Image Velocimetry (PIV) system consisting of a Solo 200XT pulsed dual-head Nd:YAG laser, with an energy output of 200 mJ at a wavelength of λ = 532 nm. In addition, one CCD Imperx 5MP camera with a 2448 px $\times$ 2050 px resolution and a Nikkor f/2, 50 mm lense were used. The seeding particles were silver coated hollow glass spheres with an average diameter of $14\,\mu\mathrm{m}$ and a density of $1.7\,\mathrm{g/cc}$. In order to mitigate surface reflections, a coating of matt black paint was applied to the sail with a second coating of rhodamine B. A third coating of acrylic was applied to protect the rhodamine B coating from water. An optical filter was used on the camera to subtract the wavelength of rhodamine B and minimise the reflected light. Additionally, background subtraction was performed [13] that allowed measurements to be made in close proximity to the wall. The leading edge region, however, was not affected by laser reflections due to the curvature of the sail and the direction of the laser sheet.

The laser beam was redirected through two mirrors and an array of underwater LaVision optics to generate a laser sheet parallel to the flow. The laser sheet was fully submerged as shown in Fig. 2. The thickness of the laser sheet was approximately $2\,\mathrm{mm}$. Three cross sections of the sail were recorded: plane A, B and C, respectively (Fig. 1). These are located at $1/2^{\mathrm{nd}}$, $3/4^{\mathrm{th}}$ and $7/8^{\mathrm{th}}$, respectively, of the span of the sail from its base.

PIV pair images were sampled at 7.5 Hz. A two pass adaptive correlation was applied. The first pass had a $64\,\mathrm{px} \times 64\,\mathrm{px}$ interrogation window, with a Gaussian weighting and 50% window overlap. The second pass had a $24\,\mathrm{px} \times 24\,\mathrm{px}$ interrogation window and a 75% window overlap. Averaged fields were generated from the full time series and a 3×3 filter was used to smoothen the vector fields.

2.4 VORTEX DETECTION CRITERIA

The γ_1 and the γ_2 vortex detection criteria were developed by [8] to overcome the intermittence due to low-scale turbulence of methods that rely, on local quantities such as velocity gradients or vorticity. The method is defined as a non-local scheme by [19] and has been applied successfully to PIV data (e.g. [22, 12] and [21]). The γ_2 criterion is the non-Galilean invariant version of the γ_1 criterion, as the local convection velocity is subtracted. Figure 3 shows a schematic drawing of the γ_1 algorithm. The γ_1 criterion at a point P is computed using the PIV data within a square window S of dimension l centred in P. At each point M within S, the sine of the angle θ_M between the vector **PM** and the velocity $\mathbf{u}_\mathrm{M}$ is computed.

The γ_1 value in P is given by

$$\gamma_1 = \frac{1}{N}\sum_S \frac{\mathbf{PM}\times\mathbf{u}_\mathrm{M}}{||\mathbf{PM}||\cdot||\mathbf{u}_\mathrm{M}||} = \frac{1}{N}\sum_S \sin(\theta_\mathrm{M}), \qquad (1)$$

where N is the number of grid points in S.

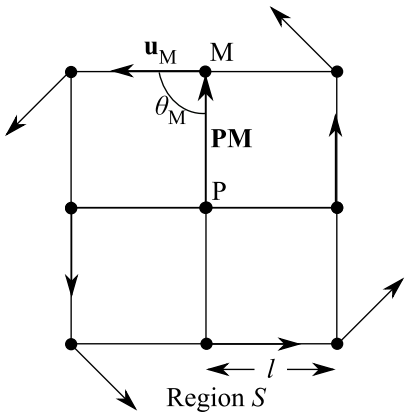

Figure 3: Vortex detection algorithm.

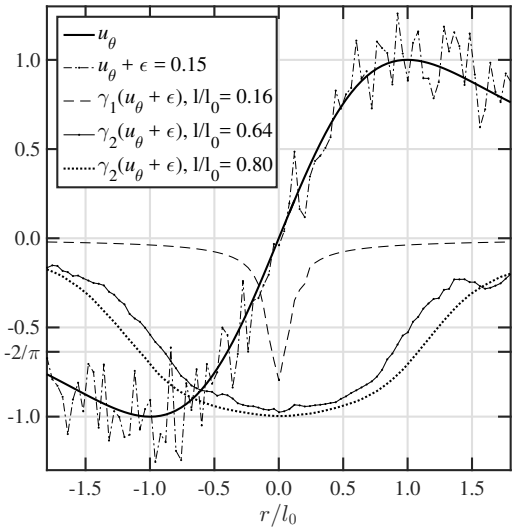

Figure 4: γ_1 and γ_2 criteria for a Lamb-Oseen vortex.

In the γ_2 criterion, the average convection velocity $\langle\mathbf{u}\rangle$ in the region S is subtracted from every velocity point in the interrogation window, such that

$$\gamma_2 = \frac{1}{N}\sum_S \frac{\mathbf{PM}\times(\mathbf{u}_\mathrm{M}-\langle\mathbf{u}\rangle)}{||\mathbf{PM}||\cdot||\mathbf{u}_\mathrm{M}-\langle\mathbf{u}\rangle||}, \qquad (2)$$

where

$$\langle\mathbf{u}\rangle = \frac{1}{N}\sum_S \mathbf{u}_\mathrm{M}. \qquad (3)$$

2.5 CALIBRATION OF THE VORTEX DETECTION CRITERIA

To calibrate the vortex detection criteria, the γ_1 and γ_2 algorithms are implemented for an isolated Lamb-Oseen vortex. The tangential velocity of the Lamb-Oseen vortex is

$$u_\theta = \frac{\Gamma}{2\pi r}\left(1-\exp\left(-\frac{r^2}{l_0^2}\right)\right), \qquad (4)$$

where Γ is the strength of the vortex, r is the radial coordinate and l_0 is the core vortex size, defined as the radial coordinate where the tangential velocity is maximum.

The γ_1 and γ_2 criteria for the Lamb-Oseen vortex are shown in Fig. 4. The γ_2 criterion is computed for two different sizes l of the interrogation window S: $l/l_0 = 0.64$ and 0.80; for γ_1, $l/l_0 = 0.15$. The centre of the vortex is identified by the maximum of both the γ_1 and γ_2 criteria, while the radius of the vortex core is identified by $|\gamma_2| = 2/\pi$.

A random error $\epsilon = 15\%\, u_\theta$ is included to model the effect of PIV noise that is generated during acquisition and post-processing [19]. A 15% noise in γ_1 is found to decrease the magnitude of the detection peak by 30%. When l/l_0 decreases, γ_2 shows greater fluctuations and it behaves more like a local criterion. This leads to the underestimation of the vortex core size. For the γ_1 criterion, the smaller the l/l_0 is set, the narrower the detection peak becomes [8].

In the present experiment, the LEV core size is found to be ca. $l_0 = 0.1c$. The size l of the interrogation window is set to $l/l_0 = 0.16$ and 0.80 for γ_1 and γ_2, respectively. The noise level in the experiment is estimated to be ca. $15\%\, u_\theta$. In fact, the maximum $|\gamma_1|$ on the sail is 0.7.

2.6 COMPLEX POTENTIAL MODEL

In order to estimate the contribution of the LEV to the lift of the sail, a potential flow model of a circular arc is developed. This has the same chord c and maximum thickness t than the considered sail's section, and it experiences a uniform flow with the same free stream velocity U_∞ and angle of attack α with respect to the chord. The arc can be mapped onto a rotating circular cylinder that has the same circulation and lift than the arc. The cylinder is defined in the complex plane ζ, where the complex coordinate

$$\zeta \equiv X + iY \equiv re^{i\theta} \qquad (5)$$

identifies a position vector in the Cartesian coordinates (X, Y) and in the polar coordinates (r, θ). The velocity potential $\phi = \phi(\zeta)$ and the stream function $\psi = \psi(\zeta)$ are such that the velocity in the $X-$direction is

$$U \equiv \frac{\partial\phi}{\partial X} \equiv \frac{\partial\psi}{\partial Y}, \qquad (6)$$

and the velocity in the $Y-$direction is

$$V \equiv \frac{\partial\phi}{\partial Y} \equiv -\frac{\partial\psi}{\partial X}. \qquad (7)$$

The complex potential is

$$F(\zeta) \equiv \phi(\zeta) + i\psi(\zeta), \qquad (8)$$

and the complex velocity is

$$W(\zeta) \equiv \frac{\partial F(\zeta)}{\partial \zeta} = U - iV. \tag{9}$$

The complex velocity provides the velocity field around the rotating cylinder. The cylinder is centred in $\zeta_0 = \mu e^{i\pi/2} = i\mu$ and has a radius $R = c/(4\cos\beta)$, where $\beta = \arcsin(2t/c)$ (Fig. 5).

The velocity field in the ζ plane of the cylinder can be mapped onto the plane $\hat{z}$ of the circular arc with the Joukowski transformation

$$\hat{z} = \zeta + \frac{(R\cos\beta)^2}{\zeta}. \tag{10}$$

In the $\hat{z}$ plane, the coordinate system is centred in the middle of the chord, such that the $\hat{x}-$axis is in the direction of the chord and positive toward the trailing edge, and the $\hat{y}-$axis is positive toward the suction side.

Finally, a further transformation

$$z = \hat{z}e^{-i\alpha} \tag{11}$$

allows a description of the flow field in the flume reference system, where the $x-$axis is aligned with the free stream velocity U_∞. These two transformations are shown in Fig. 6.

The complex potential of the cylinder in the ζ plane is

$$F_0(\zeta) = U_\infty(\zeta - \zeta_0)e^{-i\alpha} + \frac{U_\infty R^2 e^{i\alpha}}{\zeta - \zeta_0} - \frac{i\Gamma_0}{2\pi}\ln(\zeta - \zeta_0), \tag{12}$$

where

$$\Gamma_0 = -4\pi U_\infty R\sin(\alpha + \beta) \tag{13}$$

is the circulation of the cylinder. Circulation values are defined positive anticlockwise.

The LEV can be modelled as a free vortex in the ζ plane. The circulation of the free vortex Γ_{LEV} is computed from the measured flow field, as the integral of the tangential velocity over the closed iso-line $\mathbf{l}$ of the γ_2 criterion, where $\gamma_2 = 0.70$:

$$\Gamma_{\mathrm{LEV}} = \oint_{|\gamma_2|=0.70} \mathbf{u}\cdot \mathrm{d}\mathbf{l}. \tag{14}$$

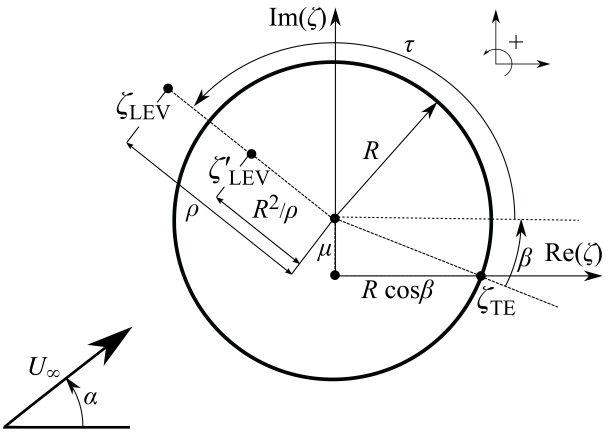

Figure 5: Complex potential model in the ζ plane.

The coordinates of the centre of the LEV, determined with the γ_2 criteria, are used to compute its polar coordinates in terms of ρ and τ in the ζ plane

$$\zeta_{LEV} = \rho e^{i\tau} + \mu e^{i\pi/2}. \tag{15}$$

If only one free vortex was added, the cylinder would no longer be impermeable and in the $\hat{z}$ plane, the Kutta condition would not be satisfied at the trailing edge. In order to restore the impermeability of the cylinder, a mirror vortex with circulation $-\Gamma_{\mathrm{LEV}}$ must be placed inside of the cylinder at the inverse square point

$$\zeta'_{LEV} = \frac{R^2}{\rho}e^{i\tau} + \mu e^{i\pi/2}. \tag{16}$$

To cancel the circulation of the mirror vortex $-\Gamma_{\mathrm{LEV}}$, the bound circulation of the cylinder is increased by Γ_{LEV}. Moreover, to satisfy the Kutta condition, the bound circulation of the cylinder Γ_b must be different from the circulation Γ_0 of the cylinder in isolation. The total circulation inside of the boundary of the cylinder is $\Gamma_b - \Gamma_{\mathrm{LEV}} + \Gamma_{\mathrm{LEV}} = \Gamma_b$.

The resulting complex potential is

$$\begin{aligned} F(\zeta) = {} & U_\infty(\zeta - \zeta_0)e^{-i\alpha} \\ & + \frac{U_\infty R^2 e^{i\alpha}}{(\zeta - \zeta_0)} - \frac{i(\Gamma_\mathrm{b} + \Gamma_{\mathrm{LEV}})}{2\pi}\ln(\zeta - \zeta_0) \\ & - \frac{i\Gamma_{\mathrm{LEV}}}{2\pi}\ln\frac{\zeta - \zeta_{\mathrm{LEV}}}{\zeta - \zeta'_{\mathrm{LEV}}}. \end{aligned} \tag{17}$$

where the first line is the contribution of the free stream, the second line is due to the cylinder and the circulation in the centre of the cylinder and the third line is due to the free vortices in ζ_{LEV} and ζ'_{LEV}. By derivation of the complex potential, we compute the complex velocity as

$$\begin{aligned} W(\zeta) = {} & U_\infty e^{-i\alpha} \\ & - \frac{U_\infty R^2 e^{i\alpha}}{(\zeta - \zeta_0)^2} - \frac{i(\Gamma_\mathrm{b} + \Gamma_{\mathrm{LEV}})}{2\pi}\frac{1}{\zeta - \zeta_0} \\ & - \frac{i\Gamma_{\mathrm{LEV}}}{2\pi}\frac{\zeta - \zeta'_{\mathrm{LEV}}}{\zeta - \zeta_{\mathrm{LEV}}}. \end{aligned} \tag{18}$$

Having derived the complex velocity for a generic Γ_b, it is now possible to compute the Γ_b that satisfies the Kutta condition. The ζ_{TE} coordinate, corresponding to the trailing edge of the circular arc in the $\hat{z}$ plane, must be a stagnation point of the cylinder. Using Eq. (18) to evaluate $W(\zeta = \zeta_{TE}) = 0$, we find that

$$\Gamma_b = \Gamma_0 - \kappa\Gamma_{\mathrm{LEV}}, \tag{19}$$

where

$$\kappa \equiv \frac{1 - \frac{\rho}{R}\cos(\beta + \tau)}{\frac{1}{2}[(\frac{\rho}{R})^2 + 1] - \frac{\rho}{R}\cos(\beta + \tau)}. \tag{20}$$

is a geometric coefficient that takes into account the relative position of the LEV. Due to the proximity of the LEV to the surface of the circular arc, $\rho \approx R$ and thus $\kappa \approx 1$. This result shows that if the LEV introduces new circulation, the bound circulation must decrease by almost the same amount, i.e.

$$\Gamma_b + \Gamma_{\mathrm{LEV}} \approx \Gamma_0. \tag{21}$$

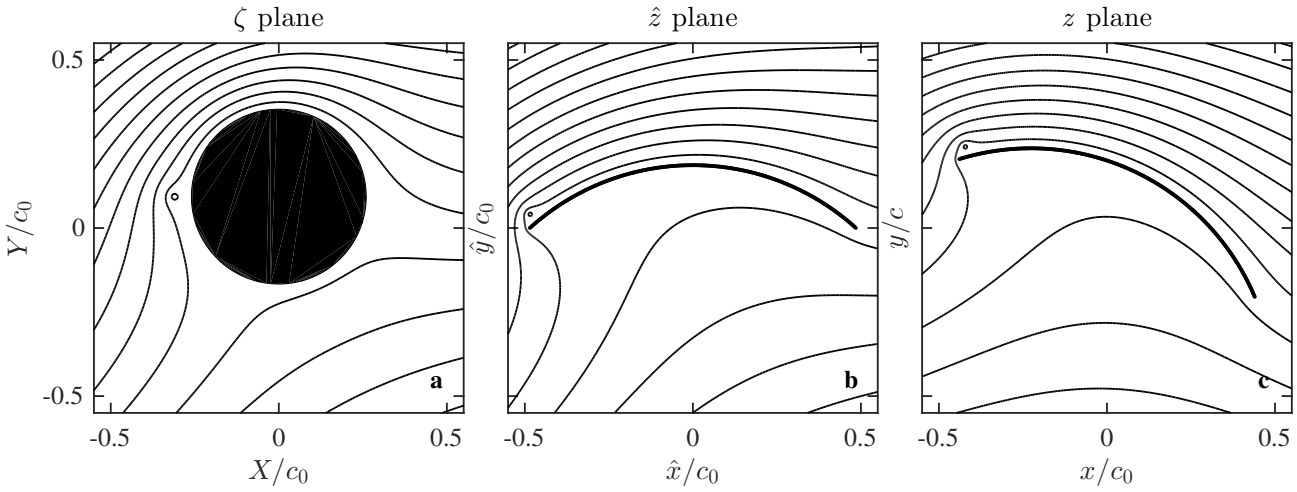

Figure 6: Velocity potential streamlines in the ζ plane (**a**) and the transformations in Eq. 10 (**b**) and Eq. 11 (**c**).

Using the Kutta-Joukowski theorem, the lift coefficient for the circular arc in the presence of the LEV is written as

$$C_L = -\frac{\Gamma_b + \Gamma_{\text{LEV}}}{\frac{1}{2}U_\infty c} = -\frac{\Gamma_b}{\frac{1}{2}U_\infty c} - \frac{\Gamma_{\text{LEV}}}{\frac{1}{2}U_\infty c}. \quad (22)$$

In the Results, the lift coefficient contribution due to the bound circulation

$$C_{L_b} \equiv -\frac{\Gamma_b}{\frac{1}{2}U_\infty c} \quad (23)$$

and the lift coefficient contribution due to the LEV

$$C_{L_{\text{LEV}}} \equiv -\frac{\Gamma_{\text{LEV}}}{\frac{1}{2}U_\infty c} \quad (24)$$

will be compared.

3 RESULTS

3.1 FLOW AND VORTICITY FIELDS

Figure 7 shows the time-averaged vector fields, streamlines and vorticity contours for the planes A, B and C. The local angle of attack increases from plane A to plane C due to the twist of the sail. The maximum camber also increases from plane A to plane C. Planes A and B show flow separation at the leading edge and flow reattachment further downstream. The leading edge vortex is shown by the concentric streamlines at the leading edge (Fig. 7e). The instantaneous wall normal velocity profiles (yellow lines in Figs. 7a and 7b) show reattachment downstream of the LEV in 90% of the image pairs. Differently to a laminar separation bubble (LSB), the separation of the LEV occurs at the leading edge and its diameter grows towards the tip of the sail (from plane C to plane A). The streamlines are concentric and swirl towards the centre of the vortex, where high speed flow is ejected along its axis of rotation.

On plane C, the flow remains attached at the leading edge but separates at $x/c = -0.3$ without reattaching. Vorticity contours show the shear layer generated at the leading edge for the three planes. The separated shear layer curves down in planes A (Fig. 7g) and B (Fig. 7h) showing the effect of the high circulation on these planes, while it is straighter on plane C (Fig. 7i) where trailing edge separation occurs.

3.2 VORTEX TOPOLOGY

The γ_2 contours for the instantaneous velocity fields of planes A, B and C are presented in Fig. 8. A sequence of 9 consecutive images is presented for a total period of time $\Delta t^* = 1.1$, where the time t is made non-dimensional with the chordwise convection period c_0/U_∞, i.e. $t^* \equiv tU_\infty/c_0$. The sequences are taken at different times on each plane, since the experimental setup does not allow simultaneous recording of the planes. On planes A and C, vortices are shed with a convective velocity of $0.6U_\infty$ in plane A and $0.3U_\infty$ in plane C. On planes A and B, a stable LEV that remains attached to the leading edge is observed. Indeed, the LEV on these planes is intermittently stable. For example, on plane B, during the sampling period of $0.0 < t^* < 42.3$, a stable LEV was found for $0.0 < t^* < 9.0$, $16.0 < t^* < 23.6$ and $36.7 < t^* < 42.3$.

Fig. 9 shows the γ_1 and γ_2 criteria on planes A and B, averaged over the course of the entire sampling period $0.0 < t^* < 42.3$. The vortex size grows from plane B (Fig. 9b) to plane A (Fig. 9a), i.e. in the direction of the tip which is where the vorticity is extracted. The γ_1 criterion has one global maximum at the centre of the LEV. The maximum γ_1 is 0.7 in plane A and 0.8 in plane B. Conversely, the γ_2 criterion has two local maxima on each plane. On plane A, the maxima are both 0.79. On plane B, these are 0.79 near the leading edge and 0.76 at ca. $x/c = -0.2$.

In Fig. 10, the γ_2 criterion is computed for the time-averaged flow fields corresponding to the sequence in Fig. 8, for a period $\Delta t^* = 1.1$. The region near the leading edge is zoomed in to give a closer look at the LEV on planes A and B. On plane A, the γ_2 iso-lines with low value have an

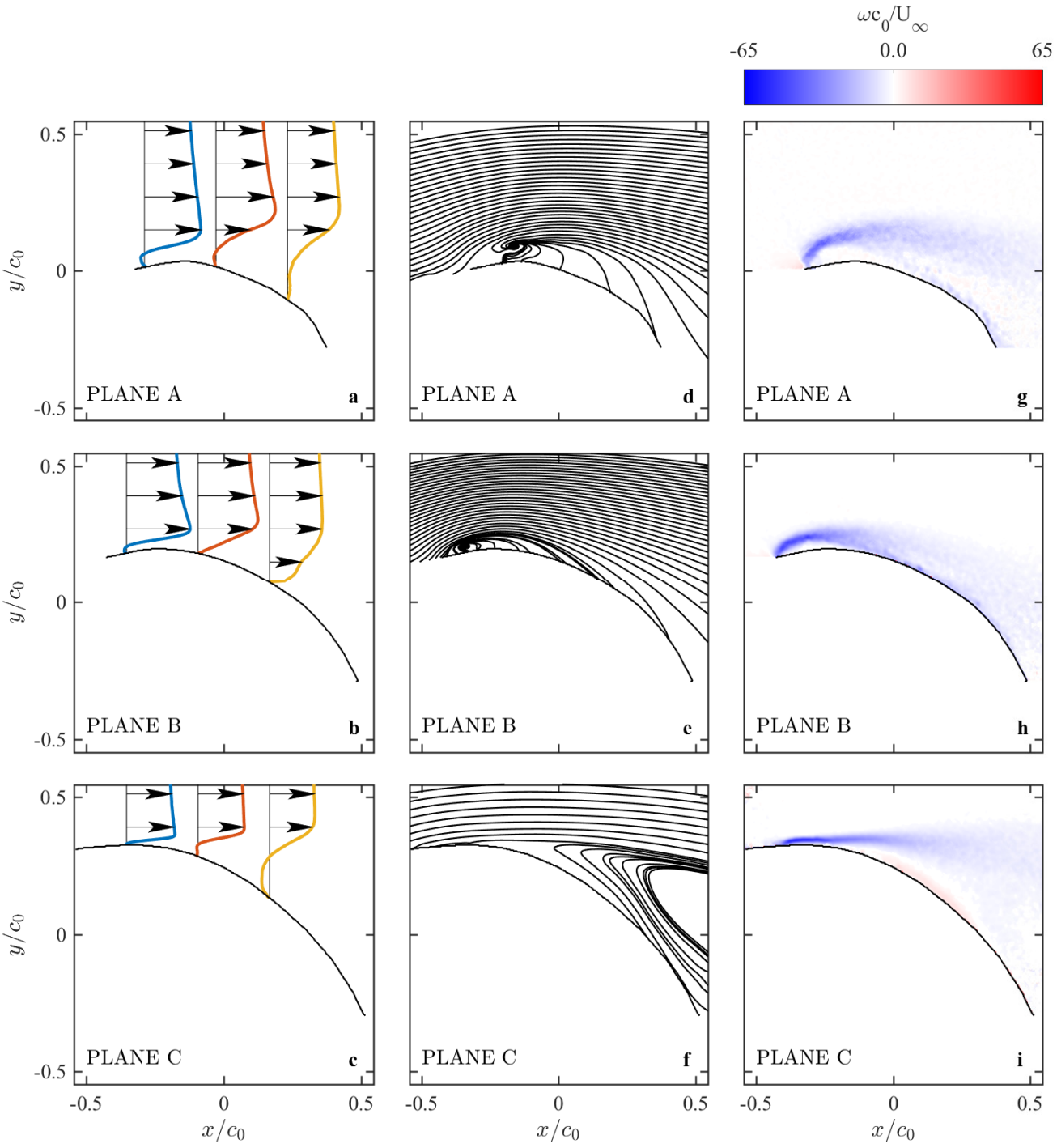

Figure 7: Time-averaged velocity profiles (**a, b, c**), streamlines (**d, e, f**) and contours of non-dimensional vorticity (**g, h, i**) on the planes A, B and C. Data is averaged over a period $0.0 < t^* < 42.3$.

elongated shape, but the LEV has only one core near the leading edge. Conversely, on plane B, the LEV is split into two co-rotating cores, as on a dual LEV [11, 9].

3.3 COMPLEX POTENTIAL MODEL

The underlying question that this work aims to address, is the effective contribution of the LEV to the sail performance. Recalling that the total lift coefficient can be broken down into the contribution of the bound circulation C_{L_b} and the contribution of the LEV $C_{L_{\mathrm{LEV}}}$, the ratio $C_{L_{\mathrm{LEV}}}/C_{L_b} = \Gamma_{LEV}/\Gamma_b$ is computed. The conservative estimate is made that the Kutta

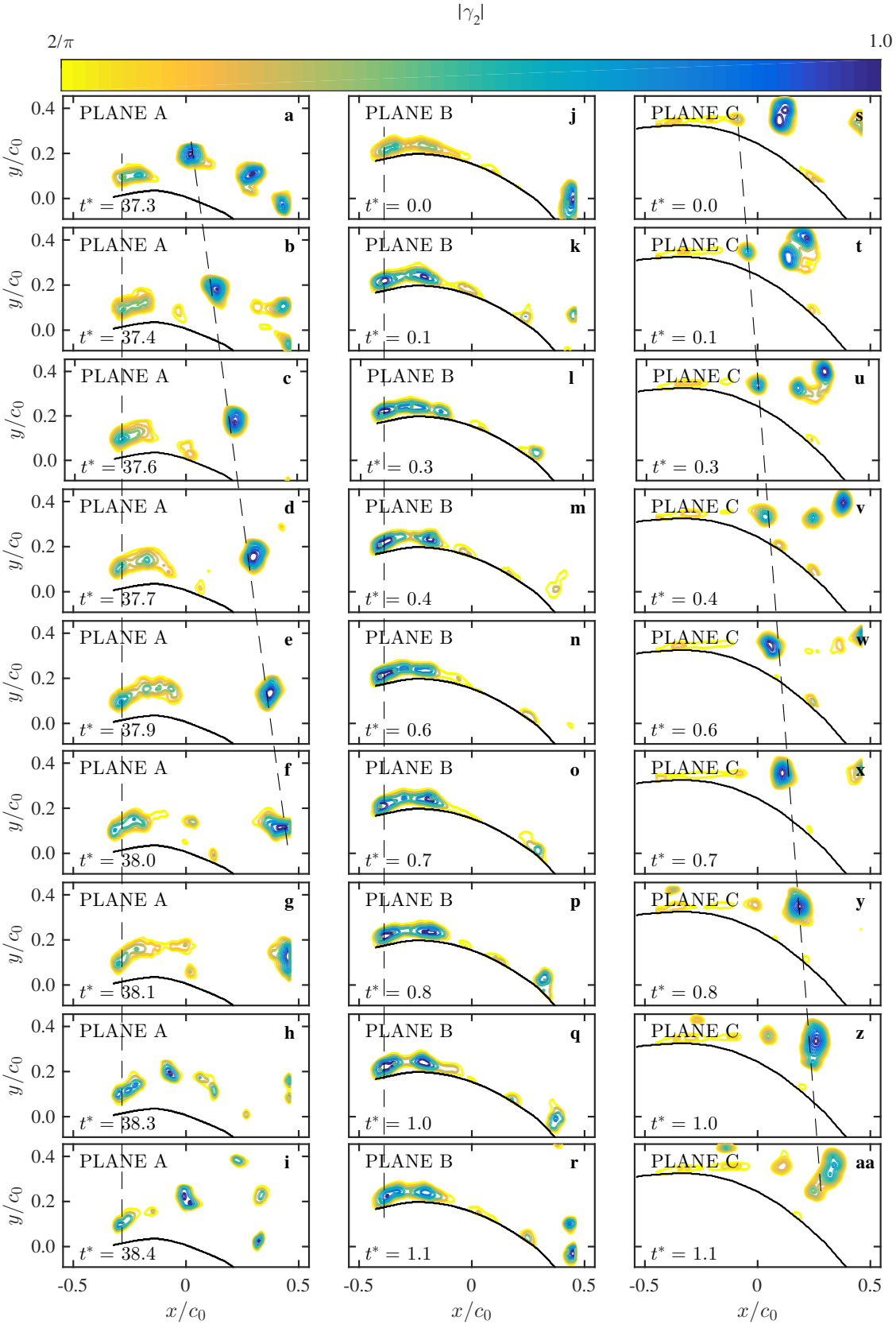

Figure 8: γ_2 criterion on instantaneous velocity fields for planes A (**a**-**i**), B (**j**-**r**) and C (**s**-**aa**). Data corresponds to a period of $\Delta t^* = 1.1$, in the interval $0.0 < t^* < 42.3$.

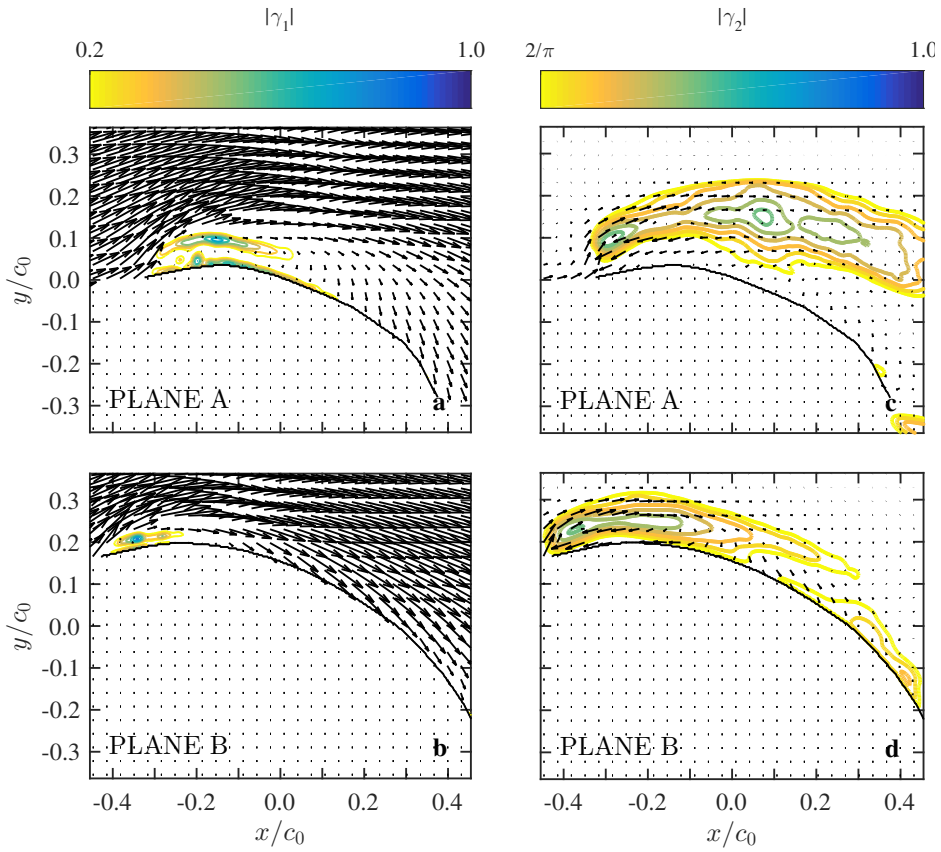

Figure 9: γ_1 and γ_2 criteria of the time-averaged velocity field measured for $0.0 < t^* < 42.3$ on the planes A and B.

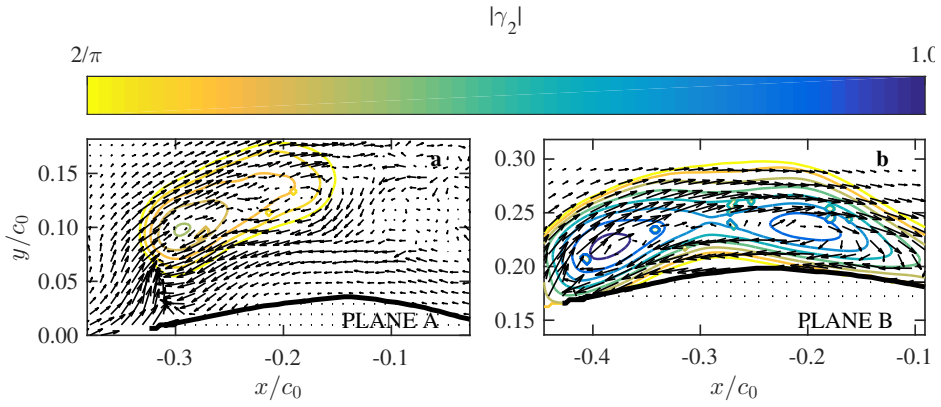

Figure 10: γ_2 criterion of the velocity field measured on planes A and B and time-averaged over the periods $\Delta t^* = 1.1$ presented in Fig. 8.

condition is satisfied when the LEV is present. Since trailing edge actually occurs and the Kutta condition is not satisfied, the computed bound circulation is higher than the actual value.

The circulation of the LEV Γ_{LEV} is computed by integrating along the iso-line of $\gamma_2 = 0.7$, the flow velocity tangential to the iso-line. The bound circulation is computed from Eqs. 13, 19, and 20. Eqs. 19 and 20 show that Γ_b increases with the distance of the LEV from the sail (i.e. with ρ/R) and with the angle of attack α. Table 1 shows the experimental values of the different parameters that contributes to compute Γ_b. It can be seen that from plane A to plane B, ρ/R decreases but α increases, leading to two similar values of κ. It is found that $C_{L_{\mathrm{LEV}}}/C_{L_b} = \Gamma_{\mathrm{LEV}}/\Gamma_b = 0.21$ and 0.16 on planes A and B, respectively. Therefore, the contribution of the LEV is of paramount importance in the performances of the sails.

Table 1: Input values and results of the complex potential flow model for planes A and B.

	α	β	τ	t/c	ρ/c	κ	Γ_{LEV}/Γ_b
Plane A	22^o	18.8^o	180^o	0.17	0.34	0.87	0.21
Plane B	25^o	18.8^o	180^o	0.17	0.31	0.91	0.16

4 CONCLUSIONS

Recent high-fidelity numerical simulations [24] suggested that a LEV is formed at the leading edge of asymmetric spinnakers and that it remains stably attached to the sail providing lift augmentation. This finding is investigated in the present paper. A model-scale asymmetric spinnaker is tested in uniform flow in a water flume. The Reynolds number based on the chord c_0 at 3/4$^{\text{th}}$ of the mitre and the free stream velocity U_∞ is 1.3×10^4. PIV shows that the LEV is absent or of negligible dimensions on the lower half of the sail, where trailing edge separation is dominant. The separation point is found well upstream of the mid-chord. On the higher half of the sail, the LEV is formed and it grows in size towards the head of the sail, where it merges with the tip vortex. Downstream of the LEV, the flow reattaches and a turbulent boundary layer is formed. The LEV remains attached to the leading edge intermittently. For a period of time of the order of $10c/U_\infty$, the LEV is stably attached, and then for a period of similar length the LEV is continuously shed. When the LEV is attached, its contribution to the lift on the upper half of the sail is between 16% and 21%. The contribution on the total lift could not be measured, but given that the majority of the lift is generated by the upper half of the sails, it is expected to be higher than 10%. These results suggest that the performance of asymmetric spinnakers could be enhanced significantly by controlling the formation and stability of the LEV.

5 ACKNOWLEDGEMENTS

This work was funded by the Consejo Nacional de Ciencia y Tecnología (CONACYT).

REFERENCES

[1] F. Bethwaite. *High Performance Sailing*. Waterline Books, UK, 1993.

[2] I. Borazjani and M. Daghooghi. The fish tail motion forms an attached leading edge vortex. *Proc R Soc B*, 280:20122071, 2013.

[3] I. M. Bot, P.and Viola, R. G. J. Flay, and J.-S. Brett. Wind-tunnel pressure measurements on model-scale rigid downwind sails. *Ocean Eng*, 90:84–92, 2014.

[4] T. C. Corke and F. O. Thomas. Dynamic stall in pitching airfoils: Aerodynamic damping and compressibility effects. *Annu Rev Fluid Mech*, 47:479–505, 2015.

[5] C. P. Ellington. The novel aerodynamics of insect flight: applications to micro-air vehicles. *J Exp Biol*, 202(23):3439–3448, 1999.

[6] D. J. Garmann, M. R. Visbal, and P. D. Orkwis. Three-dimensional flow structure and aerodynamic loading on a revolving wing. *Phys Fluids*, 25(3), 2013.

[7] R. E. Gordnier, M. R. Visbal, I. Gursul, and Z. Wang. Computational and experimental investigation of a non-slender delta wing. *AIAA J*, 47(8):1811–1825, 2009.

[8] L. Graftieaux, M. Michard, and N. Grosjean. Combining PIV, POD and vortex identification algorithms for the study of unsteady turbulent swirling flows. *Meas Sci Technol*, 12(1201):1422–1429, 2001.

[9] I. Gursul, R. Gordnier, and M. Visbal. Unsteady aerodynamics of nonslender delta wings. *Prog Aerosp Sci*, 41(7):515–557, 2005.

[10] I. Gursul, Z. Wang, and E. Vardaki. Review of flow control mechanisms of leading-edge vortices. *Prog Aerosp Sci*, 43(7-8):246–270, 2007.

[11] R. R. Harbig, J. Sheridan, and M. C. Thompson. Relationship between aerodynamic forces, flow structures and wing camber for rotating insect wing planforms. *J Fluid Mech*, 730:52–75, 2013.

[12] R. R. Harbig, J. Sheridan, and M. C. Thompson. Reynolds number and aspect ratio effects on the leading-edge vortex for rotating insect wing planforms. *J Fluid Mech*, 717:166–192, 2013.

[13] M. Honkanen and H. Nobach. Background extraction from double-frame PIV images. *Exp Fluids*, 38(3):348–362, 2005.

[14] T. Y. Hubel and C. Tropea. The importance of leading edge vortices under simplified flapping flight conditions at the size scale of birds. *J Exp Biol*, 213(11):1930–1939, 2010.

[15] T. Jardin and L. David. Spanwise gradients in flow speed help stabilize leading-edge vortices on revolving wings. *Phys Rev E*, 90(1):013011, 2014.

[16] J. W. Larsen, S. R. K. Nielsen, and S. Krenk. Dynamic stall model for wind turbine airfoils. *J Fluid Struct*, 23(7):959–982, 2007.

[17] D. Lentink, W. B. Dickson, J. L. van Leeuwen, and M. H. Dickinson. Leading-edge vortices elevate lift of autorotating plant seeds. *Science*, 324(5933):1438–1440, 2009.

[18] D. Lentink, U. K. Müller, E. J. Stamhuis, R. de Kat, W. van Gestel, L. L. M. Veldhuis, P. Henningsson, A. Hedenström, J. J. Videler, and J. L. van Leeuwen.

How swifts control their glide performance with morphing wings. *Nature*, 446(7139):1082–1085, 2007.

[19] C. E. Morgan, H.r Babinsky, and J. K. Harvey. Vortex detection methods for use with PIV and CFD data. In *47th AIAA Aerospace Sciences Meeting*, Orlando, Florida, 2009.

[20] F. T. Muijres, L. C. Johansson, R. Barfield, M. Wolf, G. R. Spedding, and A. Hedenström. Leading-Edge Vortex Improves Lift in Slow-Flying Bats. *Science*, 319(5867):1250–1253, 2008.

[21] C. Pitt Ford and H. Babinsky. Lift and the leading-edge vortex. *J Fluid Mech*, 720:280–313, 2013.

[22] J. Rabinovitch, V. Brion, and G. Blanquart. Effect of a splitter plate on the dynamics of a vortex pair. *Phys Fluids*, 24(7), 2012.

[23] R. B. Srygley and A. L. R. Thomas. Unconventional lift-generating mechanisms in free-flying butterflies. *Nature*, 420(6916):660–664, 2002.

[24] I. M. Viola, S. Bartesaghi, T. Van-Renterghem, and R. Ponzini. Detached eddy simulation of a sailing yacht. *Ocean Eng*, 90:93–103, 2014.

[25] I. M. Viola and R. G. J. Flay. Force and pressure investigation of modern asymmetric spinnakers. *International Journal of Small Craft Technology Transaction RINA Part B2*, 151(2):31–40, 2009.

[26] I. M. Viola and R. G J Flay. Pressure distributions on modern asymmetric spinnakers. *International Journal of Small Craft Technology Transaction RINA Part B1*, 152(1):41–50, 2010.

[27] I. M. Viola and R. G. J. Flay. Sail aerodynamics: Understanding pressure distributions on upwind sails. *Exp Therm and Fluid Sci*, 35(8):1497–1504, 2011.

[28] I. M. Viola and R. G. J. Flay. Sail pressures from full-scale, wind-tunnel and numerical investigations. *Ocean Eng*, 38(16):1733–1743, 2011.

[29] I. M. Viola and R. G. J. Flay. Sail aerodynamics: on-water pressure measurements on a downwind sail. *J Ship Res*, 56(4):197–206, 2012.

[30] I. M. Viola and R. G. J. Flay. Aerodynamics of head-sails: a review of measured surface pressures and expected flow fields. In *5th High Performance Yacht Design Conference*, Auckland, New Zealand, 2015.

6 AUTHORS BIOGRAPHY

Dr Ignazio Maria Viola is Senior Lecturer at the Institute for Energy Systems of the School of Engineering, University of Edinburgh and a Fellow of the Royal Institution of Naval Architects. He is Editor-in-Chief of the Journal of Sailing Technology (SNAME), and Member of the Editorial Board of Ocean Engineering (Elsevier) and the International Journal of Small Craft Technology (RINA). His background is in yacht sail aerodynamics, and his current research focuses on the control of vortical flow structures by means of flexible surfaces. He wrote more than 100 scientific publications and was awarded two RINA Medals of Distinctions and a RINA Medal of Exceptional Merit.

Abel Arredondo-Galeana is a PhD student at the University of Edinburgh, working under the supervision of Dr Viola. He has a background in Mechatronics Engineering and industrial experience as a wireline field engineer in the oil and gas industry. He was awarded a masters degree with honours in Sustainable Energy Systems at the University of Edinburgh in 2014. His thesis aimed at the developing a novel experimental rig for testing model-scale self-damping Flettner rotors for wind-assisted ship propulsion. Successively, he was funded a scholarship by the Consejo Nacional de Ciencia y Tecnología (CONACYT) to pursue his PhD project. His research aims to gain new insights on the vortex flow of yacht sails to enhance sail performances by design.